Numerical Modelling of Lava Dynamics

Zur Erlangung des akademischen Grades eines

DOKTORS DER NATURWISSENSCHAFTEN (Dr. rer. nat.)

von der KIT-Fakultät für

Bauingenieur-, Geo- und Umweltwissenschaften
des Karlsruher Instituts für Technologie (KIT)

genehmigte

DISSERTATION

von

Natalya Zeinalova, M.Sc.

Tag der mündlichen Prüfung: 28. Mai 2025
Hauptreferent: Priv.-Doz. Dr. Alik Ismail-Zadeh
Korreferent: Prof. Dr. Augusto Neri

Karlsruhe (2025)

Summary

Effusive eruptions are among important volcanological studies. Lava flow mostly associated with low viscosity advances on long distances, whereas high viscous lava tends to form lava domes. Effusive eruptions are generally less dangerous than explosive eruptions. However, the lava effusions, dome collapses and associated pyroclastic flow hazards cause significant damage to the infrastructure and property surrounding a volcano. The main factors controlling the morphology of lava flows and lava domes are the lava rheology, discharge rate and ground topography. Numerical models of lava flows help to analyse the influence of the lava rheology, the role of crystal content, temperature and discharge rate on morphological features of lava flows and lava domes. In this work several numerical models of lava dome growth and lava flows are developed. The modelling approaches include two- and three-dimensional simulations of two phase viscous incompressible fluid flow approximating the extrusion of lava into air under isothermal and thermal conditions. The simulations are performed using finite volume methods implemented in Ansys Fluent and OpenFOAM software. Also, simplified models are employed based on the cellular automaton approach and on the shallow water approximation.

In the isothermal modelling of lava dome growth, we analyze the influence of the magma viscosity, the crater geometry, the conduit location, the effective viscosity of dome carapace and the discharge rates on the lava dome morphology at Volcán de Colima in Mexico during a long dome-building episode lasting three years. The viscosity in this case solely depends on the crystallization. Due to the interplay between the lava extrusion and the gravity forces, the dome reaches a height threshold, and despite high effective viscosity a horizontal gravity spreading starts to play an essential role in the lava dome evolution. These results reveal that the development of the dome carapace of higher viscosity due to cooling is likely to influence the dome growth and its morphology during long dome-building growth by retarding horizontal advancement and resulting in a steep-sided lava dome development.

Thermo-mechanical numerical modelling of long-term lava dome growth at Volcán de Colima focuses on understanding the influence of various heat sources and thermal conditions on lava dome morphology. The model results demonstrate how convective and non-linear convective-radiative heat transfer mechanisms at the lava-air interface affect the morphological shape of the lava dome during long episodes of dome building. The latent heat release due to

crystallization leads to an increase in temperature in the lava dome interior and to a relative flattening of the dome. Meanwhile, the heat source due to viscous dissipation within the lava dome is negligible, as it does not affect the lava dome growth. Variations in the thermal boundary conditions at the model conduit wall and crater base influence the crystal content and temperature distributions within the model conduit but do not significantly affect the morphological shape of the lava dome. The temperature-dependent volume fraction of crystal content at equilibrium state leads to a slight decrease in crystal content within the dome interior.

The numerical results of these models highlight the following key points: In the isothermal model, where the lava viscosity is solely influenced by the crystallization process, rapid crystallization results in the viscosity approaching its maximum value. Afterward, the lava behaves as a fluid of a constant viscosity, spreading horizontally on the topography. In the thermal case study, where the model accounts for radiative-convective heat transfer at the lava-air interface, the corresponding cooling of the upper layer of the lava dome and subsequent carapace formation due to the heat transfer lead to alterations in the morphological shape and the internal structure of the lava dome.

The next part of the thesis focuses on the analysis of the influence of Newtonian, Bingham and Herschel-Bulkley rheological models on lava flow morphology and its advancement. Numerical simulations are performed using a two-dimensional cellular automaton model which simulates lava flow advancement. The model results reveal that changes in the crystal content, relaxation time, and yield strength impact lava flow patterns. Low melt viscosity promotes lava to advance, whereas high melt viscosity encourages lateral spreading of the lava flow. The higher the volume fraction of crystals at the equilibrium state is the shorter the lava flow. The results also demonstrate that the interplay between the yield strength and the melt viscosity determines the lava flow direction, its thickness and advancement pattern.

Other numerical simulations are conducted using a three-dimensional fluid dynamics model and its simplified depth-averaged model based on the shallow water approximation. Initially, we performed isothermal lava flow modelling using different rheological models. The results show that increased yield strength significantly influences the lava flow morphology by restricting flow advance and promoting upward growth of lava flows. Secondly, to access the impact of temperature on lava flow morphology, we perform a set of simulations using temperature-dependent rheological models. The results of the thermal numerical models

demonstrate that Newtonian and Bingham fluids behave similarly, the viscosity distributions in both cases remain relatively low within the flow, promoting further lava advancement. The Herschel-Bulkley model due to the highest viscosity values results in the shortest flow advancement among all three temperature-dependent rheological models. Comparing the results between the isothermal and thermal cases, we observe that the lava flow in the isothermal cases advances rapidly. In contrast, the lava flows in the thermal cases cease its rapid advancement due to increased thickness at the flow front and elevated viscosity. For validation purposes we perform benchmark tests against the analytical solution of the axisymmetric viscous gravity current problem. The results of the numerical models align closely with the analytical solution, with the depth averaged model providing the best match to analytics due to the shared foundations of the analytical approach and the shallow water approximation.

Finally, as an application to a real lava flow, we model the effusive phase of Mt. Etna's December 2015 eruption utilizing the temperature-dependent Newtonian, Bingham and Herschel-Bulkley models. All thermal rheological models approximate the real lava flow width accurately, with the Newtonian model providing the best match for flow extent and developing the same morphological features as the real lava emplacement. While the Herschel-Bulkley model shows slight deviation in lava flow length, the Bingham model results closely match the observed main flow branch, with minor divergence in the upper branches. Furthermore, the modelled thickness distribution aligned well with the observational thickness, presenting increased lava accumulation near the crater and at the flow front.

Zusammenfassung

Effusive Eruptionen gehören zu den wichtigsten vulkanologischen Untersuchungen. Niedrigviskose Lavaströme können über weite Strecken fließen, während hochviskose Lava zur Bildung von Lavadomen neigt. Effusive Eruptionen sind im Allgemeinen weniger gefährlich als explosive Eruptionen. Dennoch verursachen Lavaausflüsse, kollabierenden Lavadomen und die mit ihnen einhergehenden Ströme erhebliche Schäden an Infrastruktur und Bebauung in der Umgebung eines Vulkans. Die wichtigsten Faktoren, die die Morphologie von Lavaströmen und Lavadomen steuern, sind die Lavarheologie, die Abflussrate und die Bodentopografie. Mit Hilfe numerischer Modelle von Lavaströmen kann der Einfluss der Lavarheologie, des Kristallgehalts, der Temperatur und der Abflussrate auf die morphologischen Merkmale von Lavaströmen und Lavadomen analysiert werden. In dieser Arbeit werden mehrere numerische Modelle für das Wachstum von Lavadomen und Lavaströmen entwickelt. Die Modellierungsansätze umfassen zwei- und dreidimensionale Simulationen einer zweiphasigen viskosen inkompressiblen Flüssigkeitsströmung, welcher die Extrusion von Lava in Luft unter isothermen und thermischen Bedingungen simuliert. Die Simulationen werden mit Finite-Volumen-Methoden in den Softwarepaketen Ansys Fluent und OpenFOAM durchgeführt. Zusätzlich werden vereinfachte Modelle entwickelt, das auf dem Ansatz des cellular Automaten basiert und auf der Flachwassernäherung beruht.

Bei der isothermen Modellierung des Lavadomwachstums analysieren wir den Einfluss der Magmaviskosität, der Kratergeometrie, der Lage des Conduits, der effektiven Viskosität des Kuppelpanzers und der Abflussraten auf die Morphologie des Lavadoms am Volcán de Colima in Mexiko während einer langen Lavadombildungsepisode von drei Jahren. Das Viskositätsmodell hängt in diesem Fall ausschließlich von den Kristallisation ab. Aufgrund des Zusammenspiels zwischen der Lavaextrusion und den Schwerkräften erreicht der Dom eine Höhenschwelle, und trotz der hohen effektiven Viskosität beginnt die horizontale Schwerkraftausbreitung eine wesentliche Rolle bei der Entwicklung des Lavadoms zu spielen. Diese Ergebnisse zeigen, dass die Entwicklung des Kuppelpanzers mit höherer Viskosität aufgrund der Abkühlung wahrscheinlich das Lavadomwachstum und seine Morphologie während des langen Lavadomwachstums beeinflusst, indem sie die horizontale Vorwärtsbewegung verzögert und zu einer steilwandigen Lavadomentwicklung führt.

Die thermomechanische numerische Modellierung des langfristigen Wachstums von Lavadomen am Volcán de Colima konzentriert sich auf das Verständnis des Einflusses verschiedener Wärmequellen und thermischer Bedingungen auf die Morphologie der Lavadome. Die Modellergebnisse zeigen, wie konvektive und nichtlineare konvektiv-radiative Wärmeübergänge an der Grenzfläche zwischen Lava und Luft die morphologische Form des Lavadoms während langer Episoden der Dombildung beeinflussen. Die latente Wärmefreisetzung aufgrund der Kristallisation führt zu einem Anstieg der Temperatur im Inneren des Lavadoms und zu einer relativen Abflachung des Doms. Gleichzeitig ist die Wärmequelle aufgrund der viskosen Dissipation innerhalb des Lavadoms vernachlässigbar, da sie das Wachstum des Lavadoms nicht beeinflusst. Variationen der thermischen Randbedingungen an der Wand des Modellkanals und der Kraterbasis beeinflussen die Verteilung des Kristallgehalts und der Temperatur innerhalb des Modellkanals, haben jedoch keinen signifikanten Einfluss auf die morphologische Form des Lavadoms. Der temperaturabhängige Volumenanteil des Kristallgehalts im Gleichgewichtszustand führt zu einem leichten Rückgang des Kristallgehalts im Inneren des Doms.

Die numerischen Ergebnisse dieser Modelle zeigen die folgenden Punkte auf: Im isothermen Modell, bei dem die Viskosität der Lava ausschließlich durch den Kristallisationsprozess beeinflusst wird, führt eine schnelle Kristallisation dazu, dass sich die Viskosität ihrem Maximalwert nähert. Die Lava verhält sich dann wie eine Flüssigkeit mit konstanter Viskosität, die sich horizontal auf der Topografie ausbreitet. Im thermischen Fall, bei dem das Modell den radiativ-konvektiven Wärmeübergang an der Grenzfläche zwischen Lava und Luft berücksichtigt, führen die entsprechende Abkühlung der oberen Schicht des Lavadoms und die anschließende Panzerbildung aufgrund des Wärmeübergangs zu Veränderungen der morphologischen Form und der inneren Struktur des Lavadoms.

Der nächste Teil der Arbeit befasst sich mit der Analyse des Einflusses der rheologischen Modelle nach Newton, Bingham und Herschel-Bulkley auf die Morphologie des Lavastroms und sein Fortschreiten. Numerische Simulationen werden mit einem zweidimensionalen cellular Automatenmodell durchgeführt, das das Voranschreiten des Lavastroms simuliert. Die Modellergebnisse zeigen, dass sich Änderungen des Kristallgehalts, der Relaxationszeit und der Fließgrenze auf das Fließverhalten der Lava auswirken. Eine niedrige Schmelzviskosität begünstigt das Ausfliesen der Lava, während eine hohe Schmelzviskosität die seitliche Ausbreitung des Lavastroms fördert. Je höher der Volumenanteil der Kristalle im

Gleichgewichtszustand ist, desto kürzer ist der Lavastrom. Die Ergebnisse zeigen auch, dass das Zusammenspiel von Fließgrenze und Schmelzviskosität die Richtung des Lavastroms, seine Mächtigkeit und das Vorstoßmuster bestimmt.

Andere numerische Simulationen werden mit einem dreidimensionalen Fluiddynamikmodell und einem vereinfachten, tiefengemittelten Modell auf der Grundlage der Flachwassernäherung durchgeführt. Initial wird die isotherme Lavastrommodellierung mit verschiedenen rheologischen Modellen durchgeführt. Die Ergebnisse zeigen, dass die erhöhte Fließgrenze die Morphologie des Lavastroms erheblich beeinflusst, indem sie das Voranschreiten des Stroms einschränkt und das Aufwärtswachstum des Lavastroms fördert. Um die Auswirkungen der Temperatur auf die Morphologie der Lavaströme zu untersuchen, führen wir außerdem eine Reihe von Simulationen mit temperaturabhängigen rheologischen Modellen durch. Die Ergebnisse der thermischen numerischen Modelle zeigen, dass sich Newton‘sche und Bingham Flüssigkeiten ähnlich verhalten; die Viskositätsverteilungen bleiben in beiden Fällen innerhalb des Stroms relativ niedrig, was das weitere Voranschreiten der Lava fördert. Das Herschel-Bulkley-Modell führt aufgrund der höchsten Viskositätswerte zu dem kürzesten Fließfortschritt aller drei temperaturabhängigen rheologischen Modelle. Ein Vergleich der Ergebnisse des isothermen und des thermischen Falls zeigt, dass der Lavastrom in den isothermen Fällen weit und schnell voranschreitet. Im Gegensatz dazu bremsen in den thermischen Fällen die größere Dicke der Fließfront und die erhöhte Viskosität den Lavafluss. Zu Validierungszwecken führen wir Vergleichstests mit der analytischen Lösung des achsensymmetrischen viskosen Schwerkraftstromproblems durch. Die Ergebnisse der numerischen Modelle stimmen eng mit der analytischen Lösung überein, wobei das tiefengemittelte Modell aufgrund der gemeinsamen Grundlagen des analytischen Ansatzes und der Flachwassernäherung die beste Übereinstimmung aufweist.

Als Anwendung auf einen realen Lavastrom modellieren wir schließlich die effusive Phase des Ausbruchs des Ätna im Dezember 2015 unter Verwendung der temperaturabhängigen Newton‘schen, Bingham- und Herschel-Bulkley-Modelle. Alle thermorheologischen Modelle nähern sich der Breite des realen Lavastroms genau an, wobei das Newton‘sche Modell die beste Übereinstimmung mit der Ausdehnung des Stroms liefert und die gleichen morphologischen Merkmale wie die reale Lavaeinlagerung entwickelt. Während das Herschel-Bulkley-Modell eine geringfügige Abweichung in der Länge des Lavastroms zeigt, passt das Bingham-Modell gut zum Hauptstromzweig, mit einer geringfügigen Abweichung in den oberen Zweigen. Darüber hinaus stimmt die modellierte Mächtigkeitsverteilung gut mit der beobachteten Mächtigkeit überein und zeigt eine verstärkte Lavaakkumulation in der Nähe des Kraters und an der Fließfront.

Acknowledgments

First and foremost, I owe sincere gratitude to my supervisor PD Dr. Alik Ismail-Zadeh, Alik is the best mentor a student could wish for. Without his guidance, constant support, vast expertise and experience in computational geodynamics and geohazard modelling, this thesis would not exist. I am deeply grateful for the countless hours Alik spent reviewing my work, providing constructive suggestions and comments and always being available to discuss results, answer and explain questions, and any other matter that arose during this research. Looking back at the time when I commenced my doctoral studies makes me realise how much I learned from Alik and benefited from his vast mathematical, geophysical and general research experience. I would also like to thank Alik and his family for the support and care they have given me since the very first days of my PhD studies. The beginning of my PhD study fell at the time when the world was in lockdown and their warmth and kindness were crucial, both from a professional and personal point of view. In conclusion, I am very grateful for the chance Alik provided me to carry out this study under his supervision, it has been a great pleasure for me to be his PhD student.

I would like to express my sincere thanks to my co-supervisor, Prof. Dr. Frank Schilling, for providing me with the opportunity to conduct this research in his group, for always finding time to review and comment on my work as well as to discuss any problems I encountered during my research. I thank Prof. Dr. Augusto Neri, Prof. Dr. Armin Zeh, Prof. Dr. Nevena Tomašević and Prof. Dr. Agnes Kontny for their interest in my research and their role as members of my PhD committee. I am also grateful to Jessica Blackwell and Silke Schlichting, whose administrative support from the very beginning of my PhD was very helpful.

I am grateful to my good colleague Igor Tsepelev for his help and guidance in all technical aspects related to numerical modelling. I would like further to acknowledge the support of Dr Oleg Melnik and Prof. Jon Blundy, who hosted me during my research stay at the University of Oxford. Their guidance and ideas in the study of the influence of magma dynamics in the conduit on the morphology of lava domes have greatly contributed to establishing a trajectory for future studies.

My thanks also go to my colleagues and co-authors, Giuseppe Bilotta, Annalisa Cappello, and Gaetana Gance, who warmly hosted me in the Italian National Institute of Geophysics and Volcanology (INGV) in Catania. They shared their expertise in numerical modelling of lava flows, allowed me to perform simulations with their numerical codes and assisted me in implementing additional equations, which was a big contribution to my research. I am grateful to Francesco Zuccarello for his assistance with the GPUFLOW model and for having me on a hike of Mt. Etna which was an inspiring experience.

I express thanks to all co-authors for their contributions to the papers and to the reviewers for their thoughtful comments and thorough reviews.

I am thankful to Diana Lieber, Andreas Schenk and GRACE Graduate School for funding support that enabled my research stay at the University of Oxford. I also appreciate their encouragement to participate in courses and summer schools, providing networking opportunities with other PhD students and enriching my academic journey.

Finally, I am grateful to my mother, who has supported my pursuit of studies throughout all stages of my life, starting from my earliest school days. Her belief in the value of education and constant encouragement have paved the way for me to achieve this milestone. I am also thankful to my fiancé, Tomi, for his patience, understanding, and unwavering encouragement throughout this journey.

The present study was funded by the Deutsche Forschungsgemeinschaft (project DFG IS203/14-1).

Related Publications

The content of this thesis is based in parts on the following references, published during the course of my PhD study. The contributions of the co-authors are highly acknowledged.

Peer-reviewed journal publications

Zeinalova, N.; Ismail-Zadeh, A.; Melnik, O.; Tsepelev, I.; Zobin, V. (2021). Lava Dome Morphology and Viscosity Inferred from Data-Driven Numerical Modeling of Dome Growth at Volcán de Colima, Mexico During 2007-2009. Frontiers in Earth Science, 9, 735914. doi:10.3389/feart.2021.735914

Zeinalova, N.; Ismail-Zadeh, A.; Tsepelev, I.; Melnik, O.; Schilling, F. (2024). Numerical thermo-mechanical modelling of lava dome growth during the 2007-2009 dome-building eruption at Volcán de Colima. Geophysical Journal International, 236 (1), 290–304. doi:10.1093/gji/ggad415

Zeinalova, N., Bilotta, G., Ismail-Zadeh, A. et al. Influence of rheological parameters on lava flow morphology inferred from numerical modelling. Int J Earth Sci (Geol Rundsch) (2025). doi:10.1007/s00531-025-02513-2

Peer-reviewed book chapters and conference proceedings

Zeinalova N, Ismail-Zadeh A, Melnik O, Tsepelev I., and Schilling F. (2023). Numerical modelling of lava dome evolution. Presented at MathSEE Symposium 2023, Karlsruhe, Germany, 27-29 September. Springer Proceedings on Applications of Mathematical Methods (accepted for publication).

Ismail-Zadeh, A.; Korotkii, A.; Melnik, O.; Starodubtsev, I.; Starodubtseva, Y.; Tsepelev, I.; Zeinalova, N. (2023). Inverse Problems in Lava Dynamics. Applications of Data Assimilation and Inverse Problems in the Earth Sciences. Ed.: A. Ismail-Zadeh, 196–208, Cambridge University Press (CUP). doi:10.1017/9781009180412.013

Conference contributions

Zeinalova, N.; Ismail-Zadeh, A. (2021). Numerical Modeling of the 2007-2009 Lava Dome Growth in the Crater of Volcán de Colima, México. Presented at GeoKarlsruhe (DGGV 2021), Karlsruhe, Deutschland, Online, 19–24 September. doi:10.48380/dggvt14h-wg06

Zeinalova N.R., Ismail-Zadeh A.T., Melnik O.E., Tsepelev I.A., Zobin, V.M. (2021). Numerical modeling of lava dome growth at Volcán de Colima. Presented at II All-Russian Scientific Conference with international participation "Modern methods of seismic hazard assessment and earthquake prediction “, Moscow, Russia, Online, 29-30 September.

Zeinalova, N.; Ismail-Zadeh, A.; Melnik, O.; Tsepelev, I.; Zobin, V. (2021). Data-Driven Numerical Modeling of the Lava Dome Growth at Volcán de Colima, Mexico During 2007-2009. Presented at American Geophysical Union (AGU) Fall Meeting (2021), New Orleans, USA, Online, 13–17 December.

Zeinalova, N.; Ismail-Zadeh, A.; Melnik, O.; Tsepelev, I. (2022). Mathematical and Numerical Models of Lava Dome Dynamics. Presented at 33rd IUGG Conference on Mathematical Geophysics (CMG 2022), Seoul, South Korea, Online, 20–24 Juni.

Zeinalova, N.; Ismail-Zadeh, A.; Tsepelev, I.; Melnik, O.; Schilling, F. (2023). Numerical thermo-mechanical modelling of lava dome growth during the 2007-2009 dome-building eruption at Volcán de Colima. Presented at EGU23-1068, Copernicus, Vienna, Austria, 23-28 April. doi:10.5194/egusphere-egu23-1068

Zeinalova, N.; Ismail-Zadeh, A.; Tsepelev, I.; Melnik, O.; Schilling, F.; Zobin, V. (2023). Modelling of the lava dome growth the 2007-2009 dome-building eruption at Volcán de Colima, Mexico. Presented at XXVIII General Assembly of the International Union of Geodesy and Geophysics (IUGG), GFZ German Research Centre for Geosciences, Berlin, Germany, 11-20 July. doi:10.57757/IUGG23-0298

Other contributions

Zeinalova N., Ismail-Zadeh A., Melnik O., Tsepelev I., Zobin, V.(2022). Numerical modeling of lava dome growth at Volcán de Colima. Presented at Physics of Volcanoes 2022 virtual workshop 3-4 March.

Zeinalova, N.; Ismail-Zadeh, A.; Tsepelev, I.; Melnik, O.; Schilling, F. (2022). Numerical thermo-mechanical modelling of lava dome growth. Presented at KCDS X GRACE Crossover Workshop 12 December.

Zeinalova, N.; Ismail-Zadeh, A.; Melnik, O.; Tsepelev, I.; Schilling, F., Zobin, V. (2025). Numerical modelling of lava emplacement. Presented at the Department of Earth Sciences, University of Oxford, 29 April.

Presentations on the study were also delivered during seminar talks organized by the Institute of Applied Geosciences at KIT.

Contents

List of Figures

List of Tables

Nomenclature

Acronyms

Symbol	Description
1D	One-dimensional
2D	Two-dimensional
3D	Three-dimensional
CA	Cellular automata
SWE	Depth-averaged flow model based on the shallow water approximation
SPH	Smoothed Particles Hydrodynamics
LBM	Lattice Boltzmann methods
CFD	Computational fluid dynamics
CCGT	Characteristic time of crystal content growth
E-W	East-West orientation
SLAE	Set of linear algebraic equations
VOF	Volume of fluid method
HT	Heat transfer
DSM	Digital surface model
FVM	Finite volume method
AFT	Ansys fluent
OFM	OpenFOAM

Greek symbols	Description	Units
$\alpha(t,\mathbf{x})$	Volume fraction of fluid	-
α	Topography slope angle	-

$a_{cr}, \beta_{cr}, \delta_{cr}$	Empirical parameters, Eq. 1.8	-
β_u	Bousinesq shape factor	-
δ_s	Dirac delta function	m^{-1}
δ, ξ, γ	Rheological parameters	-
ε	Effective emissivity	-
ϕ	Volume fraction of crystals	-
$\phi_{\max}$	Maximum crystal packing content	-
ϕ_*	Critical solid volume fraction of crystal content	-
ϕ_{eq}	Volume fraction of crystals at the equilibrium state	-
ϕ_{in}	Initial volume fraction of crystals in the magma entering the model conduit	-
ϕ_{ct}	Volume fraction of crystals in the magma in the model conduit	-
$\dot{\gamma}$	Strain rate	s^{-1}
γ_{fr}	Friction coefficient	s^{-1}
η	Bulk viscosity	$\mathrm{Pa\,s}$
η_{mt}	Melt viscosity/crystal-free magma viscosity	-
η_{cr}	Relative viscosity, depending on the volume fraction of crystals	-
κ	Thermal diffusivity	$\mathrm{m}^2\,\mathrm{s}^{-1}$
λ	Coefficient of convective heat transfer	$\mathrm{J\ s}^{-1}\,\mathrm{m}^{-2}\,\mathrm{K}^{-1}$
λ_n	Nonlinear convective heat transfer coefficient	$\mathrm{J\ s}^{-1}\,\mathrm{m}^{-2}\,\mathrm{K}^{-4/3}$
μ	Dynamic viscosity	$\mathrm{Pa\,s}$
μ_{app}	Apparent viscosity	$\mathrm{Pa\,s}^{\mathrm{n}}$

μ_*	Reference viscosity	$\mathrm{Pa\,s^{n}}$
μ_{GD}	Temperature-dependent viscosity model for etnean lavas	-
ν	Consistency index	$\mathrm{Pa\,s^{n}}$
ρ	Density	$\mathrm{kg\ m^{-3}}$
σ	Stefan–Boltzmann constant	$\mathrm{J\ s^{-1}\,m^{-2}\,K^{-4}}$
$\sigma_{\max}$	Maximum deviatoric shear stress	Pa
τ	Characteristic time of crystal content growth (*relaxation time*)	days
$\tau_0\ /\ S_y$	Yield strength	Pa
τ_{st}	Shear stress	Pa

Roman Symbols

Symbol	**Description**	Units
A	Cell area	m
A_{Arr}	Constant, Eq. 1.2	-
$A_{VFT}, B_{VFT}, C_{VFT}$	Parameters in the Vogel–Fulcher–Tammann (VFT) equation	-
a_1, b_1, c_1	Parameters, Eq 4.11	-
B	Einstein coefficient	-
C	Specific heat capacity	$\mathrm{J\ kg^{-1}\ K^{-1}}$
c_n	Dimensionless constant depending on the power law index	-
c_t	Constant, Eq. 6.14	-
E_a	Activation energy	$\mathrm{kJ\ mol^{-1}}$
$\dot{e}$	Deviatoric strain rate	$\mathrm{s^{-1}}$
f	Fractional area of the exposed inner core	-

g	Gravity acceleration	$\mathrm{m\ s^{-2}}$
H	Terrain surface	-
h	Thickness of lava	m
h_{cr}	Critical thickness	m
k	Thermal conductivity	$\mathrm{J\ s^{-1}\ m^{-1}\ K^{-1}}$
L_*	Latent heat of crystallization coefficient	$\mathrm{J\ kg^{-1}}$
m_{dis}	Empirical parameter in the viscous dissipation term	-
n	Power law index	-
n_{dif}	Empirical parameter in the conductive term	-
p	Pressure	Pa
Q	Lava flow rate per unit width	$\mathrm{kg\ m^{-1}\ s^{-1}}$
q	Volumetric flux	$\mathrm{m^3\ s^{-1}}$
q_{tot}	Total flux of the cell	$\mathrm{m^3\ s^{-1}}$
R	Universal gas constant	$\mathrm{J\ K^{-1}\ mol^{-1}}$
T	Temperature	K
T_A	Air temperature	K
T_{ct}	Initial temperature of the magma in the conduit, K	K
T_{in}	Temperature of the new magma entering the conduit, K	K
T_g	Glass transition temperature	K
T_C	Temperature, Eq. 4.8	$^{\circ}\mathrm{C}$
T_{sp}	Temperature, Eq. 4.11	$^{\circ}\mathrm{C}$
T_{gr}	Ground temperature	K

u_{ext}	Extrusion rate	$\mathrm{m\ s^{-1}}$
u_{dis}	Discharge rate	$\mathrm{m^3\ s^{-1}}$
u_p	Velocity of the plug	$\mathrm{m\ s^{-1}}$

Superscripts

Symbol	**Description**
L	Lava
A	Air
N	Newtonian rheology
B	Bingham fluid
HB	Herschel-Bulkley fluid
$\tilde{}$	Depth averaged
rad	Radiative heat transfer
cond	Conductive heat transfer
conv	Nonlinear convective heat transfer
diss	Viscous dissipation

Chapter 1: Introduction

1.1 Motivation and thesis overview

Lava flow and lava dome growth are two significant phenomena of effusive (non-explosive) volcanic eruptions. The effusive type of volcanic eruptions is usually attributed to less hazardous. The lava propagation in this case is usually slow, which allows scientists and civil protection to respond promptly once the effusive event is underway by setting up the scenarios of the current event and then preparing safety plans. Although during lava flow propagation it is most likely possible to avoid human deaths by evacuating people promptly, the lava effusions result in significant damage to infrastructure and property (e.g., Behncke et al., 2005; Kauahikaua, 2007; Crisci et al., 2008). An example is the 2018 eruption of Kīlauea volcano in Hawaii, when lava flows destroyed homes, roads, power lines and forced more than thousands of people to leave their houses. Economic losses from the eruption-related damages amounted to more than $800 million[1]. The 2021 Cumbre Vieja volcanic eruption in La Palma is another example of economic damage due to the lava flow propagation. The lava flow covered over 1000 hectares, destroying on its way more than 3000 buildings, forcing the emergency evacuation of about 7000 people and causing about $900 million [2]in damage. Main factors controlling the morphology of lava flows are the lava rheology, the lava effusion rate (Kilburn, 2015) and the ground topography (Griffiths, 2000). Therefore, it is essential to understand the role of these parameters in lava dynamics.

Lava dome eruption from one side is associated with a relative passive and unthreatening effusions, from the other side a sudden disruption or collapse of lava domes may result in pyroclastic density currents further triggering rainfalls and lahars (Calder et al., 2015). Such collapses can severely affect nearby infrastructure, agriculture, and communities. Continuous lava dome growth at Sinabung, Indonesia (2010-2017) resulted in multiple collapses, damaging homes and agricultural lands, displacing thousands of people, causing the total value of losses amounts to $80 million (Tampubolon et al., 2018). The morphology of lava domes is

---

[1] https://en.wikipedia.org/wiki/2018_lower_Puna_eruption

[2] https://en.wikipedia.org/wiki/2021_Cumbre_Vieja_volcanic_eruption

controlled by a combination of lava rheology, ground topography, ascent dynamics, and the mechanism of dome growth (Calder et al., 2015).

The losses and damages associated with effusive eruptions necessitate the development and use of numerical models, both for advancing scientific understanding of the lava dynamics, its morphology, and thermal evolution and for generating reliable forecasts of lava flow paths both spatially and temporally (Costa & Macedonio, 2005a; Tsepelev et al., 2016). Numerical modelling of lava flows is essential for planning evacuations, mitigating risks, and organizing the diversion through natural or artificial barriers (e.g., Macedonio & Longo, 1999) in response to lava flow hazards (Costa & Macedonio, 2005b). Numerical model aims to apply and link mathematical equations that describe the main parameters controlling the lava dynamics (e.g., velocity, temperature and viscosity) with its observed data (e.g., morphology and erupted volume). Such models for lava dynamics have undergone major developments over the past years, from analytical and simplified models (steady state, 1D models) to more complex 2D/3D models that incorporate complex rheological models, thermal effects and temporal evolution.

Numerical models of lava dynamics help to understand the influence of the rheological properties of magma on morphological features of the lava flows and lava domes. They also clarify the role of crystal content, temperature, pressure, and discharge rate on the lava morphology (Hale & Wadge, 2003; Husain et al., 2018; Tsepelev et al., 2020).

Within this context, this PhD study focuses on both numerical modelling of lava dome growth and lava flows. The scientific objectives regarding the lava dome growth include (i) understanding how the viscosity of magma/lava, the lava discharge rate, the conduit location, and the topography of the crater influence the dome morphology (ii) studying the influence of different heat transfer mechanisms at the lava-air interface on the lava dynamics and the evolution of the dome carapace (iii) evaluating the impact of the latent heat of crystallization, the viscous dissipation and thermal boundary conditions on the lava dome dynamics. The numerical modelling of lava dome growth describes the 2007-2009 endogenous stage of lava dome growth at Volcán de Colima, México.

The second part related to the lava flow modelling focuses on (i) investigating the influence of the physical parameters, such as the crystal content, yield strength, and magma free melt viscosity, on lava flow morphology (ii) studying the impact of isothermal and temperature dependent linear and non-linear rheologies on lava flow emplacement (iii) benchmarking several numerical codes of different complexity to assess their computational performance with regard to lava flow modelling. In numerical modelling of lava flow we use the effusive phase of Mount Etna’s eruption from December 6 to 8 in 2015 as a case study.

For these purposes we employed several numerical models including Cellular Automata, two- and three-dimensional fluid dynamics models and a depth-averaged model. The Cellular Automata approach is implemented using GPUFLOW model (Cappello et al., 2022). The 2-D and 3-D models are developed employing Ansys Fluent and OpenFOAM software. Both numerical codes are based on the finite volume method. The depth averaged model based on the shallow water approximation is developed using the OpenFOAM software.

The thesis is organised as follows: Chapter 1 provides the basic knowledge of volcanic activities, types of volcanic eruptions, lava flows and lava domes, and lava rheology. Chapter 2 provides an overview of the main numerical methods that are currently adopted for the simulation of lava dynamics. Chapter 3 presents a quantitative modelling study of the 2007-2009 endogenous stage of slow dome-building process at Volcán de Colima in México. The main goal of this study is to understand how the lava viscosity, the lava discharge rate, the conduit location and the topography of the crater affect the dome morphology at Volcán de Colima. Chapter 4 presents a numerical study of the thermo-mechanical evolution of the lava dome at Volcán de Colima during 2007-2009. The main objective of this research is to show the impact of different heat transfer mechanisms including convective, conductive and radiative heat transfers at the lava-air interface on the lava dynamics and the evolution of the dome carapace as well as evaluating the impact of the latent heat of crystallization, the viscous dissipation and variations of thermal boundary conditions on the internal development of the lava dome. Chapter 5 provides a comparison of the two above mentioned models to analyse the influence of temperature, carapace formation and heat transfer at the lava-air interface on the growth of the modelled lava domes. Chapter 6 presents a sensitivity analysis of the influence of rheological parameters, such as crystal content, yield strength, and magma free melt viscosity on lava flow morphology. Chapter 7 present a study of the influence of Newtonian, Bingham and Herschel-Bulkley rheological models on lava flow morphology under isothermal and non-isothermal conditions using a three-dimensional fluid dynamics model and a simplified depth-averaged model based on the shallow water approximation. Additionally, this chapter demonstrates an application of the depth averaged model to simulate the emplacement of a natural lava flow and presents a comparison of the modelled results with the observational data from the December 2015 eruption at Mount Etna. The main objective of this work is to show how temperature-dependent Newtonian, Bingham and Herschel-Bulkley rheological models affect the lava flow morphology. The major findings of this thesis and possible directions for future studies are covered in Chapter 8. Appendices A1 and A2 present the numerical approach and the derivation of the model extrusion rate, respectively in the isothermal modelling of lava dome growth. Appendix B provides a justification for the negligible impact of viscous heating in the thermo-mechanical modelling of lava dome growth.

1.2 Types of volcanic eruptions

Volcanic eruptions are one of the most fascinating expressions of nature powerful forces. Active volcanoes have captivated and terrified civilizations for thousands of years. To assess the hazards threatening the growing number of people living in close proximity to active volcanoes, and to mitigate the risks associated with these hazards, it is essential to study the physical behaviour of volcanoes (Fagents et al., 2013).

A volcanic eruption is the release of gas, rock fragments and magma. Magma, that is a high-temperature mixture containing molten mantle-crustal rocks, melt, crystals, gases, and bubbles, rises up from the interior of the Earth through a vent on the Earth’s surface into the atmosphere. When magma reaches the surface and erupts, it is referred to as *lava*. The distribution of volcanoes is closely related to the boundaries of lithospheric plates.

Volcanic activity can be generally divided into two main categories: explosive and effusive (Parfitt & Wilson, 2008; Gonnermann & Manga, 2013). Explosive eruptions occur during magma fragmentation, in which magma undergoes a phase transition from a liquid phase with dispersed gas bubbles to a gas phase with pyroclasts (magma fragments). The explosive force is generated by the conversion of the potential energy of expanding magma into the kinetic energy of the gas phase with individual pyroclasts. This explosion is further amplified by the thermal expansion of the gas-particle mixture (Cashman & Scheu, 2015). The explosive eruptions are accompanied by the ejection of ash, rocks, and gas into the air at high discharge rates, resulting in pyroclastic density currents, i.e., hot, fast-moving mixtures of volcanic particles and gas. These are the most devastating and hazardous types of volcanic activities

(e.g., explosive eruptions at Mount St. Helens in 1980, and at Mount Pinatubo in 1991, Figure 1.1)


(a) (b)

Figure 1.1: Explosive eruption of (a) Mount St. Helens (USA) in 1980 (photo credits: USGS[3]); and (b) Mount Pinatubo (Philippines) in 1991 (photo credits: USGS[4]).

Effusive eruptions occur when magma becomes poor in volatiles as it ascends to the surface. Effusive volcanism is associated with the non-explosive extrusion of magma at the Earth's surface. These kinds of eruptions are characterised by lava flow emplacements and, in the case of silica-rich lava, lava dome growth. Magma with low viscosity generates lava flows, while high viscous magma tends to accumulate around a volcanic vent, forming lava domes. Since the effects of lava flow or lava dome-forming (effusive) eruptions are mainly limited to the vicinity of the volcano, they are often less dangerous than explosive eruptions. However, large mafic lava flows can still cause significant damage, such as destruction of properties (e.g., in San Sebastiano, Italy in 1944) and human death (as in Nyiragongo, Congo in 1977) (Kilburn, 2015). Such tragic events reveal the importance of understanding how lavas behave.

Lava dome eruptions can vary significantly, ranging from relatively passive and low-risk effusions to highly unpredictable and dangerous activities (Merapi, Indonesia, 2010). The hazards associated with lava domes include dome collapse, pyroclastic density currents and sometimes lateral blasts. Dome collapse can further cause secondary hazards leading to lahars and debris avalanches (Calder et al., 2015). Thus, understanding the physical processes of lava dome growth is crucial for mitigating the risks posed by such eruptions.

---

[3] https://volcanoes.usgs.gov/volcanic_ash/mount_st_helens_health.html

[4] https://volcanoes.usgs.gov/volcanic_ash/pinatubo_1991.html

In this work, we are interested in studying the dynamics of lava flows and lava domes growth that characterize the effusive events (Figure 1.2).

(a) (b)

Figure 1.2: Effusive eruption of (a) lava flow at Mount Etna (Sicily), June 2022 Credits: INGV[5]; (b) lava dome growth at Volcan de Colima, (Mexico), September 2009. Credits: Wikimedia Commons[6]

1.3 Lava Flows

Lava flows are one of the most common volcanic phenomena on Earth. Their advancement and behaviour are strongly controlled by the effusion rate at the volcanic vent, the lava viscosity (in general terms, the lava rheology, which describes a relationship between the stress and the strain rate), and the local environmental conditions (e.g., ground slope, topography) (Kilburn, 2015). Lava flows consist of outpourings of molten rock (magma), which solidifies into magmatic rocks. Solidified lavas are predominantly silicate minerals, such as feldspars, olivine, pyroxenes, amphiboles, quartz and some others. Silicate lavas are molten mixtures dominated by oxygen and silicon with smaller quantities of Al, Ca, Mg, Fe, Na, K, and minor amounts of other elements. Silica content (SiO_2) controls the viscosity of lava, based on that silicate lavas are classified into four types: silicic (with the silica content >63%), andesitic (52% to 63%), basaltic (45% to 51%), and ultramafic (<45%) lavas (Philpotts & Ague, 2009; Rogers, 2015). The viscosities of basaltic lava flows are typically in the range from 10^2-10^3 Pa s to 10^5 -10^6 Pa s for cooler and more crystallized basalts. Lava viscosities increase with silica

---

[5] https://www.volcanodiscovery.com/etna/news/183229/Etna-volcano-update-lava-flow-eruption-from-SE-crater-continues-short-lava-spill-out-on-N-slope-has-.html

[6] https://commons.m.wikimedia.org/wiki/File:Volcan_de_Colima_Crater_con_tapon.JPG

content, so that an andesitic lava may have a viscosity between 10^5 and 10^7 P as, while a rhyolite lava could vary between 10^7 and 10^{10} Pa s (Harris & Rowland, 2015).

Based on the surface morphology and crustal appearance, lava flows can be categorized into three types: pahoehoe, ‘a’a, and block lava (Harris, 2013; Kilburn, 2000). Pahoehoe lava has a smooth, glassy surface folded into a series of ripples called ropes. (e.g., Mount Vesuvius, Italy). In contrast, ‘a’a lava is characterized by rough rubbly surfaces composed of broken lava fragments, ranging in size from centimetres to decimetres (e.g., Mt Etna, Italy). Blocky lava (e.g., Nea Kameni Santorini, Greece) like ‘a’a has also a fractured surface composed of large, angular lava fragments, sometimes up to meters across, with smooth planar surfaces (Kilburn, 2000, 2015).

Depending on the eruption volume the lava flow fields can range from a few kilometres in length (e.g., Lonquimay, Chile; Nea Kameni, Greece) to tens of kilometres (e.g., Kilauea & Mauna Loa, Hawaii; Etna, Italy). In some cases, (e.g., Trident, Alaska; Lonquimay, Chile) lava flow can reach thicknesses of hundreds of meters (Kilburn, 2015). The duration of a single eruption can range from days to months, although there have been eruptions that have persisted for decades. The effusion rates of lava flows are usually slow, that is why it is usually possible for people to escape the hazardous area in time, there are exceptions, however. For example, a tragic exception occurred in the Democratic Republic of Congo in January 2002, when lava erupted from a lower flank fissure with a high effusion rate and travelled downhill at an average rate of 15 km per hour, reaching a small village and causing the deaths of 70 people (Kilburn, 2015). Another example of the rapid lava flow propagation is the 1977 eruption of Nyiragongo, when lava accelerated up to 60 km per hour and caused death of more than 600 people (Nakamura & Aoki, 1980). Such tragedies prove the necessity of preparing for potential lava invasions before an eruption begins.

Although such incidents are rare, and most lava flows advance slowly and do not pose a threat to humans, once lava erupted, it advances destroying everything in its path (Blong, 1984; Harris & Rowland, 2015) . Therefore, it is essential to have post-event plans in place such as the replacement of infrastructure and the evacuation of affected communities in case if human intervention (e.g., through diversion, deflection, or the construction of barriers) has failed. However, all such measures require necessary preparation, planning, and allocation of resources and finances (Harris et al., 2016).

The development of numerical models that can simulate lava flow propagation play an important role in understanding lava flow dynamics (Costa & Macedonio, 2005a; Cordonnier et al., 2015; Ismail-Zadeh et al., 2016). The aim of such models is to describe the rheology, lava flow heat loss, crystallinity, velocity, and morphological features of lava flows. The computational methods that can be applied in modelling lava dynamics are described in detail in Chapter 2. Chapters 6 and 7 are based on the numerical modelling of lava flow advancement using the December 2015 eruption at Mt. Etna as a case study.

1.4 Lava Domes

Viscous and silica-rich magma forms lava domes. Lava domes tend to accumulate around a vent as magma degasses and cools (Calder et al., 2015; Acocella, 2021). Dome eruptions have much lower discharge rates than lava flows or explosive eruptions and this factor importantly effects their structural stability (Voight & Elsworth, 2000; Calder et al., 2015). The lava that forms the domes can have a very wide range of composition from basaltic to rhyolitic, but the majority of dome lavas are usually andesitic and dacitic. Active lava domes comprise of a hot, ductile inner core surrounded by a cooler and brittle outer carapace (Fink et al., 1990; Calder et al., 2015).

Lava domes can range in diameter from a few tens of meters to several kilometres, with heights reaching up to 1 km. The morphological shape of the domes can vary from steep-sided to tabular in cross section, and from circular or elliptical to irregular in top view. Domes are often confined to crater areas and in these cases their shape is almost circular. When lava erupts on the flanks of volcanic edifices, the dome shape tends to elongate downhill (Calder et al., 2015).

The morphology of lava domes is controlled by variation in the magma rheology, underlying topography, ascent dynamics, and the mechanism of dome growth (i.e., endogenous or exogenous). When a dome grows by intrusion of new magma into its interior, it is called endogenous growth, when it grows by extrusion of new surface lobes on top of its carapace it is called exogenous growth.

Domes can form relatively rapidly, within days to weeks, but eruptive phases generally last for years to decades. Effusion rates of lava domes may range from as low as 0.01 to over 100 m^3 s^{-1} (Voight & Elsworth, 2000; Calder et al., 2015). Such variations in effusion rates contribute to the unpredictable transitions from relatively passive and unthreatening effusion to highly hazardous and explosive events.

Potential threats associated with lava domes include the lava dome collapse and rockfalls caused by dome instability, pyroclastic flows and debris avalanches, and can even lead to lahars (Calder et al., 2015; Acocella, 2021). In some cases, the rupture of a carapace due to pressure build-up within the dome, leads to violent explosions (e.g. Unzen, Soufriere Hills, 1990; Santa Maria Volcano, Guatemala, 1929) causing deaths from hundreds to thousands of people. The collapses of lava domes can also sometimes trigger pyroclastic density currents and thus result in substantial fatalities (El Chicho´n, Mexico in 1982; Merapi, Indonesia in 2010, Santiaguito volcano, Guatemala in 1929) (Calder et al., 2015).

Extensive monitoring of active lava domes has revealed periodic behaviour in lava dome eruptions on the timescale from hours to decades (Voight et al., 1999; Barmin et al., 2002). These observations indicate that dome eruptions are characterized by pulsatory magma ascent (Calder et al., 2015).

As volcanic regions become more populated, understanding the dynamics of lava dome growth becomes important task for risk mitigation. The possibility of sudden dome collapse, the unpredictable transitions between effusive and explosive behaviour, and the periodic behaviour of eruptive episodes pose challenges to the prediction of such eruptions. Numerical models of lava dome growth can help to understand the dynamics of lava dome evolution and the processes affecting its morphological structure. They clarify how the rheological properties of magma within a lava dome influence its shape and internal structure (Hale & Wadge, 2003; Husain et al., 2018; Tsepelev et al., 2020). Chapters 3, 4 and 5 are based on numerical modelling of lava dome growth using the growth from 2007 to 2010 at Volcan de Colima as a case study.

1.5 Lava rheology

One of the key factors that control the morphology of lava flow is its viscosity (e.g., lava flow propagation, solidification) (Harris, 2013). Viscosity is the property of a fluid describing its resistance to flow. It is quantified as the ratio of shear stress to shear strain rate. Shear stress is the force per unit area acting on a fluid, and strain rate is a deformation rate experienced by the fluid under an applied stress.

Based on the relationship between stress and strain rate, fluids can be classified into Newtonian linear and non-linear rheologies. Newtonian fluid is the simplest often studied fluid, in which the ratio between the applied stress τ_{st} and the strain rate $\dot{\gamma}$ is linear, and the ratio itself is the dynamic viscosity μ. All geological melts have been shown experimentally to be Newtonian except under shear strain rates approaching those of structural relaxation (Dingwell, 1986; Webb & Dingwell, 1990). The linear relationship between shear stress and shear rate in Newtonian fluids is defined as:

$$\tau_{st} = \mu\dot{\gamma} \tag{1.1}$$

Fluids where the rate of deformation is not directly proportional to a change in the applied stress are called non-linear (non-Newtonian fluids). In the non-linear fluids the constant dynamic viscosity is replaced by an apparent viscosity $\mu_{app}\left(\dot{\gamma}\right) = \nu\dot{\gamma}^{n-1}$, where ν is a consistency index. The non-Newtonian behaviour of basaltic lava (and magma) is supported by field data from Pinkerton & Sparks (1978), which show that lava has a yield strength and deforms in a pseudoplastic manner as shear stress increases. In our modelling, as an example of a non-linear rheology, we study the Heschel Bulkley rheology which is characterized by yield strength τ_0, a power law exponent *n* and the consistency index ν and is given by:

$$\begin{cases} \dot{\gamma} = 0, & \left|\tau_{st}\right| \le \tau_0 \\ \left|\tau_{st}\right| = \tau_0 + \nu\dot{\gamma}^n, & \left|\tau_{st}\right| > \tau_0 \end{cases} \tag{1.2}$$

When *n*=1 in the Herschel–Bulkley rheology we obtain Bingham fluids. Dragoni et al. (1986) suggested that bulk behaviour of a lava flow is Bingham rather than Newtonian. Bingham fluids will only spread as long as shear stress attains the value of the yield strength. In the non-linear rheology (Bingham or Herschel Bulkley) the yield strength can also affect the viscosity of the lava and can be calculated as a function of the temperature and crystallinity (Harris, 2013).

Silicate melt viscosity plays an important role in controlling melt production, magma ascent dynamics and physicochemical processes (e.g., degassing, crystallization). The melt viscosity of natural silicate magmas depends on several variables such as temperature, pressure, and magma composition. There are three ways to parametrise and predict the viscosity of geological melts (Russell et al., 2022). One of the earliest approaches to estimate lava viscosity involved measuring surface velocities in active lava channels and calculate channel geometry and slope (Nichols, 1939; Lev & James, 2014) . Such calculations assume either Newtonian or Bingham rheology and use the corresponding equation for the velocity profile in a channel confined fluid to inform on the viscosity and yield strength. This approach is particularly useful in the field studies, where direct sampling and experimentation may not be possible.

The second approach is a direct measurement of viscosity for geological melts. Depending on the variation of the viscosity due to temperature there are several approaches to measure directly the viscosity, including concentric cylinder viscometer (Dingwell, 1986), micropenetration and a parallel plate viscometry (Gent, 1960; Russell et al., 2022). Such methods help to derive an experimental expression of the viscosity of the specific lava/melt for a specific volcano. The data obtained during the direct measurements have filled gaps in the knowledge of melt physical properties in response to variations in temperature and melt composition and have quantified the viscous properties of most terrestrial melts (Dingwell, 1986; Hess & Dingwell, 1996; Giordano & Dingwell, 2003).

Lava is a complex mixture comprising melt, crystals, bubbles (Harris & Rowland, 2015). These factors introduce another non-linear effects into its rheology. Covering the full range of the processes driven by temperature variations, crystallization, volatiles, bubbles and gases in the lava viscosity pose a challenge. Therefore, the third approach is the development of new predictive viscosity models based on the available experimentally obtained viscosity data. The main goal of the viscosity models is to reliably predict melt viscosity at the conditions found in natural systems (Russell et al., 2022). Such viscous models are important in numerical simulations of magmatic and volcanic processes.

Next, we provide a brief overview of the existing and popular melt viscosity models starting with a basic model of temperature dependent lava viscosity and later expanding into models that incorporate other variables such as crystal content.

The temperature dependence of viscosity is one of the most important variables (that influence) in lava flows. The simplest form for predicting the viscosity of silicate melts as a function of melt composition and temperature is an Arrhenian relationship, in which, for every 10°C increase in temperature, the rate of chemical reaction doubles (Bottinga & Weill, 1972; Persikov, 1991; Harris, 2013):

$$\eta_{mt} = A_{Arr} \exp(-E_a / RT) \tag{1.3}$$

where η_{mt} is the viscosity, E_a is the activation energy for viscous flow, A_{Arr} is the constant, R is the universal gas constant, and T is the temperature (K). The Arrhenian assumption was fully consistent with the early available data; however, the current database of viscosity measurements covers a substantially wider range of melt compositions and temperatures (Richet & Bottinga, 1995; Russell et al., 2003).

The Vogel–Fulcher–Tammann (VFT) equation is an empirical expression of the non-Arrhenian temperature dependence of viscosity (Angell, 1991; Richet & Bottinga, 1995; Rossler et al., 1998).The VFT expression is given by:

$$\log \eta_{mt} = A_{VFT} + \frac{B_{VFT}}{T - C_{VFT}} \tag{1.4}$$

where A_{VFT}, B_{VFT}, C_{VFT} are parameters that are adjusted according to the melt composition. The VFT model has been widely applied to geologically important silicate melts (i.e., those showing relatively small differences from Arrhenian behaviour) (Richet & Bottinga, 1995; Rossler et al., 1998) and is used in the present work to model the melt viscosity at Volcan de Colima in Chapter 4.

There are three more similar functions which commonly used to model temperature dependent melt viscosity. Based on configurational entropy (a thermochemical property of silicate melts and glasses) - the Adam–Gibbs (AG) functions provide a connection between the transport properties, relaxation timescales of melts, and their thermochemical properties (Adam & Gibbs, 1965; Richet & Bottinga, 1995; Avramov, 2013; Russell & Giordano, 2017). Avramov & Milchev (1988) model determines the temperature dependence of the mean jump frequency of moving building “molecules” and, through it, the viscosity (Russell et al., 2022). The main assumption is that the viscosity depends on total entropy (Avramov, 2013). Mauro et al. (2009) has derived another three-parameter equation for the temperature dependence of the melt viscosity. Their model offers a realistic extrapolation of configurational entropy in both the high- and low-temperature limits.

In this work, we use the viscosity model of the basaltic hydrous melt from Mount Etna (Chapter 7) obtained by Giordano & Dingwell (2003). The viscosity model shows how temperature influences the viscosity of Etna's basaltic lava (Fig.1.3)

$$\log_{10} \eta_{mt} = -4.643 + \frac{(5812.44 - 427.04 \times wt)}{T - 499.31 + 28.74 \times \ln(wt)} \tag{1.5}$$

where η_{mt} is the viscosity, *wt* is the water content, and *T* is the temperature in Kelvin.

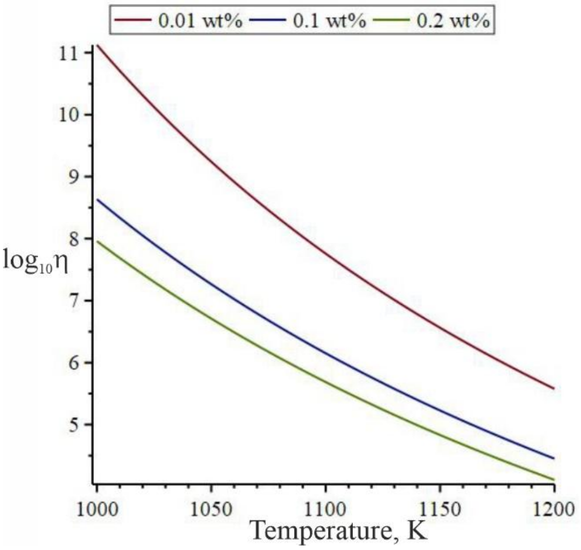

Figure 1.3: The temperature dependent viscosity with varying water content (Giordano & Dingwell, 2003).

Earlier we considered the impact of melt in lava viscosity, however lava is a mixture of fluid (melt) and solids (crystals), and crystals increase the lava viscosity (Lejeune & Richet, 1995; Caricchi et al., 2007; Lavallée et al., 2007). So, to obtain the bulk viscosity the crystallization should be also taken into account. For small crystal volume fractions $\phi < 10-30\%$ and low strain rates, the viscosity of the crystalline magma (crystal free melt) can be approximated using the Einstein Roscoe relationship (e.g., Marsh, 1981; Pinkerton & Stevenson, 1992):

$$\eta_{cr} = \frac{\eta}{\eta_{mt}} = \left(1 - \frac{\phi}{\phi_{\max}}\right)^{a_{cr}} \tag{1.6}$$

in which η is the bulk viscosity, η_{mt} is the melt viscosity, ϕ is a volume fraction of crystals, $R = 1/\phi_{\max}$, where $\phi_{\max}$ is the maximum crystal packing content and $a_{cr} \approx -2.5$ (Llewellin & Manga, 2005).

Ah higher ϕ and strain rates, the expression is provided by Caricchi et al. (2007):

$$\eta_{cr} = \frac{\eta}{\eta_{mt}} = \left[1+\left(\frac{\phi}{\phi_{\max}}\right)^{\delta_{Cr}}\right]\left[1-\alpha_{Cr}\,\mathrm{erf}\left(\frac{\sqrt{\pi}}{2\alpha_{Cr}}\frac{\phi}{\phi_{\max}}\left[1+\left(\frac{\phi}{\phi_{\max}}\right)^{\beta_{Cr}}\right]\right)\right]^{-B\phi_{\max}} \tag{1.7}$$

here B = 2.5 and δ_{Cr}, α_{Cr}, and β_{Cr} are the empirical parameters (Gonnermann & Manga, 2013).

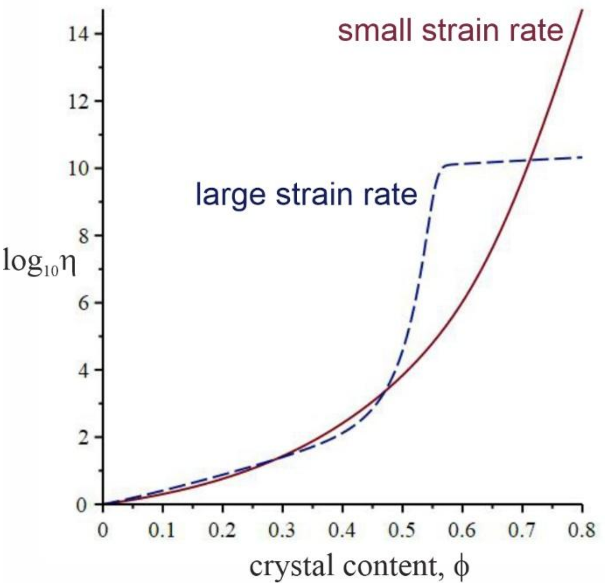

Figure 1.4: The effect of crystal content on the viscosity of the crystalline magma (Gonnermann & Manga, 2013)

Bubble formation, presence of volatiles and pressure can also contribute to the changes in the bulk viscosity of the lava (Crisp et al., 1994; Manga et al., 1998; Llewellin & Manga, 2005; Harris, 2013), but are not directly considered in the applied, in this research, viscosity models.

Chapter 2: Numerical modelling of lava dynamics

Lava flow modelling can be distinguished for the stochastic or deterministic approaches, the numerical methods employed, and the complexity of the physics adopted (Costa & Macedonio, 2005a; Cordonnier et al., 2015). Therefore, the numerical codes differ depending on their physical implementations, numerical accuracy, and computational efficiency.

Stochastic models describe the lava flow as a gravity current flowing the topography along the steepest slope without considering temporal evolution. The state of the system in such models is described by probabilistic distributions. In principle any numerical code could be used for stochastic modelling, assuming that the simulation can be run several times with slightly different parameter values, but usually only codes with very simplified physics are adopted for the sake of computational time. Therefore, the main advantage of the models is the short computation time required for running simulations, which makes them useful for rapid evaluation of potential hazard areas. Examples of probabilistic models for lava-flow emplacement include DOWNFLOW (Favalli et al., 2005; Tarquini & Favalli, 2016), ELFM (Damiani et al., 2006), LAZSLO (Bonne et al., 2008). However, due to the oversimplified physics, embedded in the models and lack of temporal evolution, the stochastic models mostly account only for the topographic effects and thus can't provide detailed information about the dynamics of the flow and the physical processes taking place within it.

Deterministic models on the other hand can simulate lava flow behaviour in much detail allowing for two-dimensional (2-D) and three-dimensional (3-D) flow models including thermal evolution, changes in rheology and other processes (e.g., Costa & Macedonio, 2005a; Vicari et al., 2007; Hérault et al., 2011; Tsepelev et al., 2021; Cappello et al., 2022; Biagioli et al., 2023; Starodubtsev et al., 2023; Zeinalova et al., 2021, 2024). The models are based on the solution of the governing equations, such as conservation of mass, momentum and energy, and account for the magma rheological properties. The solution in this case is achieved by a given unique set of initial and boundary conditions. Deterministic models require the initial data including topography data and eruptive input conditions: discharge rate, vent geometry, effusion temperature and physical properties of the lava (e.g., density, thermal conductivity) (Costa & Macedonio, 2005a; Cordonnier et al., 2015). Running deterministic models, especially over complex terrains or for extended eruption durations, can be computationally expensive and time-consuming. Therefore, simplified approaches to modelling of lava flows sometimes adopted. Such models may assume the use of (i) analytical formulas (e.g., Dragoni et al., 1986), (ii) lower dimensionality, e.g. neglecting the vertical component of fluid flow (Costa & Macedonio, 2005b) , (iii) isothermal models (e.g., Tsepelev et al., 2016) or (iv) mesh free approaches (e.g., particles, Starodubtsev et al., 2023) among other simplifications. The simplifications allow to reduce computational time which is crucial for real-time lava flow forecasting (e.g., Cappello et al., 2016) and the production of long-term scenarios (e.g., Del Negro et al., 2013) .

Next, we give a description of the main numerical methods that are used in the present study together with the models that can be adopted for the lava flow simulation.

2.1 Cellular automata

The cellular automata approach is one of the most commonly used to model lava flow evolution with codes such as SCIARA (Crisci et al., 1986; Barca et al., 2004; Avolio et al., 2006), MAGFLOW (Vicari et al., 2007; Bilotta et al., 2012), GPUFLOW(Cappello et al., 2022), and FLOWFRONT (Young & Wadge, 1990; Wadge et al., 1994).

In the cellular automata model, the computational domain is divided into square cells. Each cell is characterized by properties such as local topography, the amount of lava present in the cell, and temperature. The state of each cell, initially determined by the thickness of the lava, is updated at each time step according to the evolution function. The cellular automata models allow for the modelling complex lava flow behaviour, incorporating various physical processes such as heat loss by convection and radiation (Cappello et al., 2022). The models are fast to run, however, the two-dimensional assumption limits their ability to capture the detailed vertical structure of lava flows, which is crucial for coupling surface and basal heat losses to the bulk rheology evolution (Cordonnier et al., 2016).

2.2 Depth-averaged models

Depth-averaged flow models, based on the shallow water equations (SWE) hypothesis were first introduced by De Saint Venant in 1871. The main assumption of the model is that the horizontal length scale is much greater than the vertical one which leads to neglection of the vertical component (Costa & Macedonio, 2005a, 2005b). The SWE models are applied in a wide range of fields, mostly for hazard assessment purposes, from flood simulation (Burguete et al., 2002) to tsunami propagation (Heinrich et al., 2001). In volcanology, they have been successfully applied to simulate pyroclastic density currents (Sheridan et al., 2005), lava flows (Costa & Macedonio, 2005b; Kelfoun & Vargas, 2016; Biagioli et al., 2021, 2023), and lahars (Procter et al., 2010).

The equations are derived by depth integrating the Navier–Stokes equations from the terrain bottom to the free surface. The model can incorporate several rheology models from the Newtonian (Costa & Macedonio, 2005b) to more complex rheologies such as Bingham (Liu & Mei, 1990; Biagioli et al., 2023) and Herschel Buckley (Balmforth et al., 2002, 2006, 2007). The SWE formulation leads to a dimension reduction as variations of the parameters with depth are neglected and are thus relatively fast to compute. While the assumption of a constant viscosity along the vertical profile limits the ability to fully capture the influence of rheology on flow dynamics, depth-averaged models remain highly efficient for lava simulations and provide valuable insights into lava flow behaviour.

2.3 Generic Computational Fluid Dynamics codes

The fundamental basis of most computational fluid dynamics (CFD) tools is the Navier–Stokes equations, which define viscous (single or multi-phase) fluid flows. Two-(2-D) and three-(3-D) CFD models provide possibilities for detailed analysis of velocity, temperature, viscosity and other variables related to lava dynamics, which is impossible to achieve using simplified models mentioned above. CFD models of lava flow often require additional equations for example to specify the rheological law, to account for crystallization or temperature-dependent physical properties, or to incorporate complex topography.

Here, we discuss two advanced CFD tools (Ansys Fluent and OpenFOAM) that are suitable for lava flow modelling and are employed in the current study for lava dome growth and lava flow modelling. Both tools still require customization to fully address the unique challenges posed by above mentioned problems.

ANSYS Fluent (developed by ANSYS Inc) is a commercial computational fluid dynamics (CFD) software used to model fluid flow, mass and heat transfer. The software is based on the finite volume method. In operating Fluent, users do not need to have extensive programming knowledge as the software offers a user-friendly interface including pre and post processing tools as well as visualisation programs, and different solution solvers depending on the problem. However, the default capabilities are limited and sometimes it is necessary to customise a problem (e.g. include complex rheology, additional transport equations). Parallel processing in ANSYS Fluent is handled internally, without requiring manual intervention in node distribution.

OpenFOAM (produced by OpenCFD Ltd) is an open-source software package with a focus on CFD applications (Jasak et al., 2007). OpenFOAM like Ansys Fluent is based on the finite volume method and has different range of features to solve problems from complex fluids, chemical reactions and turbulence flows to heat transfer, solid mechanics, acoustics and electromagnetics. The software is supplied with pre- and post-processing tools. OpenFOAM also offers the possibility to launch and handle the parallel computations using the OpenMPI permitting High-Performance Computing (HPC). Although OpenFOAM does not have a built-in package for modelling specifically lava flows, the advantage of OpenFOAM as an open-source platform is that it allows users to modify solvers, add new equations, and customize the software for user’s specific needs.

Other existing methods for lava flow modelling

In this section, we also would like to briefly mention other existing models for lava flow simulations which are not employed in the present study but remain useful and popular.

2.4 Channelled models

Channelled models reduce the complexity of lava flow simulations by assuming that lava can advance downslope only in one direction (i.e. accounting for a one-dimensional (1-D) model). Despite the limitation in the emplacement directions, the ability of channelled models to incorporate thermal effects and account for linear or non-linear rheologies (Filippucci et al., 2010) makes their application to lava flow modelling attractive. In the channelled lava flow models, the velocity profile depends on the channel dimensions (e.g., Harris et al., 2011) and the lava rheology model (Dragoni, 1989; Tallarico & Dragoni, 2000).

The main code implementing the concept of channelled lava flows is FLOWGO (Harris et al., 2011; Harris & Rowland, 2001). This code allows for simulating the advancement of finite amount of lava confined within a channel bordered by levees. The model considers a heat loss due to the radiation, convection and conduction, the temperature-dependent rheology, and crystallization. The termination of the lava advancement occurs once lava cools down enough to reach rheological properties consistent with solidification.

The FlOWGO model is fast to run, as it doesn’t involve detailed fluid motion simulation. The main limitation arises from the one-dimensional assumption, forcing the channel width to directly correlate with the ground slope (Cordonnier et al., 2016). The simplification can affect the model accuracy in representing real world lava flows. Moreover, to match the input effusion rate, the model requires to assume at-vent channel dimensions, which significantly influence the model results (Wantim et al., 2013).

2.5 Mesh free models

Mesh-free or particle methods have emerged over the past few decades as an alternative to traditional grid-based methods. The two popular particle methods that propose efficient multiphase formulations are Smoothed Particles Hydrodynamics, SPH (Hérault et al., 2011; Zago et al., 2018), and the Lattice Boltzmann methods, LBM (Parmigiani et al., 2013). The main difference between two methods is that the SPH method is based on the Navier Stokes equations, whereas the LBM solves the Discretized Boltzmann equations. To date only the SPH methos has been applied to simulate lava flows (Hérault et al., 2011; Bilotta et al., 2011, 2016; Cordonnier et al., 2015; Zago et al., 2017, 2018; Starodubtsev et al., 2023;). The fluid in the

SPH model is represented by discrete elements called particles and physical parameters are assigned to each particle. The particles influence each other within a certain spatial range, but the influence weakens as distance increases and becomes negligible beyond a certain point. An advantage of the SPH method is that computations are only performed in area covered by particles, reducing both storage requirements and computation time. Another advantage of the method is a high degree of parallelism, which allows its implementation on parallel computing hardware (e.g., Hérault et al., 2011). The main drawback of the method is that the size of the particles directly impacts the simulation time. On the one hand smaller particles result in a larger number of particles, which significantly increases the overall computation time. On the other hand, increasing particle size may speed up computations but can result in reduced accuracy.

2.6 Nuclear based models

Due to the nuclear power plant accidents at Three Mile Island in 1979 and Chernobyl in 1986, the ability to control any potential disaster in the reactor containment became a number one task for nuclear safety groups. For example, the main challenge during a severe nuclear meltdown is to urgently spread the molten fusion product (corium) over the widest possible surface area. Since the lava flow propagation and the spreading of hot fluids on the topography share certain similarities, the developed codes for nuclear disaster simulations can also be used by volcanologists. The difference between nuclear and lava flow models is that the existing nuclear-based models do not account for topography and free surface. Therefore, to make nuclear based codes applicable to lava flow modelling, these aspects must be implemented. One example of such code adaptation for lava flow simulations is LavaSIM code (Hidaka et al., 2005).

Chapter 3: Numerical modelling of lava dome growth

This chapter is originally published in the journal *Frontiers in Earth Science*.

Zeinalova N., Ismail-Zadeh A., Melnik O., Tsepelev I., Zobin V. [2021]: Lava dome morphology and viscosity inferred from data-driven numerical modeling of dome growth at Volcán de Colima, Mexico during 2007-2009; *Frontiers in Earth Science (9)*, pp.: 1-17, doi: https://doi.org/10.3389/feart.2021.735914

Abstract – Magma extrusion, lava dome growth, collapse of domes, and associated pyroclastic flow hazards are among important volcanological studies. In this paper, we analyze the influence of the magma viscosity and discharge rates on the lava dome morphology at Volcán de Colima in Mexico during a long dome-building episode lasting from early 2007 to fall 2009 without explosive dome destruction. Camera images of the lava dome growth together with recorded volumes of the erupted lava have been used to constrain numerical modeling and hence to match the history of the dome growth by nudging model forecasts to observations. Our viscosity model incorporates crystal growth kinetics and depends on the characteristic time of crystal content growth (or CCGT) and the crystal-free magma viscosity. Initially, we analyze how this viscosity, CCGT, and the rate of lava extrusion influence the morphology of the growing dome. Several model scenarios of lava dome growth are then considered depending on the crater geometry, the conduit location, the effective viscosity of dome carapace, and the extrusion rates. These rates are determined either empirically by optimizing the fit between the morphological shape of modeled domes and that of the observed dome or from the recorded lava dome volumes. The maximum height of the modeled lava dome and its horizontal extent are in a good agreement with observations in the case of the empirically-derived extrusion rates. It is shown that the topography of the crater at Volcán de Colima is likely to be inclined toward the west. The viscosity of the modeled lava dome (~10^{12} Pa s) is in a good agreement with the effective viscosity estimated experimentally from lavas of Volcán de Colima. Due to the interplay between the lava extrusion and the gravity forces, the dome reaches a height threshold, and after that a horizontal gravity spreading starts to play an essential role in the lava dome evolution. The model forecasts that the dome carapace of higher viscosity (~10^{14} Pa s) influences the dome growth and its morphology during long dome-building episodes by retarding horizontal advancement and developing steep-sided eastern edge of the dome at the volcano. The developed model can be used in assessments of future effusive eruptions and lava dome growth at Volcán de Colima or elsewhere. History matching modeling of lava dome growth sheds a light on dynamic processes inside the dome and may assist in assessing stress state in the dome carapace and in forecasting the dome failures.

***Keywords**:* Volcán de Colima, lava dome, morphology, viscosity, numerical analysis

3.1 Introduction

Lava domes grow by the extrusion of viscous magma from a volcanic conduit (e.g., Calder et al., 2015). The lavas of dome-building volcanoes have low average eruption rates and high viscosities that are commonly associated with high groundmass crystallinity and, consequently, substantial yield strength (Lavallée et al., 2007, 2008; Sheldrake et al., 2016). Nonlinear dynamics of lava dome growth is caused by crystallization and outgassing of the highly viscous lava in the volcanic conduit (Melnik & Sparks, 1999). Through the intermittent buildup of gas pressure, growing domes can often experience episodes of explosive activity (e.g., Voight & Elsworth, 2000; Heap et al., 2019).

The morphology of lava domes is controlled by the magma rheology, the crater topography, the ascent dynamics, and the mechanism of dome growth (e.g., Fink & Griffiths, 1998; Tsepelev et al., 2020). Domes may reach heights of several hundred meters, and they may grow rapidly for some days or slowly and steadily for months to years. Dome growth in the crater may alternate between endogenous to exogenous styles. Endogenous growth refers to the enlargement of a lava dome due to expansion caused by intrusion of new magma. Exogenous growth refers to dome enlargement as a result of magma forcing its way through a preexisting lava dome carapace to the surface or flowing directly from the vent and forming discrete lobes of lava that pile on top of, or adjacent to, each other (Calder et al., 2002, 2015; Watts et al., 2002; Harris et al., 2003; Simmons et al., 2005; Rhodes et al., 2018; Harnett et al., 2019).

Numerical models of lava dome growth clarify how the rheological properties of magma within a lava dome influence morphological features of the dome and what are the effects of crystal content, temperature, pressure, and the discharge rate on the morphology (Hale & Wadge, 2003; Husain et al., 2014, 2018; Harnett et al., 2018; Tsepelev et al., 2020). Numerical modeling of lava dome growth allows reconstructing the process of filling of the crater with magma and estimating the lava viscosity, the crystal content growth time (CCGT) for crystal growth, and the extrusion rate (Tsepelev et al., 2020; Starodubtseva et al., 2021). This modeling requires information about the dynamics of lava dome growth collected during monitoring of the eruption. Here, we present a quantitative modeling study of the 2007-2009 endogenous stage of lava dome growth at Volcán de Colima, México, based on data collected by the University of Colima during the monitoring of the dome growth process. The goal of this study is to understand how the viscosity of magma/lava, the lava discharge rate, the conduit location, and the topography of the crater influence the dome morphology at Volcán de Colima. Compared to other numerical models of dome growth at this volcano, which are characterized by a rapid dome building (e.g.,Walter et al., 2019), this modeling study deals with a slow dome-building process without explosive dome destruction.

3.2 Volcán de Colima and its lava dome growth during 2007-2011

The andesitic 3860-m-high stratovolcano Volcán de Colima is the most active volcano in Mexico (Luhr & Carmichael, 1980). It is located in the western part of the Trans-Mexican Volcanic Belt (Figure 3.1a), and together with the Pleistocene volcano Nevado de Colima, they form the Colima Volcanic Complex. The recent dome-building eruption at Volcán de Colima began in November 1998 and was preceded by five swarms of volcano-tectonic earthquakes recorded from November 1997. The earthquake swarms indicated the pathway used by juvenile magma to ascend into the shallow magma storage zone, which is located at depths between 4 and 12 km beneath the crater (Zobin et al., 2002). This batch of magma fed seven lava dome-building episodes occurring during the 1998-2017 eruptions. The duration of the growth of lava domes varied from 14 days (rapid growth) to 33 months (slow growth) (Zobin & Tellez, 2019). In this paper we present the results of the numerical study of the long lava dome-building episode during 2007-2009, which is characterized by an uninterrupted dome extrusion. This removes complications associated with lava dome destruction by explosions or collapses, which are difficult to incorporate in a single mathematical/numerical model and permits to analyze a dome extrusion evolving over several years.

The photos in Figure 3.1(b-d) illustrate the lava dome growth within the crater during 2007-2009. The appearance of a new lava dome was observed at the beginning of February 2007 (Figure 3.1b; Zobin et al., 2017). As shown in Figure 3.1d, the crater was filled by a lava dome by the end of November 2009. In February 2010, the initially endogenous process of the dome growth was accompanied by exogenous growth of a small lobe of lava within the western sector of the crater of the volcano. The simultaneous endogenous and exogenous growth of the dome continued until June 2011(Zobin et al., 2017). Video monitoring of lava dome growth during 2007-2011, as well as photos taken with a camera located at a distance of about 5700 m from the center of the lava dome (Bretón-González et al., 2013), allowed for outlining the morphology of the growing dome in detail (Figure 3.1e).

Dome growth was monitored by photogrammetry tools (aerial photos) and by the related seismic recording (Zobin et al., 2017). Visual inspection of aerial photos was used to calculate the volume of the lava dome (Figure 3.2a), and the average discharge rates were then estimated (Figure 3.2b). The average discharge rate until the beginning of 2009 was about 0.02 m^3 s^{-1}. By March 2009, lava dome volume reached about 1,400,000 m^3, filling roughly 80% of the total crater. In fall 2009, the dome reached the western rim of the crater as shown in Figure 3.1d (Zobin et al., 2017).

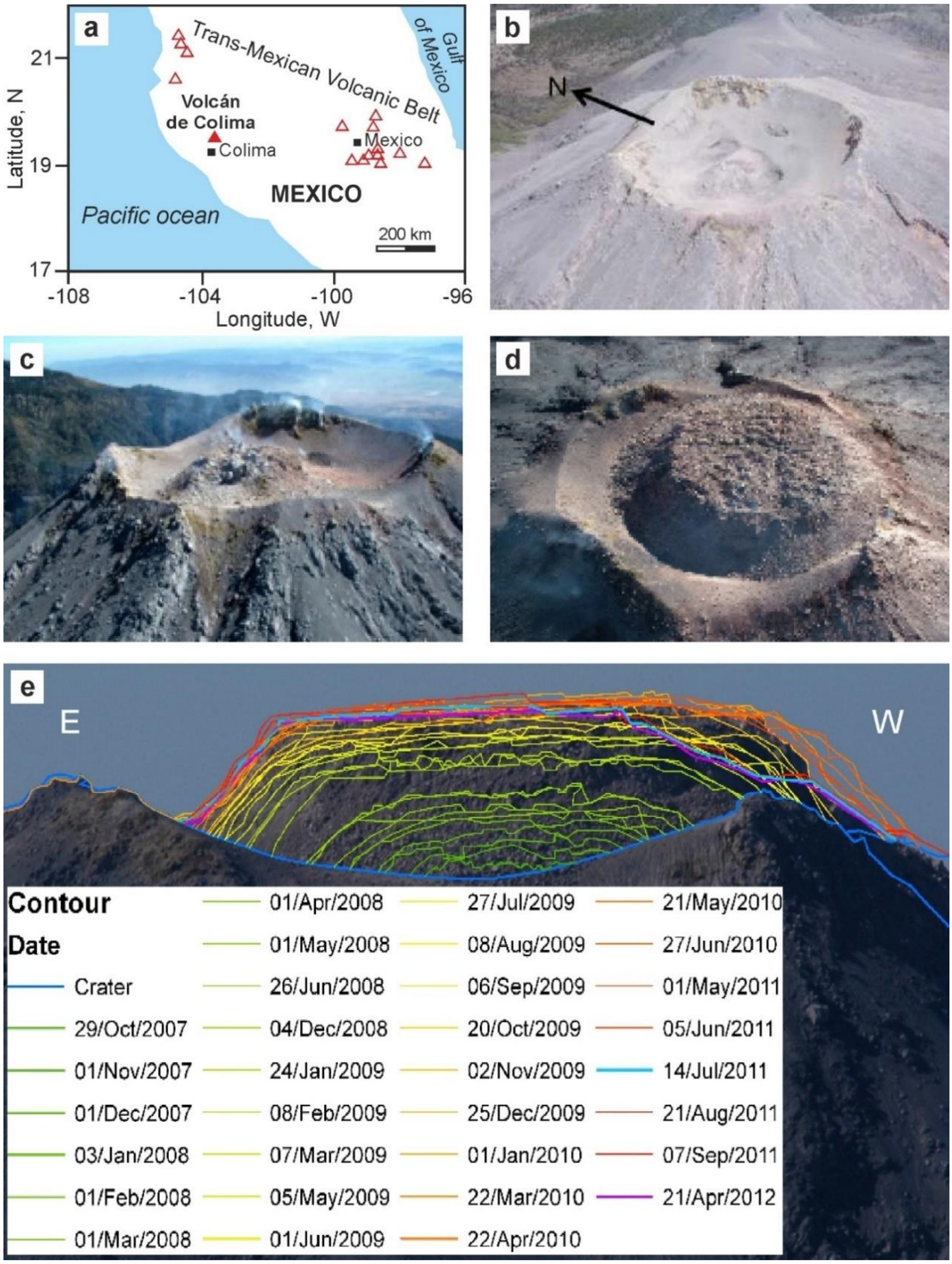

Figure 3.1: Lava dome growth at Volcán de Colima during 2007-2011. (a) Position of Volcán de Colima within the Trans-Mexican Volcanic Belt. Active volcanoes are shown with triangles; cities are shown with squares. (b-d) Photos of the growing lava dome at Volcán de Colima taken looking toward the northeast on (b) 1 February 2007, (c) 8 March 2008 and (d) 25 November 2009 (courtesy: Jalisco Civil Protection), (e) The contours of growing lava dome along the E-W profile of the crater of Volcán de Colima for 2007 to 2012 (after Bretón-González et al., 2013).

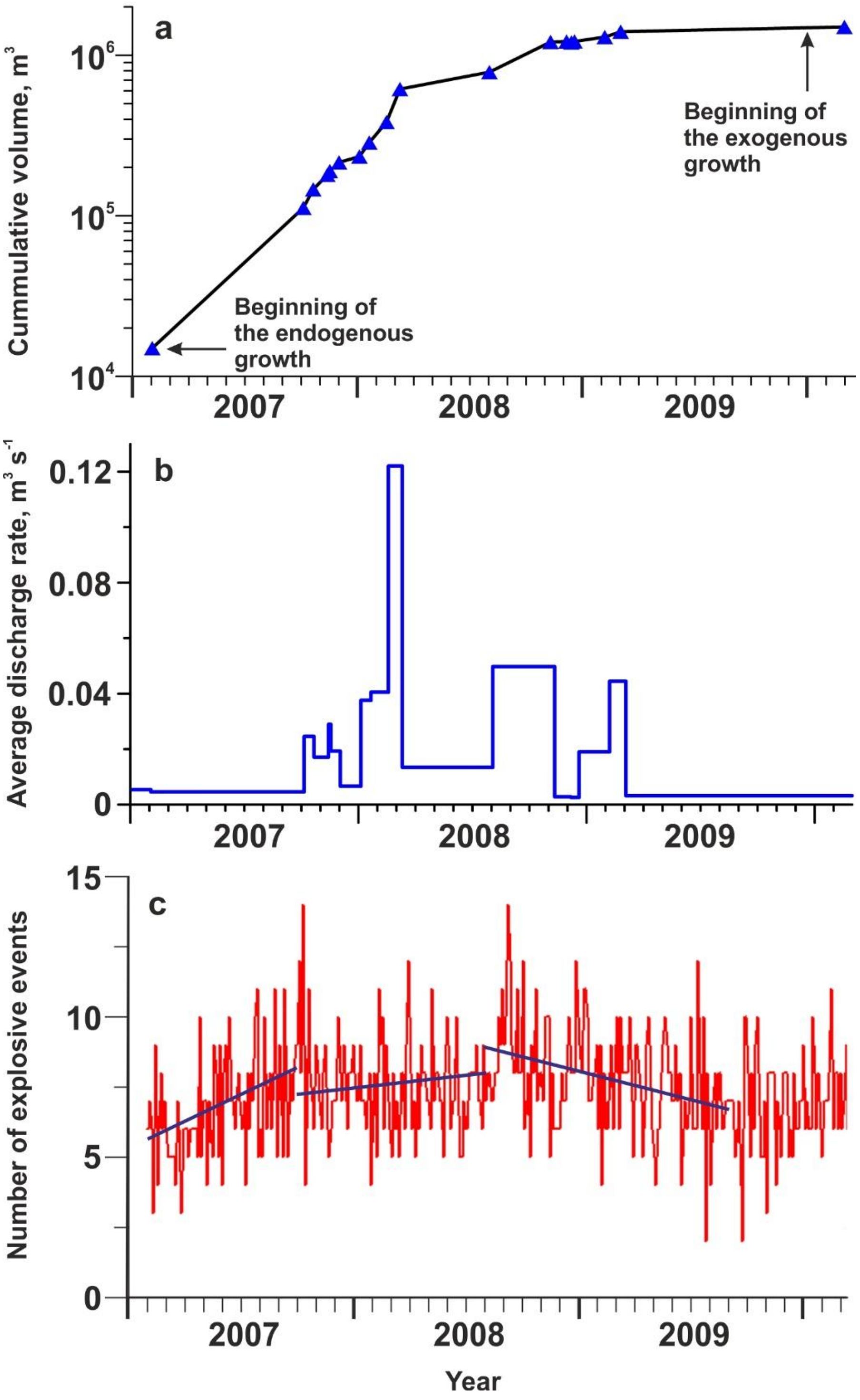

Figure 3.2: The cumulative volume of the growing lava dome (a), average discharge rate (b), and the number of explosive events (c), where the maximum likelihood regression lines (blue) present variations in the number of explosions. Source data: Zobin et al. (2015; 2017).

Figure 3.2c shows the temporal variations in the number of seismic signals generated by small gas-and-ash explosions (Zobin et al., 2015). Appearance of explosive events may serve as an indicator of magma degassing during the lava dome growth. Three periods of the degassing process can be distinguished. During February-September 2007, the number of explosions sharply increased demonstrating the activation of degassing at the initial stage of the lava dome growth. Then, during the ongoing stage of endogenous growth of the dome between October 2007 and January 2009, the level of degassing stayed at rather high level. Later the level of degassing continuously decreased up to the end of the lava dome growth in June 2011 (Zobin et al., 2017). The maximum likelihood regression lines shown in Figure 3.2c illustrate the tendency in the variation of the number of explosions during three periods of lava dome growth.

3.3 Statement of the problem and model setup

3.3.1 Geometry

A two-dimensional model geometry presented in Figure 3.3a approximates the observed geometry of the crater rim of Volcán de Colima across the E-W profile (Figure 3.1e) with an assumption that the lava dome base is located 20 m below the central part of the visible crater's rim (Bretón-González et al., 2013). Although the crater geometry varies in numerical experiments, the following parameters of the model domain remain the same: the width of the crater is 257 m, the width and the depth of the conduit are 14.5 m and 30 m, respectively (Zobin et al., 2015). In model domain Ω (Figure 3.3a), we consider a two-dimensional, viscous, incompressible, two-phase, immiscible fluid flow approximating an extrusion of lava (one fluid phase) into the air (another fluid phase) on the surface of the crater of Volcán de Colima.

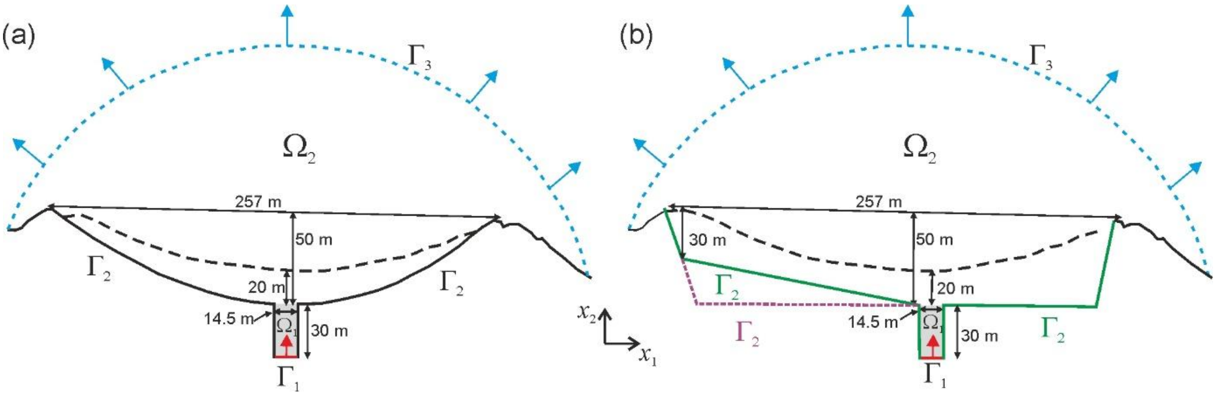

Figure 3.3: (a) The sketch of the model domain $\Omega = \Omega_1 \cup \Omega_2$ in exps. 1-4 and 7. The bold black line (Γ_2) presents the base of the crater and the vertical boundaries of the model conduit; the dashed black line is the observed rim of the crater; the red line (Γ_1) is the part of the model boundary, where a new magma enters into the conduit (sub-domain Ω_1) filled by an older magma (gray-shaded), and the red arrow indicates the direction of the new magma ascent within the conduit. The blue line (Γ_3) marks the upper boundary of the domain, through which the air escapes from the model; blue arrows show the direction of the escape. The geometry of boundary Γ_3 depends on the size of an evolving lava dome. (b) The sketch of the model domain in experiments 5, 6, 8-10. The green bold line presents the base of the modeled crater in exp. 5, 8 and 10, and the purple dashed line is a modified part of the crater in exp. 6 and 9. All other notations as in (a).

3.3.2 Governing equations with the initial and boundary conditions

A lava dome growth is described mathematically by the Navier-Stokes equations (Eq.(3.1)) with the initial condition $\mathbf{u}(t = 0, \mathbf{x}) = \mathbf{u}_0$, the continuity equation (Eq.(3.2)), and the advection equation (Eq.(3.3)) for the interface between the air and the lava:

$$\frac{\partial(\rho\mathbf{u})}{\partial t} + \langle \mathbf{u}, \nabla \rangle (\rho\mathbf{u}) - \nabla \cdot \left(\eta \left(\nabla\mathbf{u} + \nabla\mathbf{u}^T \right) \right) = -\nabla p - \rho\mathbf{g}, \tag{3.1}$$

$$\nabla \cdot \mathbf{u} = 0, \tag{3.2}$$

$$\frac{\partial\alpha}{\partial t} + \nabla \cdot (\alpha\mathbf{u}) = 0, \tag{3.3}$$

where $\mathbf{x} = (x_1, x_2) \in \Omega$ are the Cartesian coordinates; t is the time; $\mathbf{u} = (u_1(t,\mathbf{x}),\ u_2(t,\mathbf{x}))$ is the velocity; ρ is the density; η is the viscosity; $p = p(\mathbf{x})$ is the pressure; $\mathbf{g} = (0, g)$, and g (=9.81 m·s^{-2}) is the acceleration due to gravity; $\alpha(t,\mathbf{x})$ takes the value of one for the lava and zero for the air at each point $\mathbf{x}$ and time t; ∇, $\nabla \cdot$, ^{T}, and $\langle \cdot,\cdot \rangle$ denote the gradient operator, the divergence operator, the transposed matrix, and the scalar product of vectors, respectively. We consider that the model density and viscosity are presented as $\rho = \rho_L \alpha(t,\mathbf{x}) + \rho_A(1-\alpha(t,\mathbf{x}))$ and $\eta = \eta_L \alpha(t,\mathbf{x}) + \eta_A(1-\alpha(t,\mathbf{x}))$, respectively, where ρ_A = 1.225 kg·m^{-3} and η_A = 10^{-3} Pa·s are the density and viscosity of the air; ρ_L = 2500 kg·m^{-3} and η_L are the lava density and viscosity, respectively.

At the initial time, the sub-domain Ω_1 (the model conduit) is filled by an older magma with high volume fraction of crystals ($\phi = 0.8$), and hence $\alpha(t=0,\mathbf{x}) = 0$ for $\mathbf{x} \in \Omega_2$ and 1 for $\mathbf{x} \in \Omega_1$. The initial velocity field $\mathbf{u}_0$ is chosen so as to generate a laminar flow in the entire model domain, including the part filled by the air (see *A1:Appendix*). In the numerical modeling, we neglect the dependence of the density on temperature and/or phase transformation due to crystallization or volatile exsolution.

The following conditions are imposed on the model boundary $\Gamma = \Gamma_1 \cup \Gamma_2 \cup \Gamma_3$ (Figure 3.3). A new lava (with the volume fraction of crystals $\phi = \phi_{in}$) enters into the model domain at a specified extrusion rate $\mathbf{u}_{ext}$ = $(0, u_{ext})$ through the part Γ_1 of the model boundary. The lava extrusion rate (m s^{-1}) in the modeling is determined either (i) empirically from camera images of the morphological shapes taken during lava dome growth from 2007 to 2009 (Figure 3.1e) or (ii) from the observed volumes of extruded lava and calculated discharge rates (m^3 s^{-1}) (see *A2:Appendix*). In case (i), we vary the model extrusion rate and choose one that provides the best fit between the morphological shapes of modeled and observed domes at specified times. A no-slip condition $\mathbf{u} = 0$ is prescribed at Γ_2. The outflow conditions are determined at Γ_3 (the blue curve) by removing the air from the model domain proportional to the lava discharge rate and to guarantee the condition of incompressibility: $\mathbf{u}_{out} = u_{out}\mathbf{n}$ and $u_{out} = -|\Gamma_3|^{-1} \int_{\Gamma_1} \langle \mathbf{u}_{ext}, \mathbf{n} \rangle d\Gamma$, where $\mathbf{n}$ is the outward unit normal vector at a point on the model boundary.

3.3.3 Lava viscosity

Degassing-induced (i.e., temperature independent) crystallization is the main driving force in the bulk viscosity increase in conduits and lava domes compared to the cooling-induced viscosity increases of the melt and crystallization (e.g., Chevrel et al., 2013; Tsepelev et al., 2020). Meanwhile, a cooling-induced increase in the viscosity of the dome carapace becomes important during long episodes of lava dome growth. Hence, although the lava dome rheology is more complex, we assume here that the lava viscosity η_L depends on the volume fraction of crystals only (Costa et al., 2009):

$$\eta_L(\varphi) = \eta_{mt}\left(1+\varphi^{\delta}\right)\left[1-(1-\xi)\cdot \operatorname{erf}\left(\frac{\sqrt{\pi}}{2(1-\xi)}\varphi(1+\varphi^{\gamma})\right)\right]^{-B\phi_*}, \tag{3.4}$$

where η_{mt} is the crystal-free magma viscosity; $\varphi = \phi / \phi_*$, ϕ is the volume fraction of crystals; ϕ_* is the specific volume fraction of crystals, representing the critical solid fraction at the onset of the exponential increase of the lava viscosity (here we assume $\phi_* = 0.384$); the empirical parameters $\delta = 7.24$, $\xi = 4.63\times 10^{-4}$, and $\gamma = 5.76$ are taken from Lejeune & Richet (1995) and Costa et al. (2009); and $\operatorname{erf}(\cdot)$ is the error function. The coefficient *B* is determined from the Einstein equation as $B = (\eta_L(\phi)-1)/\phi$ (Mardles, 1940). It was experimentally determined that this coefficient varies from 1.5 to 5 (Jeffrey & Acrivos, 1976); and we assume *B* = 2.5 (Costa et al., 2009).

The volume fraction of crystals ϕ is determined from the evolutionary equation describing the simplified crystal content growth kinetics of degassing-induced crystallization (e.g., Tsepelev et al., 2020):

$$\frac{\partial \phi}{\partial t} + \nabla\cdot(\alpha\phi\mathbf{u}) = -\alpha\frac{\phi-\phi_{eq}}{\tau}, \tag{3.5}$$

with the initial condition for the volume fraction of crystals $\phi(t=0,\mathbf{x}) = 0$ for $\mathbf{x}\in\Omega_2$ and $\phi(t=0,\mathbf{x}) = 0.8$ for $\mathbf{x}\in\Omega_1$. Here, ϕ_{eq} is the volume fraction of crystals at the equilibrium state, which depends on the fraction of water dissolved in magma and temperature; τ is the characteristic time of crystal content growth (CCGT) needed by crystals to reach ϕ_{eq}. We assume that $\phi_{eq} = 0.83$, which is in the range of experimental constraints (Riker et al., 2015; Cashman, 2020). The smaller CCGT, the faster the crystallization process converges to its equilibrium state. CCGT is referred to as the *relaxation time* (Tsepelev et al., 2020), which is required to reduce the difference between the actual (ϕ) and equilibrium (ϕ_{eq}) values of the volume fractions of crystals by a factor of *e* with respect to the difference ($\phi_{in} - \phi_{eq}$), where ϕ_{in} is the volume fraction of crystals in the magma entering the model conduit at Γ_1 (in the modeling we assume that $\phi_{in} = 0.4$).

3.4 Method

We consider the problem of lava dome viscosity determination from observations of the dome morphology (e.g. the observed height and horizontal extent of the dome). The relevant mathematical problem belongs to the class of inverse problems. There are several methods to solve the problem, that is, to determine the distribution of lava dome viscosity from relevant observations. One of the methods is based on optimization using data assimilation techniques and helps solving the inverse problem (and determining the viscosity) by organizing an iteration process to minimize the difference between the model solution and observations (e.g., (Ismail-Zadeh et al., 2016; Korotkii et al., 2016)). This method involves an analytical derivation of the optimization (adjoint) problem, and hence it is restricted to simple cases. Another method is based on the use of image processing and machine learning to determine the viscosity of a lava dome by analyzing images of the observed and modeled morphological shapes of the dome at each time of lava dome growth (Starodubtseva et al., 2021). An inverse problem can be replaced by the direct problem conjugated with the inverse problem, and the direct problem can be solved by varying model parameters and fitting observations. Although this method is simpler than the previous two approaches, it requires a significant number of numerical experiments to fit the observations. In this work we use the latter method, namely, we solve numerically Eq. (3.1) - (3.5) with the relevant initial and boundary conditions and vary the model parameters to get the best fit to the height and width of the lava dome during its growth.

To solve this problem numerically, we employ the Ansys Fluent software, where the finite volume method is used to solve numerical models on multiprocessor computers. The software is based on the volume of fluid (VOF) method (Hirt & Nichols, 1981) allowing for computationally inexpensive treatment of a moving interface between two fluid phases, e.g., the lava and the air. The cells containing the interface between the lava and air have α values between zero and one depending on the lava proportion in the cells. Because of the large discontinuity between the lava and air viscosity, the interface of the two fluids does not represent a sharp boundary, and some smearing can be observed during computations. More detail about the numerical approach can be found in *A1:Appendix*.

3.5 Numerical results

We have performed a number of numerical experiments, and the experiments with relevant values of model parameters are listed in Table 3.1.

Table 3.1: Numerical experiments and their model parameters.

No. exp.	**Extrusion rate u_{ext}, m s^{-1}**	**Crystal-free magma viscosity η_{mt}, Pa s**	**CCGT τ, day**
1.1	1×10^{-5}	1.6×10^{5}	5
1.2	1×10^{-5}	8×10^{5}	5
1.3	1×10^{-5}	8×10^{6}	5
2.1	1×10^{-5}	1.6×10^{5}	5
2.2	1×10^{-5}	1.6×10^{5}	15
2.3	1×10^{-5}	1.6×10^{5}	50
2.4	1×10^{-5}	1.6×10^{5}	100
3.1	5×10^{-6}	1.6×10^{5}	5
3.2	1×10^{-5}	1.6×10^{5}	5
3.3	5×10^{-5}	1.6×10^{5}	5
4	• 5×10^{-6} for 300 days • 7.5×10^{-6} from day 301 to day 455 • 2×10^{-5} from day 456 to day 1020	• 1.6×10^{5} for 150 days • 8×10^{5} from day 151 to day 1020	5
5	• 5×10^{-6} for 300 days • 7.5×10^{-6} from day 301 to day 455 • 2×10^{-5} from day 456 to day 1020	• 1.6×10^{5} for 150 days • 8×10^{5} from day 151 to day 1020	5
6	• 5×10^{-6} for 300 days • 7.5×10^{-6} from day 301 to day 455 • 2×10^{-5} from day 456 to day 1020	• 1.6×10^{5} for 150 days • 8×10^{5} from day 151 to day 1020	5
7	• 5×10^{-6} for 368 days • 2.25×10^{-5} from day 369 to day 434 • 1.07×10^{-5} from day 435 to day 704 • 2.71×10^{-6} from day 705 to day 1020	• 1.6×10^{5} for 150 days • 8×10^{5} from day 151 to day 1020	5

8	- 5×10^{-6} for 368 days - 2.25×10^{-5} from day 369 to day 434 - 1.07×10^{-5} from day 435 to day 704 - 2.71×10^{-6} from day 705 to day 1020	- 1.6×10^{5} for 150 days - 8×10^{5} from day 151 to day 1020	5
9	- 5×10^{-6} for 368 days - 2.25×10^{-5} from day 369 to day 434 - 1.07×10^{-5} from day 435 to day 704 - 2.71×10^{-6} from day 705 to day 1020	- 1.6×10^{5} for 150 days - 8×10^{5} from day 151 to day 1020	5
10	- 5×10^{-6} for 300 days - 7.5×10^{-6} from day 301 to day 455 - 2×10^{-5} from day 456 to day 480 - 1.7×10^{-5} from day 481 to day 1020	- 1.6×10^{5} for 150 days - 8×10^{5} from day 151 to day 1020	5

3.5.1 Sensitivity analysis

We develop initially a series of numerical experiments of lava dome growth varying the model parameters to understand how each of them influences the morphological shape of the lava dome (e.g., its height and width). Particularly, we have performed a sensitivity analysis with respect to the crystal-free magma viscosity η_{mt}, CCGT τ , and extrusion rate u_{ext}.

Experiments 1: We study the influence of the crystal-free magma viscosity η_{mt} on the dome morphology. In the experiments, this factor varies from 1.6×10^{5} to 8×10^{6} Pa s. At higher viscosity, the erupted magma tends to remain close to the vent, forming obelisks, rather than to advance horizontally forming lava flows. Figure 3.4a shows that the dome height increases with the crystal-free magma viscosity while the lateral extent of the dome decreases. Therefore, the crystal-free magma viscosity controls the height and extent of lava domes.

Experiments 2: These experiments explore the influence of CCGT on the morphology of lava domes. The crystal-free magma viscosity is prescribed to be $\eta_{mt} = 1.6\times10^{5}$ Pa s. All other parameters are the same as in experiments 1. Figure 3.4b shows the dome morphology for the four CCGT. The greater CCGT the more the lava dome advances horizontally and less vertically. To better fit the shape of the observed lava dome, we choose 5 days for CCGT in our modeling.

Experiments 3: These numerical experiments explore the influence of the lava extrusion rate on the dome morphology. Figure 3.4c illustrates the morphological shapes of lava domes at various effusion rates. The higher the rate the larger the dome as it accommodates the larger volume of the extruded lava.

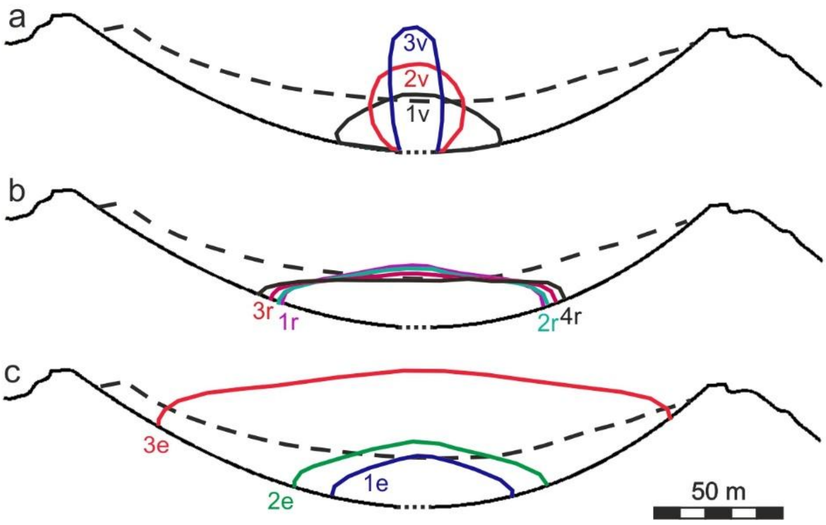

Figure 3.4: Lava dome growth in experiments 1-3. The dashed line presents the crater's rim. **(a)** Black curve 1v (exp. 1.1), red curve 2v (exp. 1.2), and blue curve 3v (exp. 1.3) present the morphological shape at the time t = 70 days for the crystal-free magma viscosity $\eta_{mt} = 1.6\times10^5$, 8×10^5, and 8×10^6 Pa s, respectively. **(b)** Purple curve 1r (exp. 2.1), green curve 2r (exp. 2.2), red curve 3r (exp. 2.3), and black curve 4r (exp. 2.4) present the morphological shape at the time t = 150 days for CCGT of 5, 15, 50, and 100 days, respectively. **(c)** Blue curve 1e (exp. 3.1), green curve 2e (exp. 3.2), and red curve 3e (exp. 3.3) present the morphological shape at the time t = 150 days for the extrusion rate 5×10^{-6}, 10^{-5}, and 5×10^{-5} m s^{-1}, respectively.

3.5.2 Lava dome morphology

Based on the sensitivity analysis, we have constrained the model parameters to get a better fit between the observed and modeled heights of the lava dome at Volcán de Colima. We present here the results of three numerical experiments, which are consistent with the observations on the dome growth from 1 February 2007 to 20 October 2009. The model parameters are listed in Table 3.1; the model experiments differ from each other by their geometry.

In these model experiments, the lava extrusion rate u_{ext} is obtained empirically from the analysis of the lava dome images at different times and from the results of the sensitivity analysis with respect to varying rates of extrusion (experiments 3) This empirical approach is supported theoretically (see Eq. (A4) in *A2:Appendix*, we note that the calculated values of the rate are in close vicinity to the rates obtained empirically). To match the observed and modeled heights of the lava dome, the following extrusion rates u_{ext} have been assigned (see Figure 3.5):

5×10^{-6} m s^{-1} for the first 300 days, 7.5×10^{-6} m s^{-1} from day 301 to day 455, and 2×10^{-5} m s^{-1} from day 456 until day 1020, the end time of the numerical experiments.

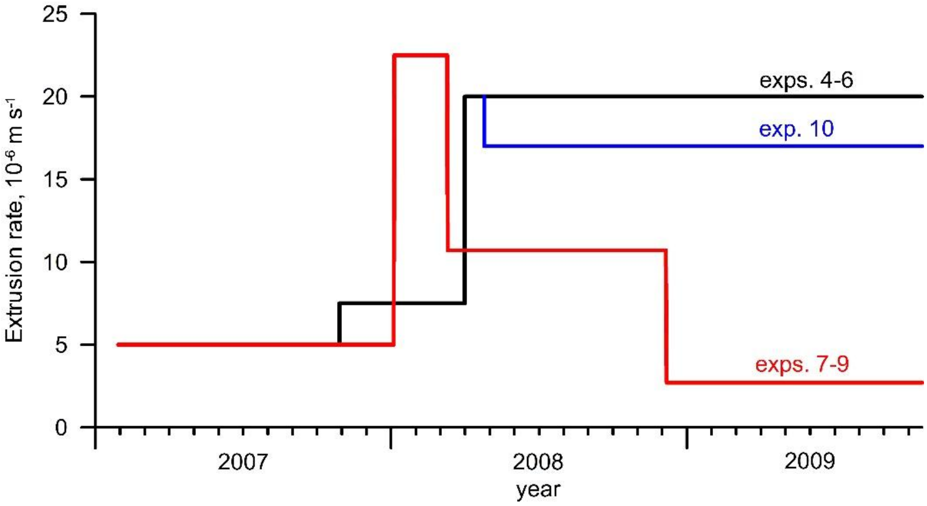

Figure 3.5: Model extrusion rate in experiments 4-10.

The crystal-free magma viscosity is assumed to be 1.6×10^{5} Pa s for 150 days, and it has been increased by a factor of 5 (8×10^{5} Pa s) after that and kept unchanged until the end of the experiments. This increase of the model viscosity can be attributed to the increased degassing at the initial stage of the lava dome growth evident from seismic records (Figure 3.2b). We note that the effects of volatiles and bubbles on the magma rheology are not considered explicitly in the model. This would complicate the model by additional equations, describing the bubble dynamics. Also, volatile exsolution is not equilibrium in high viscosity magmas, and faster extrusion rates lead to higher amounts of dissolved volatiles. This increase of the model viscosity favors upward growth of the dome compared to horizontal spreading of the extruded lava.

Experiment 4. The morphological shapes of the modeled lava dome are presented in Figure 3.6a,d. The results show that the extruded lava develops a dome structure, which fills the volcano crater (Figure 3.6a). Due to the interplay between the extrusion rate and the lava viscosity, the dome grows up and advances horizontally. While dome dynamics is dominated by vertical growth for at least 480 days, a horizontal advancement becomes dominant later due to gravitational spreading of the erupted lava.

The maximum heights of the modeled and observed lava domes show a good agreement (Figure 3.6d and Figure 3.7). Meanwhile, the morphological shapes of both domes do not fit each other well on the left side of the model domain (or in the eastern part of the crater). Although the photo of the dome initiation in February 2007 (Figure 3.1b) shows that it started to build nearly in the center of the crater, with time the extruded lava seems to have been moving toward the west (Figure 3.1d). This westward slope in the dome building could be due to the location of the lava vent, which is likely to be opened closer to the western side of the crater, and/or due to a westward inclination of the crater topography promoting the lava advancement in the direction. Moreover, it was proposed that the upper part of the conduit at Volcán de Colima may be bending westward close to the surface (Lavallée et al., 2012; Salzer et al., 2014). To test the hypotheses, we have modified the geometry of the crater and performed two other experiments.

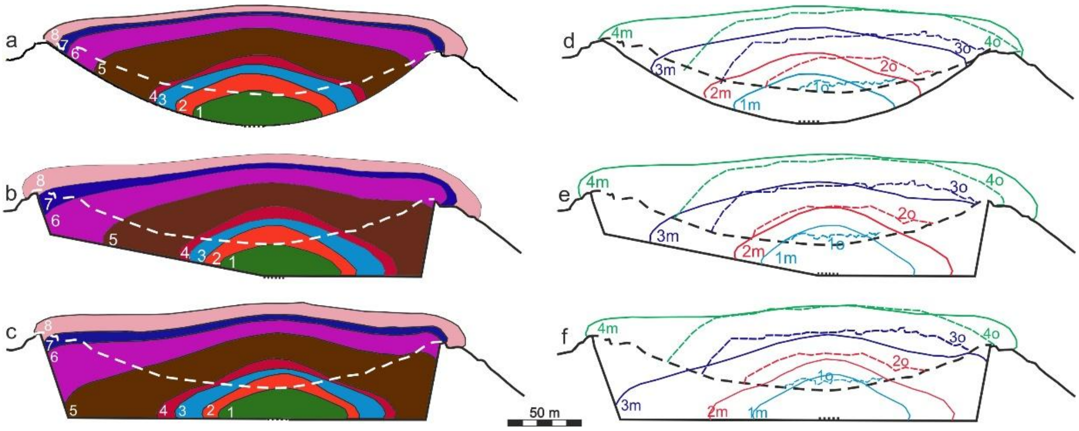

Figure 3.6: Lava dome growth in experiment 4 (**a** and **d**), 5 (**b** and **e**), and 6 (**c** and **f**). **(a-c)** The dome morphology at day 150 (the curve marked by 1), 300 (2), 434 (3), 480 (4), 700 (5), 852 (6), 912 (7), and 1020 (8). The white dashed line is the crater's rim. **(d-f)** Comparison of the morphological shapes of the modeled (curves with index m) and observed (dashed curves with index o; see Figure 3.1e) lava domes at day 300, 1 November 2007 (cyan curves); day 480, 1 May 2008 (red curves); day 704, 4 December 2008 (blue curves); and day 1020, 20 October 2009 (green curves). The black dashed line is the crater's rim. The black bold line presents the base of the crater, and the black dotted line is the top of the conduit.

Experiment 5. This experiment differs from exp. 4 by the geometry of the computational domain (Figure 3.3b). The topography of the crater is assumed to be flat on its right side and inclined on its left side. The location of the conduit is shifted to the right of the model domain (to the west) by the size of the conduit's diameter (14.5 m). The model parameters are the same as in exp. 4.

Figure 3.6 (b,e) illustrates the model dome evolution in exp. 5. Since initiation of the lava dome growth, the dome moves easily toward the west (to the right side of the model domain) because of the slope of the crater's topography on the left side of the model domain. Once the lava reaches the western border of the crater, the dome builds up in the west and extends horizontally to the east (Figure 3.6b). At the later stage of the dome growth, the morphological shapes of the domes in experiments 4 and 5 show similarity.

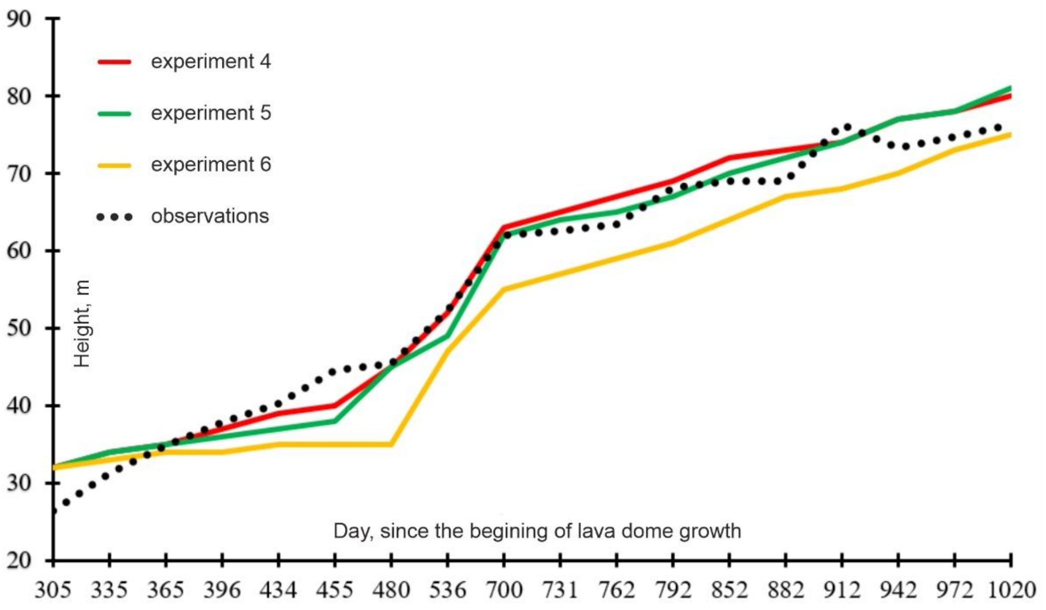

Figure 3.7: Comparison of the maximum heights of the lava dome at Volcán de Colima (Bretón-González et al., 2013) with those of the modelled domes.

Figure 3.6e shows that the morphological shapes of the observed and modeled lava domes fit well enough at least until 1 May 2008 (day 480), and the maximum heights of both domes are close to each other (see also Figure 3.7). Although the shapes of both domes on the western part of the crater converge better in exp. 5 compared to exp. 4, there are still discrepancies between the shapes on the eastern side of the crater, namely, the eastern side of the observed dome is steeper than that of the modeled dome. More complex geometry of the crater on its eastern side as well as an increasing viscosity, as the lava fully solidifies at the edges, could explain the observed morphology of the dome.

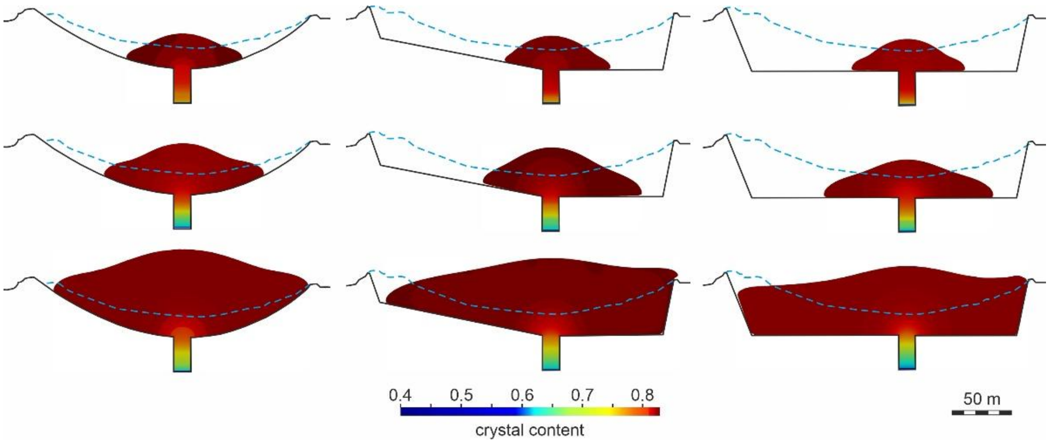

Figure 3.8:The modelled crystal content at times of 2007/11/01 (upper panels), 2008/05/01 (middle panels), and 2009/04/01 (lower panels) in experiments 4 (left column), 5 (middle column), and 6 (right column).

Experiment 6. In this experiment, the crater base is flat (Figure 3.3b), and the conduit is shifted (by 14.5 m) toward the west compared to the geometry of the crater in the case of exp. 4. The model parameters are the same as in exp. 4. Figure 3.6 (c, f) illustrates the modeled dome evolution in this experiment. The flat topography of the model crater promotes the lava dome to advance in both direction (to the west and to the east), although the lava reaches the western side of the crater faster than its eastern side due to the location of the conduit in the model (Figure 3.6c). The morphological shapes of the modeled and observed domes fit each other rather good at least until May 2008 (Figure 3.6f). However, later the maximum heights of the modeled lava dome are smaller than those of the observed lava dome. Comparing the maximum heights of the modeled domes, one can see that the dome heights in exps. 4 and 5 agree well with the observed data especially for the time interval from 480 to 704 days. Meanwhile, the heights of the modeled dome in exp. 6 do not match well those of the observed dome except the time closer to the end of 2009. As all parameters of the model in exps. 4-6 are the same except the model geometry, we consider that the best fit of the modeled dome height and width to the observations is achieved in exp. 5, where the crater floor is inclined westward on the left of the vent and the floor is horizontal on its right.

3.5.3 Lava dome viscosity

We illustrate here the distribution of the modeled crystal content, viscosity, and velocity for times of 1 November 2007, 1 May 2008, and 1 April 2009 in the case of experiments 4-6. The crystal content within the model conduit and the lava dome is presented in Figure 3.8. A new magma enters the model conduit with the initial volume of the crystal content equal to 0.4, and it reaches almost its equilibrium value 0.83 at the surface near the vent, because the magma crystalizes rapidly at small extrusion rates and small CCGT. We note the magma viscosity remains finite at $\phi_{eq} = 1$ in terms of viscosity formulation (see Eq. 3.4) by Costa et al. (2009). Moreover, 100% crystal content is never observed in eruptive products. According to Eq. 3.4, more rapid growth in viscosity occurs at lower crystal contents of 0.4 to 0.7 depending on the crystal shape and size distribution. The volume fraction of crystal and melt content in the magma uplift controls its effective (bulk) viscosity(Hess & Dingwell, 1996; Melnik & Sparks, 2005). This volume fraction changes with pressure and flow velocity, and the resulting morphology of a lava dome can be affected (Watts et al., 2002; Melnik & Sparks, 2005).

The viscosity distribution in the lava dome mimics the distribution of the crystal content (Figure 3.9). The lava dome viscosity reaches 10^{12} Pa s, while the viscosity of magma in the conduit varies from about $10^{9.8}$ to about $10^{11.9}$ Pa s. For lavas from Volcán de Colima, Lavallée et al. (2007) estimated the melt viscosity and the effective viscosity to be $10^{8.58}$ Pa s and $10^{11.28}$ Pa s, respectively, where the effective viscosity was calculated using the Einstein-Roscoe equation (Einstein, 1906; Roscoe, 1952). The viscosity obtained in the model is in a good agreement with the estimated effective viscosity of lavas from Volcán de Colima, although direct comparison between calculated and measured viscosities has some difficulties including strain localization, shear heating and other effects. For example, the apparent viscosity of lavas from Volcán de Colima estimated experimentally by Lavallée et al. (2008) is between about 10^{9} Pa s and $10^{9.4}$ Pa s at stress of 8 MPa. At small extrusion rates and the prolonged duration of the dome growth, the higher viscosity provides the lava dome to grow upward (see exp. 1), while the lower viscosity leads to a horizonal advancement of the lava dome and an insignificant vertical growth. The higher viscosity could be associated with magma degassing during the lava dome building and rapid crystallization as recorded by the increased seismic activity (Figure 3.2b) during 2007-2009. The velocity field shows higher flow rates in the conduit and near the vent oriented almost vertically, and the rates decay with the increase of the dome height.

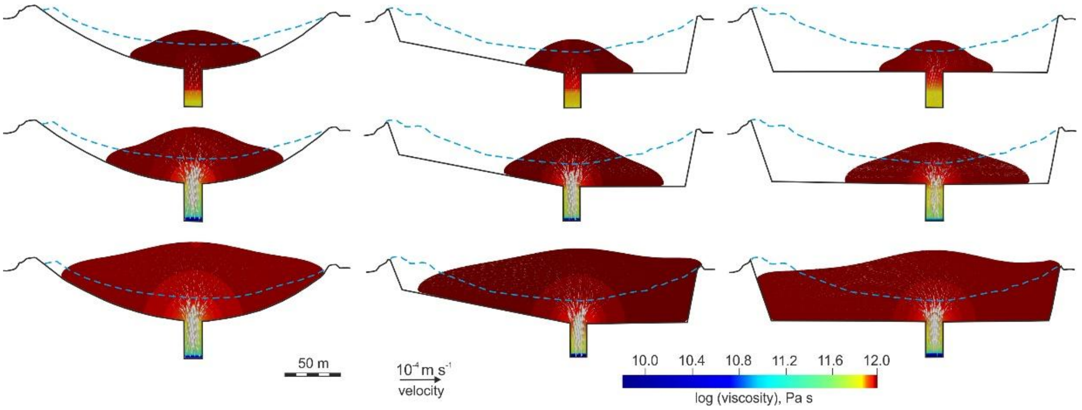

Figure 3.9: The modelled viscosity and velocity (arrows) in experiments 4 (left column), 5 (middle column) and 6 (right column) on 2007/11/01 (upper panels), 2008/05/01 (middle panels), and 2009/04/01 (lower panels).

3.5.4 Extrusion rates

In the following experiments, we employ the extrusion rates calculated from the observed lava dome volumes and calculated discharge (effusion) rates using Eq. (A5) in *A2:Appendix* (see also Figure 3.2b). In the experiments, the initial extrusion rate is $u_{ext} = 5.6 \times 10^{-6}$ m s^{-1}; it increases to 2.25×10^{-5} m s^{-1} from day 368 to day 434, decreases to 1.07×10^{-5} m s^{-1} from day 435 to day 704 (see Figure 3.5). Starting from day 705 and until day 1020, the extrusion rate decreases to 2.71×10^{-6} m s^{-1}. The numerical experiments here differ from each other by the geometry of the model domain: in exp. 7 the model geometry is the same as in exp. 4 (Figure 3.3a), in exp. 8 as in exp. 5, and in exp. 9 as in exp. 6 (Figure 3.3b).

Initially the morphological shape and the maximum height of the lava domes in experiments 7-9 (Figure 3.10) follow closely those in experiments 4-6, respectively, as the initial extrusion rate is the same in both sets of the experiments (Table 3.1; Figure 3.5). However, the subsequent evolution of the lava dome in experiments 7-9 differs from that in experiments 4-6 starting from day 368, and it is associated with the increase of the extrusion rate by a factor of about 4 in experiments 7-9. The decrease of the extrusion rate after day 434 results in the gravitational spreading of lava dome instead of its growth upward. The dome height reaches its maximum value at day 704 as after that the extrusion rate decreases by a factor of about 4, and the dome starts to advance horizontally. Unfortunately, the morphology of the modeled domes does not fit that of the observed dome, and the dome heights are low compared to the observations (Figure 3.10).

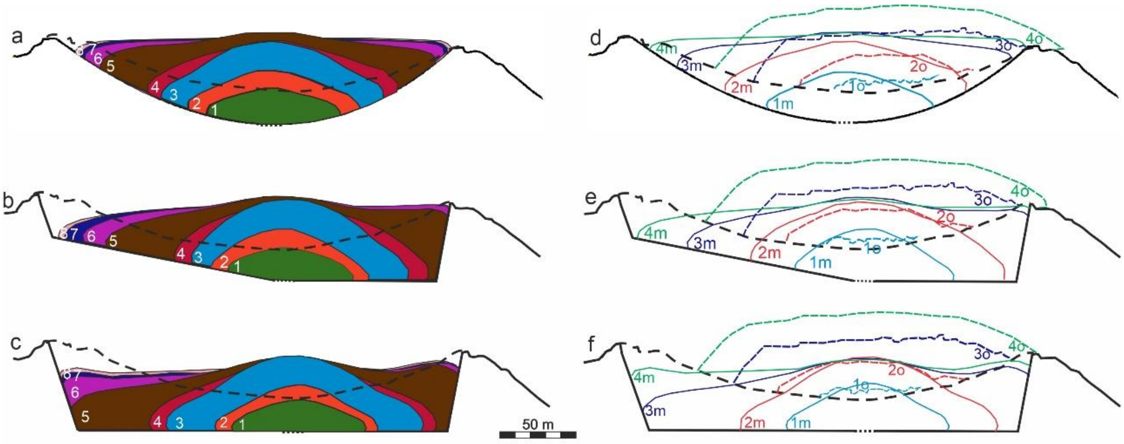

Figure 3.10: Lava dome growth in experiment 7 (a, d), 8 (b, e), and 9 (c, f). See Figure 3.6 for notations.

3.5.5 Lava dome carapace

Lava domes usually have a solid surface layer (carapace) but remain mobile and undergo deformation for days to months (Anderson & Fink, 1990). Iverson (1990) highlighted the importance of the thermal carapace in determining the morphology of domes. The role of the surface cooling and the carapace formation were analysed in laboratory and numerical experiments (e.g., Fink & Griffiths, 1998; Griffiths, 2000; Hale et al., 2007; Hale, 2008; Hale & Wadge, 2008; Husain et al., 2014, 2018, 2019; Harnett et al., 2018).

A thickness of the thermal boundary layer ($\sqrt{\kappa t}$), which is associated with a rigid part of the lava dome carapace, ranges from ~1 m to ~10 m for dome growth time *t* from 10 days to three years, respectively (assuming the coefficient of the thermal diffusivity to be $\kappa = 10^{-6}$ m^2 s^{-1}. Tsepelev et al. (2020) showed that at high discharge rates and for a short time duration of lava extrusion, this lava generates a thin carapace due to cooling, which influence only slightly the morphology of a dome promoting a steeper slope similar to that observed during the dome growth at Volcán de Colima.

To simulate a thermal carapace development during lava dome growth, our mathematical/numerical model should be supplemented by the heat equation, which would complicate the model and computations. Therefore, to keep the same numerical model, we modify the lava dome viscosity by introducing a higher viscous layer at the interface between the dome and its surrounding in order to simulate a dome carapace (see *A1:Appendix*).

In experiment 10, we assume that the crater geometry and the model parameters are the same as in exp. 5, except for the extrusion rate. This numerical experiment starts at day 481 of the model dome growth as in exp. 5. A higher viscosity carapace of ~6 m thick is introduced in the model at day 481 simultaneously with a decrease of the extrusion rate by 15 % compared to the rate in exp. 5 (see Figure 3.5). This decrease in the extrusion rate has been introduced to reduce the volume of erupted lava and to better fit the observed morphological shapes.

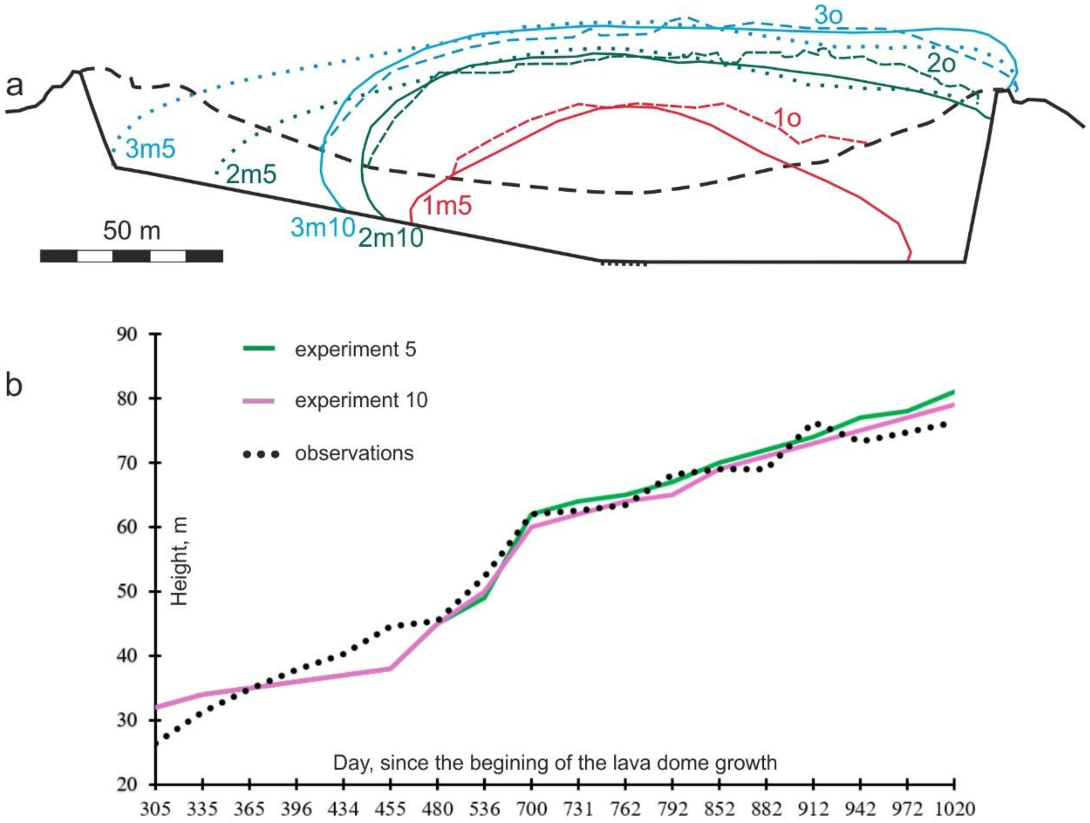

Figure 3.11: Lava dome growth in experiment 10. (a) Comparison of the morphological shapes of the modelled dome in exp. 10 (solid curves with index m10) with that in exp. 5 (dotted curves with index m5) and with observed lava domes (dashed curves with index o) on (1) 1 May 2008 (red curves), (2) 4 December 2008 (green curves), and (3) 1 April 2009 (blue curves). The black dashed line is the crater's rim. The black bold line presents the base of the crater, and the black dotted line is the top of the conduit. (b) Comparison of the maximum heights at the center of the lava dome at Volcán de Colima (Bretón-González et al., 2013) with those of the modelled dome in exp. 10 (purple curve) and in exp. 5 (green curve).

Figure 3.11 presents several stages of the dome growth in exp. 10. The dome morphology differs significantly compared to that in exp. 5 (Figure 3.11a). Particularly, (i) the dome develops a steep flank on its left side, which fits observations at Volcán de Colima rather well, and (ii) the advancement of lava dome at its left side is retarded by about 50 m for 334 days, compared to dome advancement in exp. 5. Meanwhile, the dome heights in both experiments (Figure 3.11b) are in a good agreement with the observations. The modeled viscosity and velocity in the lava dome are presented in Figure 3.12 together with the images of the dome at Volcán de Colima for three stages of its growth. It is seen that exp. 10 provides much better fit between the model and observations.

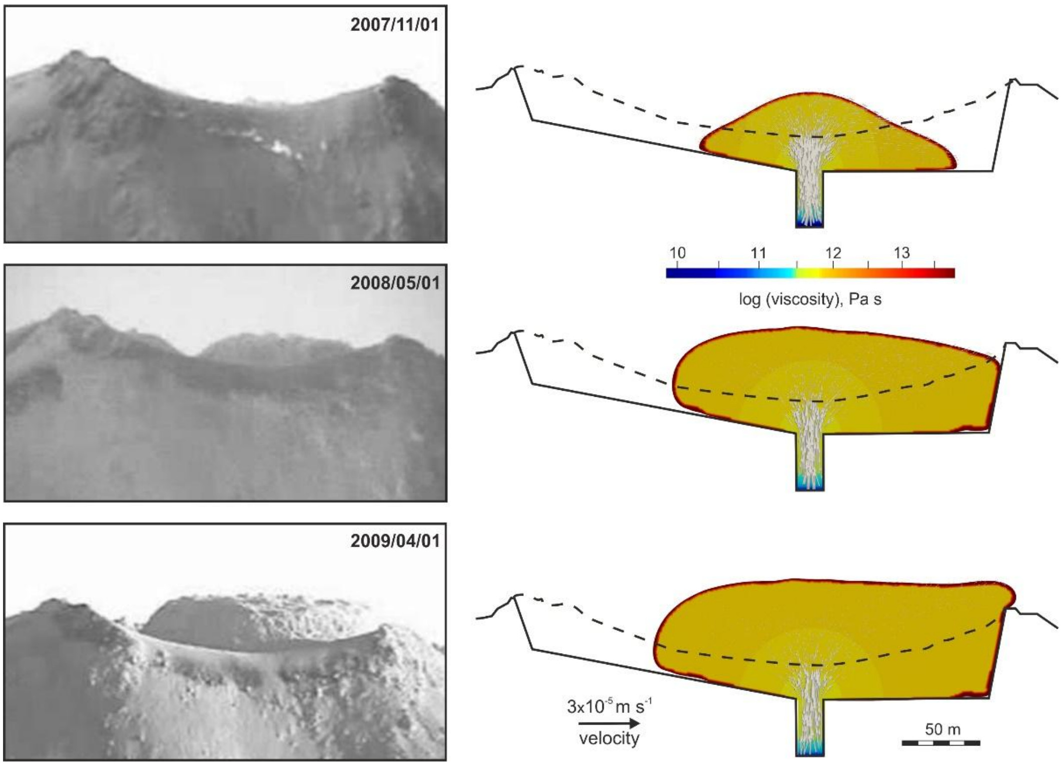

Figure 3.12: The lava dome morphology at Volcán de Colima (left panels; images from Bretón-González et al., 2013) and the modelled viscosity and velocity (arrows) in exp. 10 (right column) at times of 2007/11/01 (upper panels), 2008/05/01 (middle panels), and 2009/02009/04/01 (lower panels).

3.6 Discussion and conclusion

3.6.1 Model outcomes

We have presented a plausible numerical model for lava dome growth at Volcán de Colima during the long dome-building episode lasting from early 2007 to fall 2009 without explosive dome destruction. This numerical study has allowed for estimating the influence of the model geometry (the crater topography and the conduit's location), extrusion rates, and a high-viscous carapace on the morphology of the lava dome. Three geometries of the crater have been explored with the different locations of the vent, and it has been shown that the crater topography is likely to be inclined toward the west as shown in experiments 5 and 10.

The numerical results show that the extrusion rates calculated empirically from 2-D images of the morphological shapes of the lava dome at different times lead to a better fit between the observed and modeled shapes. The best fit provides the reduced extrusion rates as shown in exp. 10; the extrusion rates calculated using the erupted lava dome volumes yield to underestimation of the maximum height of the observed lava dome. As a lava advancement within the dome depends on the surface topography of the crater as well as the conduit geometry, two-dimensional (2-D) models cannot capture complexity of the three-dimensional (3-D) lava dome growth.

The developed model has shown that high viscosity of the dome is required to maintain a vertical growth. As the viscosity depends on the volume fraction of crystals in our model, and the latter depends on CCGT, the crystal content grows rapidly in the uppermost conduit at low discharge rates (Figure 3.2b), and lava becomes highly viscous. The modeled lava viscosity within the dome core varies from $10^{9.8}$ Pa s to 10^{12} Pa s and is consistent with the viscosity measurements of lavas from Volcán de Colima. Viscosity changes can influence growth rates of domes at Volcán de Colima (Yokoyama, 2009; Lavallée et al., 2012).

Using recorded dataset from Volcán de Colima we have shown that solidification and rheological stiffening within a lava dome are controlled in part by cooling and degassing-induced crystallization. While the crystallization due to degassing is a dominant process in dome-building eruptions (e.g., Melnik & Sparks, 1999), especially during short dome-building episodes (e.g., Tsepelev et al., 2020), the model forecasts indicate that a high-viscous carapace significantly influences the dome growth process during long lava dome-building episodes. A carapace of higher viscosity (about 10^{14} Pa s) prevents a rapid dome advancement to the east and promotes the development of a steep slope on the dome's eastern side.

Cooling influences the lava viscosity at the interface between the dome and its surrounding making the dome carapace more viscous and promoting a development of lobe-shaped lava dome (Tsepelev et al., 2020; Watts et al., 2002). In the cases of short episodes of lava dome growth, the thermal carapace of the lava dome is not thick enough to present significant resistance to lava dome horizontal advancement (e.g., Bourgouin et al., 2007; Tsepelev et al., 2020). The dome carapace becomes thicker in the case of radiative and convective heat transfer at the lava/air interface (Tsepelev et al., 2019) or in the cases of long dome-building episodes, as shown in this work. Further studies related to the influence of temperature on the viscosity of the carapace during long lava dome-building episodes can refine the current results.

3.6.2 Model limitations

The numerical model is unlikely to represent exact dynamics of lava dome growth due to the complexity of magmatic processes at depths and unknowns such as degassing, initial crystal volume content, and viscosity. Any model comes with its simplifications (e.g., less complex viscosity, and 2-D or axisymmetric instead of 3-D geometry) and assumptions (e.g., temperature-independent density and viscosity, and no density change due to crystallization). For example, difficulties related to 3-D data-driven numerical modeling (e.g., data assimilation, inversions, and computational cost) are also associated with data issues. Several techniques for volcano monitoring are available to collect and use data on lava dome growth, for example, video recording (Bretón-González et al., 2013), infrared camera imaging (Stevenson & Varley, 2008), terrestrial photogrammetry (James & Varley, 2012), and satellite radar observations (e.g.,Salzer et al., 2014; Walter et al., 2019). Meanwhile, it is still challenging to determine precise 3-D morphological changes during dome growth, especially when the data come from the records using a single video (photo) camera as 2-D images have a limited information related to a 3-D object. Other challenging issues are related to the determination of the detailed crater geometry prior a new dome starts to evolve, and the location and geometry of the uppermost conduit (e.g., Pinel et al., 2011).

The problem of a search for the best fit between the morphological shapes of observed and modeled lava domes tuning the parameters of the lava viscosity belongs to the class of inverse problems. The solution to the inverse problem can be non-unique; for example, different discharge rates and different CCGT can produce similar lava dome shapes (Starodubtseva et al., 2021). As for the discharge rate, it can be determined from observations, and, therefore, this rate can be considered as a known characteristic of the lava dome dynamics constraining the model. In our numerical modeling the optimization of the misfit between the modeled and observed morphologies has been based on tuning CCGT, extrusion rates, and the crystal-free magma viscosity at the times of available observations.

Matching the timing of lava dome growth at Volcán de Colima to its morphology is challenging, because the estimation of the volume of the erupted lava is restricted to analysis of camera images and hence uncertain; the existing 3-D temporal coverage of the extrusion process is not complete; the location of the vent is not precisely documented; and the determination of the extrusion rate in 2-D models is complicated. Therefore, with more observations 3-D numerical models of lava domes should provide additional information on lava dome growth and their eventual collapse.

3.6.3 Model applications

The developed model in this work and similar models can be used to analyze future effusive eruptions and lava dome growth at Volcán de Colima or elsewhere after proper calibration based on history matching of dome growth by nudging model forecasts to observations (i.e., minimizing misfits between the modeled and observed morphological shapes of domes). The model can be used to assess a stress localization in the dome carapace and its potential failure, which may lead to pyroclastic flow hazards.

In the future, every potentially hazardous volcanic eruption should be accompanied by its virtual numerical model that is constantly tuned by a history matching procedure and gives short- and long-term forecasts of the eruption dynamics and associated hazards. This will require increasing the accuracy of monitoring techniques and considerable investment in geophysical studies of volcanic systems.

AUTHOR CONTRIBUTIONS

AIZ, OM and VZ contributed to the conceptualization of the paper. VZ provided data on the dome growth and also an insight into the development of the dome at Volcán de Colima during 2007-2009. NZ processed the data, developed a numerical model, and performed all model experiments. AIZ supervised the study, and assisted NZ in numerical modeling and data processing. IT contributed to the numerical statement of the problem, data processing, and the development of numerical codes. All authors contributed to the interpretation of numerical results. AIZ and NZ performed writing – original draft preparation and figures. All co-authors performed writing – review and editing.

ACKNOWLEDGMENTS

This is a contribution to the research project funded by the Russian Science Foundation’s grant (project RSF 19-17-00027). NZ thanks also Deutsche Forschungsgemeinschaft (project DFG IS203/14-1) for support. We are grateful to Frank Schilling for providing helpful insight into physical properties of lavas. Also, we are thankful to Valerio Acocella, Shanaka de Silva, and two anonymous reviewers for careful reviews of the initial manuscript and constructive comments.

Chapter 4: Numerical thermo-mechanical modelling of lava dome growth

This chapter is originally published in the *Geophysical Journal International*.

Zeinalova N., Ismail-Zadeh A., Tsepelev I., Melnik O., Schilling, F. [2024]: Numerical thermo-mechanical modelling of lava dome growth during the 2007-2009 dome-building eruption at Volcán de Colima; *Geophysical Journal International (236)*, pp.: 290-304, doi: https://doi.org/10.1093/gji/ggad415

Abstract

Lava domes form during effusive eruptions due to an extrusion of highly viscous magmas from volcanic vents. In this paper we present a numerical study of the lava dome growth at Volcán de Colima, Mexico during 2007-2009. The mathematical model treats the lava dome extrusion dynamics as a thermo-mechanical problem. The equations of motion, continuity, and heat transfer are solved with the relevant boundary and initial conditions in the assumption that magma viscosity depends on the volume fraction of crystals and temperature. We perform several sets of numerical experiments to analyse the internal structure of the lava dome (i.e., the distributions of the temperature, crystal content, viscosity, and velocity) depending on various heat sources and thermal boundary conditions. Although the lava dome growth at Volcán de Colima during short (a few months) dome-building episodes can be explained by an isothermal model of lava extrusion with the viscosity depending on the volume fraction of crystals, we show here that cooling plays a significant role during long (up to several years) episodes of dome building. A carapace develops as a response to a convective cooling at the lava dome-air interface. The carapace becomes thicker if the radiative heat loss at the interface is also considered. The thick carapace influences the lava dome dynamics preventing its lateral advancement. The release of the latent heat of crystallization leads to an increase of the temperatures in the lava dome interior and to a relative flattening of the dome. Meanwhile, the heat source due to viscous dissipation inside the lava dome is negligible, and it does not influence the lava dome growth. The developed thermo-mechanical model of the lava dome dynamics at Volcán de Colima can be used elsewhere to analyze effusive eruptions, dome

morphology, and carapace evolution including its failure potentially leading to pyroclastic flow hazards.

***Keywords**:* numerical modelling, lava rheology and morphology, heat transfer, crystallization, Volcán de Colima

4.1 Introduction

An effusive eruption of highly viscous magma leads to a lava dome growth in the volcanic crater interrupted by its collapse due to gas pressure building-up or gravitational instability. The collapse events may completely or in part remove the dome and result in pyroclastic density currents – high-speed avalanches of rocks and ashes. The thermo-mechanical structure of a lava dome interior (that is, the temperature, the crystal content, and the lava viscosity) is poorly known. However, this knowledge is critical for assessment of potential dome collapse and related hazards (e.g., Voight & Elsworth, 2000; Watts et al., 2002).

Lava dome dynamics is governed by crystallization and outgassing of the viscous magma in the volcanic conduit (Melnik & Sparks, 1999). The domes represent extrusions of a high viscous magma from a volcanic vent, which are affected by degassing, crystallization, and cooling. Lava dome morphology varies with the discharge rate, the kinetics of the crystal content growth, the temperature, and the vent geometry (e.g., Tsepelev et al., 2020; Mériaux et al., 2022). A highly viscous dome-forming magma prevents significant lateral advancement of the extruded lava from the vent compared to a less viscous lava, which flows along the volcano’s topographic slope. At low eruption rates, lava dome dynamics is associated with high groundmass crystallinity and substantial yield strength (e.g., Lavallée et al., 2012; Calder et al., 2015; Sheldrake et al., 2016). Due to cooling, domes develop a ‘solid’ carapace (a highly viscous surface layer of the dome). This carapace remains deformable for days to months (Anderson & Fink, 1990) influencing the dome morphology (Iverson, 1990) because of the mobility of less viscous lava within the interior of the dome.

Lava dome growth has been monitored at several volcanoes (e.g., Nakada, 1999; Watts et al., 2002; Harris et al., 2003; Wadge et al., 2014; Zobin et al., 2015; Nakada et al., 2019). Monitoring allows mapping the spatial and temporal development of lava domes and determining the morphological changes during the growth as well as the changes in the lava volume over time. Since 1998 seismic and other types of geophysical and geodetic monitoring at Volcán de Colima, Mexico, revealed several lava dome-building episodes of different duration from days to several years (Zobin & Tellez, 2019). According to Zobin et al. (2017), one of the longest dome-building episodes at the volcano occurred from early 2007 until late 2009. Camera images (Figure 4.1) outline the morphology of the growing lava dome at Volcán de Colima for several years (Bretón-González et al., 2013). The observed morphological shapes of the lava dome help to constrain the results of numerical modelling by fitting the modelled dome shapes to the observed shapes.

Analogue and numerical models play an essential role in understanding lava extrusion dynamics (e.g., Fink & Griffiths, 1998; Cordonnier et al., 2015). Numerical models of lava dome growth help to analyse the influence of the rheological properties of magma including degassing-induced crystallization, and heat transfer on the dome morphology (e.g.,Hale & Wadge, 2003; Husain et al., 2014; Harnett et al., 2018; Starodubtseva et al., 2021; Tsepelev et al., 2019, 2020; Zeinalova et al., 2021). Numerical models of a rapid dome-building process at Volcán de Colima in 2013 have been developed by Walter et al. (2019) and Tsepelev et al. (2021b). Zeinalova et al. (2021) developed a numerical model of a slow lava dome-building process at Volcán de Colima to analyse the influence of the magma viscosity and discharge rates on the dome growth during 2007-2009. Their viscosity model incorporated the crystal-dependent viscosity and the constant crystal-free melt viscosity, while the model did not depend on temperature. By introducing an artificial thin carapace of a high viscosity at the interface between the lava dome and the air, Zeinalova et al. (2021) showed that this carapace helps to constrain a lateral advancement of the lava dome and keeps the model results in a good agreement with the observation. The model by Zeinalova et al. (2021) does not consider thermal effects on the lava dome growth and hence does not allow a carapace to be formed and evolved due to cooling.

Here, we present a numerical study of the thermo-mechanical evolution of the lava dome at Volcán de Colima during 2007-2009 to understand the lava dome extrusion dynamics and the dome growth using a more sophisticated model. The research questions we try to answer in this study include: How does temperature influence the lava dynamics and the evolution of the dome carapace? How do the latent heat of crystallization and the viscous dissipation impact the lava dome dynamics? How do the thermal boundary conditions and the heat transfer at the lava-air interface influence the dome dynamics and its morphology? Below we introduce a thermo-mechanical model of lava dome extrusion dynamics and the dome growth (in section 4.2), present the results of numerical experiments with varying physical characteristics of the lava dome (in section 4.3), and discuss the results (in section 4.4).

4.2 Model description

4.2.1 Geometry and governing equations

We model a lava dome growth in a two-dimensional (2-D) domain $\Omega = \Omega_1 \cup \Omega_2 \subset \mathbb{R}^2$. The geometry of the domain (Figure 4.2) is asymmetric with respect to the model conduit. We choose one of the model geometries used by Zeinalova et al. (2021), allowing the horizontal spreading of the modelled lava dome to be in a good agreement with the lava dome spreading at Volcán de Colima across the E-W profile. The lava dome base is assumed to be located 20 m below the central part of the visible crater's rim (Bretón-González et al., 2013), the width of the crater is 257 m, and the width and the depth of the conduit are 14.5 m and 30 m, respectively (Zobin et al., 2015). The model 'conduit' is assumed to be a near-surface vertical channel filled with old, solidified rocks; fresh magma (with the prescribed temperature, crystal content, and discharge rate) enters through the bottom of the channel, moves up, and extrudes to the surface. In contrast to the work of Husain et al. (2018), we separate the model of magma extrusion and lava dome growth from the model of magma flow in a volcanic conduit and concentrate in this study on the physical processes within the growing lava dome.

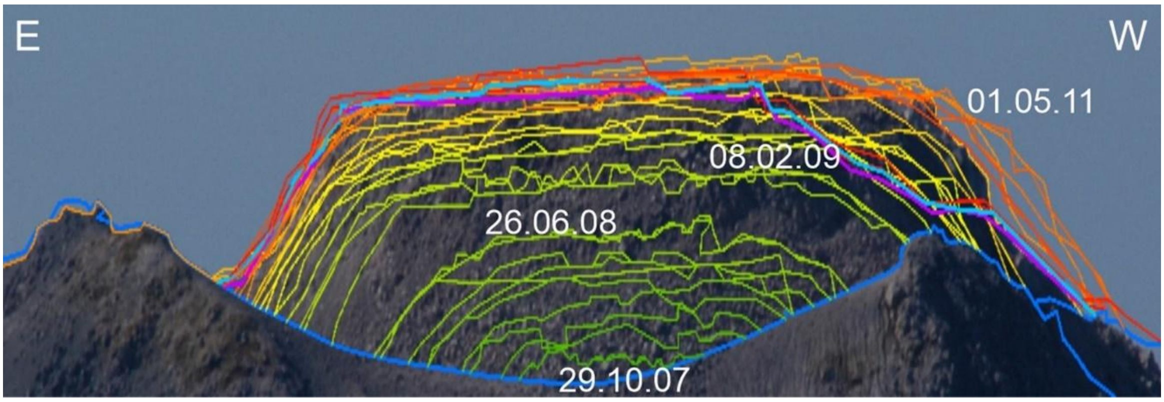

Figure 4.1: The lava dome at andesitic stratovolcano Volcán de Colima (based on Bretón-González et al., 2013). The coloured outlines of the growing lava dome along the E-W profile over the rim of the volcano crater (the blue curve) present the morphological shapes of the dome for 29 October 2007 to 5

May 2009 (greenish colours), 1 June 2009 to 1 January 2010 (yellowish colours), and 22 March 2010 to 1 May 2011 (brownish colours). The cyan and purple outlines present the morphology of the lava dome on 14 July 2011 and 21 April 2012. The dome outlines are interpreted from a sequence of camera images overlaid on one particular frame.

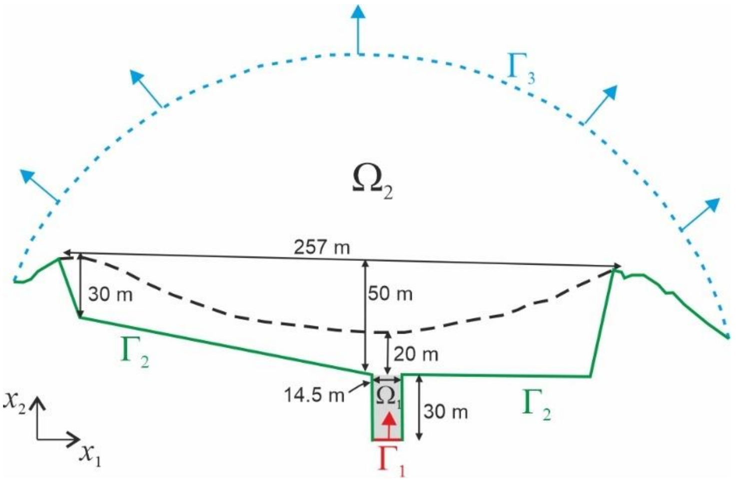

Figure 4.2: Sketch of the model domain. The model conduit (sub-domain Ω_1) is filled by an older magma (grey-shaded), and the red arrow indicates the direction of the rise of new magma through Γ_1 (the red line) within the conduit. The green bold line Γ_2 marks the lava dome base, and the black dashed curve presents the visible crater's rim. The blue dashed curve (Γ_3) illustrates the upper boundary of the domain, through which the air escapes from the model, and blue arrows show the direction of the escape.

In model domain Ω, we consider a two-dimensional incompressible, two-phase, immiscible viscous fluid flow approximating an extrusion of the lava (one fluid phase) into the air (another fluid phase) on the surface of the crater. The interface between the lava and the air presents a stress-free surface. The influence of the air phase on the lava dome growth is insignificant due to a large ratio between densities/viscosities of the air and the lava. The lava dynamics is described by the Navier-Stokes equations with the initial condition $\mathbf{u}(t = 0, \mathbf{x}) = 0$

$$\frac{\partial(\rho\mathbf{u})}{\partial t}+\langle\mathbf{u},\nabla\rangle(\rho\mathbf{u})-\nabla\cdot\left(\eta\left(\nabla\mathbf{u}+\nabla\mathbf{u}^T\right)\right)=-\nabla p-\rho\mathbf{g}, \tag{4.1}$$

the continuity equation

$$\nabla\cdot\mathbf{u}=0, \tag{4.2}$$

and the heat equation with the initial condition for the temperature $T(t=0,\mathbf{x})=T_{cr}$ for $\mathbf{x}\in\Omega_1$ and $T(t=0,\mathbf{x})=T_A$ for $\mathbf{x}\in\Omega_2$

$$\frac{\partial\left(c\rho T\right)}{\partial t}+\nabla\cdot\left(\mathbf{u}\left(c\rho T\right)\right)=\nabla\cdot\left(k\nabla T\right)+LH-HF+VD. \tag{4.3}$$

Here, t is the time; $\mathbf{x}=(x_1,x_2)$ is the position vector in 2-D Cartesian coordinates; $\mathbf{u}=(u_1,u_2)$ is the velocity; p is the pressure; $\mathbf{g}=(0,\ g)$, g is the acceleration due to gravity; T is the temperature. The term $LH=L^*\rho_L\dfrac{\mathrm{d}\phi}{\mathrm{d}t}$ describes the latent heat release in magma/lava due to crystallization (Kirkpatrick, 1976; Costa, Melnik, & Sparks, 2007), where L^* ($=3.5\times10^5$ J kg^{-1}; (Costa, Melnik, & Sparks, 2007)) is the latent heat of crystallization; ϕ is the volume fraction of crystals; and $\dfrac{\mathrm{d}\phi}{\mathrm{d}t}\equiv\dfrac{\partial\phi}{\partial t}+\nabla\cdot(\phi\mathbf{u})$. The term HF accounts for either the convective heat transfer at the interface of the lava and the air $HF_l=\left[\lambda(T-T_A)\right]\delta_s$ or the radiative and nonlinear convective heat transfer at the interface $HF_n=\left[\varepsilon\sigma(T^4-T_A^4)+\lambda_n(T-T_A)^{4/3}\right]\delta_s$ (Neri, 1998; Tsepelev et al., 2019), where λ is the convective heat transfer coefficient, ε (=0.9; Ramsey et al., 2019) is the effective emissivity of the lava dome solid surface; σ is the Stefan–Boltzmann constant; λ_n is the nonlinear convective heat transfer coefficient measured in [W m^{-2} K$^{-4/3}$] (Neri, 1998); T_A is the air temperature; δ_s is the special function determined at interface S between the lava and the air measured in [m^{-1}]. The term $VD=\eta\left(\nabla\mathbf{u}+\nabla\mathbf{u}^T\right):\nabla\mathbf{u}$ describes the viscous dissipation. Symbols ∇ is the gradient operator, $\nabla\cdot$ is the divergence operator, ^{T} is the transposed matrix, : is the double-dot product (the trace of the inner product) of two matrices, and $\langle\cdot,\cdot\rangle$ is the scalar product of vectors, respectively. The model density ρ, viscosity η, thermal conductivity k, and specific heat capacity c are represented as

$$\rho(t,\mathbf{x})=\rho_L\alpha(t,\mathbf{x})+\rho_A(1-\alpha(t,\mathbf{x})),\qquad \eta(t,\mathbf{x})=\eta_L\alpha(t,\mathbf{x})+\eta_A(1-\alpha(t,\mathbf{x})), \tag{4.4}$$

$$k(t,\mathbf{x})=k_L\alpha(t,\mathbf{x})+k_A(1-\alpha(t,\mathbf{x})),\qquad c(t,\mathbf{x})=c_L\alpha(t,\mathbf{x})+c_A(1-\alpha(t,\mathbf{x})), \tag{4.5}$$

where ρ_A, η_A, k_A, and c_A are the air density, viscosity, thermal conductivity, and specific heat capacity, respectively (we consider these parameters to be constant); and ρ_L, η_L, k_L, and c_L are the lava density, viscosity, thermal conductivity, and specific heat capacity, respectively (these parameters are not constant and may depend on the temperature, volume fraction of crystals, and other physical variables; to be specified below). The function $\alpha(t,\mathbf{x})$ equals 1 for the lava and 0 for the air at each point **x** and at time *t*, and this function is transported with the velocity **u** according to the advection equation with the initial condition $\alpha(t=0,\mathbf{x})=1$ for $\mathbf{x}\in\Omega_1$ and $\alpha(t=0,\mathbf{x})=0$ for $\mathbf{x}\in\Omega_2$

$$\frac{\partial\alpha}{\partial t}+\nabla\cdot(\alpha\mathbf{u})=0\,. \tag{4.6}$$

4.2.2 Lava rheology

The lava viscosity η_L measured in [Pa s] is defined here as a multiplication of the melt viscosity η_{mt} and the relative viscosity, depending on the volume fraction of crystals η_{cr}:

$$\eta_L(T,\phi)=\eta_{mt}(T)\eta_{cr}(\phi)\,. \tag{4.7}$$

The melt viscosity $\eta_{mt}(T)$ (measured in [Pa s]) experimentally determined for lavas at Volcán de Colima is presented by the Vogel–Fulcher–Tammann equation:

$$\log_{10}\eta_{mt}(T_C)=A_{VFT}+\frac{B_{VFT}}{T_C-T_g}\,, \tag{4.8}$$

where the melt viscosity was fitted for the temperatures from $1000^\circ\mathrm{C}$ down to the glass transition temperature $(T_g=710^\circ\mathrm{C})$ for a strain rate of one, A_{VFT} = 0.29, B_{VFT} = 606.9°C, T_C is the temperature in °C (Lavallée et al., 2012). We adopt the model proposed by Costa et al. (2009) to define the dimensionless viscosity depending on the volume fraction of crystals as

$$\eta_{cr}(\phi)=\left(1+\varphi^{\delta}\right)\left[1-(1-\xi)\mathrm{erf}\left(\frac{\sqrt{\pi}}{2(1-\xi)}\varphi(1+\varphi^{\gamma})\right)\right]^{-B\phi_*}\,, \tag{4.9}$$

where $\varphi=\phi/\phi_*$; ϕ_* is the specific volume fraction of crystals representing the critical solid fraction at the onset of the exponential increase of $\eta_{cr}(\phi)$ (Costa et al., 2009); *B* is the theoretical value of the Einstein coefficient; δ, ξ, and γ are the rheological parameters (Lejeune & Richet, 1995; Costa et al., 2009;). Although the crystal-dependent viscosity is influenced by the shape, size, and orientation of crystals (Cimarelli et al., 2011; Frontoni et al., 2022), we do not use the dependence because of the lack of information on the crystal characteristics for the lavas from Volcán de Colima erupted from 2007-2009. As the crystal-bearing melt viscosity for lava samples from Volcán de Colima was estimated to be $10^{11.28}$ Pa s (Lavallée et al., 2007), we limit the lava viscosity η_L to a value of 10^{12} Pa s in all numerical experiments except two, where the effect of the higher viscosity (up to 10^{14} Pa s) of the lava dome carapace is analysed.

In the modelling, the volume fraction of crystals is determined from the evolutionary equation describing the simplified crystal content growth kinetics of degassing-induced crystallization (e.g., La Spina et al., 2016; Tsepelev et al., 2020)

$$\frac{\mathrm{d}\phi}{\mathrm{d}t} = -\frac{\phi - \phi_{eq}}{\tau}, \tag{4.10}$$

with the initial condition $\phi(t=0,\mathbf{x}) = \phi_{ct}$ for $\mathbf{x} \in \Omega_1$ and $\phi(t=0,\mathbf{x}) = 0$ for $\mathbf{x} \in \Omega_2$. Here, ϕ_{eq} is the volume fraction of crystals at the equilibrium state depending on the concentration of water dissolved in magma and temperature (Riker et al., 2015; Cashman, 2020); and τ is the relaxation time (the characteristic time of the crystal content growth needed by crystals to reach ϕ_{eq}), which is required to reduce the difference between the actual (ϕ) and equilibrium (ϕ_{eq}) values of the volume fractions of crystals by a factor of *e* with respect to the initial difference ($\phi_{in} - \phi_{eq}$), where ϕ_{in} is the initial volume fraction of crystals in the magma. In the modelling, we assume ϕ_{eq} to be either a constant or temperature-dependent variable. The constant $\phi_{eq} = 0.83$ describes a hyper-concentrated regime of a magma/lava flow with the strong interaction of crystals and the considerable increase of the viscosity (e.g., Costa, 2005; Frontoni et al., 2022). The temperature-dependent ϕ_{eq} was determined from laboratory measurements of Volcán de Colima lava samples at various temperatures (Moore & Carmichael, 1998) by fitting parameters a_1, b_1, and c_1 to get the following relationship:

$$\phi_{eq}(T) = 1/\left(1 + exp\left[a_1 + b_1 T_C / T_{sp} + c_1 (T_C / T_{sp})^2\right]\right), \tag{4.11}$$

where $T_{sp} = 1000°\mathrm{C}$, $a_1 = -42.4$, $b_1 = 51.04$, and $c_1 = -11.11$.

4.2.3 Initial and boundary conditions

At the initial time, the model conduit (subdomain Ω_1) is filled by a lava with the volume fraction of crystals ϕ_{ct} at temperature T_{ct}, and the subdomain Ω_2 by air at temperature T_A The following conditions are imposed on the model boundary $\Gamma = \Gamma_1 \cup \Gamma_2 \cup \Gamma_3$ (Figure 4.2), where Γ_1 is the part of the boundary from where new magma enters into the model via conduit; Γ_2 is the part of the boundary related to the crater surface and its nearby surrounding; and Γ_3 is the upper boundary of the model domain, through which the air escapes from the model. A new magma (of the density ρ_L, the viscosity η_L, the volume fraction of crystals $\phi = \phi_{in}$, and the temperature T_{in}) enters into the model domain at the specified extrusion rate $\mathbf{u}_{ext} = (0, u_{ext})$ through Γ_1 (red line). The initial volume fraction of crystals ϕ_{in} is taken to be 0.4 as the critical crystal fraction separating the diluted (non-interacting suspended particles) and particle-concentrated regimes of magma/lava flow (Lejeune & Richet, 1995; Frontoni et al., 2022). Although ϕ_{in} is constant in the model, we test a sensitivity of the model results with respect to a higher value of the initial volume fraction of crystals.

The lava extrusion rate (m s^{-1}) is derived from the discharge rate (m^3 s^{-1}) constraining it by optimization of the fit between the two-dimensional morphological shape of the observed dome (Bretón-González et al., 2013) and that of the modelled domes (Zeinalova et al., 2021). To match the observed and modeled heights of the lava dome, the following extrusion rates $\mathbf{u}_{ext}$ have been chosen following Zeinalova et al. (2021): 5×10^{-6} m s^{-1} for the first 300 days, 7.5×10^{-6} m s^{-1} from day 301 to day 455, 2×10^{-5} m s^{-1} from day 456 to day 480, and 1.7×10^{-5} until day 822.

The conditions imposed on the model boundary Γ_1 are simplified; namely, constant (time-independent) values of density, viscosity, the volume fraction of crystals, temperature, and the extrusion rate can be considered as approximations to the dynamic conditions in a volcanic conduit. A proper coupling between the conduit and the lava dome (using dynamic conditions on the boundary) may result in a cyclic behaviour of lava dome growth (e.g., Costa et al., 2012).

No-slip condition $\mathbf{u} = 0$ is prescribed at Γ_2. To satisfy the incompressibility condition (Eq. 4.2) due to lava extrusion and hence to preserve the volume of the model domain, the air should be removed from the domain at the lava discharge rate. Hence, the outflow condition is determined at Γ_3 (the blue curve) as $\mathbf{u}_{out} = u_{out}\mathbf{n}$, $\phi = 0$, and $\alpha = 0$, where $u_{out} = -|\Gamma_3|^{-1} \int\limits_{\Gamma_1} \langle \mathbf{u}_{ext}, \mathbf{n} \rangle d\Gamma$, and $\mathbf{n}$ is the outward unit normal vector at a point on the model boundary.

4.2.4 Solution method

To solve numerically the problem described above, we employ the Ansys Fluent software (Ansys Fluent 2021R2; https://www.ansys.com/products/fluids/ansys-fluent), where the finite volume method (e.g., Ismail-Zadeh & Tackley, 2010) is used to solve the models of lava dome dynamics on multiprocessor computers by numerical simulations of multi-phase viscous fluid flow and heat transfer. The software uses the volume of fluid (VOF) method (Hirt & Nichols, 1981), which allows for computationally inexpensive treatment of a moving interface between two fluid phases, e.g., the lava and the air. The model domain is discretized by about 60,000 cells (finite volumes), and the linear size of the cells is about 0.8 m. A finer spatial discretization of the model domain slightly refines the numerical results but significantly increases the time of computations. The cells containing the interface between the lava and the air have α values between zero and unity depending on the lava proportion in the cells. The term *HF* in Eq. (4.3) containing the special function (the Dirac delta function) is calculated in a thin layer of the cells adjacent to the interface between the lava and the air, and the special function is approximated by the ratio of the length of a relevant cell to the cell's area.

Following Zeinalova et al. (2021), the second-order upwind schemes are employed to approximate the Laplacians, and the monotonic schemes are used to discretize convective terms in the equations. The p-$\mathbf{u}$ coupling is handled by the SIMPLE method (S. V. Patankar & Spalding, 1972), where the relaxation parameters are chosen to be 0.01 and 0.3 for P and $\mathbf{u}$, respectively. We assign 0.5 to the relaxation parameters for α, T, and ϕ. A time step is chosen in the range of 1 to 40 s depending on the stability and optimization of the numerical solution to assure a convergence of a set of linear algebraic equations (SLAE), which is obtained after the discretization of the governing equations. In the modelling, we employ the conjugate-gradient method to solve SLAE.

A second-order implicit time integration scheme is employed to solve the numerical problem. To test the stability of the numerical solution of the problem, several tests have been performed at different relaxation parameters and time steps. We note that the implicit scheme is unconditionally stable with respect to the size of time steps. An employment of explicit schemes in the model led to unstable numerical results even for the small Courant number (Courant et al., 1928). The high viscosity ratio between the lava and the air presents some computational challenges at their interface. Although the implicit time integration scheme used in this modelling allows for any time step size, the large time steps lead to a high numerical diffusion at the lava–air interface and to the physically implausible results; therefore, the time step was chosen sufficiently small. Also, because of the viscosity discontinuity at the lava-air interface the choice of the relaxation parameters in the SIMPLE method is critical, and sometimes the parameters were lowered to ensure the solution's stability. The numerical accuracy attains 10^{-3} for the solution of the SLAE to find p and $\mathbf{u}$, and 10^{-6} for the solution of SLAE to find α , T, and ϕ .

Numerical experiments were carried out on the multiprocessor computer (bwHPC) of the Karlsruhe Institute of Technology. The time of computations of the numerical models depends on several factors including the complexity of the mathematical problem, the number of computational cells, the number of cores, and the time-step size. For example, one day of the lava dome growth in the model (Eqs. 4.1-4.10 with the initial and boundary conditions described in sect. 4.2.3) is computed by eight cores for about six minutes, using the model time step 40 s. Figures 4.3-4.5, 4.7-4.8, 4.10-4.11 were made with ParaView visualisation software (version 5.9.0-RC3 64-bit, https://www.paraview.org).

4.3 Numerical results

Here, we present the results of numerical experiments analysing the influence of the following thermal conditions on the dome growth and its morphology: (i) the heat transfer at the interface between the lava and the air, (ii) the latent heat release during crystallization, (iii) the viscous dissipation, (iv) the temperature-dependence of the volume fraction of crystal at the equilibrium state, and (v) the heat transfer at the interface between the lava and the conduit wall / the crater. Finally, we use the model to study the lava dome growth during the 2007-2009 dome-building eruption at Volcán de Colima. The principal purpose of this analysis is to understand how the thermal conditions (i)-(v) influence the dome evolution individually and in combination, and which of the conditions influence the model results most significantly. Equations (4.1) - (4.11) have been employed to solve the models of lava dome growth. The numerical experiments are described in Table 4.1, and the model parameters used in the experiments are listed in Table 4.2. The first and second sets of numerical experiments concern the influence of the convective (described in sect. 4.3.1) and convective-radiative (in sect. 4.3.2) heat flux at the lava-air interface on the morphology of modelled lava domes, when the latent heat release during crystallization, the viscous dissipation, and the temperature-dependent volume fraction of crystals are accounted. The third set of experiments (in sect. 4.3.3) consider the effects of various thermal conditions at the conduit wall and the crater surface, and the fourth set of two experiments (in sect. 4.3.4) deal with the evolution of the lava dome at Volcán de Colima for several years.

4.3.1 Convective heat transfer at the lava-air interface

In the case of the convective heat transfer at the interface between the lava and the air ($HF=HF_l$ in Eq. 4.3), we study the lava dome growth with no latent heat (LH=0) and no viscous dissipation (VD=0) terms in the heat equation (Eq. 4.3) (experiment 1.1), with the added VD term (exp. 1.2), the added LH term and constant ϕ_{eq} (exp. 1.3), and the added LH term and the temperature-dependent ϕ_{eq} as defined in Eq. 4.11 (exp. 1.4). The results of the numerical experiments, namely, the temperature, crystal content, viscosity, and flow velocity at day 300 are presented in Figure 4.3.

The dome in these experiments builds upward and advances horizontally with a higher velocity toward the right due to the crater's geometry chosen in the model. The magma at temperature 1250 K enters the model conduit and extrudes on the surface forming a lava dome. This temperature is in a good agreement with the temperatures of dome-building eruptions at Volcán de Colima (Lavallée et al., 2008). The convective heat transfer at the interface between the lava and the air results in a temperature decrease and in the development of a cold surface layer of the lava dome (carapace). In the dome interior, the lava remains hot enough and less viscous, and hence behaves as a ductile and mobile material throughout the entire period of the dome growth. This occurs because the thin dome carapace is unable to restrain the less viscous lava in the dome interior.

As the characteristic time of the crystal content growth τ is chosen to be 5 days, crystals reach their equilibrium state rapidly already within the conduit, and the volume fraction of crystals stays constant (=0.83) in the lava dome after that (see Figure 4.3, exps. 4.1.1–4.1.3). The smaller the relaxation time, the faster the crystallization process converges to its equilibrium state, the lava viscosity increases, and the more viscous lava builds dome rather vertically than horizontally (e.g., Tsepelev et al., 2020; Zeinalova et al., 2021). The crystal-dependent viscosity reaches the value $\eta_{cr}(\phi = 0.83) \sim 10^6$, and hence, the dynamics of the lava dome depends on the temperature and the melt viscosity.

The dynamics of magma flows in a conduit is also controlled by thermal effects due to heat generation by the viscous dissipation (Costa, Melnik, & Vedeneeva, 2007). In exp. 1.2, we have investigated the influence of the viscous dissipation on the lava dome development. We found that the effect of the heat generation due to the viscous dissipation is negligible: the temperature change is within a degree compared to the case of exp. 1.1 (see *B: Appendix*). This leads to almost invisible change in lava viscosity and the morphological shape of the dome (see Figure 4.3, exp. 1.2).

The latent heat of crystallization is a part of the entire heat budget of the thermal history of lava domes. The latent heat released during the crystallization influences the conduit and lava dome temperature and contributes to variations in the lava viscosity (Costa, Melnik, & Sparks, 2007; Hale, Wadge, et al., 2007; Morse, 2011). In exp. 1.3, we have analysed the influence of the latent heat on the lava dome temperature and its viscosity. Due to a convective heat loss at the lava-air interface, the high-viscous carapace develops. The temperature increases in the dome interior from 1250K to 1367 K due to the latent heat release (Figure 4.3, exp. 1.3; the area of the elevated temperature is marked by a white curve) compared to the case with no latent heat (Figure 4.3, exp. 1.1). The higher temperature within the dome interior promotes dome flattening and its lateral advancement to the right compared to that without the latent heat transfer.

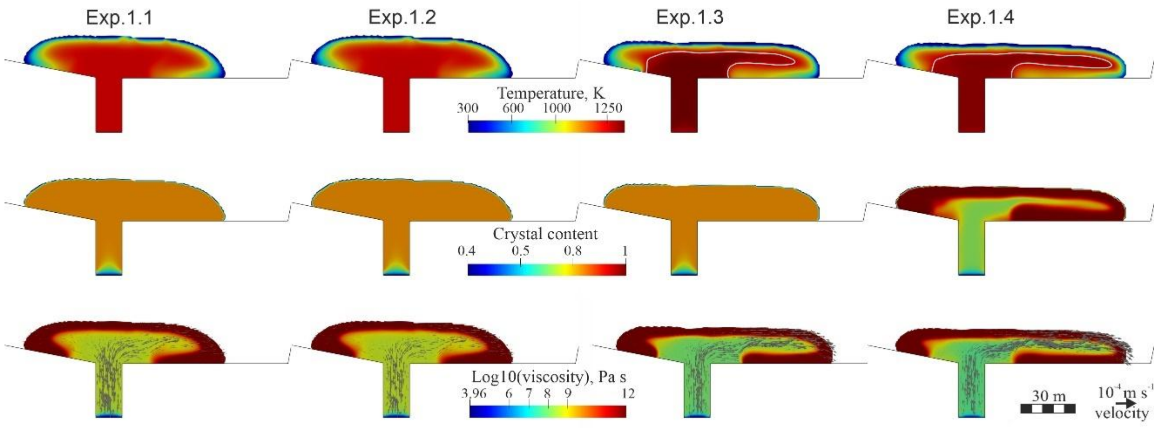

Figure 4.3: Modelled lava dome growth presenting the temperature, crystal content, and viscosity together with the velocity vectors for the convective heat transfer at the lava-air interface at time t = 300 days.

When the volume fraction of crystals depends on temperature (exp. 1.4), the release of the latent heat postpones the crystallization, this lowers slightly the lava viscosity, and it results in a further flattening of the lava dome and its horizontal advancement (Figure 4.3, exp. 1.4). In experiment 1.4, all parameters are the same as in exp. 1.3 except $\phi_{eq}(T)$, which is now a temperature-dependent variable. The equilibrium value $\phi_{eq}(T)$ decreases to about 0.7 due to the increased temperature as a result of the latent heat release (Figure 4.4). The maximum temperature of the modelled lava dome drops to the value of 1329K compared to the maximum temperature of 1367K in the case of exp. 1.3; this is associated with the reduction in $\phi_{eq}(T)$ and the subsequent decrease of the latent heat release. The crystal content becomes lower, while the lava viscosity in the dome interior slightly decreases to about $10^{7.5}$ Pa s in the right overhang of the lava dome. This leads to a minor increase in the flow velocity and the lava dome advances to the right more than in the case of exp. 1.3. The height of the dome decreases accordingly. Despite the viscosity of the carapace is higher compared to that of the dome interior, it cannot restrict the horizontal flow. We note that although the temperature-dependence of the crystal content (Eq. 4.11) might be plausible for the use in lava dome modelling, it raises uncertainties about being a well-parameterized representation for high-silica magmas at temperatures lower than 1250K (e.g., Moore & Carmichael, 1998).

The difference between the shapes of the modelled domes in exps. 1.1-1.2 and in exps.1.3-1.4 is associated with the distribution of the lava viscosity in the dome interior. A higher viscosity of the lava dome interior (exp. 1.1-1.2) is required to maintain a vertical growth. The lava dome (exp. 1.3-1.4) tends to flatten due to its lower viscosity in the dome interior (ranging from about $10^{8.7\text{-}9.3}$ Pa s to 10^{10} Pa s) compared to the viscosity of the dome interior in the case of exp. 1.1 or exp. 1.2 (ranging from about $10^{10.3}$ Pa s to about $10^{11.8}$ Pa s).

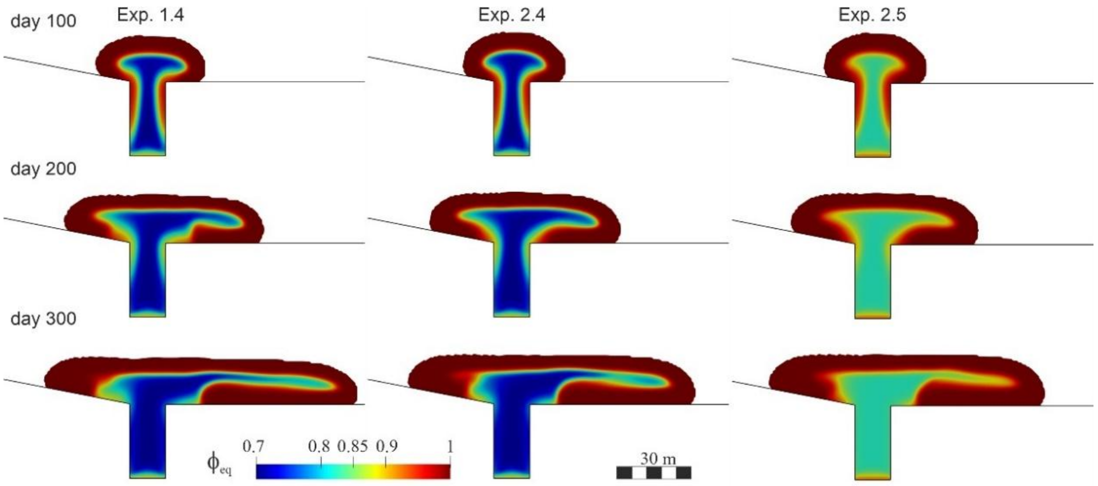

Figure 4.4: The evolution of the temperature-dependent volume fraction of crystals at the equilibrium state at times of 100, 200, and 300 d.

4.3.2 Nonlinear convective and radiative heat transfer at the lava-air interface

We present here the results of numerical experiments on the lava dome growth accounting for nonlinear convective and radiative heat transfer ($HF=HF_n$ in Eq. 4.3) at the interface between the lava and the air. As in the previous case (sect. 4.3.1), we study models of the lava dome growth with no latent heat and no viscous dissipation accounted (experiment 2.1), with the viscous dissipation term (exp. 2.2), and the latent heat term (exp. 2.3). Also, we analyse the influence of the temperature-dependent ϕ_{eq} (exp. 2.4) and the initial volume fraction of crystals ϕ_{in} (exp. 2.5) on the lava dome morphology.

A thick carapace forms at the lava-air interface due to the nonlinear convective-radiative heat flux. The thicker carapace (compared to the carapace in the case of the convective heat transfer only; sect. 4.3.1) retards the horizontal advancement of the lava dome (Figure 4.5) and promotes the growth of the dome upwards. The temperature and viscosity structures of the lava dome interior in exps. 2.1-2.4 are similar to those in exps. 1.1-1.4.

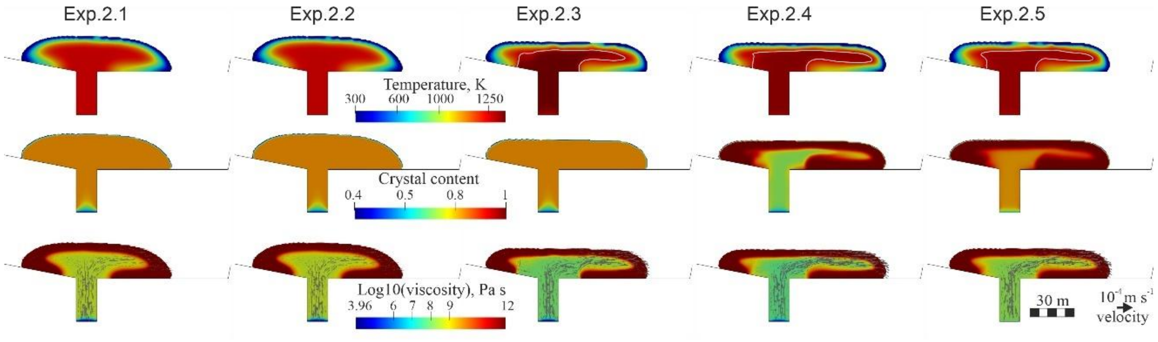

Figure 4.5: Modelled lava dome growth presenting the temperature, crystal content, and viscosity together with the velocity vectors for the convective radiative heat transfer at the lava-air interface at time t = 300 days.

To analyse the influence of the initial volume fraction of crystals ϕ_{in} on morphology of lava dome, ϕ_{in} has been increased (from 0.4 to 0.6) in exp. 2.5. Since the initial volume fraction of crystals in exp. 2.5 is higher compared to exp. 2.4, the temperature decreases for about 20K due to a smaller latent heat release. The lower temperature results in a higher value for $\phi_{eq} \approx 0.83$ (Figure 4.4, exp. 2.5) in contrast to exp. 2.4, where $\phi_{eq} \approx 0.73$ (Figure 4.4, exp.2.4). This leads to a slight increase of the viscosity $\sim 10^8$ compared to $\sim 10^{7.5}$ in exp. 2.4, and to a retardation in the lava advancement to the right (Figure 4.5). While there are some insignificant differences in shapes of the lava dome, the internal structure of the lava dome remains relatively consistent in both experiments. Therefore, the change of the initial volume fraction of crystals by at least 0.2 does not affect significantly the dome dynamics and its morphology.

To analyse the surface heat flux in the model, we have computed the linear HF_l and nonlinear HF_n heat flow density. The modelled surface heat flow density is presented in Figure 4.6 in the cases of the convective heat transfer (exp. 1.1) and the nonlinear convective and radiative heat transfer (exp. 2.1). The modelled surface heat fluxes decrease with time. The heat flux, inferred from infrared images obtained by airborne thermal remote sensing during the lava dome building at Volcán de Colima 2007-2010 (Hutchison et al., 2013), decreases with time as well. The maximum modelled surface temperature on the onset of the lava dome growth is 555 K, and the inferred temperature from the remote sensing measurements is 550-620 K for the first few days (Hutchison et al., 2013).

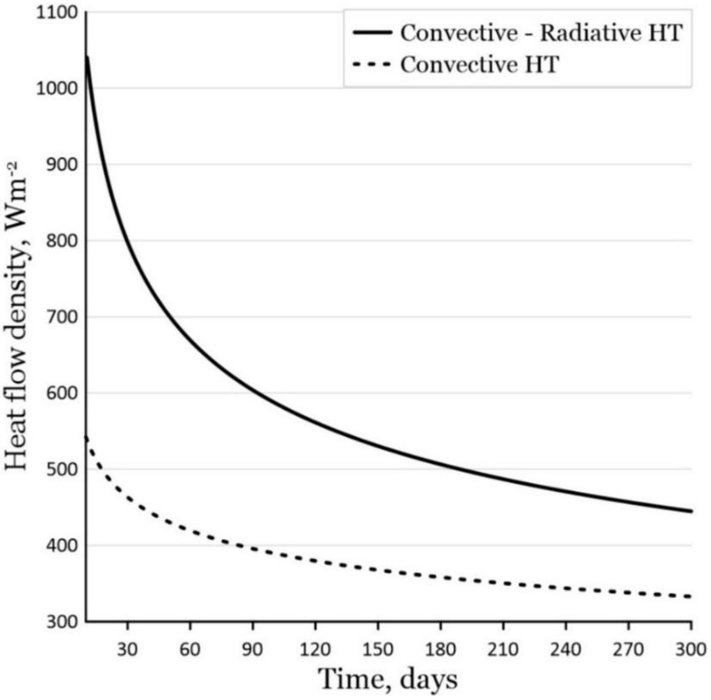

Figure 4.6: Heat flow density calculated for convective (dashed curve) and nonlinear convective and radiative (bold curve) heat transfer (HT). At each time step, the heat flow density presents the average value of the densities calculated over each cell of the lava-air interface. The average density data for 300 days has been smoothed by a power-law fit.

In the earlier stages of eruption, the dome temperatures were high as the cooled crust (carapace) on the dome was the thinnest, and hence the surface heat flux was the highest. The carapace becomes thicker with time, and the surface heat flux keeps the tendency to decrease while the temperature may vary on the surface during active dome building (Hutchison et al., 2013). Meanwhile, the heat flow densities obtained from the modelling and from the inferred temperature data (Hutchison et al., 2013) differ because of the different values of the convective heat flow coefficient and the effective emissivity used in the calculation of the heat flow density. Numerical experiments show that the heat exchange between the lava and the air plays a significant role in the development of the lava dome carapace during the long dome-forming eruptions.

4.3.3 Thermal conditions at the conduit wall and crater surface

In this section we present the results of the numerical experiments related to variations of the thermal conditions at the crater surface and the magma-rock interface. These experiments are conducted under the assumption of the convective heat transfer ($HF=HF_l$) at the interface between the lava and the air and no viscous dissipation (VD=0). In experiments 3.1-3.3, the same thermal boundary condition (temperature 350K at Γ_2, see Figure 4.2) is assumed; the volume fraction of crystals at the equilibrium state is constant in exp. 3.1 and depends on the temperature in exps. 3.2 and 3.3. In addition, the latent heat due to crystallization is introduced in exp. 3.3. In the subsequent experiments (exps. 3.4-3.6), different thermal boundary conditions at the crater surface and the magma-rock interface and the constant ϕ_{eq} are employed. Namely, in exp. 3.4, a conductive heat flux is assumed at Γ_2 corresponding to the wall-rock temperature $T = 350$ K, thermal conductivity 3.5 J s^{-1} kg^{-1} K^{-1}, and the zero-thickness of the wall. In exp. 3.5 and 3.6, the temperature $T = 350$ K at the crater surface and the temperature $T = 500$ K at the conduit wall in case of exp. 3.5 and $T = 700$ K in exp. 3.6 are assumed. The experiments show how the different conditions affect the temperature, crystal content, viscosity, and velocity in the modelled conduit and lava dome.

The inclusion of the temperature-dependent ϕ_{eq} (exp. 3.2) slightly alters the viscosity distribution, retards the lava advancement and leads to vertical growth compared to exp. 3.1 (Figure 4.7). In the case of exp. 3.3, the latent heat release leads to increased temperatures, reduction of the crystal content, and lowering the lava viscosity. This decrease in viscosity contributes to horizontal advancement of the lava and flattening the lava dome (Figure 4.7). The change in temperature and heat flux at boundary Γ_2 (Figure 4.7, exps. 3.1–3.6) leads to cooling of the lava dome at the contact with the crater surface and with the conduit wall. The hot lava concentrates in the conduit centre, where the velocity increases. The changes in the thermal conditions at the crater surface and the conduit wall do not significantly influence the morphological shapes of the lava domes in exp. 3.1, 3.4-3.6. Meanwhile, we note that as the eruption proceeds, the heat flux from the ascending magma will gradually decrease due to heating up the surrounding rocks.

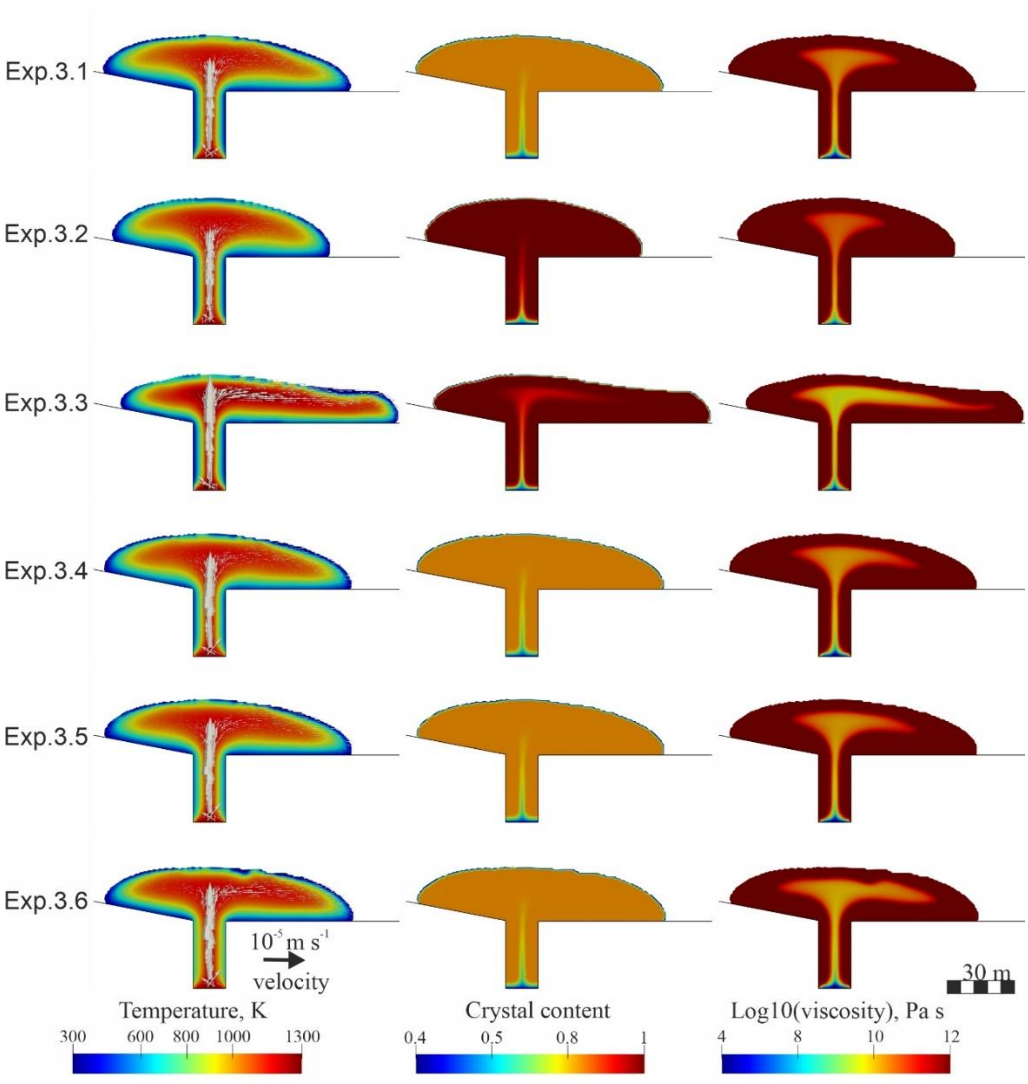

Figure 4.7: Modelled lava dome growth. The temperature together with the velocity vectors (left column), crystal content (middle column), and viscosity (right column) at time t = 300 days.

4.3.4 Lava dome growth at Volcán de Colima from 2007 to 2009

In this section we present the results of two numerical experiments (exp. 4.1 and exp. 4.2) related to the lava dome growth from the start of the lava extrusion in February 2007 until April 2009. In both experiments, the numerical model includes Eqs. (4.1) - (4.10) with the initial and boundary conditions described in sect. 4.2.3, assuming the nonlinear convective and radiative heat transfer at the lava-air interface and including the latent heat of crystallization and the viscous dissipation (even though its effect is negligible) in Eq. (4.3). We employ the constant (exp. 4.1) and the temperature-dependent (exp. 4.2) ϕ_{eq} in the modelling.

Laboratory and numerical experiments showed earlier that cooling increases the viscosity of the uppermost part of the lava dome and results in developing a high-viscosity carapace (e.g., Fink & Griffiths, 1998; Griffiths, 2000; Hale & Wadge, 2003, 2008; Hale et al., 2007; Husain et al., 2014, 2018, 2019; Harnett et al., 2018; Tsepelev et al., 2020). As the viscosity of the model dome carapace is higher than 10^{12} Pa s at lower temperatures, the threshold of the lava viscosity (Eq. 4.7) was raised to 10^{13} Pa s (and to $10^{13.5}$ Pa s at day 600) in both experiments. The increase of the viscosity in the carapace allows for simulating a lava dome, which morphological shape fits better the dome shape observed at Volcán de Colima. We have used several thresholds (from $10^{12.5}$ Pa s to 10^{14} Pa s) and found that the lava dome still advances horizontally at $10^{12.5}$ Pa s and develops an obelisk-type dome at 10^{14} Pa s, and both scenarios of the dome development contradict the observations on the lava dome growth at Volcán de Colima.

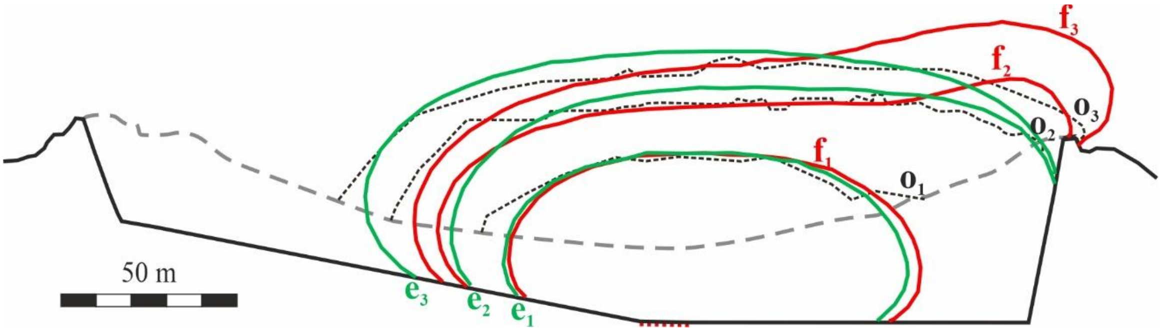

Figure 4.8: Comparison of the morphological shapes of the modelled domes in exp. 4.1 (solid green curves with index *e*) and exp. 4.2 (solid red curves with index *f*) alongside with the observed shapes of the lava dome (dotted black curves with index *o*) on 1 May 2008 (index 1), 4 December 2008 (index 2), and 1 April 2009 (index 3). The grey dashed line is the crater's rim. The black bold line presents the base of the crater, and the red dotted line is the top of the conduit.

Zeinalova et al. (2021) used a similar approach but introduced an artificial thin carapace with the viscosity 10^{14} Pa s in the model of lava dome growth at day 481 after the commencement of the lava extrusion to mimic the growth of the observed lava dome, as their model did not consider thermal effects (that is, Eqs. 4.3, 4.5, and 4.8 were not used) and, hence, could not generate a high viscosity carapace. Here, we show how the carapace evolves self-consistently due to cooling of the uppermost part of the dome.

Figure 4.8 presents the morphological shapes of the modelled lava dome at times of 1 May 2008 (day 480), 4 December 2008 (day 704), and 1 April 2009 (day 822). The increased viscosity of the carapace due to cooling restrains the lateral advancement of the dome. The modelled dome develops steep flanks, and its morphology fits observations at Volcán de Colima with a few meter differences in the length of the dome.

Initially, the morphological shapes of the modelled domes (Figure 4.8, green and red curves with index *e* and *f*, respectively) fit quite well the observed shape of the lava dome. Later, the lava advances to the right in exp. 4.2 compared to that in the case of exp. 4.1, and this can be associated with a minor decrease (to about $10^{7.5}$ Pa s) in the viscosity of the dome interior (Figure 4.9). These results underscore that the variations in viscosity, particularly between the dome interior and its carapace, along with the introduction of the temperature-dependent ϕ_{eq}, influence the lava dome growth and its morphological shapes.

To quantitatively compare the morphological shape of the modelled dome with that of the observed dome (Figure 4.8), we evaluate the closeness of the shape $\tilde{F}$ of the part $\tilde{L}$ of the observed dome, which is visible over the crater's rim (dotted black curves), and the shape F_i of the part L_i of the modelled dome also visible over the crater's rim. We employ the quality functional J_i, which is based on the symmetric difference (Starodubtseva et al., 2021):

$$J_i(\tilde{F},F_i)=\frac{S\left((\tilde{L}\cup L_i)\setminus(\tilde{L}\cap L_i)\right)}{S(\tilde{L})}, \tag{4.12}$$

where indices $i = 1$ and $i = 2$ denote the modelled domes in exp. 4.1 and exp. 4.2, and S is the area measured in [m^2]. The closeness of the function J_i to zero means the closeness of the observed shape $\tilde{F}$ to the model shape F_i. The functional J_1 takes the values 0.12, 0.16, and 0.11 and the functional J_2 the values 0.12, 0.17, and 0.25 for days 480, 704, and 822, respectively. The numbers show that while the morphological shapes of both modelled domes fit the observed shape with the almost same accuracy for the first 704 days, the modelled shapes deviate from each other considerably later. Namely, in exp. 4.2, the lava advances considerably to the right moving over the crater's rim and develops an overstepping feature, while the modelled dome heights do not fit well the height of the observed lava dome. In the case of exp. 4.1, the morphological shape of the modelled dome agrees better with the observation.

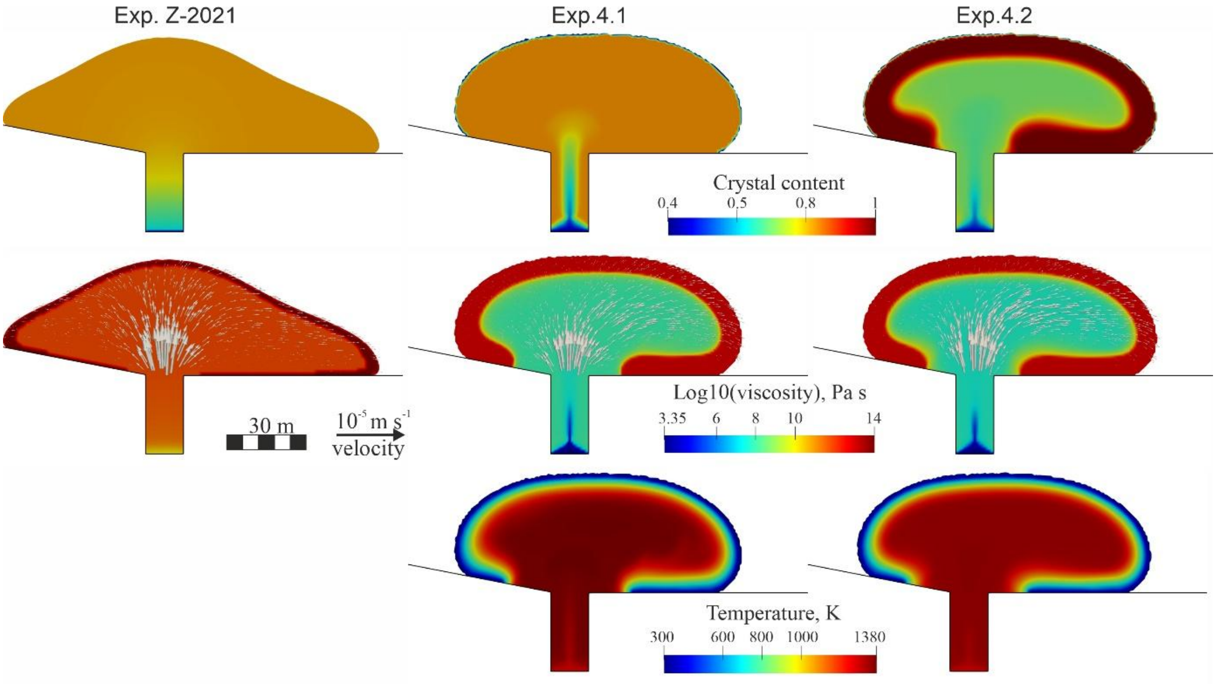

Figure 4.9: Comparison between three models of the lava dome growth at Volcán de Colima at time t = 480 days: (the left-hand panels) the crystal content and viscosity in exp. Z-2021 by Zeinalova et al. (2021); the crystal content, the viscosity, and temperature in exp. 4.1 (the middle panels) and exp. 4.2 (the right-hand panels). The flow velocity vectors are shown in the modelled domes.

The carapace of the viscosity 10^{14} Pa s in the model by Zeinalova et al. (2021) (Figure 4.9a) is thinner than that of the viscosity $10^{13.5}$ Pa s in the studied models (Figure 4.9b, c and Figure 4.10). The thicker carapace constrains the lava dome advancement despite its viscosity lower than in the case of the modelled carapace by Zeinalova et al. (2021). The interior of the lava domes in exps. 4.1 and 4.2 has a low viscosity ranging from about $10^{7.5\text{-}8}$ to 10^9 Pa s.

Although the volume fraction of crystals in exp. 4.1 remains relatively consistent with that in exp. Z-2021 (Zeinalova et al., 2021), the viscosity of the modelled dome interiors in these experiments differs significantly from each other and should influence the dome's shape. The temperature-dependent volume fraction of crystals at the equilibrium state exerts an impact on the crystal content (exp. 4.2) leading to a decrease in crystal content within the dome interior from 0.83 (Figure 4.9b) to 0.7 (Figure 4.9c). This crystal content's reduction has a corresponding effect on the latent heat release during crystallization, decreasing the temperature from 1380K (in exp. 4.1) to 1335K (in exp. 4.2). Meanwhile the shapes of the modelled domes (in exps. 4.1 and 4.2) remain very similar. Therefore, the viscosity and the thickness of the carapace influence more profoundly the morphological shapes of lava domes.

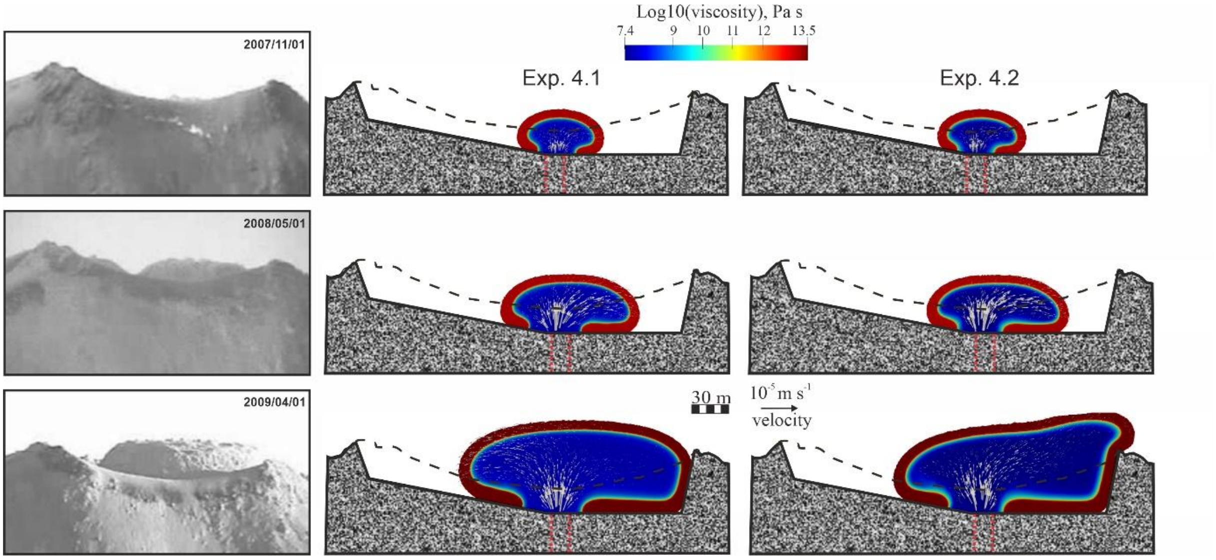

Figure 4.10: Images of the lava dome evolution at Volcán de Colima (left column; Bretón-González et al., 2013) versus the modelled lava dome growth in exp.4.1 (middle column) and exp. 4.2 (right column) at times of 1 November 2007 (upper panels), 1 May 2008 (middle column) and exp. 4.2 (right column) at times of 1 November 2007 (upper panels), 1 May 2008 (middle panels), and 1 April 2009 (lower panels). The middle and right columns present the lava viscosity distribution with the flow velocity vectors. The black dashed line is the crater's rim, and the red dashed line is the position of the conduit.

The modelled domes are presented in Figure 4.10 together with the recorded images of the lava dome at Volcán de Colima (Bretón-González et al., 2013). The dome interior in both experiments remains hot and therefore ductile throughout the dome growth during the studied period of the lava extrusion.

4.4 Discussion and conclusion

Lava dome eruptions at Volcán de Colima are episodic and vary in the dome building duration from days to months and years without explosive dome collapses. The eruption started in February 2007 with the extrusion of hot rocks from a rising plug of the older magma filling the uppermost part of the conduit (Hutchison et al., 2013). The dome grew continuously, and from the beginning of 2008 its morphology resembled closely that of a truncated cone (Bretón-González et al., 2013; Figure 4.1).

Our numerical thermo-mechanical models of the lava dome growth are validated against recorded dataset from Volcán de Colima during the long dome-building episode lasting from 2007 to 2009 (Bretón-González et al., 2013). We show that long episodes of the dome building require a viscosity model depending on both the crystal content and the temperature to allow for generating a thermal, highly viscous carapace (e.g., Zeinalova et al., 2021). This numerical study has estimated the influence of the lava temperature, thermal boundary conditions, the crystal content, the latent heat of crystallization, the heat due to the viscous dissipation, and the heat transfer mechanisms at the lava-air interface on the lava dome dynamics and its morphology.

Although degassing-induced crystallization plays a significant role in lava dome building process, especially during short dome-building episodes (e.g.,Walter et al., 2019; Tsepelev et al., 2021b; Zeinalova et al., 2021), we have shown that the rheological stiffening within the lava dome is essentially controlled by cooling during long dome-building episodes. Cooling influences the viscosity of the lava dome at its interface with the air making the dome carapace more viscous and promotes a development of lobe-shaped lava dome (Watts et al., 2002; Tsepelev et al., 2020). The model results indicate that a high-viscous carapace of the lava dome at Volcán de Colima retards the dome lateral advancement and promotes the development of steep slopes on the dome sides. We have demonstrated that (i) the dome carapace becomes thicker in the case of the convective-radiative heat transfer at the interface between the lava and the air; (ii) the latent heat of crystallization leads to elevated temperature in the conduit and in the lava dome interior and to further flattening of the dome; (iii) the heat source within the dome due to the viscous dissipation is negligible, and can be omitted in the modelling of the lava dome growth; and (iv) thermal boundary conditions influence the magma flow pattern and the crystal content in the conduit with an insignificant impact to the dynamics of the dome interior, and hence, to the morphological shapes of the lava dome.

The dynamics of dome eruptions can be more complicated than that described in this work due to the complex interplay between magma decompression, degassing, degassing-induced crystallization, pore-fluid dynamics, temperature, and rheological properties of the erupted lava (e.g., Fink & Griffiths, 1998; Melnik & Sparks, 1999; Calder et al., 2015;). Particularly, our current model cannot simulate a brittle, but ductile only, behaviour of the dome carapace. Tsepelev et al. (2020) showed that in the case of the strain-rate dependent viscosity, the viscosity of the dome carapace increases with the decrease of the strain rate, and vice versa. This dependence of the viscosity on strain rates presents a typical behaviour of a non-Newtonian Herschel-Bulkley fluid exhibiting rigid body properties at low strain rates and viscous fluid properties at higher rates.

The dome morphology shall also vary with the strain rate resulting in short and wide domes at higher strain rates, and tall and narrow domes at lower rates (Tsepelev et al., 2020). The form of crystals influences the lava viscosity (Frontoni et al., 2022) and, hence, may lead to changes in the dome morphology. Discrepancies in the shapes of the modeled dome compared to the observed dome shapes can also be associated with a brittle behavior of the natural dome carapace and its failures, which are important components in natural lava dome developments. Furthermore, two-dimensional numerical models cannot capture complexity of natural lava dome growth, and three-dimensional models should provide additional insight into lava dome dynamics.

Although no numerical model is likely to represent the exact lava dome extrusion dynamics, the thermo-mechanical model accounts for the main dynamic processes and characteristics within the shallow conduit and lava dome, such as the mass and heat transfer (Eqs. (1)-(6)), the degassing-induced crystallization kinetics (Eq. 10), the latent heat of crystallization, the convective and radiative heat flux at the lava interface with the air, conductive heat flux at the crater surface and the shallow conduit wall, and the lava viscosity depending on the volume fraction of crystals and the temperature (Eqs. 7-9). The present model can be further developed by incorporating the water content and stress-dependence into the lava viscosity model, although efficient degassing, as observed during lava-building eruptions at Volcán de Colima, results in a low (about 9%) mean porosity (Lavallée et al., 2007) and low water contents (2.5 to 0.1 wt.%) of Colima eruptive products (Reubi & Blundy, 2008).

Using observations (i.e., morphological shapes of the lava dome at Volcán de Colima and experimentally derived material properties of lava samples from the volcano) and models (i.e., crystal growth kinetics, lava viscosity, and various heat transfer), this contribution demonstrates that the lava dome growth at Volcán de Colima for 2007-2009 can be well described. Although it was known that the cooling at the interface of the lava dome and the air plays a significant role in the evolution of dome carapaces, we have shown here that the combined effects of the thermal evolution and crystallization in the dome interior and the cooling at the lava-air interface shape the lava dome during long episodes of its building. The developed thermo-mechanical model of the lava dome evolution can be used at other volcanoes during effusive eruptions, long episodes of lava dome building, the dome carapace formation, and its potential failure, which may lead to pyroclastic flow hazards.

Data availability statement

The data supporting the conclusions of this article and input model files for Ansys Fluent will be made available by the authors without undue reservation.

4.4.1 Author contribution

AIZ and NZ (a PhD student) contributed to the conceptualization of the paper. NZ processed the data, developed a numerical model, and performed all model experiments. AIZ supervised the study and assisted NZ in numerical modelling and data processing. IT contributed to the development of numerical codes and modelling. AIZ, FS, NZ, and OM contributed to interpretation of numerical results. AIZ and NZ performed writing–original draft preparation and figures. All co-authors performed writing–review and editing.

4.4.2 Acknowledgments

We thank the editor Jörg Renner, Juan Carlos Afonso, Tobias Keller, and anonymous reviewer for their review and constructive comments. This is a contribution to the research project funded by the Deutsche Forschungsgemeinschaft (project DFG IS203/14-1). OM is supported by the PAUSE program (grant #C7H-PUB23A59). We are grateful to Vyacheslav Zobin for discussion on the dome growth at Volcán de Colima during 2007-2009.

Table 4.1: Numerical experiments.

No. Exp	**Convective heat transfer**	**Convective-radiative heat transfer**	**Latent heat release**	**Viscous dissipation**	**Thermal conditions at the model boundary**	ϕ_{eq} / ϕ_{in}
1.1	✓				Heat flux =0	0.83 / 0.4
1.2	✓			✓	Heat flux =0	0.83 / 0.4
1.3	✓		✓		Heat flux =0	0.83 / 0.4
1.4	✓		✓		Heat flux =0	$\phi_{eq}(T)$ / 0.4
2.1		✓			Heat flux =0	0.83 / 0.4
2.2		✓		✓	Heat flux =0	0.83 / 0.4
2.3		✓	✓		Heat flux =0	0.83 / 0.4
2.4		✓	✓		Heat flux =0	$\phi_{eq}(T)$ / 0.4
2.5		✓	✓		Heat flux =0	$\phi_{eq}(T)$ / 0.6
3.1	✓				Temperature 350 K at Γ_2	0.83 / 0.4
3.2	✓				Temperature 350 K at Γ_2	$\phi_{eq}(T)$ / 0.4
3.3	✓		✓		Temperature 350 K at Γ_2	$\phi_{eq}(T)$ / 0.4
3.4	✓				Conductive heat flux at Γ_2	0.83 / 0.4
3.5	✓				Temperature 350 K at the crater surface, 500 K at the conduit wall	0.83 / 0.4
3.6	✓				Temperature 350 K at the crater surface, 700 K at the conduit wall	0.83 / 0.4
4.1		✓	✓	✓	Heat flux =0	0.83 / 0.4
4.2		✓	✓	✓	Heat flux =0	$\phi_{eq}(T)$ / 0.4

Table 4.2: Model parameters and their values.

Symbol	Parameter, unit	Value
B	the Einstein coefficient (in Eq. 9)	2.5
c_A	specific heat capacity of air, J kg^{-1} K^{-1}	1006
c_L	specific heat capacity of lava, J kg^{-1} K^{-1}	1200
g	acceleration due to gravity, m s^{-2}	9.81
k_A	thermal conductivity of air, J s^{-1} m^{-1} K^{-1}	0.025
k_L	thermal conductivity of lava, J s^{-1} m^{-1} K^{-1}	3.0
L^*	latent heat coefficient, J kg^{-1}	3.5×10^5
T_A	air temperature, K	300
T_{ct}	initial temperature of the magma in the conduit, K	1150
T_{in}	temperature of the new magma entering the conduit, K	1250
$\mathbf{u}_{ext}$	extrusion rate, m s^{-1} from day 1 to day 300 from day 301 to day 455 from day 456 to day 480 from day 481 to day 822	 5.0×10^{-6} 7.5×10^{-6} 2.0×10^{-5} 1.7×10^{-5}
δ	rheological parameter (in Eq. 9)	7.24
ε	effective emissivity	0.9
ϕ_{ct}	initial volume fraction of crystals in the magma in the model conduit	0.8
ϕ_{in}	volume fraction of crystals of the new magma entering the model conduit	0.4
ϕ_*	specific volume fraction of crystals	0.591
γ	rheological parameter (in Eq. 9)	5.76
η_A	air viscosity, Pa·s	0.001
λ	coefficient of convective heat transfer, J s^{-1} m^{-2} K^{-1}	3.0
λ_n	nonlinear convective heat transfer coefficient, J s^{-1} m^{-2} K$^{-4/3}$	5.5
ρ_A	air density, kg m^{-3}	1
ρ_L	lava density, kg m^{-3}	2500

σ	Stefan–Boltzmann constant, J s^{-1} m^{-2} K^{-4}	5.67×10^{-8}
τ	characteristic time of the crystal content growth, days	5
ξ	rheological parameter (in Eq. 9)	4.63×10^{-4}

Chapter 5: Numerical Approaches to Modelling of Lava Dome Growth

This chapter is reproduced from the manuscript that has been accepted to publishing in *Springer Proceedings on Applications of Mathematical Methods*, Zeinalova N., Ismail-Zadeh A., Tsepelev I., Melnik O., Schilling, F.

Abstract

Non-explosive volcanic eruptions can result in the formation of lava domes when highly viscous magmas extrude on the surface. To distinguish between different mechanisms during the evolution of lava domes, isothermal and non-isothermal numerical models were used to explore the processes behind the evolution of the internal structure and morphological shape. To model the lava dome growth, we assume that the lava behaves as a viscous fluid, and use the Navier-Stokes, continuity, and the heat equations, along with relevant initial and boundary conditions. Additionally, an advection equation is employed to describe the movement of the interface between air and lava. The lava viscosity depends on the melt viscosity and the volume fraction of crystals. The latter is determined from an evolutionary equation that describes simplified crystal growth kinetics of degassing-induced crystallization. Numerical modelling employs finite volume and volume of fluid methods. The models demonstrate how lava dome dynamics are influenced by crystallization, the radiative-convective heat transfer, and the rheological stiffening driven by cooling. If the lava viscosity mainly depends on the volume fraction of crystals (as in the isothermal case study), the lava dome grows upward initially and later advances horizontally. The non-isothermal model shows that a highly viscous layer (carapace) forms within the uppermost part of the lava dome due to cooling, which restricts rapid dome broadening by creating steep slopes on the sides during long periods of dome building. Both models provide insights into the underlying processes and mechanisms of the evolution of lava domes, including their growth, carapace formation, and morphological modifications.

Keywords: fluid dynamics, numerical modelling, heat transfer, crystallization, lava dome

5.1 Introduction

Extrusion of a viscous magma on the surface can result in the growth of a lava dome depending on the magma's extrusion rate and its viscosity (see Table 5.1 for the volcanological terminology used in this paper). The lavas from dome-building volcanoes typically exhibit low average eruption rates and high viscosities, commonly attributed to their high crystallinity (e.g., Sheldrake et al., 2016). Numerical modelling assists in understanding the dynamics of lava domes and, particularly, in explaining the impact of the rheological properties of magma (its crystal content, temperature, and the discharge rate) on the morphological shape of lava domes (e.g., Hale & Wadge, 2003; Husain et al., 2014; Harnett et al., 2018; Tsepelev et al., 2020; Zeinalova et al., 2021, 2024).

Zeinalova et al. (2021) developed a numerical model focusing on the gradual lava dome-building process at Volcán de Colima, examining how magma viscosity and discharge rates influenced the dome growth during years 2007-2009. Their viscosity model accounted for the crystal-dependent viscosity and the constant crystal-free melt viscosity. They showed that a highly viscous carapace is required to keep the model dome growing up and not spreading horizontally. To generate the carapace in a self-consistent way, Zeinalova et al. (2024) developed a thermomechanical model of a long-term lava dome evolution and analysed the lava dome growth depending on various heat sources and boundary conditions. Their model showed that cooling and carapace formation play a significant role during long duration of dome building.

Here, we present two case studies: (i) an isothermal case, where lava viscosity solely depends on the crystallization process, and (ii) a non-isothermal case, where viscosity is temperature- and crystallinity-dependent. Compared to the previous numerical models, which exhibit rapid (up to a few months) dome building with potential explosive destruction of the lava dome (e.g., (Walter et al., 2019; Tsepelev et al., 2021a), these case studies focus on a long (up to a year) dome-building, which was observed, for example, in Volcán de Colima, México (Zobin et al., 2015; Zeinalova et al., 2021). Following Zeinalova et al. (2024), we demonstrate that the radiative-convective heat flux leads to cooling of the lava at the interface with the surrounding air, resulting in the formation of a thick carapace. We compare the results of two case studies to analyse the influence of temperature and heat transfer on the growth of the modelled lava domes.

5.2 Mathematical Statement

5.2.1 Geometry

The geometry of model domain $\Omega = \Omega_1 \cup \Omega_2$ (Figure 5.1) corresponds to a configuration of the crater of Volcán de Colima (Zobin et al., 2015), which was used in numerical modelling by Zeinalova et al. (2024). The width of the crater is 257 m, while the conduit has 14.5 meters in width and 30 meters in depth. In the domain, we analyse a two-dimensional, viscous, incompressible, two-phase, immiscible fluid flow simulating an extrusion of lava (one fluid phase) into the surrounding air (another fluid phase) and its subsequent advancement. The sub-domain Ω_1 (the model conduit) is filled with the solidified rocks from previous eruption, and the sub-domain Ω_2 is filled with air. Fresh magma enters through the conduit, pushes the older rocks up to the surface, until it eventually reaches the surface itself, and contributes to the development of a lava dome. We note that the influence of the air phase on the lava dome growth is negligible due to a large ratio between densities/viscosities of the air and the lava.

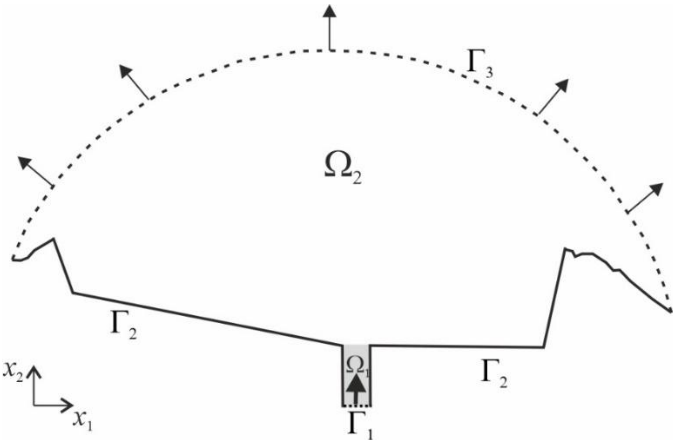

Figure 5.1: Sketch of the model domain. The model conduit (sub-domain Ω_1) is occupied by older magma (grey-shaded), the thick arrow represents the upward ascent of new magma through Γ_1 (the dotted line). The bold line Γ_2 outlines the lava dome base (the crater's surface). The upper boundary

of the domain is represented by a dashed curve (Γ_3), facilitating the escape of the air from the model, with the direction of escape illustrated by arrows perpendicular to Γ_3.

5.2.2 Governing equations

The following governing equations describe the fluid flow approximating lava dynamics (e.g., Ismail-Zadeh & Tackley, 2010; Tsepelev et al., 2020; Zeinalova et al., 2021, 2024):

the Navier-Stokes equations

$$\frac{\partial(\rho\mathbf{u})}{\partial t}+\langle\mathbf{u},\nabla\rangle(\rho\mathbf{u})-\nabla\cdot\left(\eta\left(\nabla\mathbf{u}+\nabla\mathbf{u}^T\right)\right)=-\nabla p-\rho\mathbf{g}, \tag{5.1}$$

the continuity equation

$$\nabla\cdot\mathbf{u}=0, \tag{5.2}$$

and the equation for advection of the interface between the air and the lava:

$$\frac{\partial\alpha}{\partial t}+\nabla\cdot(\alpha\mathbf{u})=0, \tag{5.3}$$

where t is the time; $\mathbf{u}=(u_1(t,\mathbf{x}),\ u_2(t,\mathbf{x}))$ is the velocity; $\mathbf{x}=(x_1,x_2)\in\Omega$ is the position vector in the Cartesian coordinates; ; ρ is the density; η is the viscosity; $p=p(\mathbf{x})$ is the pressure; $\mathbf{g}=(0,g)$, and g (=9.81 m s^{-2}) is the acceleration due to gravity; $\alpha(t,\mathbf{x})$ takes the value of one for the lava and zero for the air at each point $\mathbf{x}$ and time t; ∇, $\nabla\cdot$, ^{T}, and $\langle\cdot,\cdot\rangle$ denote the gradient operator, the divergence operator, the transposed matrix, and the scalar product of vectors, respectively. We consider that the model density and viscosity are presented as:

$$\rho=\rho_L\alpha(t,\mathbf{x})+\rho_A(1-\alpha(t,\mathbf{x})), \qquad \eta=\eta_L\alpha(t,\mathbf{x})+\eta_A(1-\alpha(t,\mathbf{x})), \tag{5.4}$$

where ρ_A and η_A are the density and viscosity of the air, and ρ_L and η_L are the lava density and its viscosity.

To study the influence of temperature on the development of lava domes, the heat equation is added to Eqs. (1)-(4) (Zeinalova et al., 2024):

$$\frac{\partial\left(c\rho T\right)}{\partial t}+\nabla\cdot\left(\mathbf{u}\left(c\rho T\right)\right)=\nabla\cdot\left(k\nabla T\right)-HF. \tag{5.5}$$

Here T is the temperature; the term HF accounts for the radiative and nonlinear convective heat transfer at the air-lava interface $HF=\left[\varepsilon\sigma(T^4-T_A^4)+\lambda_n(T-T_A)^{4/3}\right]\delta_s$ (e.g., Tsepelev et al., 2020; Zeinalova et al., 2024); ε (=0.9; Ramsey et al., 2019) is the effective emissivity of the lava dome solid surface; σ is the Stefan–Boltzmann constant; λ_n is the nonlinear convective heat transfer coefficient measured in (W m^{-2} K$^{-4/3}$) (Neri, 1998); T_A is the air temperature; δ_s is the special function (approximating the Dirac delta function; measured in (m^{-1}) determined at interface (*S*) between the lava and the air. The model heat conductivity *k* and the specific heat capacity *c* are represented as:

$$k(t,\mathbf{x}) = k_L\alpha(t,\mathbf{x}) + k_A(1-\alpha(t,\mathbf{x})), \qquad c(t,\mathbf{x}) = c_L\alpha(t,\mathbf{x}) + c_A(1-\alpha(t,\mathbf{x})), \tag{5.6}$$

where k_A and c_A are the thermal conductivity and the specific heat capacity of the air, and k_L , and c_L are the thermal conductivity and the specific heat capacity of the lava, respectively.

5.2.3 Lava viscosity

The viscosity of lava η_L (measured in (Pa s)) is described as the product of the melt viscosity $\eta_{mt}(T)$ depending on temperature and the relative viscosity depending on the volume fraction of crystals $\eta_{cr}(\phi)$:

$$\eta_L(T,\phi) = \eta_{mt}(T)\cdot\eta_{cr}(\phi). \tag{5.7}$$

In the isothermal case study, we assume that the melt viscosity η_{mt} is constant. In the non-isothermal case study, a temperature-dependent melt viscosity is described by the following experimental relationship (Lavallée et al., 2012):

$$\log_{10}\eta_{mt}(T_C) = A_{VFT} + \frac{B_{VFT}}{T_C - T_g}, \tag{5.8}$$

where T_C is the temperature in °C, T_g = 710°C is the glass transition temperature, A_{VFT} = 0.29, and B_{VFT} = 606.9°C. Temperature T_C should be greater than the glass transition temperature T_g , if not $T_C = T_g + 1$.

To define the dimensionless viscosity, we employ the model proposed by (Costa et al., 2009):

$$\eta_{cr}(\phi) = \left(1+\varphi^{\delta}\right)\left[1-(1-\xi)\mathrm{erf}\left(\frac{\sqrt{\pi}}{2(1-\xi)}\varphi(1+\varphi^{\gamma})\right)\right]^{-B\phi_*}, \tag{5.9}$$

where $\varphi = \phi/\phi_*$; ϕ is the volume fraction of crystals; ϕ_* is the specific volume fraction of crystals representing the critical solid fraction at the onset of the exponential increase of $\eta_{cr}(\phi)$ assumed to be $\phi_* = 0.591$ (Costa et al., 2009); the empirical parameters $\delta = 7.24$,

$\xi = 4.63\times10^{-4}$, and $\gamma = 5.76$ are sourced from Lejeune & Richet (1995) and Costa et al. (2009); and $\mathrm{erf}(\cdot)$ is the error function; and the theoretical value of *B* is the Einstein coefficient (Mardles, 1940). It was experimentally determined that this coefficient varies from 1.5 to 5 (Jeffrey & Acrivos, 1976); and we set *B* = 2.5 (Costa et al., 2009).

The volume fraction of crystals ϕ is determined from the evolutionary equation describing the simplified crystal growth kinetics of degassing-induced crystallization (e.g., Tsepelev et al., 2019):

$$\frac{\partial\phi}{\partial t} + \nabla\cdot(\alpha\phi\mathbf{u}) = -\alpha\frac{\phi-\phi_{eq}}{\tau}, \tag{5.10}$$

with the initial condition for the volume fraction of crystals $\phi(t=0,\mathbf{x})=0$ for $\mathbf{x}\in\Omega_2$ and $\phi(t=0,\mathbf{x})=0.8$ for $\mathbf{x}\in\Omega_1$. Here, ϕ_{eq} is the volume fraction of crystals at the equilibrium state; τ is the characteristic time of crystal content growth needed by crystals to reach ϕ_{eq}. We assume that $\phi_{eq}=0.83$, which is in the range of experimental constraints (Riker et al., 2015; Cashman, 2020).

Thus, in the numerical modelling, we employ Eqs. (5.1) - (5.4), (5.7), (5.9), and (5.10) in the isothermal case study, and Eqs. (5.1) - (5.10) in the non-isothermal case study, together with relevant initial and boundary conditions described below.

5.2.4 Initial and boundary conditions

At the initial time, the flow velocity is assumed to be $\mathbf{u}(t=0,\mathbf{x})=\mathbf{u}_0$. The sub-domain Ω_1 (the model conduit) is filled by the older magma ($\alpha(t=0,\mathbf{x})=1$) with the volume fraction of crystals $\phi_{ct}=0.8$ and temperature T_{ct} (in non-isothermal case study). The sub-domain Ω_2 is filled by the air ($\alpha(t=0,\mathbf{x})=0$) with the volume fraction of crystals $\phi=0$ and temperature of the air T_A (in non-isothermal case study).

The following conditions are applied on the model boundary $\Gamma=\Gamma_1\cup\Gamma_2\cup\Gamma_3$ (Figure 5.1). A new magma with the volume fraction of crystals ϕ_{in} (assumed to be 0.4 in the modelling), and the temperature T_{in} (assumed to be 1250K in the non-isothermal case) enters the model domain at a specified extrusion rate $\mathbf{u}_{ext}$ = $\left(0,\ 5\times10^{-6}\right)$ (m s^{-1}) through the part Γ_1 of the model boundary. No-slip condition $\mathbf{u} = 0$ and zero heat flux (in the non-isothermal case) are prescribed at Γ_2. To guarantee the incompressibility condition (Eq. 5.2) due to lava extrusion and thereby maintain the volume of the model domain, the air should be removed from the domain at the lava discharge rate. Hence, the outflow condition is determined at Γ_3 (the upper dashed curve) as $\mathbf{u}_{out} = u_{out}\mathbf{n}$, $\phi = 0$, and $\alpha = 0$, where $u_{out} = -|\Gamma_3|^{-1} \int_{\Gamma_1} \langle \mathbf{u}_{ext}, \mathbf{n} \rangle d\Gamma$, and $\mathbf{n}$ is the outward unit normal vector at a point on the model boundary.

5.3 Solution method

The finite volume (e.g., Ismail-Zadeh & Tackley, 2010) and the volume of fluid (VOF; Hirt & Nichols, 1981) methods are used in the modelling. The VOF method allows for computationally inexpensive treatment of a moving interface between two fluid phases, e.g., the lava and the air. The cells containing the interface between lava and air are assigned α values ranging between zero and one, indicating the respective proportions of lava within them. The numerical solver operates within a discretized model domain consisting of approximately 60,000 hexahedral cells.

The pressure is discretized by the second-order staggered scheme PRESTO! (e.g., Peyret, 1996). To approximate the Laplacian, we use the numerical scheme of the second-order accuracy, and the monotonic schemes are used to discretize convective terms in the equations (e.g., Ismail-Zadeh & Tackley, 2010). The pressure-velocity coupling is handled by the SIMPLE method (S. V. Patankar & Spalding, 1972), where the relaxation parameters are chosen to be 0.01 and 0.3 for the velocity and pressure, respectively. We assign 0.5 to the relaxation parameter for the function α, and the volume fraction of crystals. Considering a discontinuity between the lava and air viscosities, the choice of the relaxation parameters is critical and sometimes it was lowered to ensure the solution’s stability. A time step is chosen in the range of 0.1–40 s depending on the stability and optimization of the velocity to assure a convergence of a set of linear algebraic equations (SLAE), which is obtained after the discretization of the Navier-Stokes equations. The implicit scheme maintains stability in computations even with relatively larger time steps. The use of explicit schemes within the model results in numerical instability, despite employing small Courant numbers. In the modelling, we employ the conjugate-gradient method to solve SLAE. The numerical accuracy attains 10^{-3} for the velocity and pressure and 10^{-6} for the function α and the volume fraction of crystals.

We note that the Reynolds number in the model of the lava dome dynamics remains small within the conduit and lava dome due to the high lava viscosity and hence slow flow. This results in insignificant influence of the inertial terms in the Navier-Stokes equations on the lava dynamics. Conversely, the air dynamics in the model exhibits a large Reynolds number, where inertial terms significantly affect the system. To ensure a laminar flow within the air subdomain and the stability of numerical solutions, we set $\mathbf{u}(t=0,\mathbf{x})=0$ initially and use small time steps (ranging from 10^{-1} s to 10^{-3} s and spanning from 100 to 1,000 time steps) to determine the model velocity, which is then used to run subsequent computations with larger time steps . The presence of the air phase has a negligible effect on the growth of the lava dome, primarily due to the significant differences in density and viscosity between the magma and the air.

A second-order upwind scheme has been implemented to solve the heat equation, where a relaxation parameter of 0.5 is assigned for *T*. The numerical accuracy achieved for the solution of SLAE to find T is 10^{-6}. The term *HF* in Eq. (5.5) is calculated in a thin layer of the cells adjacent to the interface between the lava and the air, and the special function δ_s is approximated by the ratio of the length of a relevant cell to the cell's area.

For numerical computations, we employ Ansys Fluent software[7]. Numerical experiments were conducted using the multiprocessor computer (bwHPC) at the Karlsruhe Institute of Technology. The processor type is Intel Xeon Gold 6230 and the processor frequency is 2.1 Ghz. The computational time for the numerical models varies based on several factors, such as the complexity of the mathematical problem, the quantity of computational cells, the number of cores utilized, and the time-step size. As an example: one day of the lava dome growth in the isothermal case study requires approximately four minutes using eight cores with a model time step of 40 seconds. In the non-isothermal case using the same parameters, the calculation time for one day of lava dome growth extends to around 6 minutes.

---

[7] https://www.ansys.com/products/fluids/ansys-fluent

5.4 Numerical results

5.4.1 Isothermal case study

Fresh magma enters the model domain via the boundary Γ_1 at the prescribed extrusion rate 5×10^{-6} m s^{-1}. The melt viscosity is set at 1.6×10^{5} Pa s for the initial 150 days, and subsequently increased by a factor of 5 (reaching 8×10^{5} Pa s) from day 150 to day 300. All other parameters are listed in Table 5.2. Figure 5.2 presents the results of the numerical isothermal modelling showing the snapshots of the extruded lava, which develops a dome structure for 300 days. During the initial 100 days the lava advances both vertically and horizontally, but later a more profound horizontal spreading of the lava can be observed. With the chosen characteristic time for crystal content growth of 5 days, the crystals achieve their equilibrium state already within the conduit. Following this, the volume fraction of crystals stabilizes, maintaining a constant value of 0.83 during the further lava dome growth. The subsequent increase of the melt viscosity leads to the increase of the lava viscosity and hence constrains the lateral boundary of the lava dome promoting the growth of the dome upwards. Over time, the dome exhibits a horizontal advancement with a vertical growth. The initiation of lava dome growth indicates a notable westward movement towards the right side of the model domain because of the slope of the crater's topography on the left side of the model domain.

The long-term evolution of the lava dome, where the lava rheology is solely dependent on the volume fraction of crystals, results in a nearly constant viscosity (see Figure 5.2, day 300). The lava advances then as a fluid with a constant (even increased after 150 days) viscosity and spreads horizontally due to gravity. This lava spreading occurs due to the absence of a carapace, capable of keeping the lava from horizontal advancement on the surface of the crater.

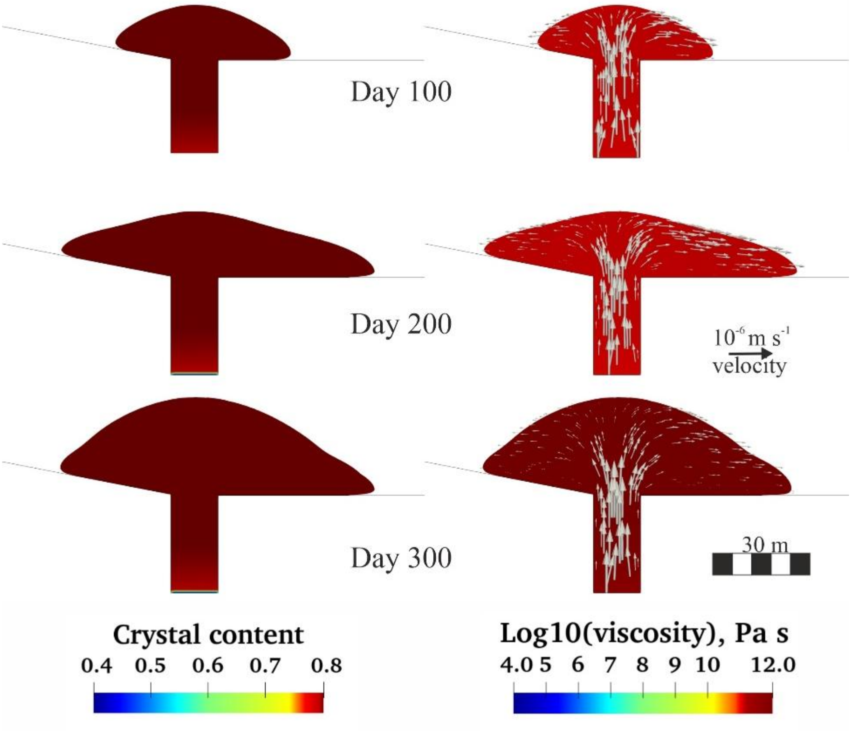

Figure 5.2: The modelled crystal content (in the left column) and the viscosity overlaid by velocity vectors (white arrows) (in the right column) at days: 100 (the upper panel), 200 (the middle panel) and 300 (the lower panel).

5.4.2 Non-isothermal case study

To generate a carapace on the top of the lava dome, we use a non-isothermal numerical model. A magma enters the model conduit through the boundary Γ_1 at the same (as in the isothermal case study) extrusion rate 5×10^{-6} m s^{-1} and at temperature 1250 K and extrudes on the surface forming a lava dome. Other parameters of the model are listed in Table 5.2. The melt viscosity depends on the temperature, and we do not increase it as in the isothermal case study. Figure 5.3 presents the results of the numerical modelling.

As in the isothermal case, the crystals achieve their equilibrium state already within the conduit (Figure 5.3, the left column). This rapid crystallization leads to an increase in the lava viscosity. As the crystal-dependent viscosity attains the value $\eta_{cr}(\phi = 0.83) \sim 10^6$, the lava viscosity and hence the dynamics of the lava dome become dependent only on the temperature.

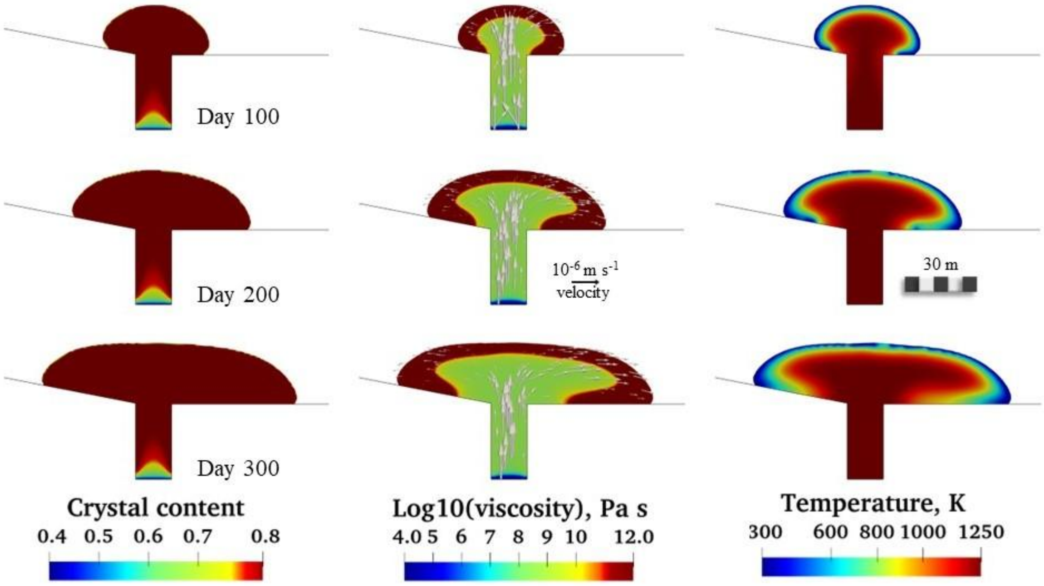

Figure 5.3: The modelled crystal content (left column), the viscosity overlaid by velocity vectors (white arrows) (middle column) and the temperature (right column) at days 100 (upper panel), 200 (middle panel), and 300 (lower panel).

The radiative-convective heat transfer at the interface between the lava and the air results in the temperature decrease (Figure 5.3, the right column) and the viscosity increase (Figure 5.3, the middle column) in the uppermost part of the dome, and, therefore, in the development of a carapace. This carapace retards the horizontal advancement of the lava dome and promotes steep lateral lava fronts. The lava remains sufficiently hot within the dome interior maintaining the lower viscosity (Figure 5.3, the middle column) and exhibiting ductile behaviour during the entire duration of the dome growth, as shown in Zeinalova et al. (2024).

5.5 Discussion

The results of the numerical models related to the two case studies provide a valuable insight into the complex dynamics of lava dome growth under varying rheological properties, and clarify the role of the temperature, melt viscosity, crystal content, and heat transfer at the air-lava interface in the lava dome dynamics. In the isothermal case study, the modelled dome initially grows upward, and later it exhibits predominantly horizontal advancement resulting in a flattening of the dome (Figure 5.4). If the melt viscosity increases resulting in the increase of the lava viscosity, the dome resumes its vertical grows. On the contrary, in the non-isothermal case, the carapace develops self-consistently due to the radiative-convective heat loss at the air/lava interface and it initially restricts lateral advancement of the modelled dome, resulting in a more compact shape within the first 200 days (Figure 5.4). Subsequently, the lava dome starts to advance horizontally due to a stabilization of the extrusion and gravity forces, generating a flat top of the dome.

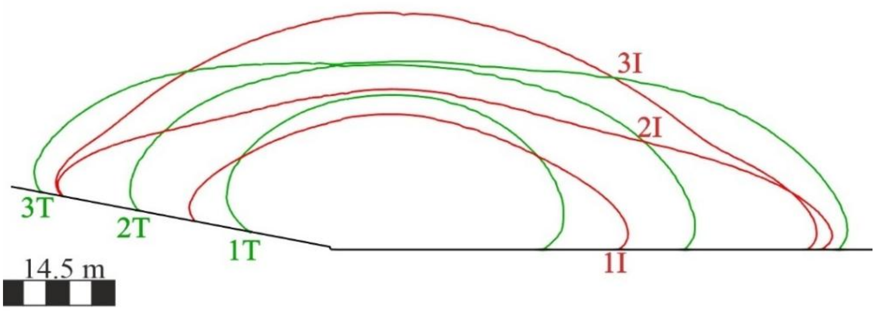

Figure 5.4: Comparison of the morphological shapes of the modelled domes in the isothermal case study (red curves with index I) and in the non-isothermal case study (green curves with index T) at days 100 (index 1), 200 (index 2), and 300 (index 3).

The model results highlight the substantial influence of heat transfer and the carapace development on the lava dome morphology and its internal structure. While in the isothermal case, the viscosity increases almost uniformly within the dome, the radiative-convective heat exchange with the air in the non-isothermal case lowers the temperature and elevates the lava viscosity at the air-lava interface. Meanwhile, the lava within the dome interior remains rather hot and less viscous.

To quantitatively compare the morphological shapes of the two modelled domes (Figure 5.4), we evaluate the closeness of the shape of the dome obtained in the isothermal case ($\tilde{F}$) with that obtained in the non-isothermal case (F). For this comparison, we employ the quality functional *J* based on the symmetric difference (Starodubtseva et al., 2021):

$$J(\tilde{F},F)=\frac{S\left((\tilde{L}\cup L)\setminus(\tilde{L}\cap L)\right)}{S(\tilde{L})}\ , \tag{5.11}$$

where S is the area measured in (m^2), $\tilde{L}$ is the domain of modelled dome in the isothermal case, and L is the domain of the modelled dome in the non-isothermal case. The functional *J* takes the values 0.34, 0.39, and 0.37 for days 100, 200, and 300, respectively. The closeness of the function J to zero means the closeness of the shapes $\tilde{F}$ and F. The obtained values of the functional J show that the morphological shapes of the lava domes in the two case studies differs by about 37%.

The numerical results highlight two key points in dynamics of lava domes. In the isothermal model, where the lava viscosity is solely influenced by the crystallization process, a rapid crystallization results in the viscosity approaching its maximum value, and the lava behaves after that as a fluid of a constant viscosity spreading horizontally on the topography. In the non-isothermal case, the model accounts for the radiative-convective heat transfer at the air/lava interface, and this leads to an alteration in the morphological shape and the internal structure of the lava dome cause by the cold and more viscous carapace. The developed isothermal and non-isothermal models of the lava dome evolution can be used in numerical modelling of lava dome building and the dome carapace formation.

5.5.1 Author contribution

AIZ and NZ (a PhD student) contributed to the conceptualization of the paper. AIZ supervised the study and assisted NZ in numerical modelling and data processing. NZ processed the data, developed a numerical model, and performed all model experiments. IT contributed to the development of numerical codes. AIZ, FS, NZ, and OM contributed to interpretation of numerical results. NZ and AIZ performed writing, and co-authors editing.

5.5.2 Acknowledgments

This is a contribution to the research project funded by the Deutsche Forschungsgemeinschaft (project DFG IS203/14-1). OM acknowledges support from College de France, PAUSE program (C7H-PUB23A59).

Table 5.1:Volcanological terminology.

Term	**Definition**
Carapace	the outer solid layer of a lava dome.
Conduit	a channel that connects the magma chamber to the volcanic vent.
Crater	a depression that usually lies directly above the vent from which volcanic material is ejected (source: U.S. National Park Service).

Crystallization	a process at which crystals start to grow in magmas mainly due to cooling and/or degassing.
Degassing	a process by which magma loses its volatiles.
Discharge rate	a rate at which magma erupts.
Lava	magma emerging as a fluid onto Earth’s surface. The term ‘lava’ is also used for the solidified rock formed by the cooling of a molten lava flow (source: online Encyclopedia Britannica).
Lava dome	any steep-sided mound that is formed when lava reaching the Earth’s surface is so viscous that it cannot flow away readily and accumulates around the vent (source: online Encyclopedia Britannica).
Magma	molten or partially molten rocks.
Magma chamber	a reservoir of magma in the Earth’s crust where the magma may reside temporarily on its way from the uppermost mantle to the Earth’s surface (source: online Collins Dictionary).
Rock	a naturally occurring and coherent aggregate of one or more minerals (source: online Encyclopedia Britannica).
Volcano	an opening where lava, tephra (small rocks), ash, and gases erupt onto the Earth’s surface. Volcanic eruptions can last days, months, or even years (sources: U.S. Geological Survey and the National Geographic Education Program).

Table 5.2: Model parameters and their values.

Symbol	Parameter, unit	Value
B	the Einstein coefficient	2.5
c_A	specific heat capacity of air, J kg^{-1} K^{-1}	1006
c_L	specific heat capacity of lava, J kg^{-1} K^{-1}	1200
g	acceleration due to gravity, m s^{-2}	9.81
k_A	thermal conductivity of air, J s^{-1} m^{-1} K^{-1}	0.025
k_L	thermal conductivity of lava, J s^{-1} m^{-1} K^{-1}	3.0
T_A	air temperature, K	300
T_{in}	temperature of the new magma entering the conduit, K	1250
T_{ct}	initial temperature of the magma in the conduit, K	1150
$\mathbf{u}_{ext}$	extrusion rate, m s^{-1}	5.0×10^{-6}
ε	effective emissivity	0.9
ϕ_{ct}	initial volume fraction of crystals in the magma in the model conduit	0.8
ϕ_{in}	volume fraction of crystals of the new magma entering the model conduit	0.4
ϕ_{eq}	volume fraction of crystals at the equilibrium state	0.83
ϕ_*	specific volume fraction of crystals	0.591
η_A	air viscosity, Pa s	0.001
λ_n	nonlinear convective heat transfer coefficient, J s^{-1} m^{-2} K$^{-4/3}$	5.5
ρ_A	air density, kg m^{-3}	1.225
ρ_L	lava density, kg m^{-3}	2500
σ	Stefan–Boltzmann constant, J s^{-1} m^{-2} K^{-4}	5.67×10^{-8}
τ	characteristic time of the crystal content growth, days	5
ξ	rheological parameter	4.63×10^{-4}
δ	rheological parameter	7.24
γ	rheological parameter	5.76

Chapter 6: Influence of rheological parameters on lava flow morphology inferred from numerical modelling

This chapter is originally published in the *International Journal of Earth Sciences*.

Zeinalova N., Bilotta G., Ismail-Zadeh A., Cappello A., Ganci G., Schilling F. [2025]: Influence of rheological parameters on lava flow morphology inferred from numerical modelling, *Int J Earth Sci (Geol Rundsch)*, doi: https://doi.org/10.1007/s00531-025-02513-2

Abstract

The dynamics and morphology of lava flows are influenced by lava viscosity. However, the rheological parameters used in lava flow modelling are often subject to considerable uncertainties. To address this, we analyse the influence of key rheological parameters on the advancement and morphology of lava flows using GPUFLOW, a two-dimensional cellular automaton model that simulates Bingham fluid flow on the flanks of Mt. Etna. Our results demonstrate that variations in the initial volume fraction of crystals, the volume fraction of crystals in the equilibrium state, the characteristic time of crystal content growth (i.e., the relaxation time), the melt viscosity, and yield strength significantly impact lava flow patterns. An increased volume fraction of crystals – either at the time of eruption or in the equilibrium state – is associated with reduced advancement of the lava flow. This reduction is attributed to increased viscosity, which promotes vertical thickening of the lava flow and limits its lateral extent. In contrast, when relaxation times exceed the lava flow runout times, the crystal content evolves slowly, allowing the lava flow to advance further with a viscosity close to that of the crystal-free melt viscosity. Lower melt viscosity enhances lava flow mobility, whereas higher melt viscosity encourages shorter and thicker flows. Additionally, the slope of the volcano flank, yield strength, and melt viscosity influence the lava critical thickness, thereby exerting control over the extent of lava advance. These findings provide improved insights into the rheological controls on lava flow dynamics and have important implications for flow hazard assessment and forecasting of lava flows.

***Keywords*:** lava flow, morphology, crystallization, cellular automata

6.1 Introduction

Lava flows can seriously damage or even destroy living environments as happened in and around Catania, Sicily, during the eruption of Mt. Etna volcano in 1669 (Branca et al., 2013). Effusive volcanic eruptions yield to a variety of lava flow types depending on the chemical composition, degree of crystallization, and temperature of the erupted magma, the topography of the surface over which lava flows advance, and the effusion rate (e.g., Rowland & Walker, 1990; Griffiths, 2000; Castruccio & Contreras, 2016; Tsepelev et al., 2019).

Accurate modelling of lava flow behaviour depends on the ability to predict changes in lava rheology during the flow history (e.g., Harris, 2013). Numerical modelling plays a crucial role in understanding of the lava flow patterns, morphologies, and thermal evolution of lava flows (Costa & Macedonio, 2005b; Cordonnier et al., 2016; Tsepelev et al., 2019; Cappello et al., 2022; Ismail-Zadeh et al., 2023). Numerical modelling of lava flows serves as a foundation tool for researchers aiming to understand the complexities of volcanic phenomena and for decision-makers tasked with assessing volcanic hazards and developing mitigation strategies (Cappello et al., 2011; Harris et al., 2011; Centorrino et al., 2021). Existing lava flow-emplacement models vary widely, ranging from deterministic to stochastic/probabilistic approaches, and differ in the numerical methods and levels of physical complexity they incorporate (e.g., Cordonnier et al., 2015; Biagioli et al., 2023; and references therein).

Physics-based computational fluid dynamics software, such as OpenFOAM and Ansys Fluent, offer a detailed analysis of two- (2-D) and three-dimensional (3-D) numerical models of lava flows. While 3-D physics-based models are computationally expensive (e.g., Cordonnier et al., 2016; Tsepelev et al., 2020, 2021a; Zeinalova et al., 2021, 2024), meshless methods, such as smooth particle hydrodynamics (e.g., Hérault et al., 2011; Bilotta et al., 2016; Zago et al., 2018; Starodubtsev et al., 2023), can speed up computations of physics-based models of lava flows. Furthermore, physics-based models with depth-averaged variables provide a computationally efficient option compared to 3-D models (Costa & Macedonio, 2005b; Biagioli et al., 2023).

A cellular automata (CA) approach has also been used to model lava flow emplacement (e.g., Crisci et al., 1986; Barca et al., 1994; Avolio et al., 2006; Vicari et al., 2007; Cappello et al., 2016; 2022). The CA approach significantly simplifies depth-averaged numerical models and leads to rapid computations of lava flows. This approach allows for considering a lava flow as a dynamic system evolving in accordance with the local interactions of their constituent parts (e.g., Crisci et al., 1986). Hence, solving a set of differential equations governing the lava dynamics on a surface slope is replaced by the distribution of lava over a topographic grid (cells). The lava flows from one cell to its neighbouring cells according to the CA rules (e.g., Ishihara et al., 1990).

The rheology of lava flows is one of the main factors influencing lava flow dynamics (Harris, 2013). Lava has been considered to behave as a Newtonian or non-Newtonian (e.g., Bingham) fluid in numerical modelling. Many lava flow models use rheological parameters that are either constant during lava flow advancements or vary as a function of temperature (Chevrel et al., 2019). The objective of this paper is to investigate the influence of the following rheological parameters on lava flow morphology: the initial volume fraction of crystals, the volume fraction of crystals in the equilibrium state, the characteristic time of the crystal content growth (or the relaxation time), the melt viscosity without crystals, and the lava yield strength. These parameters play a significant role in shaping the behaviour of lava flows during effusive eruptions. Crystals within magma alter the rheological properties of the magma-crystals mixture, which in turn influences the eruption dynamics and subsequent lava flow advancements (Cashman & Blundy, 2000) Yield strength represents the minimum shear stress required to initiate viscous flow (Hulme, 1974), while pure melt viscosity quantifies the resistance to flow within a lava (Bilotta et al., 2012; Russell et al., 2022). The influence of rheological parameters on lava dynamics provides insight into the mechanisms driving lava flows, which in turn contributes to the refinement of quantitative approaches to volcanic hazard assessment (Bilotta et al., 2012).

In the following sections, we present the mathematical background for the flow of lava on an inclined plane. We then describe the GPUFLOW cellular automaton model used in this study and discuss the numerical approach to solve the model. Finally, we present the results of the numerical model and discuss how rheological model parameters influence the lava flow morphologies.

6.2 A model of lava flow and solution method

6.2.1 Lava flow on an inclined plane

Here, we present a mathematical model for the flow of lava on an inclined plane (e.g., Dragoni et al., 1986; Lister, 1992). The description of the theoretical background is based on the paper by Miyamoto & Sasaki (1998).

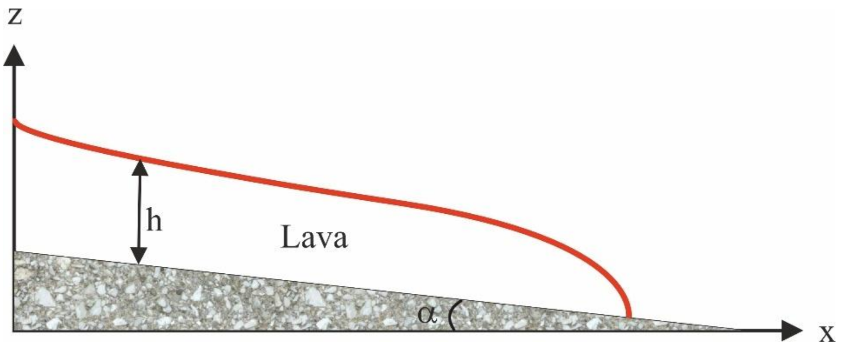

Figure 6.1: Sketch of lava flow advancement on an inclined plane; α is the slope angle of the plane, and h is the lava thickness.

A lava of thickness h flows with the velocity (u, 0) in the x direction (Figure 6.1). Gravity and the pressure gradient due to changes in the lava flow thickness drive the flow. It is assumed that (i) the lava dynamics is described by a laminar flow of an incompressible fluid, neglecting the vertical flow, and (ii) the lava viscosity is high enough so that the inertial terms in the Navier-Stokes equations can be ignored. In this case, the equation of motion can be reduced to the following expression of the Stokes equation:

$$\eta \frac{\partial^2 u}{\partial z^2} = \rho g \left(\sin\alpha - \frac{\partial h}{\partial x} \cos\alpha \right) \tag{6.1}$$

where η is the dynamic viscosity of the lava depending on the *x*-coordinate, ρ is the lava density, g is the acceleration due to gravity, *h* is the lava thickness, and α is the slope angle of the plane. We assume that the density of lava is constant, although it can change with lava crystallization and cooling as well as with the growth of bubbles in the solidifying lava (e.g., (Schmincke, 2004). The bubbles reduce the lava density, while both cooling and crystallization increase it (Kilburn, 2000). Equation (6.1) is considered with the boundary conditions: no-slip at the lava flow base $u = 0$ and no shear stress at the flow free surface $\partial u/\partial z = 0$.

6.2.2 Lava rheology

Lavas on Mt. Etna are considered to behave as a Newtonian fluid (Walker, 1967) or a non-Newtonian (Bingham) fluid (Robson, 1967). A Newtonian fluid starts to flow as soon as a force is applied, while a Bingham fluid begin to flow only if the applied force exceeds a threshold value (Vicari et al., 2007; Harris, 2013). The principal argument supporting a Bingham fluid as the lava rheology is that "a lava flow having the properties of a Newtonian fluid would continue to flow until no lava at all remained on the sloping surface" (Robson, 1967). Therefore, we assume in the modelling that lava behaves as a Bingham fluid, and the deviatoric strain rate $\dot{e}$ can be then determined as:

$$\dot{e} = \frac{\partial u}{\partial z} = \begin{cases} 0 & , \ \sigma \le S_y \\ (\sigma - S_y)/\eta, & \sigma > S_y \end{cases}, \tag{6.2}$$

where σ is the magnitude of the deviatoric shear stress, and S_y is the yield strength. The yield strength is assumed to be constant in the modeling, although it decreases with temperature (Ishihara et al., 1990). According to Eq. (6.2), the lava exhibits a plastic behaviour (no flow) until the maximum deviatoric shear stress reaches the yield strength value, and then it flows as a Newtonian fluid.

While the melt viscosity can be measured in laboratories as a function of temperature (e.g., Giordano et al., 2008), the effect of crystals on the lava viscosity is more difficult to quantify because the mixture of melt and crystals behaves as a non-Newtonian fluid (e.g., Chevrel et al., 2019; Tsepelev et al., 2020; Frontoni et al., 2022). Erupted magmas and lavas at Mt. Etna are degassed to a significant extent (e.g., Allard et al., 1991; Caltabiano et al., 2004), and degassing-induced crystallization leads to increasing the viscosity (e.g., Lipman et al., 1985). As the viscosity of lava should account for the melt viscosity and the effect of crystals, we assume the following relationship for the lava viscosity (Costa et al., 2009):

$$\eta = \eta_* \left(1 + \varphi^{\delta}\right) \left[1 - (1 - \xi) \cdot \operatorname{erf}\left(\frac{\sqrt{\pi}}{2(1-\xi)} \varphi (1 + \varphi^{\gamma})\right)\right]^{-B\phi_*} \tag{6.3}$$

where η_* is the melt viscosity assumed to be constant in this study; $\varphi = \phi / \phi_*$; ϕ is the volume fraction of crystals; ϕ_* (=0.591) is the specific volume fraction of crystals representing the critical solid fraction at the onset of the exponential increase of crystals; B (=2.5) is the Einstein coefficient's theoretical value; $\delta\ (= 7.24)$, $\xi\ (= 4.63 \times 10^{-4})$, and $\gamma\ (= 5.76)$ are the rheological parameters (Lejeune & Richet, 1995; Costa & Macedonio, 2005b), which may depend on the shear strain rate (e.g., Tsepelev et al., 2020), but, for simplicity, considered here to be constant. The volume fraction of crystals, depending on time *t* and spatial coordinate *x*, is determined from the evolutionary equation describing the simplified crystal content growth kinetics of degassing-induced crystallization (e.g., Tsepelev et al., 2020; Zeinalova et al., 2024):

$$\frac{\partial \phi}{\partial t} + u\frac{\partial \phi}{\partial x} = \frac{\phi_{eq} - \phi}{\tau}, \tag{6.4}$$

where ϕ_{eq} represents the volume fraction of crystals in the equilibrium state; τ is the relaxation time required to reduce the difference between the equilibrium (ϕ_{eq}) and actual (ϕ) values of the volume fractions of crystals by a factor of *e* with respect to the initial difference $\phi_{eq} - \phi_{in}$, where ϕ_{in} is the initial volume fraction of crystals in the magma (e.g., Tsepelev et al., 2020). At the static condition ($u = 0$), the relaxation time can be obtained analytically from Eq. (6.4) and the initial condition $\phi(t=0) = \phi_{in}$:

$$\tau = -t\left(\ln\frac{\phi_{eq} - \phi}{\phi_{eq} - \phi_{in}}\right)^{-1} \tag{6.5}$$

6.2.3 Critical thickness of lava flow and mass flow rate

In the model configuration (Figure 6.1), lava flows downward, and hence the shear stress is positive, reaching its maximum value on the lava bottom and its minimum value of zero on the free surface, as per the imposed boundary conditions. Integrating Eq. (6.1) and accounting for Eq. (6.2), we obtain:

$$\eta\frac{\partial u}{\partial z} = \begin{cases} \rho g(\sin\alpha - \frac{\partial h}{\partial x}\cos\alpha)(h - z) - S_y, & 0 < z < z_{cr} \\ 0, & z_{cr} \le z < h \end{cases}, \tag{6.6}$$

where z_{cr} is the lava thickness, at which the shear stress at the lava bottom equals the yield strength, i.e. $\rho g(\sin\alpha - \frac{\partial h}{\partial x}\cos\alpha)(h - z_{cr}) = S_y$, and hence

$$z_{cr} = h - \frac{S_y}{\rho g\left(\sin\alpha - \frac{\partial h}{\partial x}\cos\alpha\right)}, \tag{6.7}$$

We define

$$h_{cr} = \frac{S_y}{\rho g\left(\sin\alpha - \frac{\partial h}{\partial x}\cos\alpha\right)} \tag{6.8}$$

as the critical thickness, corresponding to the thickness of the unyielded region of the Bingham fluid (with a zero-strain rate) commonly known as the plug. If $h \le h_{cr}$, the lava cannot advance, because the shear stress at the lava bottom is smaller than the yield strength. As $h_{cr} > 0$, Eqs. (6.7) and (6.8) are valid only under the condition $\partial h/\partial x < \tan\alpha$.

Integrating Eq. (6.6) beneath the plug (between $z = 0$ and $z = z_{cr} = h - h_{cr} > 0$) and using the boundary condition u = 0 at the lava bottom, we obtain the velocity of the lava flow:

$$u(z) = \frac{1}{\eta}\left[\frac{1}{2}\rho g(\sin\alpha - \frac{\partial h}{\partial x}\cos\alpha)z(2h - z) - S_y z,\right] \quad 0 < z < h - h_{cr} \tag{6.9}$$

The velocity of the plug is obtained from Eqs. (6.8) - (6.9) as:

$$u_p = \frac{\sigma h}{2\eta}\left(1 - \frac{S_y}{\sigma}\right)^2, \quad z \ge h - h_{cr}. \tag{6.10}$$

The mass flow rate per unit length can be derived using Eqs. (6.8) - (6.10):

$$Q = \rho\int_0^h u(z)dz = \rho\frac{S_y h_{cr}^2}{3\eta}\left[\left(\frac{h}{h_{cr}}\right)^3 - \frac{3}{2}\left(\frac{h}{h_{cr}}\right)^2 + \frac{1}{2}\right] \tag{6.11}$$

Therefore, the mathematical problem of a lava flow advancement on an inclined plane is simplified, and its solution can be found from Eqs. (6.3), (6.4), (6.8) - (6.11).

6.3 GPUFLOW model and numerical method

In this study, we use the GPUFLOW model (Cappello et al., 2022), a modification of the MAGFLOW model (Vicari et al., 2007; Cappello, Hérault, et al., 2016) accounting for a parallel implementation on graphic processing units (Bilotta et al., 2011). Based on CA, the GPUFLOW model describes a flow of lava in a model domain (Figure 6.2) from one to another cell according to the mass flow rate (Eq. 6.11).

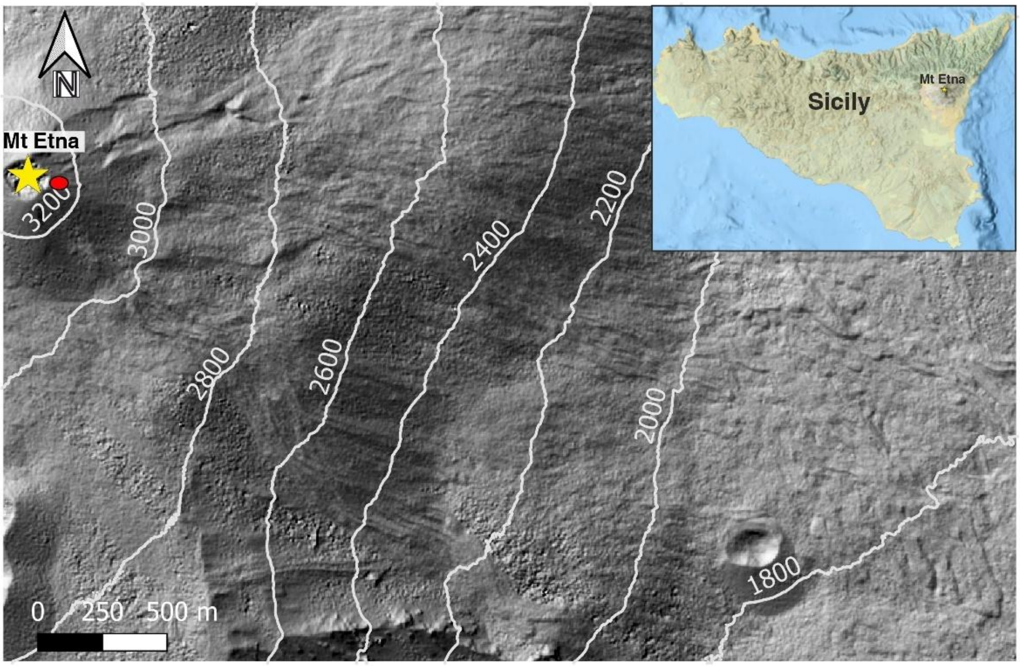

Figure 6.2: Digital elevation model of the south-east flank of Mt. Etna derived from high-resolution Pléiades satellite images acquired before the December 2015 Etna eruptions (data source: Ganci et al. 2019), illustrating elevation changes with 200-meter contour intervals. The red ellipse marks the location of the model vent, and the yellow star marks the location of the South-East Crater (SEC) of Mt. Etna. The top right inserts shows a map of Sicily (maps source: the Natural Hazards ArcGIS map on NOAA's GeoPlatform; https://www.ncei.noaa.gov/maps/hazards).

The model domain approximates the digital elevation model (DEM) of Mt. Etna volcano (Ganci et al., 2019) and is represented by horizontal cells of the size of $\Delta x \times \Delta y$, where Δx and Δy are the cell's length and width, respectively; it is assumed that $\Delta x = \Delta y = 5\ \mathrm{m}$. Each cell c contains the information about the ground elevation z_c, corresponding to the average value of the topographic height of the DEM's part bounded by the cell. The state of each cell is characterised by the lava thickness h_c and the crystal content ϕ_c of the lava. Some cells are marked as an eruptive vent with the prescribed effusion rate.

In the model, each cell interacts with its Moore neighbourhood (the eight adjacent cells in both the cardinal and main diagonal directions) allowing to assess the change in the lava thickness and its crystal content using discretized versions of Eqs. (6.4), (6.8), and (6.11). In the interaction of cell *c* with neighbouring cell *n*, the difference in the total height is computed as $\Delta z + \Delta h$, where $\Delta z = z_c - z_n$ and $\Delta h = h_c - h_n$. In the interaction between the cells, one of them is a giving cell *g* (that is, the cell from where lava flows out), and the other is the receiving cell *r* (that is, the cell to where lava flows in). The positive sign of $\Delta z + \Delta h$ determines that the flux is outgoing (i.e. flowing from cell *c* to cell *n*, and in this case, cells *g*=*c* and *r*=*n*), and the negative sign determines the incoming flux (i.e. flowing from cell *n* to cell *c*, and cells *g*=*n* and *r*=*c*).

The discretised critical thickness is obtained from Eq. (6.8) in the following form (Cappello, Hérault, et al., 2016):

$$h_{cr} \approx \frac{S_y \sqrt{\Delta z^2 + \Delta x^2}}{\rho g \left| \Delta z + \Delta h \right|}, \tag{6.12}$$

and the mass flux is computed by discretising Eq. (6.11) as:

$$q = \frac{S_y h_{cr}^2 \Delta x}{3\eta} \left(\left(\frac{h^*}{h_{cr}} \right)^3 - \frac{3}{2} \left(\frac{h^*}{h_{cr}} \right)^2 + \frac{1}{2} \right). \tag{6.13}$$

where $h^* = h_g$ is the lava thickness of a giving cell, if the ground elevation of the giving cell z_g is greater than that of the receiving cell z_r (i.e., $z_g \geq z_r$), and $h^* = h_g - (z_r - z_g)$, if $z_g < z_r$ (Cappello, Hérault, et al., 2016).

The current amount of lava gained or lost by a cell at the end of each time iteration of the CA is determined by the total mass flux of the cell *c*, q_{tot}^c, multiplied by the time step Δt. The total mass flux q_{tot}^c is computed by adding the prescribed eruption flux from a vent at the given time q_V^c, if the cell corresponds to the vent (otherwise $q_V^c = 0$), and the sum of all cross-cell fluxes $q_{c,n}$ computed using Eq. (6.13):

$$q_{tot}^c = q_V^c + \sum_{n_i} n_i q_{c,n} - \sum_{n_o} n_o q_{c,n}, \tag{6.14}$$

where the summation on n_i refers to all neighbouring cells, from which lava flows into the current cell c (incoming flow); and the summation on n_o refers to all neighbouring cells that receive lava from the current cell c (outgoing flow).

If the total mass flux of cell c is negative, the time step Δt^c is constrained so that each cell with the negative total mass flux will not lose more lava than it has received during the time step:

$$\Delta t^c < \kappa h(\Delta x)^2 / \left| q_{tot}^c \right| \tag{6.15}$$

where κ ($0 < \kappa < 1$) is a constant; in the modelling, we used $\kappa = 1/16$ (Bilotta et al., 2012). This constraint on the time step ensures that the total amount of mass flowing to and out of a cell in a single time step does not lead to non-physical results (e.g., a negative value of the lava thickness in a cell). For cells that have a positive flux, the time constraint (Eq. 6.15) is not required, and a fixed time step $\Delta t_{\max}$ is prescribed (in our case, $\Delta t_{\max} = 1$ s). The actual time step used by the CA is chosen as the minimum of the time steps computed for all the cells (Vicari et al., 2007; Bilotta et al., 2012):

$$\Delta t = \min\left(\Delta t_{\max}, \min_{\text{all cells}}\left[\kappa h(\Delta x)^2 / \left| q_{tot}^c \right|\right]\right) \tag{6.16}$$

At the initial state, the thickness of lava at each cell is set to zero, and the lava flow originates from the cells corresponding to the vent. As lava is extruded, its thickness at the vent cell gradually increases. Once this thickness surpasses the critical threshold h_{cr} (Eq. 6.12) and the basal stress exceeds the yield strength, lava begins to flow to neighbouring cells.

The lava crystal content in a cell is considered uniform. Equation (6.4) is integrated considering separately the advective and other terms of the equation. The advective contribution ($u\,\partial\phi/\partial x$) accounts for the change in the crystal content due to the incoming and outgoing mass fluxes. Hence the lava crystal content ϕ_t^c of cell c at time t is updated as

$$\phi_*^c = \left(\phi_t^c h_t^c + \frac{\Delta t}{(\Delta x)^2}\left[\sum_{n_i} q_{c,n_i}\phi_t^{n_i} - \sum_{n_o} q_{c,n_o}\phi_t^c\right]\right) \Big/ h_{t+\Delta t}^c \tag{6.17}$$

where the summations on n_i and n_o are the same as in Eq. (6.14). The final value for the crystal content of the lava in cell c at the new time, $t + \Delta t$, is then obtained integrating implicitly the time-dependent part of Eq. (6.4) and using ϕ_*^c (Eq. 6.17) as approximation for the crystal content at time *t*:

$$\phi_{t+\Delta t} = \frac{\tau\phi_*^c + \Delta t\phi_{eq}}{\tau + \Delta t} \qquad (6.18)$$

with the resulting value clamped to the range [ϕ_{in}, ϕ_{eq}].

The GPUFLOW model involves the following steps, each of which can be executed independently for each cell: (i) compute the cross-cell lava flux with the neighbouring cells (Eq. 6.14) and the time step (Eq. 6.15); (ii) find the minimum time step among the computed time steps related to the neighbouring cells and choose it for making an update (Eq. 6.16); and (iii) update the state of the cell according to the chosen time step, that is, compute the updated thickness (Eq. 6.13-6.14) and the crystal content (Eq. 6.17-6.18) of the lava. The simulation time is updated at the end of each time step (Bilotta et al., 2011, 2012; Rustico et al., 2011; Cappello).

6.4 Results

In this section, we present the results of the numerical analysis performed to investigate how changes in the rheological model parameters – the volume fraction of crystals in the equilibrium state (ϕ_{eq}), relaxation time (τ), melt viscosity (η_*), initial volume fraction of crystals (ϕ_{in}), and yield strength (S_y) – influence lava flow morphology. These numerical experiments provide insights into the effects of the rheological parameters on the length, thickness, and pattern of the lava flows. The eruptive vent is modelled as a circle area with the radius of 30 m, which is approximated by 113 cells. The location of the modelled vent is chosen in such a way as to mimic the lava flow associated with the December 2015 eruption. In all the experiments, the discharge rate is constant and set to 20 m^3 s^{-1}, which is within the range of the discharge rates of historical eruptions at the flanks of Mt. Etna (Wadge, 1978). For each numerical experiment, we chose to stop the set of simulations at the time when the flow reaches the boundary of the domain in at least one simulation within the set. Table 6.1 lists the values of the rheological model parameters used in each experiment.

In the modelling, the yield strength S_y is considered to range from 10^3 Pa to 10^4 Pa in agreement with the values used in analytical or numerical lava flow modelling on Mt. Etna (e.g., 1.25×10^3 Pa; Cappello et al., 2022; 2.5×10^5 Pa; Robson, 1967). We consider three values of the melt viscosity (10^3 Pa s, 10^4 Pa s, and 10^5 Pa s), which fall within the range of the viscosities from 4×10^3 Pa s to 1.5×10^6 Pa s determined by Walker (1967). The relaxation time ranges from 12 hours to 10 days. The initial crystallinity is considered to be 0.1 (Frontoni et al., 2022) in all experiments except set 1 of experiments, where it varies from 0 to 0.3. The volume fraction of crystals in the equilibrium state is considered to be 0.63 (in an agreement with the crystallization models for lavas at Mt. Etna; Campagnola et al., 2016) in all experiments except set 3 of experiments, where the parameter takes in addition the values of 0.43 and 0.83. We consider that $\rho = 2500$ kg m^{-3} and $g = 9.81$ m s^{-2}. (Hereinafter, we refer to ‘set N of experiments’ as ‘experiments N’.)

Experiments 1. We study the influence of the initial volume fraction of crystals (ϕ_{in}) and the relaxation time (τ) on the lava flow advancement considering three values for ϕ_{in} (0.1, 0.2, and 0.3) and four values for τ (0.5, 1, 2, and 10 days). The melt viscosity, the yield strength, and the volume fraction of crystals in the equilibrium state remain constant throughout the experiments (see Table 6.1 for the values of the model parameters).

Figure 6.3 illustrates that, as ϕ_{in} increases leading to the higher lava viscosity, the flow pattern changes from longer to shorter lava advancements accompanied by an increase in the thickness of lava flows (Figure 6.4). According to Eq. (6.11), the lava thickness grows with the lava viscosity for the prescribed mass flow rate, yield strength, critical thickness of lava, and lava density. In the case of a Newtonian fluid, the flow would be also thicker with the higher viscosity (according to the height scale $3\eta Q_{dis}/(\rho g \cos\alpha)$ of a viscous gravity current on an inclined plane for the prescribed discharge rate Q_{dis} and density; Lister, 1992).

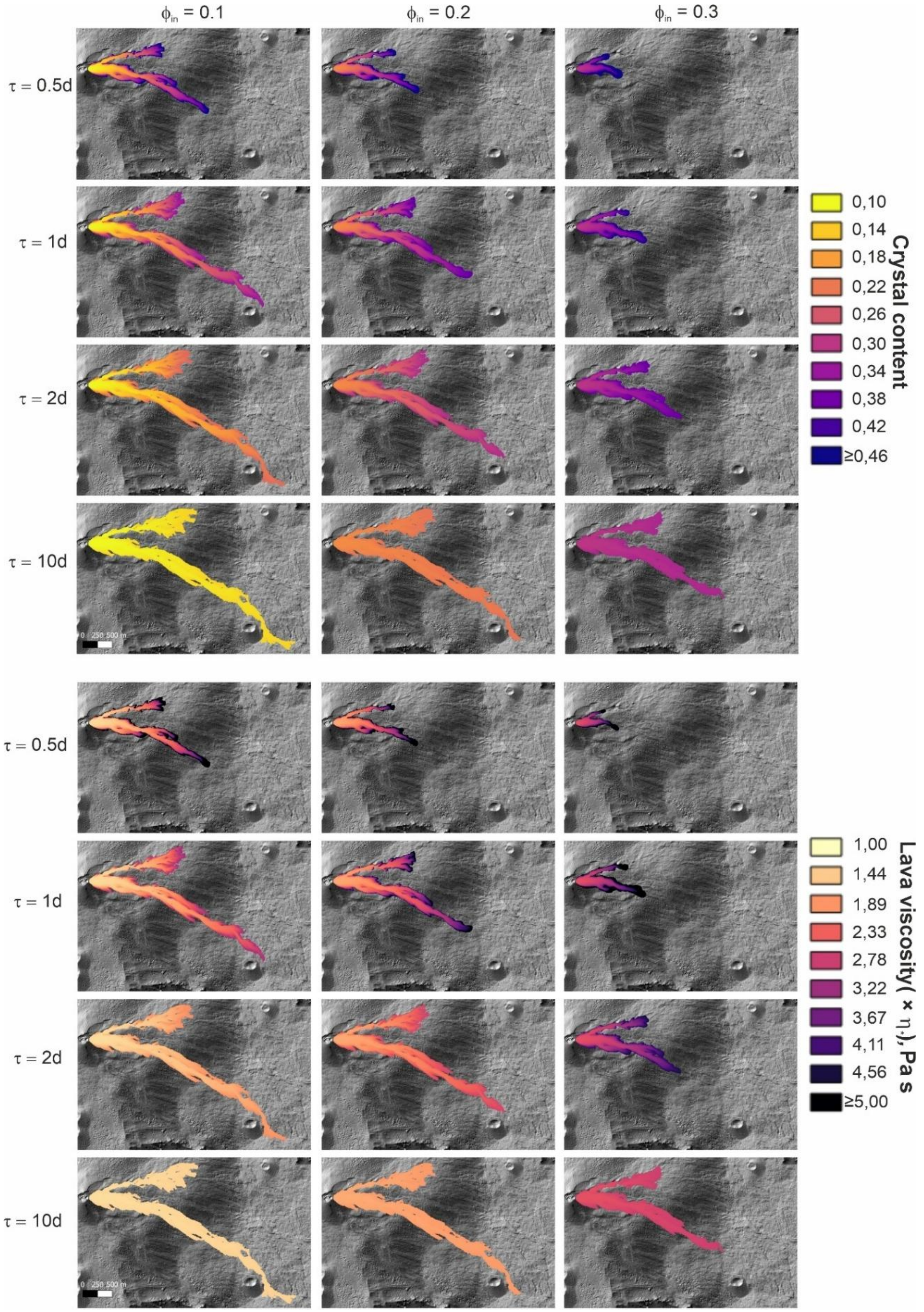

Figure 6.3: Modelled crystal content and viscosity of the lava flow in experiments 1 after 15 hours of lava advancement. The bifurcation of the lava flow into two branches (here and in other numerical experiments) is associated with a ridge between two valleys on the volcano flank near the model vent.

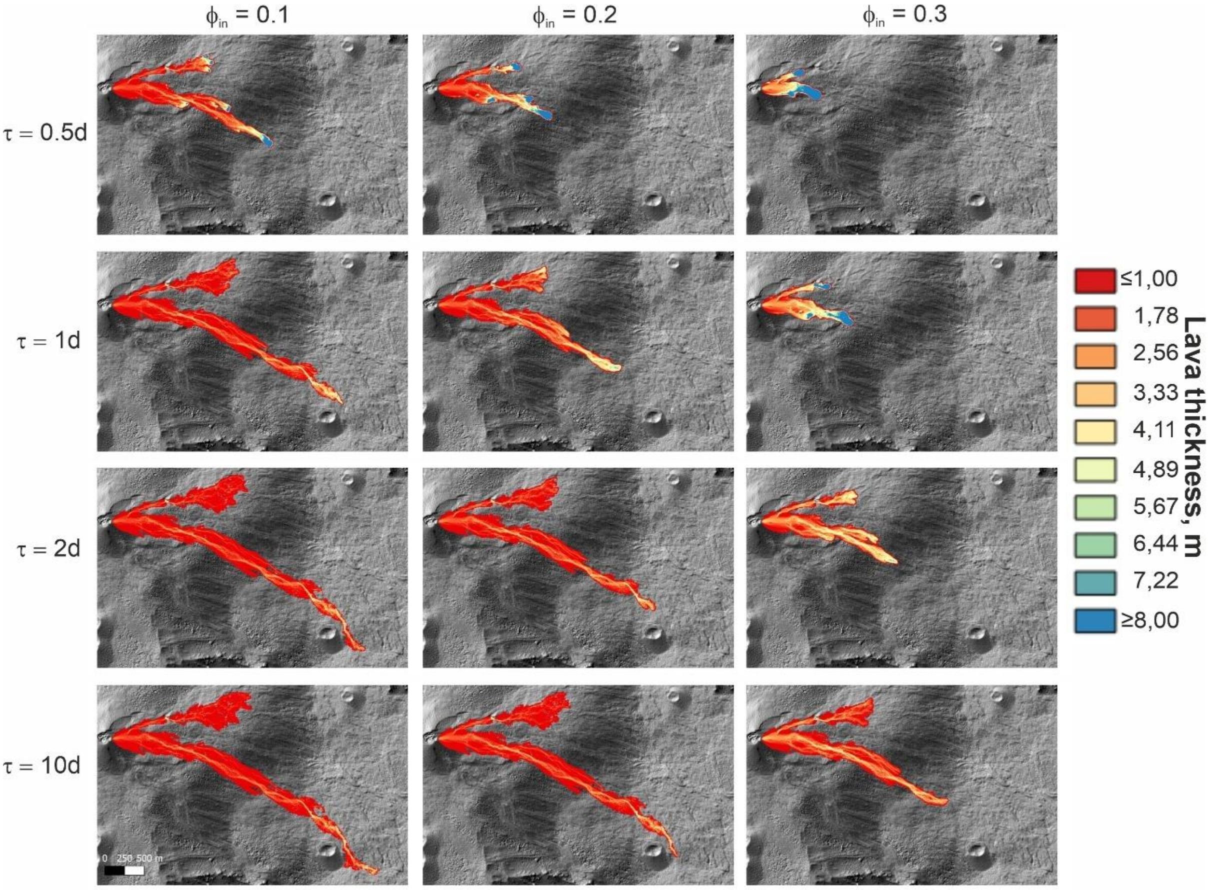

Figure 6.4: Modelled lava thickness in experiments 1 after 15 hours of lava advancement.

The duration of our numerical simulations, covering 15 hours (the runout time) of lava flow, has prompted an initial investigation into the effects of a short τ (0.5 and 1 day) on lava flow morphology. This choice enables observation of the impact of the relaxation time on lava flow behaviour. A shorter relaxation time results in more rapid crystal content growth, higher viscosity (Figure 6.3), and hence a reduced rate of lava advancement. As seen in the experiments, lava crystallizes at the marginal zones (edges and tips) of the advancing flows and contains a stream of less crystalised lava. This resembles natural lava flow features observed on Mt. Etna (e.g., Sparks et al., 1976; Harris et al., 2009). The consistency between simulated and observed features of lava flows highlights the importance of incorporating variations of τ in lava flow simulations to accurately model the complexities of lava dynamics.

For cases characterized by heightened initial volume fractions of crystals (ϕ_{in} = 0.2, 0.3), noticeable differences appear when comparing experiments conducted with shorter and longer relaxation times (Figure 6.3). At short relaxation time ($\tau = 0.5$ day) and ϕ_{in} = 0.3, the crystal content and viscosity of the lava flow increase rapidly during the lava flow runout time, and this results in the development of a short and thick lava flow. At a longer relaxation time (e.g., 2 days), the lava flow runout time should increase by a factor of four (to 60 hours) to get the same volume fractions of crystals as in the case of $\tau = 0.5$ and the runout time of 15 hours (according to Eq.6.5 in the static case). Hence, at $\tau \geq 2$ days, the crystal content (and the viscosity) grows insignificantly for 15 hours compared to the shorter relaxation times.

In the cases of τ = 0.5-1 day, the thickness of the lava reaches more than 8 m (Figure 6.4). At larger relaxation times (e.g., $\tau = 10$ days and ϕ_{in} = 0) compared to the runout time, the lava flows over the distance of about 3,500 m with an average velocity of 230 m h^{-1}. The modelling results show that in the cases of low initial values of the crystal content (e.g., 0 or 0.1) and longer relaxation time (10 days), the lava viscosity is close to the melt viscosity as the crystal content grows slowly compared to the cases of shorter relaxation times (Figure 6.3, lower left corner).

Experiments 2. We present here the results of the numerical experiments related to the influence of the melt viscosity (η_*) and the relaxation time (τ) on the morphological shapes of lava flows. We consider three values for η_* (10^3, 10^4, and 10^5 Pa s) and two values for τ (1 and 5 days) in the experiments. The initial volume fraction of crystals, the yield strength, and the volume fraction of crystals in the equilibrium state remain constant (Table 6.1).

The melt viscosity alters the length and the thickness of the lava flow (Figure 6.5). A lower melt viscosity (10^3 Pa s) facilitates a longer lava flow: the lower branch of the flow advances horizontally along the slope up to 3700 m for 2.7 hours (the lava flow runout time). A higher melt viscosity (10^5 Pa s) leads to short lava flows extending only up to 1000 m for the same runout time. With an increase in τ (from 1 day to 5 days), the crystallization process retards resulting in a slower rise in the lava viscosity (Figure 6.5). At $\eta_* = 10^3$ Pa s and $\tau = 5$ days, the crystal content and the lava viscosity do not change considerably compared to the initial crystal content and the melt viscosity, because the lava flow runout time is much shorter than the relaxation time. Hence, the length and the thickness of the lava flow do not change significantly with the increase in τ. With a higher η_* (10^5 Pa s), the lava becomes thicker, primarily in the centre and along the edges of the flow (Figure 6.5).

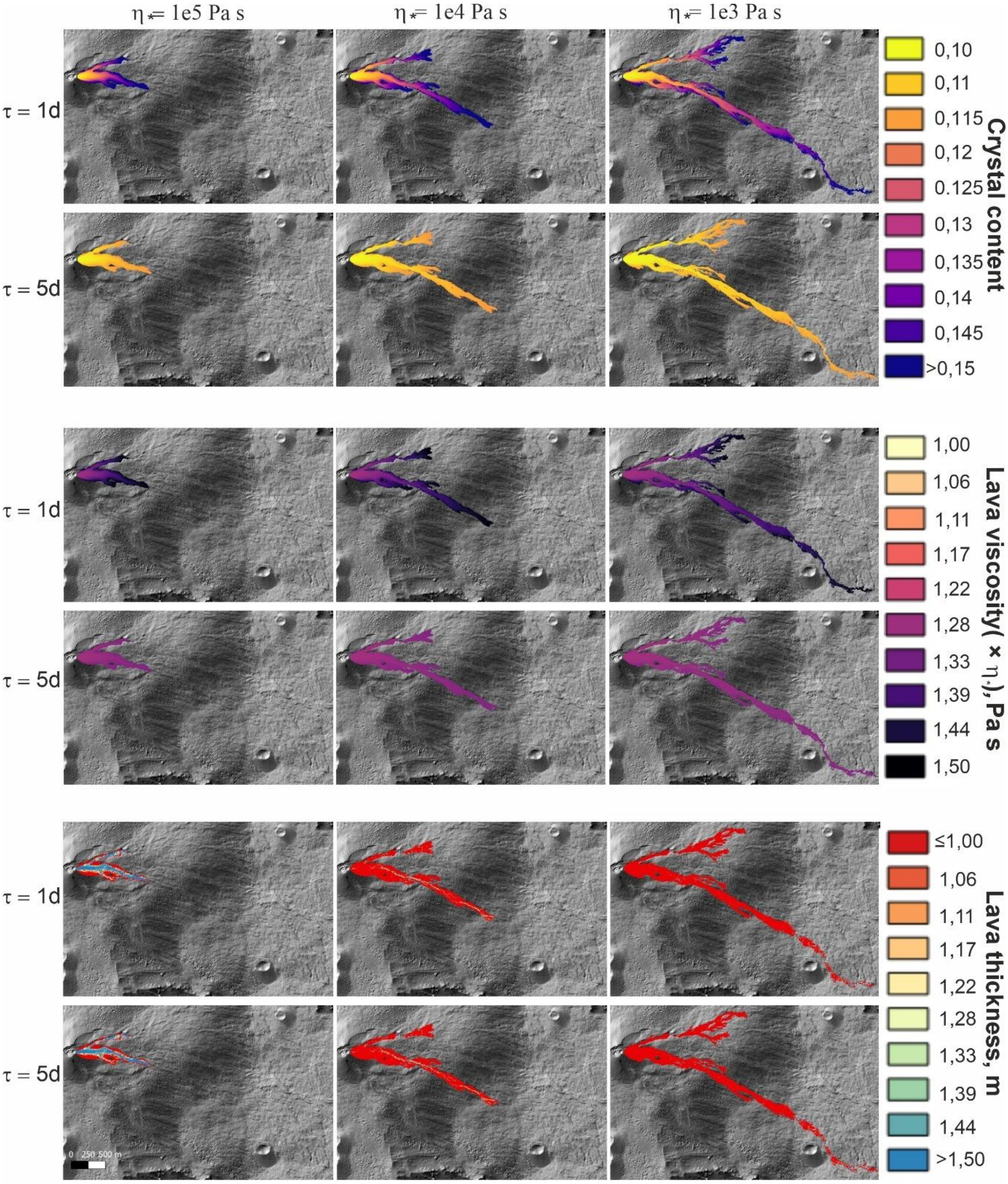

Figure 6.5: Modelled crystal content, viscosity and thickness of the lava flow in experiments 2 after 2.7 hours of lava advancement.

Experiments 3. This set of experiments addresses the interplay between two parameters: the volume fraction of crystals in the equilibrium state ϕ_{eq} (values 0.43, 0.63, and 0.83 are considered in the modelling) and the relaxation time τ (1 and 5 days). We study the influence of the parameters on the morphology of lava flows. The initial volume fraction of crystals, the yield strength, and the melt viscosity remain constant throughout the experiments (Table 6.1). The lava flow runout time is 17 hours.

At $\tau = 1$ day and the high value of $\phi_{eq} = 0.83$, the crystal content grows rapidly, especially along the flow's periphery, compared to the cases of lower values of ϕ_{eq} (Figure 6.6). The lava becomes less viscous at the centre of the flow (1.44×10^5 Pa s) and more viscous at its edges (5×10^5 Pa s). The branches of the lava flow thicken in their centres and fronts, with the maximum thickness reaching about 8 m at the front of the lower branch. At the lower value of ϕ_{eq} (0.63 and 0.43), the crystal content and the viscosity decrease, and the lava flow advances further down the slope of the volcano flank. However, in the case of the longer relaxation time ($\tau = 5$ days) compared to the runout time, the difference in the lava morphology (in the length and thickness of lava flows) is insignificant when lowering ϕ_{eq} from 0.83 to 0.43 (Figure 6.6). This occurs because both crystal content (from 0.1 to 0.2) and lava viscosity (from 1.44×10^5 Pa s to 1.88×10^5 Pa s) increase gradually over extended relaxation times that exceed the timescale of lava flow runout.

Experiments 4. We examine the effect of variations in the yield strength (S_y) and the melt viscosity (η_*) on the morphology of lava flow, considering two values for S_y (10^3 Pa and 10^4 Pa), and three values for η_* (10^5 Pa s, 10^4 Pa s, and 10^3 Pa s). The relaxation time, initial volume fraction of crystals, and the volume fraction of crystals in the equilibrium state remain constant throughout the experiments (Table 6.1). The lava flow runout time is set to be 2.7 hours.

Figure 6.7 shows that the yield strength has a notable impact on the lava flow pattern when its higher values are considered, particularly in the presence of lava with lower melt viscosity. For example, at $\eta_* = 10^4$ Pa s, the length of the lava flow reduces in its lower branch (from 2,000 m to 1,100 m) and advances in its upper branch (from 1,100 m to 1,300 m) as the yield strength increases from 10^3 Pa to 10^4 Pa. A profound shift occurs at the lower value of $\eta_* = 10^3$ Pa s, where the upper branch becomes the longest (increasing from 1,700 m to 2,500 m) while the lower branch exhibits small advancement (decreasing from 3,600 m to 500 m) (Figure 6.7, the lower row).

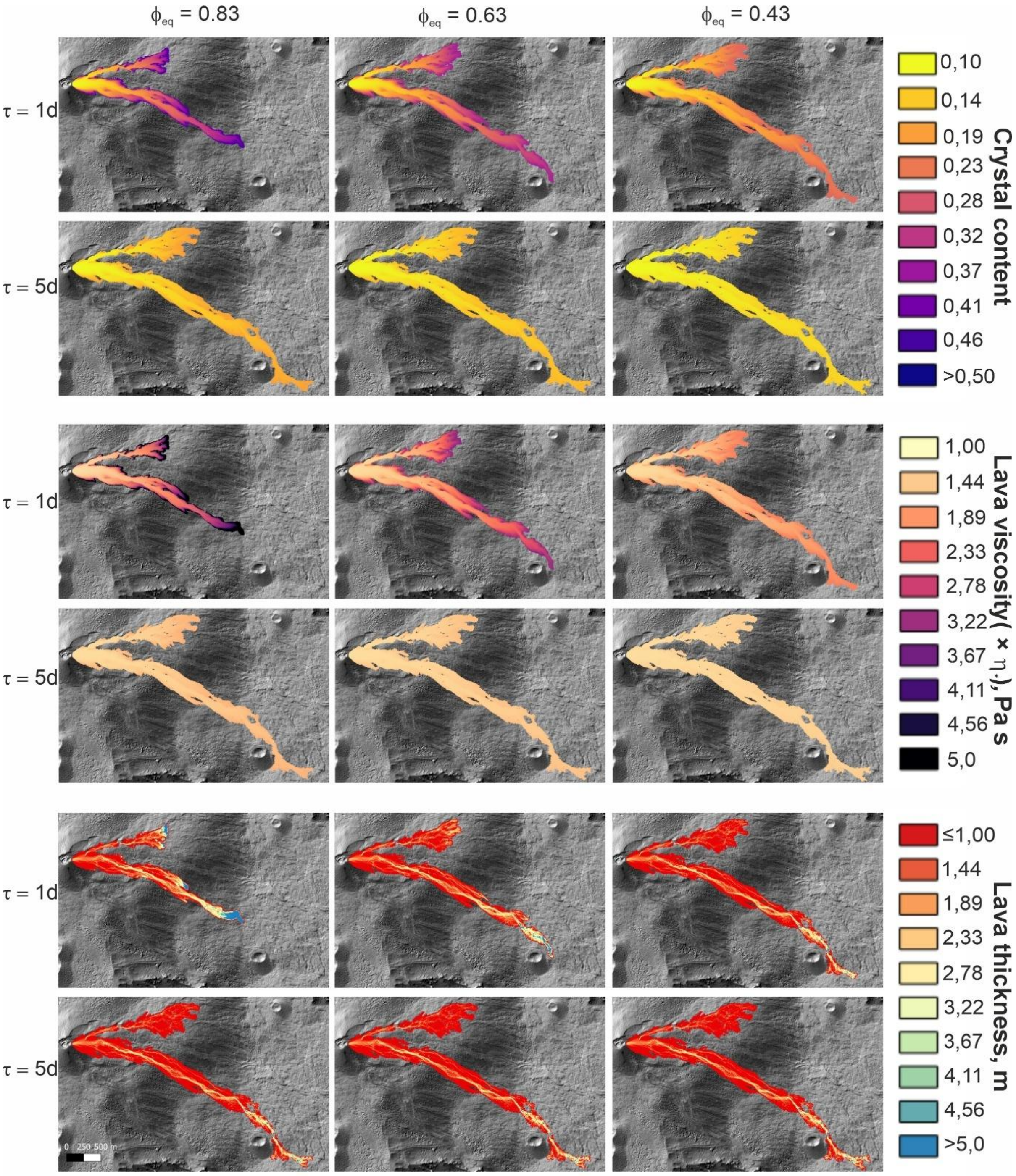

Figure 6.6: Modelled crystal content, viscosity and thickness of the lava flow in experiments 3 after 17 hours of lava advancement.

To get a detailed insight into the modelled lava flow dynamics revealed in exp. 4, we conduct additional experiments 4a, in which the yield strength increases from $10^{3.3}$ Pa to $10^{3.9}$ Pa (the aim of these experiments is to find out more details about the change in the lava flow pattern obtained in exps. 4). The relaxation time, the initial volume fraction of crystals, the melt viscosity, and the volume fraction of crystals in the equilibrium state remain constant throughout the experiments (Table 6.1). A significant alteration in the lava flow pattern occurs when the yield strength reaches a value of $10^{3.7}$ Pa (Figure 6.8). Prior to this threshold, the lower branch of the lava flow is longer than the upper branch. However, as the yield strength rises to $10^{3.7}$ Pa, the upper and lower branches reach approximately the same length. Subsequently, with a further increase in the yield strength, the upper branch becomes longer, while the lower branch shortens (Figure 6.8).

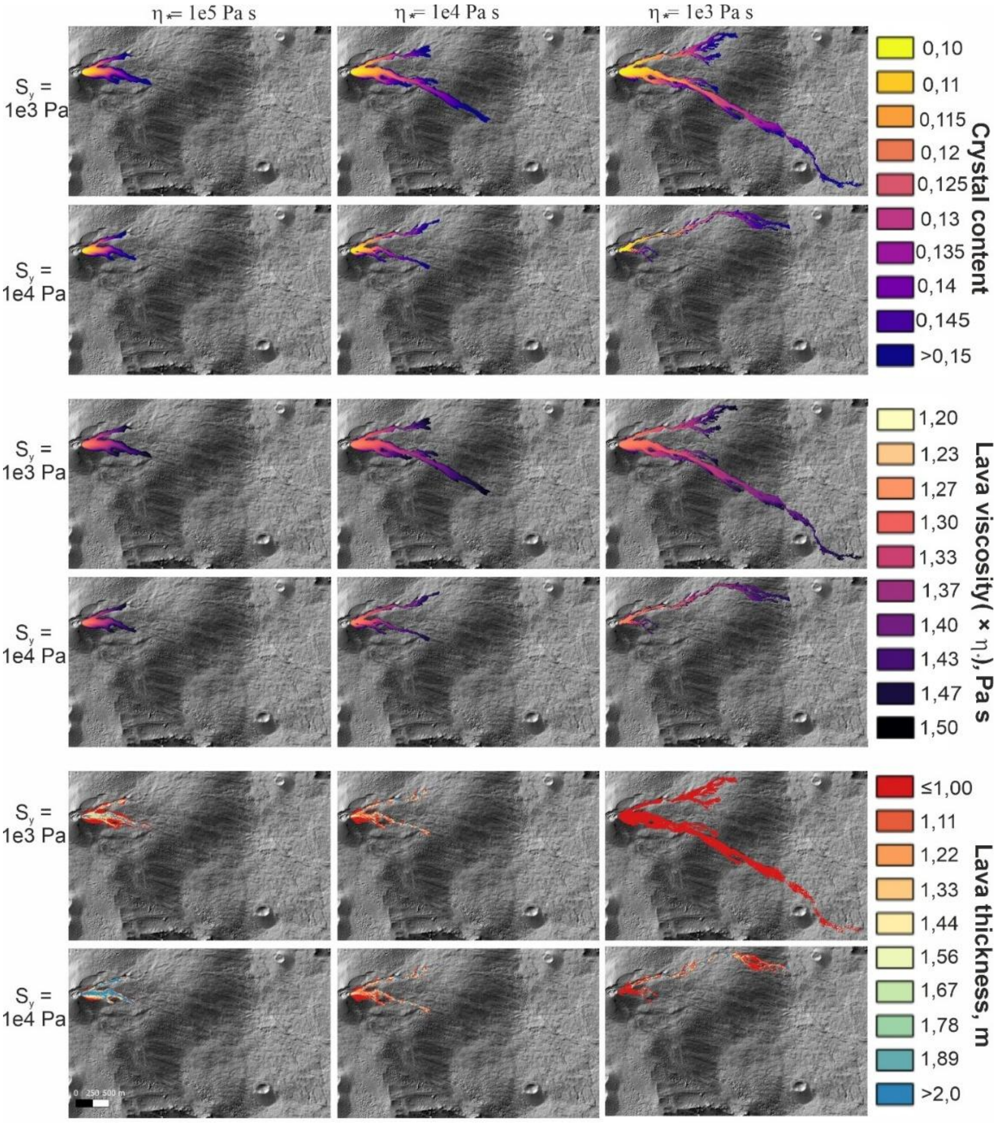

Figure 6.7: Modelled crystal content, viscosity and thickness of the lava flow in experiments 4 after 2.7 hours of lava advancement.

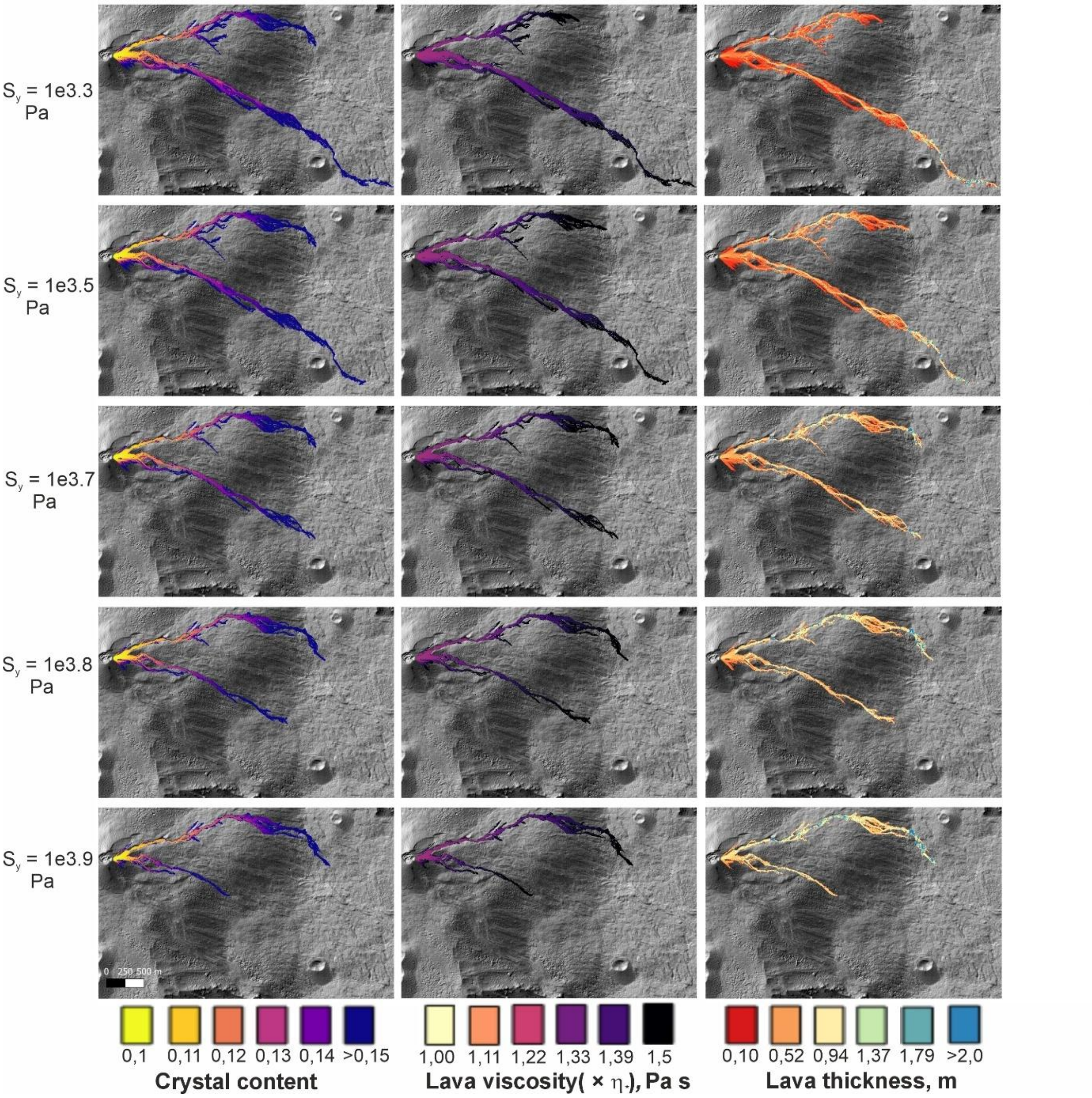

Figure 6.8: Modelled crystal content, viscosity and thickness of the lava flow in experiments 4a after 2.7 hours of lava advancement.

The flow alteration can be related to the critical thickness of a lava flow. According to Eqs. (6.8) and (6.11), the critical thickness grows linearly with the yield strength. A raise of the yield stress by a factor of 10 (from 10^3 to 10^4 Pa) leads to the increase of the critical thickness by the same factor, from 0.4 m to 4 m at the slope angle $\alpha = 0$ and from 0.146 m to 1.46 m in the case of $\alpha = 10^\circ$ (Figure 6.9). With the increase of the yield strength, the more time is needed to reach the critical thickness and to allow for a lava flow advancement. Therefore, a combined effect of the changes in the yield strength and in the slope angle of the volcano flank influence the critical thickness of the lava and results in a change of the flow pattern as illustrated in Figure 6.7 and Figure 6.8.

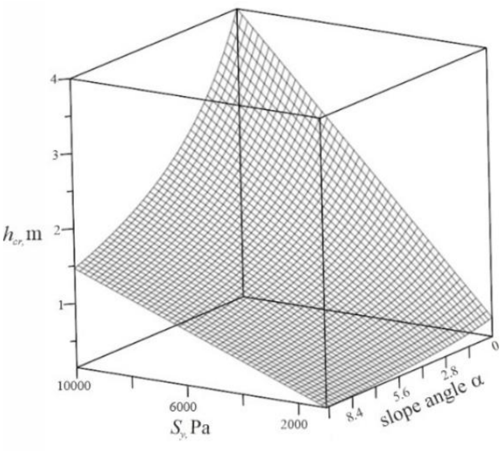

Figure 6.9: Critical thickness of lava (h_{cr}) as a function of the yield strength (S_y) and the slope angle of the volcano flank (α). The critical thickness is calculated using Eq. (6.8), where $\partial h/\partial x$ assumed to be -0.1.

Table 6.1: Numerical experiments and their model parameters.

Exps. No.	Relaxation time τ , days	Initial volume fraction of crystals ϕ_{in}	Melt viscosity η_* , Pa s	Yield strength S_y , Pa	Volume fraction of crystals at the equilibrium state ϕ_{eq}
1	0.5, 1, 2, and 10	0.1, 0.2, and 0.3	10^5	10^3	0.63
2	1 and 5	0.1	10^3, 10^4, and 10^5	10^3	0.63
3	1 and 5	0.1	10^5	10^3	0.43, 0.63, and 0.83
4	1	0.1	10^3, 10^4, and 10^5	10^3 and 10^4	0.63
4a	1	0.1	10^3	$10^{3.3}$, $10^{3.5}$, $10^{3.7}$, $10^{3.8}$, and $10^{3.9}$	0.63

6.5 Discussion

In this study, we have systematically investigated the effects of the rheological parameters – the initial volume fraction of crystals, the volume fraction of crystals in equilibrium state, the relaxation time of crystallization, the melt viscosity, and the yield strength – on lava flow dynamics and morphology. Our experiments have shown how variations in these parameters impact the length, the thickness, and the pattern of lava flows.

A higher initial volume fraction of crystals produces thicker and shorter flows. A shorter relaxation time accelerates crystal content growth, which in turn increases the viscosity and thickness of lava flows. Meanwhile, a longer relaxation time leads to a longer time of crystallisation for the same lava flow runout time, promoting the flow advancement over a longer distance. A lower melt viscosity facilitates a longer lava flow, while a higher melt viscosity restricts the flow advancement. Additionally, at higher values of the volume fraction of crystals in the equilibrium state and shorter relaxation times compared to the lava flow runout time, the crystal content grows faster, especially along the periphery of the lava flow, leading to lava flow shortening. Higher values of the yield strength increase the critical thickness of the lava (acting as a Bingham fluid) and result in alterations of the lava flow advancements. Although the slope angle of the volcano flanks plays a pivotal role in determining the direction and pattern of lava flow, the numerical results show that the yield strength can significantly influence the lava flow morphology.

While this study provides valuable insights, further investigations are needed to refine our understanding of lava flow dynamics, and to explore the complex interactions between coupled processes. It is also important to acknowledge the limitations and uncertainties of this study based on a simplified model and assumptions. Natural lava flow advancements are influenced by many factors, including variations in terrain, the lava's physical and rheological properties, and external environmental conditions. Some of these parameters may change rapidly during an eruption modifying the lava flow behaviour.

This study does not consider the effect of temperature or the bubble's content on lava dynamics. Cooling along with crystallization influence the rheological properties of lava (Harris, 2013; Zeinalova et al., 2024), and the melt viscosity can vary significantly with temperature (Russell et al., 2022). The presence of bubbles also impacts lava flow viscosity and its dynamics (e.g., (Crisp et al., 1994; Manga et al., 1998; Harris, 2013). While in this work we assume constant values for the yield strength, this parameter depends on temperature and crystallinity, which would further alter lava viscosity (Chester et al., 1985; Harris, 2013). Although the present model could be modified to include a temperature-dependent rheology of the lava or bubble growth, the results of this analysis provide insight into lava flow morphological alterations with the changes in crystallization, melt viscosity, and yield strength. The knowledge gained during this study can be used in lava flow hazard assessments.

Lava flows may cause significant damage affecting the populations and infrastructure in the vicinity of Mt. Etna (e.g., Guest & Murray, 1979; Behncke et al., 2005). Numerical simulations of potential lava flow paths combined with the frequency of eruptions and a probability of a vent opening at Mt. Etna assist in a quantitative hazard assessment (Del Negro et al., 2013). Based on observed/historical data on the morphology of lava flows at Mt. Etna (or elsewhere), numerical models can assess a range of the rheological parameters, which provide the best fit between modelled and observed flow morphologies.

For example, a lava flow emplacement after 48 h of the onset of the 2015 December eruptions at Mt. Etna (Ganci et al., 2019) is compared (in Figure 6.10) with the results of a lava flow simulation. Although this model does not match the observed volume of the lava emplacement precisely (because of the different discharge rates in the model and natural cases), the morphologies of the observed and modelled lava flows show similar features. By using the model rheological parameters as tuning variables as well as the data on the observed discharge rates and the precise vent location, it would be possible to numerically approximate a natural lava flow by the modelled flows. The comparison (Figure 6.10) provides a tool for assessments of the range of rheological parameters of the lava flow model, which yield to a morphological shape similar to that observed at Mt Etna. This approach will help to develop a series of numerical experiments accounting for potential vent locations and the range of the model parameters to provide more information for developing lava flow hazard maps.

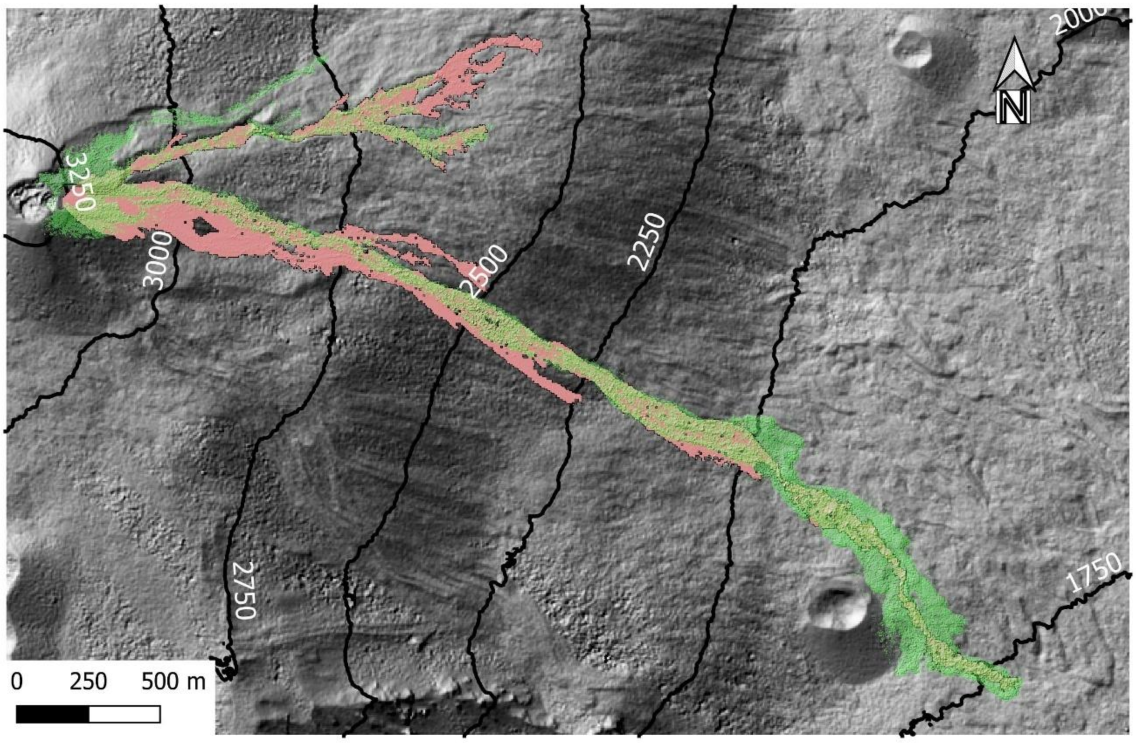

Figure 6.10 Morphological shapes of the modelled lava flow emplacement (in pink) and the lava flow formed after the 2015 December eruptions at Mt. Etna (in green; Ganci et al. 2019). In the numerical experiment, the following model parameters have been used: τ = 1 day, ϕ_{in} =0.2, $\eta_* = 10^3$ Pa s, $S_y = 10^3$ Pa, ϕ_{eq} = 0.43, $q_V^c = 20$ m^3 s^{-1}, and the runout time is 2.7 h.

6.6 Concluding remarks

The results of the numerical modelling can be applied to constrain the evolution of natural lava flows with varying discharge rates and to assess lava rheology based on observations of lava flow morphology. Understanding the mechanisms that influence the dynamics, crystallisation and solidification of lava flows, and hence their flow morphology is essential for forecasting lava flow advancement. Numerical experiments that simulate the flow of lava on the flanks of Mt. Etna with varying rheological parameters provide an insight into lava dynamics and flow morphology. This study provides new knowledge on the dynamic characteristics of lava flows, which is important for lava flow hazard assessment (e.g., Harris, 2015), and disaster risk reduction (e.g., Cutter et al., 2015) .

6.6.1 Authors contribution

AIZ, GB, and NZ (a PhD student) contributed to the conceptualization of the paper. NZ processed the data, developed a numerical model and performed numerical experiments. AIZ and GB supervised the study and assisted NZ in numerical modelling and data processing. GB contributed to the development of numerical codes, and AC and GG helped in designing the sets of tests to run and in analysing the DSM data. AIZ, FS, GB, and NZ contributed to interpretation of the results. AIZ, GB and NZ performed writing–original draft preparation and figures. All co-authors performed writing–review and editing.

Acknowledgments: The research was done in the framework of the cooperation agreement between INGV and KIT. Partial financial support from the Deutsche Forschungsgemeinschaft is acknowledged. We are grateful to the editor-in-chief Ulrich Riller, Alexander Cruden, and two reviewers for their constructive and detailed comments, which improved the initial manuscript. NZ thanks Francesco Zuccarello for his assistance with the GPUFLOW software.

Competing Interests: The authors have no competing interests to declare that are relevant to the content of this article.

Chapter 7: Influence of rheology on lava flow advancement and its morphology

This chapter is based on the manuscript in preparation "Influence of rheology on lava flow advancement and its morphology" by Natalya Zeinalova[1], Igor Tsepelev[2], Alik Ismail-Zadeh[1] to be submitted to JGR Earth Surface.

Abstract

Using numerical modelling, we study the influence of lava rheology (namely, Newtonian, Bingham, and Herschel-Bulkley fluids) on lava flow advancement and its morphology. Numerical simulations were conducted using a three-dimensional fluid dynamics model as well as its simplified depth-averaged model based on the shallow water approximation. In the case of isothermal flow models, we have shown that increased yield strength significantly influences lava flow morphology by restricting flow advance and promoting upward growth of lava flows. In the case of temperature-dependent rheological models, the Newtonian and Bingham fluids demonstrate similar lava flow morphologies and thickness distributions. The viscosity values in both cases vary from about $10^{2.7}$ – 10^6 Pa s across the central part of the lava flow to about 10^{12} Pa s near the lava flow margins. The Herschel-Bulkley model exhibits the viscosity values of 10^9 Pa s within the flow and reaches the highest viscosity values, up to 10^{16} Pa s along the periphery of the flow, resulting in the shortest lava flow. Comparing the results between the isothermal and thermal cases, we observe that the lava flow in the isothermal cases advances extensively and rapidly, spreading beyond the boundary of the model domain. In contrast, the lava in the thermal cases ceases its rapid advancement due to increased thickness at the flow front and elevated viscosity, exhibiting a narrower flow width as the highest viscosity is observed at the periphery of the flow. Finally, as an application to real lava flows, we simulate the emplacement of a natural lava flow using observational data from the December 2015 eruption at Mount Etna. The eruption, occurred from December 6 to 8, 2015, was characterised by Strombolian effusive activity originating at the New Southeast Crater (SEC) and moderate variations in the discharge rate. In the simulations we vary the modelled effusion rate based on the observed average total area discharge rates. The modelled lava flow volume ($1.15\times10^6\,m^3$) aligns closely with the observed lava flow deposition. All rheological models approximate the real lava flow width accurately, with the Newtonian model providing the best match for flow extent and developing the same morphological features as the real lava emplacement. While the Herschel-Bulkley model shows a slight deviation in the lava flow length, the Bingham model fits well the main flow branch, with minor divergence in the upper branches. Furthermore, the modelled thickness distribution aligned well with the observational thickness, presenting increased lava accumulation near the crater and at the flow front. To validate the numerical codes, we perform benchmark tests against the analytical solution of the axisymmetric viscous gravity current problem. The results of the numerical models align closely with the analytical solution, with the depth averaged model providing the best match to analytics due to the shared foundations of the analytical approach and the shallow water approximation.

Keywords: lava flow; CFD numerical modelling; flow morphology; heat transfer; Newtonian fluid; Bingham rheology; Herschel-Bulkley rheology

7.1 Introduction

A lava flow is influenced by the lava rheology, the cooling process, and the terrain’s complexity, and leads to the formation of the crust, levèes, and tubes (e.g., Costa & Macedonio, 2005a). Lava flows pose a constant threat to infrastructure and populations in the proximity of active volcanoes (Komorowski, 2002; Behncke & Neri, 2003). The risks and damages associated with effusive eruptions necessitate the development and use of numerical models, both for advancing scientific understanding of the lava dynamics and its thermal evolution and for generating reliable forecasts of lava flow paths both spatially and temporally (Costa & Macedonio, 2005a; Tsepelev et al., 2016). Numerical modelling of lava flows is also essential for planning evacuations, mitigating risks, and organizing the diversion or the presence of natural or artificial barriers (e.g., Macedonio & Longo, 1999) in response to lava flow hazards (Costa & Macedonio, 2005a). A number of computer codes have been developed to predict lava flow movement and emplacement dynamics (Crisci et al., 1986; Miyamoto & Sasaki, 1998; Costa & Macedonio, 2005b; Vicari et al., 2007; Hérault et al., 2011; Bilotta et al., 2012;

Cappello et al., 2016; Cordonnier et al., 2015; Ismail-Zadeh et al., 2023; Starodubtsev et al., 2023).

The modelling of lava flows started from the development of oversimplified models that are usually based on several assumptions (e.g., steady state) of the observed processes and describe lava flows as gravity currents advancing on the topography (due to e.g., slope, gravity). Nowadays due to the advancements in the computational resources, it is possible to develop much more complex transient 2-D/3-D numerical models that can account for fluid dynamics, thermal effects, lava rheology. Numerical models of lava flow are varied according to the approach adopted to the modelling (deterministic, stochastic), the numerical method for approximating the solution to differential equations (e.g., finite volume, finite element) employed and how complex is the physics of the model (e.g., the changes in rheology, thermal evolution of the flow). Harris & Rowland (2001) developed a simplified model of channelled lava dynamics (FLOWGO), where lava advances only in one direction. The code produces fast results as it computes 1D dynamics of the fluid while still incorporating complex lava rheology (i.e., crystallization, cooling). Another popular approach to simulate lava flow is Cellular automata. In the CA the computational domain is divided into 2-D grid of cells, each cell carries specific properties (e.g., lava height, temperature). The advancement of lava is described through the evolution of these cell properties. CA models can account for complex viscosity models (temperature dependent, crystallization), thermal effects (e.g., convection, radiation). The codes that are based on the CA approach include SCIARA (Crisci et al., 1986; Barca et al., 2004; Avolio et al., 2006), MAGFLOW (Vicari et al., 2007; Bilotta et al., 2012), GPUFLOW (Cappello et al., 2022, Zeinalova et al submitted), and FLOWFRONT (Young & Wadge, 1990; Wadge et al., 1994). Other approaches to modelling lava flows include the simplification of thermal models (e.g., accounting for isothermal models, Tsepelev et al., 2016), using mesh free approaches (e.g., particles, Hérault et al., 2011; Bilotta et al., 2016; Starodubtsev et al., 2023) or nuclear based models (e.g., LavaSIM code, Hidaka et al., 2005). In scenarios of lava flow simulations, where the ratio of vertical to horizontal flow dimensions becomes negligible, depth-averaged flow models can be applied (Costa & Macedonio, 2005a, 2005b).

Depth-averaged flow model, based on the shallow water equations (SWE) hypothesis was first introduced by De Saint Venant in 1871. The main assumption of the model is that the horizontal length scale is much greater than the vertical one which leads to neglection of the vertical component (Costa & Macedonio, 2005a, 2005b). The depth-averaged equations are derived by depth integrating the Navier–Stokes equations from the terrain bottom to the free surface. The main assumptions of the model (constant vertical profiles for the variables) lead to the constant viscosity and temperature along the vertical direction, which limits the ability to fully capture the influence of rheology on flow dynamics.

Three-dimensional (3-D) computational fluid dynamics modelling (CFD) helps to overcome this issue. CFD modelling provides a better understanding of physical processes driving lava flows as it captures the detailed fluid flow dynamics including the vertical distribution of various parameters such as temperature and velocity as well as changes in the apparent viscosity of lava, which is one of the key factors controlling the dynamics of lava flow (e.g., lava flow propagation, solidification) (Harris, 2013). The main drawback of 3-D models relates to its computational performance as they are way more expensive to solve than for example the depth-averaged model.

In the present work we employ two approaches to modelling lava flow advancement including the depth averaged model based on the shallow water approximation (as it is suitable to our study, meaning that the assumption of the negligible ratio of vertical to horizontal dimensions is satisfied) and the generic 3-D modelling.

The depth averaged model describes a viscous laminar incompressible fluid flow. The model is implemented using the finite volume method (FVM) in OpenFOAM. In the 3-D models we consider the dynamics of two phase incompressible, viscous, laminar and immiscible fluid. The 3-D models are implemented in Ansys Fluent and OpenFOAM. The numerical codes are based on the FVM to solve the governing equations that describes the fluid motion and Volume of Fluid (VOF) Method to deal with the multiphase nature of the problem.

The main objective of the study is to understand the influence of rheological models on lava flow morphology. The rheological models include Newtonian, Bingham, and Herschel Bulkley fluids in the cases of isothermal and non-isothermal modelling. The secondary objective is to benchmark the numerical codes used in the study.

In the next section (Sect. 7.2), we present a description of the three-dimensional model of lava flow followed by a derivation of the depth-averaged flow (SWE) model. Following that we briefly describe the methodology, and the numerical approaches employed in the study (Sect.

7.3). To validate the codes, we present in Sect. 7.4 a benchmark test based on the analytical solution of the axisymmetric viscous gravity current problem (Huppert, 1982). The numerical results of the isothermal modelling are presented in Sect. 7.5, here we show the influence of different rheological models on flow advancement under isothermal conditions employing 3-D and SWE models. Section 7.6 demonstrates the results of the non-isothermal modelling using the SWE model. In Section 7.7, we apply the depth averaged model to simulate a real lava flow that occurred in December 2015 at Mount Etna. The conclusions and discussion are provided in Section 7.8.

7.2 Model description

We model a lava extrusion from a volcanic vent with the subsequent lava flow advancement (Figure 7.1).

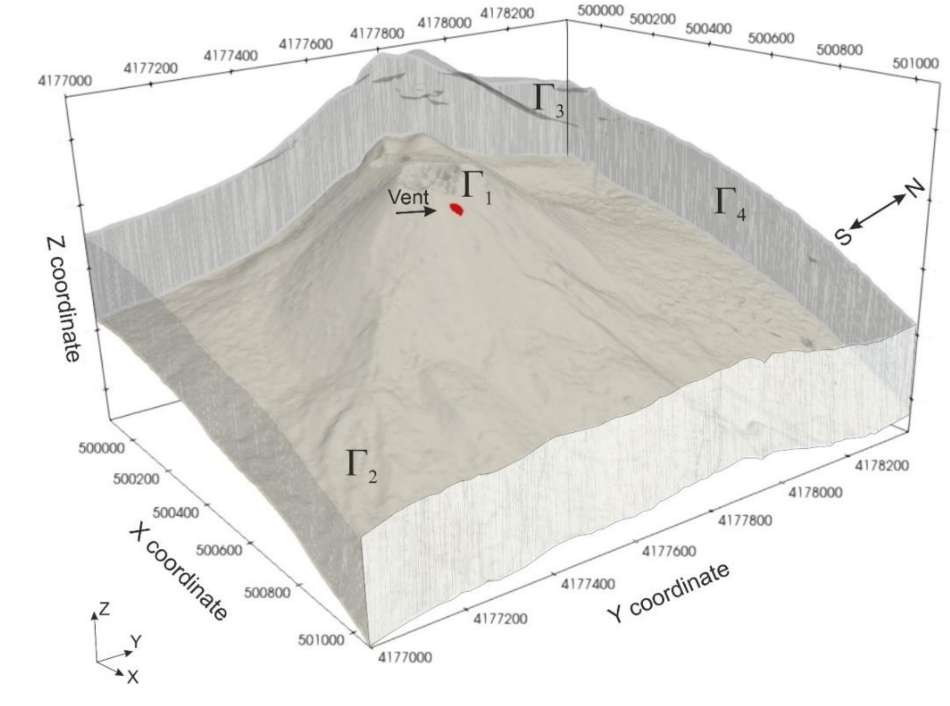

Figure 7.1: Computational model domain Ω. The location of the vent Γ_1 is shown as a red surface on the crater; Γ_2 is the lower part of the topography, which approximates the digital surface model (DSM) of Mt Etna (Ganci et al., 2019), excluding Γ_1 area; Γ_3 illustrates the upper boundary of the domain; Γ_4 marks lateral sides of the model domain. The coordinates (X and Y with elevations in meters show the distance eastward from the

UTM zone's central meridian and the distance northward from the equator, respectively) are expressed in a projected coordinate system EPSG:32633(UTM Zone 33N, WGS 84).

The governing equations for the fluid dynamics are expressed by the Navier-Stokes equations with the initial condition $\mathbf{u}(t=0,\,\mathbf{x})=0$ for $\mathbf{x}\in\mathbf{\Omega}$

$$\frac{\partial(\rho\mathbf{u})}{\partial t}+(\mathbf{u}\cdot\nabla)(\rho\mathbf{u})=-\nabla p+\nabla\cdot\left(\eta\left(\nabla\mathbf{u}+\nabla\mathbf{u}^{\mathrm{T}}\right)\right)+\mathbf{G},\qquad \mathbf{x}\in\mathbf{\Omega}, \tag{7.1}$$

the continuity equation

$$\nabla\cdot\mathbf{u}=0,\qquad \mathbf{x}\in\mathbf{\Omega}, \tag{7.2}$$

and the heat equation with the initial condition for the temperature $T(t=0,\mathbf{x})=T_A$ for $\mathbf{x}\in\mathbf{\Omega}$

$$\frac{\partial(c\rho T)}{\partial t}+\nabla\cdot\left(\mathbf{u}(c\rho T)\right)=\nabla\cdot(k\nabla T)+Q_{rad}+Q_{conv}+Q_{diss}\,. \tag{7.3}$$

Here t is the time; $\mathbf{u}=(u_1,u_2,u_3)$ is the velocity vector; $\mathbf{x}=(x_1,x_2,x_3)$ is the spatial variable; $\mathbf{G}=(0,0,-g\rho)$ is the vector of external mass forces, and g =9.81 m·s^{-2} is the acceleration due to gravity; p is the pressure; T is the temperature. The model density ρ, viscosity η, thermal conductivity k, and specific heat capacity c are represented as: $\rho(t,\mathbf{x})=\rho_L\alpha(t,\mathbf{x})+\rho_A(1-\alpha(t,\mathbf{x}))$; $\eta(t,\mathbf{x})=\eta_L\alpha(t,\mathbf{x})+\eta_A(1-\alpha(t,\mathbf{x}))$; $k(t,\mathbf{x})=k_L\alpha(t,\mathbf{x})+k_A(1-\alpha(t,\mathbf{x}))$; $c(t,\mathbf{x})=c_L\alpha(t,\mathbf{x})+c_A(1-\alpha(t,\mathbf{x}))$,

Where ρ_A, η_A, k_A and c_A are the air density, viscosity, thermal conductivity, and specific heat capacity, and ρ_L, η_L, k_L and c_L are the lava density, viscosity, thermal conductivity, and specific heat capacity, respectively. The function $\alpha(t,\mathbf{x})$ equals 1 for the lava and 0 for the air at each point **x** and at time *t.* The term $Q_{rad}=-\varepsilon\sigma(T^4-T_A^4)\delta_s$ accounts for the radiative heat transfer at the interface of the lava with the air, where ε is the effective emissivity of this interface; T_A is the temperature of the air environment (or simply, air); and σ $(=5.67\times10^{-8}$ Wm^{-2}K^{-4}) is the Stefan–Boltzmann constant. Symbol δ_s notes the special function determined at interface between the lava and the air measured in [m^{-1}]. The term $Q_{conv}=-\lambda_n(T-T_A)^{4/3}\delta_s$ accounts for the nonlinear convective heat transfer at the interface of the lava with the air, where λ_n is the nonlinear convective heat transfer coefficient measured in [W m^{-2} K$^{-4/3}$] (Neri, 1998). The term $Q_{diss}=\eta\left(\nabla\mathbf{u}+\nabla\mathbf{u}^T\right):\nabla\mathbf{u}$ describes the viscous dissipation. Symbols ∇ is the gradient operator, $\nabla \cdot$ is the divergence operator, ^{T} is the transposed matrix, ":" is the double-dot product (the trace of the inner product) of two matrices, respectively.

7.2.1 Lava rheology

Lava behaves as a fluid, and its viscosity is one of the key factors controlling the dynamics of lava flow (Harris, 2013). Based on the relationship between shear stress and strain rate, fluids can be classified into two categories: Newtonian and non-Newtonian. For Newtonian fluids, the ratio between the applied shear stress and the strain rate is linear, whereas in non-Newtonian fluids the rate of deformation is not directly proportional to a change in the applied stress. Dragoni et al. (1986) suggested that lavas behave as Bingham rather than Newtonian fluid. Bingham fluids will not flow until a certain threshold of stress, known as the yield strength, is reached. Once the yield strength is exceeded, the fluid behaves as a Newtonian fluid. The non-Newtonian behaviour of basaltic lava is also supported by field data from the work of Pinkerton & Sparks (1978), which shows that lava has a yield strength and deforms in a pseudoplastic manner as shear stress increases.

The main objective of this study is evaluating the influence of rheology on lava flow morphology. We consider Newtonian, Bingham and Herschel-Bulkley (HB) rheologies. The apparent lava viscosity η_L for the Herschel-Bulkley model is given by:

$$\eta_L = \frac{\tau_0 + \nu \dot{\gamma}^n}{\dot{\gamma}} \quad , \tag{7.4}$$

where ν is the consistency index [measured in Pa s^n], n is the power-law index, $\dot{\gamma}$ is the strain rate magnitude [s^{-1}], τ_0 is the yield strength [Pa]. The Herschel-Bulkley model reduces to a Bingham fluid when $n = 1$, and to a Newtonian fluid at both $\tau_0 = 0$ and $n = 1$.

7.2.2 Initial and boundary conditions

At the initial time, the flow velocity is assumed to be $\mathbf{u}(t=0, \mathbf{x}) = 0$. The model domain Ω is filled by the air with temperature $T_A = 300K$. No slip condition $\mathbf{u} = 0$ and zero heat flux are prescribed at the surface topography Γ_2 and also at the lateral sides Γ_4 of the model domain.

At the vent surface Γ_1, the magma with temperature $T_{in} = 1350$ K extrudes at the discharge rate of $\mathbf{u}_{dis} = 20$ m^3 s^{-1}. Outflow conditions are determined at the upper part of the model boundary Γ_3 to ensure the incompressibility. The incompressibility is achieved by removing air from the model domain in proportion to the lava extrusion rate: $\mathbf{u}_{out} = u_{out}\mathbf{n}$ and $u_{out} = -|\Gamma_3|^{-1} \int_{\Gamma_1} \langle \mathbf{u}_{ext}, \mathbf{n} \rangle d\Gamma$, where $\mathbf{u}_{ext} = 0.018 \text{ m s}^{-1}$ is the lava extrusion rate, which is calculated from the discharge rate, and $\mathbf{n}$ is the outward unit normal vector at a point on the model boundary . Therefore, the problem of the fluid flow can be described by a mathematical problem, which requires computation of the governing equations (7.1)-(7.3) along with the specified boundary and initial conditions outlined above.

7.2.3 Shallow water approximation

The shallow water approximation (SWE) assumes that the horizontal length scale is much greater than the vertical one, and hence, the vertical dynamics is negligible compared to the horizontal dynamics (Costa & Macedonio, 2005a, 2005b). The SWE models have been applied to simulate a wide range of geophysical flows: in flood simulations (Burguete et al., 2002), in tsunami propagations (Heinrich et al., 2001) as well as in volcanology, namely, in pyroclastic density currents (Sheridan et al., 2005), lava flows (Costa & Macedonio, 2005a, 2005b; Kelfoun & Vargas, 2016; Biagioli et al., 2021, 2023), and lahars (Procter et al., 2010). The SWE formulation leads to a dimension reduction as variations with depth are neglected, and this results in relatively fast computations. A SWE model can incorporate several rheology models: Newtonian (Costa & Macedonio, 2005b), Bingham (Liu & Mei, 1990; Biagioli et al., 2023), and Herschel-Bulkley (Balmforth et al., 2002, 2006, 2007) fluids.

The shallow-water equations describe a shallow layer of incompressible laminar viscous fluid flow motion, where the horizontal scale of the flow is much greater than the layer depth, bounded from below by a bottom surface and from above by a free surface (open to air). In these scenarios, the Navier-Stokes equations for incompressible flows with the free surface can be simplified by averaging over the depth, allowing the vertical dimension to be neglected. The presence of the free surface enables to simplify the viscous term in the Navier Stokes equations. The derivation of depth averaged equations necessitate the imposing of the appropriate conditions for the Navier-Stokes equations which include (i) a Navier condition with a friction coefficient $\widehat{k}$ (the tangential velocity of a fluid at the bottom surface is proportional to the tangential component of the shear stress exerted by the fluid at the surface) and a no-penetration condition on the bottom surface (Gerbeau & Perthame, 2001) , (ii) no-stress conditions on the free surface (no forces acting on the fluid at the free surface). We additionally assume the parabolic velocity profile and hydrostatic pressure distribution. Depth-averaging the vertical velocity profiles results in the loss of the velocity information, such that a bottom friction can no longer be defined as a boundary condition. Instead, the interaction between the fluid and the underlying surface must be incorporated into the model itself. The bottom friction, alongside gravitational forces, is a primary factor in the SWEs that determines fluid evolution. Thus, accurately modelling the bottom friction directly impacts the solution. Modelling such interactions in 3D models presents a complex challenge. For simplicity, it is common to impose no-slip boundary conditions on the underlying surface in 3D models. In the SWE model, frictional conditions mainly depend on the fluid's rheology. In Newtonian rheology the friction coefficient is derived from the assumption of the parabolic velocity profile. In Bingham rheology the plastic term in the friction coefficient is derived from the assumption that the stress occurs only at the bottom surface (Kelfoun & Druitt, 2005). HB rheology is the generalised form of Bingham rheology where instead of the dynamic viscosity in the friction coefficient we consider the apparent viscosity (meaning that the viscosity is a function of the strain rate in this case).

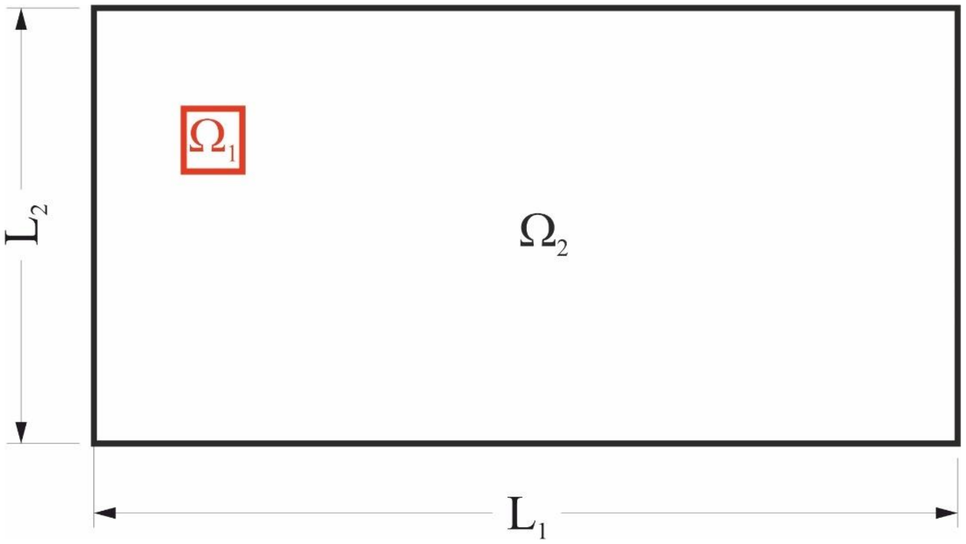

Figure 7.2: Computational model domain $\Omega_{SWA} = \Omega_1 \cup \Omega_2 = (0, L_1) \times (0, L_2)$ in the SWE model.

The shallow water equations (SWEs) are derived by simplifying the set of governing equations (7.1) - (7.3). For a detailed derivation, please refer to Gerbeau & Perthame (2001), Ferrari & Saleri (2004), Costa & Macedonio (2005b), Kelfoun & Druitt (2005), Xia & Liang (2018), and Biagioli et al. (2021). In this section, we briefly outline the derivation approach.

By integrating the continuity equation (7.2) over the flow thickness, we obtain the equation describing the evolution of the lava flow thickness:

$$\frac{\partial h}{\partial t} + \nabla \cdot \left(h\mathbf{U} \right) = w_{in}, \quad (x, y) \in \Omega_{SWA}, \tag{7.5}$$

where $h = h(t; x, y)$ is the thickness of the lava flow, $w_{in} = u_{ext}$ for $(x, y) \in \Omega_1$ and $w_{in} = 0$ for $(x, y) \in \Omega_2$ is the magnitude of the extrusion rate; $\mathbf{U}(t; x, y) = (\tilde{u}_1, \tilde{u}_2)$ where the depth-averaged components of the fluid velocity presented by:

$$\tilde{u}_1(t; x, y) = h^{-1} \int_{H(x,y)}^{H(x,y)+h(x,y)} u_1(t; x, y, z)dz,$$

$$\tilde{u}_2(t; x, y) = h^{-1} \int_{H(x,y)}^{H(x,y)+h(x,y)} u_2(t; x, y, z)dz, \tag{7.6}$$

where $H = H(x, y)$ is the terrain surface.

Gerbeau & Perthame (2001) approximated the term $\nabla \cdot \left(\eta_L \left(\nabla \mathbf{u} + \nabla \mathbf{u}^T \right) \right)$ in the Navier-Stokes equations (7.1) by the simplified expression $\gamma_{fr} \mathbf{U}$, where $\gamma_{fr} = \widehat{k} / \left(1 + \widehat{k}h / \left(3\mu \right) \right)$ is the friction coefficient depending on the fluid rheology and the terrain surface H; and constant $\widehat{k}$ is chosen so that $\widehat{k}h / \left(3\mu \right) >> 1$. Hence, by integrating Eq. (7.1)over the flow thickness, we obtain:

$$\frac{\partial \left(h\tilde{u}_1 \right)}{\partial t} + \nabla \cdot \left(\beta_u h\tilde{u}_1 \mathbf{U} \right) = -\frac{1}{2} \frac{\partial}{\partial x} \left(gh^2 \right) - gh \frac{\partial H}{\partial x} - \gamma_{fr} \tilde{u}_1, \quad (x, y) \in \Omega_2 \tag{7.7}$$

$$\frac{\partial \left(h\tilde{u}_2 \right)}{\partial t} + \nabla \cdot \left(\beta_u h\tilde{u}_2 \mathbf{U} \right) = -\frac{1}{2} \frac{\partial}{\partial y} \left(gh^2 \right) - gh \frac{\partial H}{\partial y} - \gamma_{fr} \tilde{u}_2, \quad (x, y) \in \Omega_2 \tag{7.8}$$

$$h(0; x, y) = 0, \ \tilde{u}_1(0; x, y) = 0, \tilde{u}_2(0; x, y) = 0, \quad (x, y) \in \Omega_{SWA}. \tag{7.9}$$

The gradient $\nabla H = (\partial H/\partial x, \partial H/\partial y)$ indicates the bottom slopes in both directions *x* and *y*. The parameter β_u is the Boussinesq shape factor reflecting the shear in the profile of the horizontal fluid velocity (Biagioli, 2021). This parameter depends on the fluid rheology and can be presented as $\beta_u = \frac{2(1+2n\ )}{2+3n}$ (where $0<n\leq 1$), and hence varies in the range of $1<\beta_u\leq 6/5$ (Hogg & Pritchard, 2004). In the cases of Newtonian and Bingham fluids, $\beta_u = 6/5$.

The depth-averaged heat equation is derived from Eq (7.3)with an assumption that the diffusion term in Eq (7.3) is approximated as $\nabla\cdot\left(k\nabla T\right)\approx n_{dif}k_L\left(T-T_{gr}\right)/h$ (Costa & Macedonio, 2005b):

$$c_L\rho_L\left(\frac{\partial\left(h\tilde{T}\right)}{\partial t}+\left\langle\nabla\left(h\tilde{T}\right),\mathbf{U}\right\rangle\right)=\tilde{Q}_{rad}+\tilde{Q}_{conv}+\tilde{Q}_{diff}+\tilde{Q}_{diss};\qquad \mathbf{x}\in\Omega_2,\ (7.10)$$

where $\tilde{Q}_{rad}=-\tilde{\varepsilon}\sigma f\left(\tilde{T}^4-T_A^4\right)$, $\tilde{Q}_{conv}=-\lambda_n f\left(\tilde{T}-T_A\right)^{4/3}$, $\tilde{Q}_{diff}=k_L n_{diff}h^{-1}\left(\tilde{T}-T_{gr}\right)$, and $\tilde{Q}_{diss}=m_{diss}h^{-1}\tilde{\mu}\left\|\mathbf{U}\right\|^2$ (Costa & Macedonio, 2005b), where $\left\|\mathbf{U}\right\|^2=\tilde{u}_1{}^2+\tilde{u}_2{}^2$; and $\tilde{T}(t;x,y)$ is the depth-averaged temperature of the flow determined as:

$$\tilde{T}(t;x,y)=h^{-1}(t;x,y)\int_{H(x,y)}^{H(x,y)+h(x,y)}T(t;x,y,z)dz\,. \qquad (7.11)$$

Here f is the fractional area of the exposed inner core (Crisp & Baloga, 1990), which determines the existence of a crust of the lava flow (for simplicity, we assume f to be constant in the modelling). In the viscous dissipation term, $\tilde{\mu}$ is the depth-averaged viscosity; $n_{diff}=4$ in the conductive term, and $m_{diss}=12$ in the viscous dissipation term (Costa & Macedonio, 2005b). We set $\tilde{T}(t;x,y)=T_{in}(t;x,y)$ for $(x,y)\in\Omega_1$ at $t\geq 0$ for the vent temperature.

Often in the modelling of lava flows, a constant value of the effective emissivity ε (usually set to 0.9) is assumed for both molten lava and the cooled crust. However, laboratory studies showed that the effective emissivity varies during cooling. In this work, we use an empirical relationship that links the effective emissivity with the lava temperature (Cappello et al., 2022):

$$\tilde{\varepsilon}\left(\tilde{T}\right)\ \approx\ 0.976716+4.08881^{-5}\tilde{T}-1.9506210^{-7}\tilde{T}^2. \qquad (7.12)$$

In the SWE model, the coefficient γ_{fr} is represented as $\gamma_N = \dfrac{c_n \tilde{\mu}}{\rho_L h}$ for the Newtonian rheology (Costa & Macedonio, 2005b), $\gamma_B = \dfrac{c_n \tilde{\mu}}{\rho_L h} + \dfrac{\tilde{\tau}_0}{\rho_L \|\mathbf{U}\|}$ for the Bingham fluid (Kelfoun & Druitt, 2005; Kelfoun & Vargas, 2016), and $\gamma_{HB} = \dfrac{c_n \tilde{\nu} \tilde{\dot{\gamma}}^{n-1}}{\rho_L h} + \dfrac{\tilde{\tau}_0}{\rho_L \|\mathbf{U}\|}$ for the Herschel-Bulkley fluid, where $\tilde{\tau}_0 = \tilde{\tau}_0(x, y)$ is the depth averaged yield strength, $\tilde{\nu}$ is the depth-averaged consistency index, $\tilde{\dot{\gamma}} = h^{-1}\|\mathbf{U}\|$ is the depth-averaged strain rate magnitude, and $c_n = \left(\dfrac{1+2n}{n}\right)^n$ is the dimensionless constant depending on the power law index *n* (Hogg & Pritchard, 2004) ($c_n = 3$ for the Newtonian and Bingham fluids).

In the non-isothermal cases, the constant values for the depth-averaged viscosity, the yield strength, and the power law index are replaced with the temperature-dependent relationships. Laboratory experiments indicate that the temperature dependence of the power law index n can be approximated by the following relationship (Filippucci et al., 2017):

$$n(\tilde{T}) = 1 - 1.35 + 0.85 \times 10^{-3} \tilde{T} \,. \tag{7.13}$$

To account for a temperature-dependent viscosity, we employ the model proposed by (Giordano & Dingwell, 2003):

$$\log_{10} \mu_{GD} = -4.643 + \frac{5812.44 - 427.04 \times wt}{\tilde{T} - 499.31 + 28.74 \ln\left(wt\right)} \,. \tag{7.14}$$

For the Newtonian and Bingham fluids, the depth-averaged viscosity is represented as $\tilde{\mu} = \mu_* \mu_{GD}$; for the Herschel-Bulkley rheology the consistency index is defined as $\tilde{\nu} = \mu_* \mu_{GD}$, where μ_* is the reference viscosity with a value of 1 Pa s^n. The yield strength is assumed to follow a temperature-dependent relationship given by Ishihara et al. (1990):

$$\log_{10} \tilde{\tau}_0 = 13.00997 - 0.0089 \tilde{T} \,. \tag{7.15}$$

7.3 Methods

In this section we briefly outline the key concepts of the numerical approaches and numerical codes used in the study. The 3-D models are implemented using two software packages:

ANSYS Fluent and OpenFOAM. The SWE model is implemented in the OpenFOAM package. The time of computations of the numerical models depends on several factors including the time-step size, the complexity of the mathematical problem, the number of computational cells, the number of cores. The choice of the time step size is crucial and has to be sometimes lowered to ensure the solution's stability. CPU performance and RAM size also affect the computation time. We do not use graphics cards in this study. The simulation of lava flow advancement for a duration of one hundred seconds in Fluent, executed with 16 cores and a model time step of 1 second, requires approximately 10 minutes. Similarly, in OpenFOAM, employing eight cores with a model time step of 1 second, the same simulation needs approximately six minutes. The simulation conducted in the SWE framework, utilizing 4 cores and a model time step of 10 seconds requires approximately 5 seconds.

7.3.1 ANSYS Fluent

The ANSYS Fluent software (Matsson, 2024) allows for modelling a multi-phase fluid flow with mass and heat transfer. It employs the finite volume method (e.g., Ismail-Zadeh & Tackley, 2010), to solve problem Eqs. (7.1)-(7.3) with initial and boundary conditions) and the volume of fluid (VOF) (Hirt & Nichols, 1981) method to treat with a moving interface between two fluid phases (the extruded lava and the air). The VOF method assigns values ranging between zero and one to cells containing the interface, indicating the proportions of lava within them. Therefore, the advection of the two-phase fluid with an initial condition $\alpha\left(t=0,\mathbf{x}\right)=0$ is governed by the following equation:

$$\frac{\partial\alpha}{\partial t}+\nabla\cdot\left(\alpha\mathbf{u}\right)=0\,,\qquad \mathbf{x}\in\boldsymbol{\Omega}\,,\tag{7.16}$$

where $\alpha\left(t,\mathbf{x}\right)\in\left\{0,1\right\}$ determines the volume fraction of the fluid at point $\mathbf{x}\in\boldsymbol{\Omega}$ at time t. Note that $\alpha\left(t,\mathbf{x}\right)=1$ in the lava, and $\alpha\left(t,\mathbf{x}\right)=0$ in the air. The same Eqs. (7.1) - (7.3)are used to tackle with the air's dynamics.

The Reynolds number for lava is small due to its slow movement and high viscosity, resulting in laminar lava flow. Meanwhile, the Reynolds number for air is large, and the ratio of lava viscosity to air viscosity can reach about 10^{12}. To mitigate numerical instability, we limit the air velocity magnitude, which allows us to get stable calculations with the largest allowable time step. This procedure leads to a violation of incompressibility only for the air phase and has no effect on the motion of the viscous phase (lava). The Courant number, which is crucial for stability of the numerical problem, is set to 0.5.

The pressure is discretized by the second-order staggered scheme PRESTO! (e.g., Peyret, 1996). To approximate the Laplacian operator, we use the numerical scheme of the second-order accuracy, and the monotonic schemes are used to discretize convective terms in the equations (e.g., Ismail-Zadeh & Tackley, 2010). The pressure-velocity coupling is managed by the SIMPLE method (Patankar & Spalding, 1972), where the relaxation parameters are chosen to be 0.01 and 0.3 for the velocity and pressure, respectively. We assign 0.5 to the relaxation parameter for the function α. A time step is chosen in the range of 1–10 s depending on the stability and optimization of the velocity to assure a convergence of a set of linear algebraic equations (SLAE), which is obtained after the discretization of the Navier-Stokes equations. In the modelling, we employ the conjugate-gradient method to solve SLAE. The numerical accuracy of the SLAE solution attains 10^{-3} for the velocity and pressure and 10^{-6} for the function α.

Users do not need to have extensive programming knowledge as the software offers a user-friendly interface including pre- and post- processing tools as well as visualisation programs, and different solution solvers depending on the problem. However, the default capabilities are limited and sometimes it is necessary to customise a problem (e.g., include complex rheology, additional transport equations). Parallel processing in ANSYS Fluent is handled internally, without requiring manual intervention in node distribution.

7.3.2 OpenFOAM

OpenFOAM is an open-source software package focusing on computational fluid dynamics applications (Jasak et al., 2007). OpenFOAM (Jasak, 2009), like ANSYS Fluent, is based on the finite volume method and has different range of features to solve problems from complex fluids, chemical reactions and turbulence flows to heat transfer, solid mechanics, acoustics and electromagnetics. The code is parallelized using OpenMPI (Snir et al., 1995) and includes pre- and post-processing tools. As an open-source platform, OpenFOAM allows users to modify solvers, add new equations, and customize the software for specific needs or use the code with embedded packages. Although OpenFOAM does not have a built-in package for modelling lava flows, it offers the flexibility for users to create custom solvers tailored to their requirements.

The 3-D model in OpenFOAM is realized through the utilization of two key solvers: multiPhaseInterFoam and nonNewtonianIcoFoam. The multiPhaseInterFoam solver is employed to model the motion of a multiphase incompressible fluid, considering external forces and interphase interaction forces. The nonNewtonianIcoFoam solver implements the SIMPLE algorithm for joint calculations of velocity and pressure fields common to all phases, specifically tailored for non-Newtonian incompressible fluids (Patankar, 1980).

The computational grid for ANSYS Fluent and OpenFOAM is constructed using a uniform rectangular grid $\left\{x_1^i, x_2^j : 0 \le i \le n_1, 0 \le j \le n_2\right\}$ in the rectangle $[0,l_1]\times[0,l_2]$. The hexahedrons (blocks) are defined by 8 vertices:

$$\left\{\begin{array}{l}\left(x_1^i, x_2^j, f\left(x_1^i, x_2^j\right)\right);\left(x_1^i, x_2^{j+1}, f\left(x_1^i, x_2^{j+1}\right)\right);\left(x_1^{i+1}, x_2^{j+1}, f\left(x_1^{i+1}, x_2^{j+1}\right)\right);\left(x_1^{i+1}, x_2^j, f\left(x_1^{i+1}, x_2^j\right)\right);\\ \left(x_1^i, x_2^j, f\left(x_1^i, x_2^j\right)+l_3\right);\left(x_1^i, x_2^{j+1}, f\left(x_1^i, x_2^{j+1}\right)+l_3\right);\left(x_1^{i+1}, x_2^{j+1}, f\left(x_1^{i+1}, x_2^{j+1}\right)+l_3\right);\left(x_1^{i+1}, x_2^j, f\left(x_1^{i+1}, x_2^j\right)+l_3\right)\\ 0 \le i < n_1, 0 \le j < n_2\end{array}\right\}$$

Each block is divided vertically $0 \le k \le n_3$ in such a way that the height of each cell within the block is determined as: $h_k = \frac{h}{3} + \frac{k}{n_3 - 1}\cdot\frac{h}{3}$, $h = \frac{l_3}{n_3 - 1}$, and $0 \le k < n_3$. This partitioning makes smaller the height of cells that are closer to the lower model boundary, and the vertical size of cells becomes larger when approaching the upper model boundary.

The Crank-Nicholson scheme is employed to approximate the time derivative, and linear schemes are used for the gradient and Laplacian operators. Monotonic vanLeer and minMod schemes (Wang & Hutter, 2001) are applied to discretize convective terms in the Navier-Stokes equations and phase transfer, preventing oscillations in the approximations. Pressure and velocity calculations are conducted using the SIMPLE method (Patankar & Spalding, 1972) with relaxation parameters set to 0.1 and 0.3, respectively. Considering an average mesh non-orthogonality of 20 degrees an additional pressure correction is implemented. The systems of linear algebraic equations resulting from the discretization of problems (7.1) and (7.2) are solved using multigrid methods (Patankar & Spalding, 1972; Ismail-Zadeh and Tackley, 2010).

In the SWE case studies, the OpenFOAM package initiates a uniform mesh $\Omega_{N\times M} = \left\{(x_i = ih_x, y_j = jh_y) : i = 0...N; j = 0...M; L_1 = h_x N; L_2 = h_y M\right\}$, where $N = 786$ and $M = 509$, within the rectangular domain $\Omega_{SWA} = [0, L_1]\times[0, L_2]$ (see Figure 7.2). Equations (7.5)-(7.12) are solved by the finite volume method using the OpenFOAM library. The second-order total variation diminishing scheme is applied to approximate the gradient operators with testing conducted on the minmod and superBee schemes (LeVeque, 2002). Notably, the fluid mass loss did not exceed 3% throughout simulations.

7.4 Benchmark: axisymmetric 'dam break' model

The breaking of a dam to release a reservoir of viscous fluid is a classical problem in shallow-water fluid dynamics owing to its mathematical tractability and widespread applications in hydrodynamics and other fields. The following benchmark aims to verify the accuracy of the computational codes in solving the momentum equation under isothermal conditions, replicating a numerical experiment simulating a cylindrical dam-break flow on a horizontal surface. The objective is to compare the modeled simulations with the established analytical solution proposed by Huppert (1982), which in the axisymmetric case can be determined as:

$$h(R,t) = \xi_N^{2/3}(3Q\eta / g)^{(1/4)} t^{(-1/4)} \psi(\xi / \xi_N), \quad \xi(R,t) = R\left(\frac{\rho g Q^3 t}{3\eta}\right)^{-\frac{1}{8}} \tag{7.17}$$

where *h* and *R* are the height and the radial extent of the fluid flow advancement, respectively, $\xi_N^{2/3} = \left(\frac{1024}{81\pi^3}\right)^{1/8} \approx 0.894$ is the value of ξ at $R = R_N(t)$; $R_N(t) = \xi_N\left(\frac{\rho g Q^3 t}{3\eta}\right)^{1/8}$ is the position of the front of the fluid flow advancement; $Q = 2\pi \int_0^{R_N(t)} rh(r,t)dr$ is the fluid volume and $\psi(\xi / \xi_N) = \left(3/16\left(1-\left(\xi / \xi_N\right)^2\right)\right)^{1/3}$. Note that these formulas are derived using the thin-layer approximation, that is, when the radial extent is much greater than its height.

The initial setup involves a cylindrical dam-break scenario: a red-filled rectangular cylinder (Figure 7.3) with a height (= 1 m) and diameter (=1 m). The model domain is represented by a black rectangular box with a height of 1.5 m and length of 2.475 m. The fluid is characterized by a density $\rho = 2600$ kg m^{-3} and a viscosity $\eta = 10^3$ Pa s. The density and viscosity of the air are 1.125 kg m^{-3} and 1 Pa s, respectively.

We use a transient solver for two-phase incompressible flow under the influence of gravity for the axisymmetric case. For more information, please see ANSYS Fluent Theory Guide 2024R2, Chapter 1.5[8]). Figure 7.3 presents the geometry setup used to compute the axisymmetric flow in ANSYS Fluent. The no-slip condition is assumed at the walls of the model domain and the grid resolution is 0.05 m. The OpenFOAM solver is employed to solve Eqs. (7.1) and (7.2) within the same model domain, maintaining consistent boundary conditions and the grid resolution as those used in ANSYS Fluent. Additionally, the shallow water equations solver is applied solving Eqs. (7.5)-(7.9).

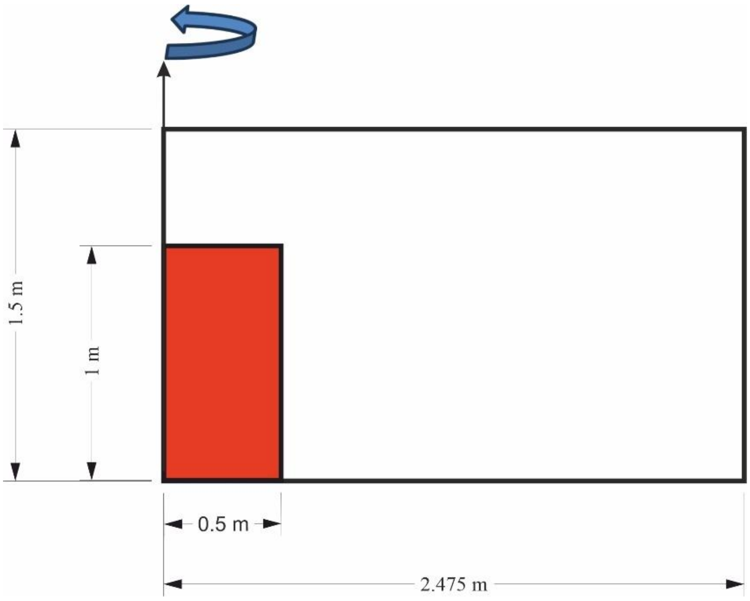

Figure 7.3: The dimensional model domain used in the benchmark. The arrow shows the rotation of the model domain around the symmetry axis.

To compare results with the analytical solution we select a random time point under the assumption that sufficient time had passed for the fluid to advance. The height of the modeled fluid flow shows a good agreement with that obtained from the analytical solution at time t= 4 s (Figure 7.4).

---

[8] https://ansyshelp.ansys.com/Views/Secured/corp/v242/en/flu_th/flu_th_uns_sec_models_swirl.html

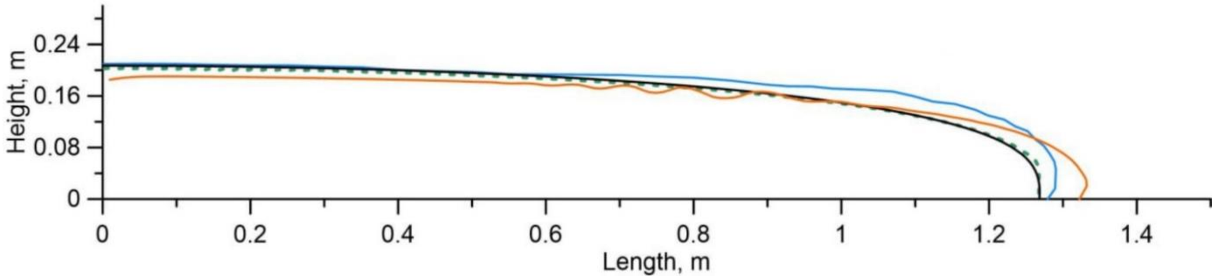

Figure 7.4: The heights of a viscous flow in the benchmark test at 4 seconds derived from the analytical solution (black solid line) and from the numerical solutions obtained by the ANSYS Fluent (blue solid line), OpenFOAM (orange solid line), and SWE (green dashed line).

The SWE model result demonstrates good agreement with the analytical solution. This alignment can be attributed to the shared foundation of the Huppert (1982) solution and the SWE model, both of which are formulated under the shallow water approximation. This approximation assumes that the vertical component is significantly smaller than the horizontal one, which is suitable for scenarios, where the fluid height is much smaller than its horizontal extent. Since the analytical solution is based on certain assumptions and simplifications, numerical results from ANSYS Fluent and OpenFOAM slightly deviate due to complexity of the models and limitation in the vertical resolution defined by mesh.

Comparing Fluent and OpenFOAM results with the analytical solution, Fluent demonstrates a closer agreement with the analytics than OpenFOAM. While both software packages provide valuable insights into the simulated scenario, Fluent exhibits the results that align more closely with the expected analytical outcomes. This discrepancy could arise from differences numerical discretization methods or solver algorithms implemented in each computational approach.

7.5 Numerical results: Isothermal case study

We conduct a series of five experiments using three isothermal rheological models implemented across three numerical codes: ANSYS Fluent, OpenFOAM, and SWE. The experiments include Newtonian case study with a constant viscosity = 10^5 Pa s. (exp. 1). In the following two experiments, we apply Bingham rheology and use two yield strength thresholds: τ_0 = 10^3 Pa in exp. 2 and τ_0 = 10^4 Pa in exp. 3, and the consistency index is set to ν = 10^5 Pa

s. In the next two experiments, we introduce Herschel-Bulkley rheology. Here the power-law index is n=1/3, the consistency index is ν = 10^5 Pa s$^{1/3}$ and the yield strength values are set at τ_0 = 10^3 and τ_0 = 10^4 Pa in exp. 4 and exp. 5, respectively. Throughout all experiments, we maintain consistency in the model domain, model parameters, and the fluid properties across the numerical codes. Due to the depth-averaged nature of the SWE model, the model domain (Figure 7.2) is defined as a 2-D region, however the grid resolution and the vent location remains consistent with the 3-D models.

Figure 7.5 illustrates the numerical results of the flow velocity performed in ANSYS Fluent (AFT), OpenFOAM (OFM), and SWE. The results obtained by the 3-D models exhibit consistency, showing a close distribution of the velocity field with the maximum velocity magnitude value in the centre of the flow. Note that the values obtained in the SWE model represent the mean velocity magnitude, which cannot be directly compared with the following results obtained in AFT and OFM, since the previous two cases represent the velocity magnitude at the free surface.

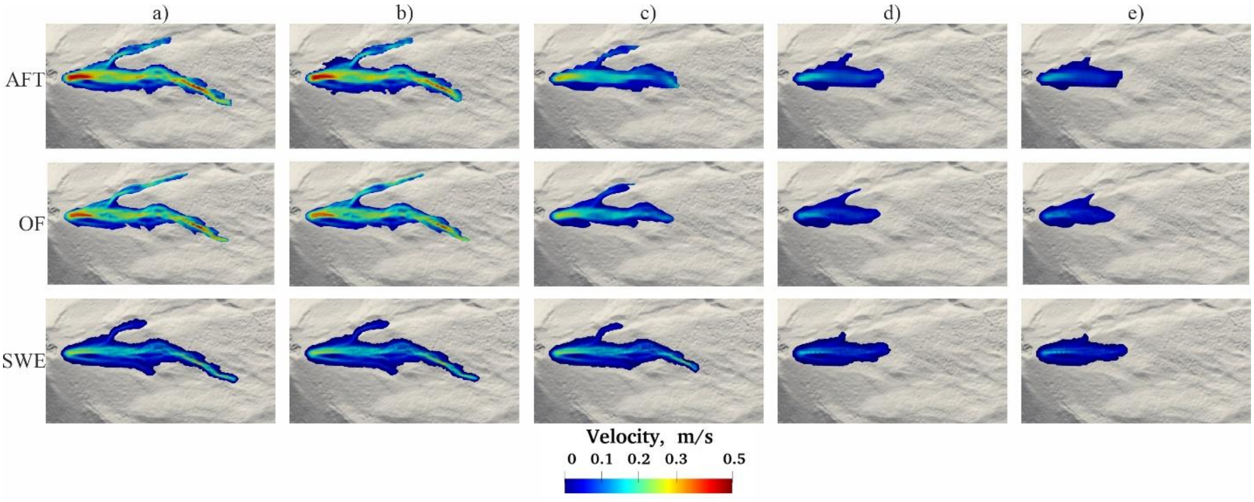

Figure 7.5: The modelled velocity magnitude for a) Newtonian fluid b) Bingham fluid with τ_0 = 10^3; c) Bingham fluid with τ_0 =10^4; d) Herschel-Bulkley fluid with τ_0 =10^3; e) Herschel-Bulkley fluid with τ_0 =10^4 obtained by AFT (upper panels), OFM (middle panels), and SWE (lower panels) at time 10000s.

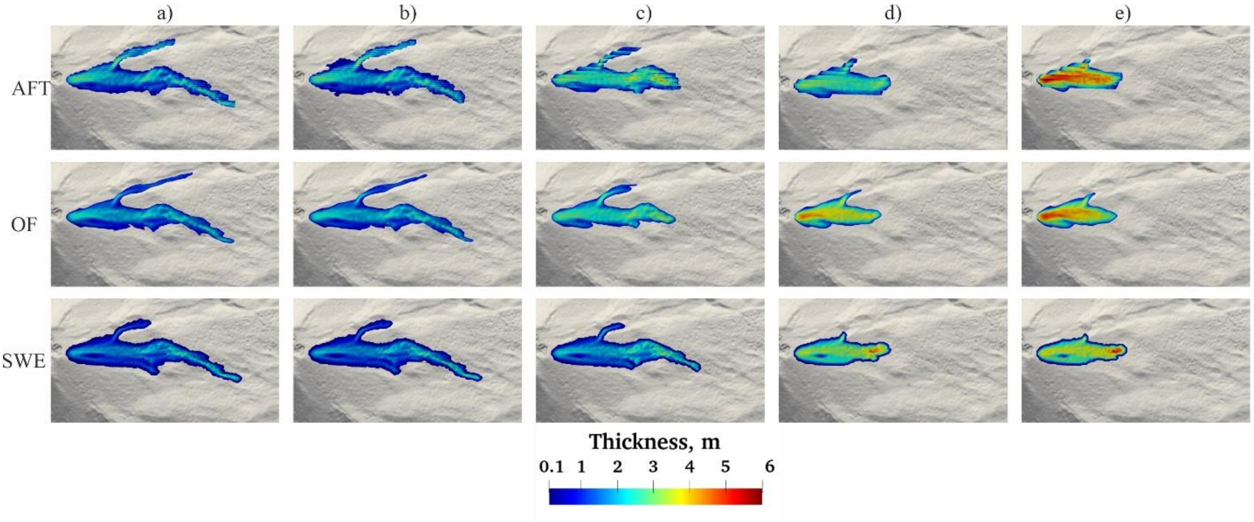

Figure 7.6: The modelled thickness of the lava flow for a) Newtonian fluid; b) Bingham fluid with τ_0 = 10^3; c) Bingham fluid with τ_0 =10^4; e) Herschel-Bulkley fluid with τ_0 =10^3; e) Herschel-Bulkley fluid with τ_0 =10^4 obtained by AFT (upper panels), OFM (middle panels), and SWE (lower panels) at time 10000s.

Figure 7.6 presents the thickness of lava flows across five experiments. In experiment 1 (Figure 7.6a), the flow thickness varies from 1 to 2 m. Figure 7.6b,c illustrate the impact of the yield strength on the morphology of the lava flow. As the yield strength (τ_0) increases, the lava viscosity also increases, resulting in slower horizontal advancement of the lava flow, and hence in an increase in the flow thickness. In exp. 2 (Figure 7.6b), the flow thickness ranges from 1.5 to 2 m. The Bingham case with the low yield strength value (Figure 7.6b) resembles the Newtonian fluid flow. In exp. 3 (Figure 7.6c), the flow thickness increases further reaching up to 2.5-3 m. The increase in the lava thickness indicates that higher yield strength results in a shorter and thicker flow. While the AFT and OFM results align closely with each other, the lava flow in the SWE model advances the farthest. Experiments 4 and 5 (Figure 7.6d,e) reveal that the flow thickness reaches its maximum in the middle of the lava flows rising to 5 m. In these experiments, the lava flows advance approximately to the same distance across all three numerical models, and the minor differences are associated with the accuracy of each method behind the models.

7.6 Numerical results: Thermal case study

To access the effect of temperature variation on the lava flow morphology we conduct another set of experiments. In these experiments we have extended the modelling time to show the influence of different thermal effects (e.g., solidification, cooling) due to radiation, convection, conduction as well the effect of viscous heating. The area of the modelled domain has been enlarged (to accommodate the lava flow advancement), but the grid resolution and the vent location remain the same as in the previous experiments. Due to high computational power demand (because of the enlarged model domain and the increased computational time) and numerical efficiency, the simulations were performed using only the SWE model.

We conducted numerical experiments using three temperature dependent rheological models: Newtonian, Bingham, and Herschel-Bulkley. In these models, the melt viscosity, yield strength, power index and the radiation coefficient are temperature dependent. We also accounted for various heat transfer mechanisms, including radiative, convective, conductive, and viscous heating due to dissipation as a heat source. Below, we present the results after 48 hours of the modelled lava advancement at a constant effusion rate. Values of the model parameters are listed in Table 7.1.

Table 7.1 Model parameters

Symbol	Definition	Value
ρ_L	density, kg m^{-3}	2500
k_L	thermal conductivity, W m^{-1} K^{-1}	2
c_L	specific heat capacity, J kg^{-1} K^{-1}	1200
g	the gravitational acceleration, m s^{-2}	9.81
u_{ext}	magnitude of the extrusion rate, m s^{-1}	0.018
T_{in}	lava eruption temperature, K	1350
T_A	air temperature, K	300
T_{gr}	temperature of the lava-ground surface, K	1253
σ	Stefan–Boltzmann constant, W m^{-2} K^{-4}	5.67×10^{-8}
λ_n	nonlinear convective heat transfer coefficient, W m^{-2} K$^{-4/3}$	5
n_{dif}	empirical parameter in the conductive term	4

m_{dis}	empirical parameter in the viscous dissipation term	12
wt	water content, %	0.1
f	fractional area of the exposed inner core	0.35

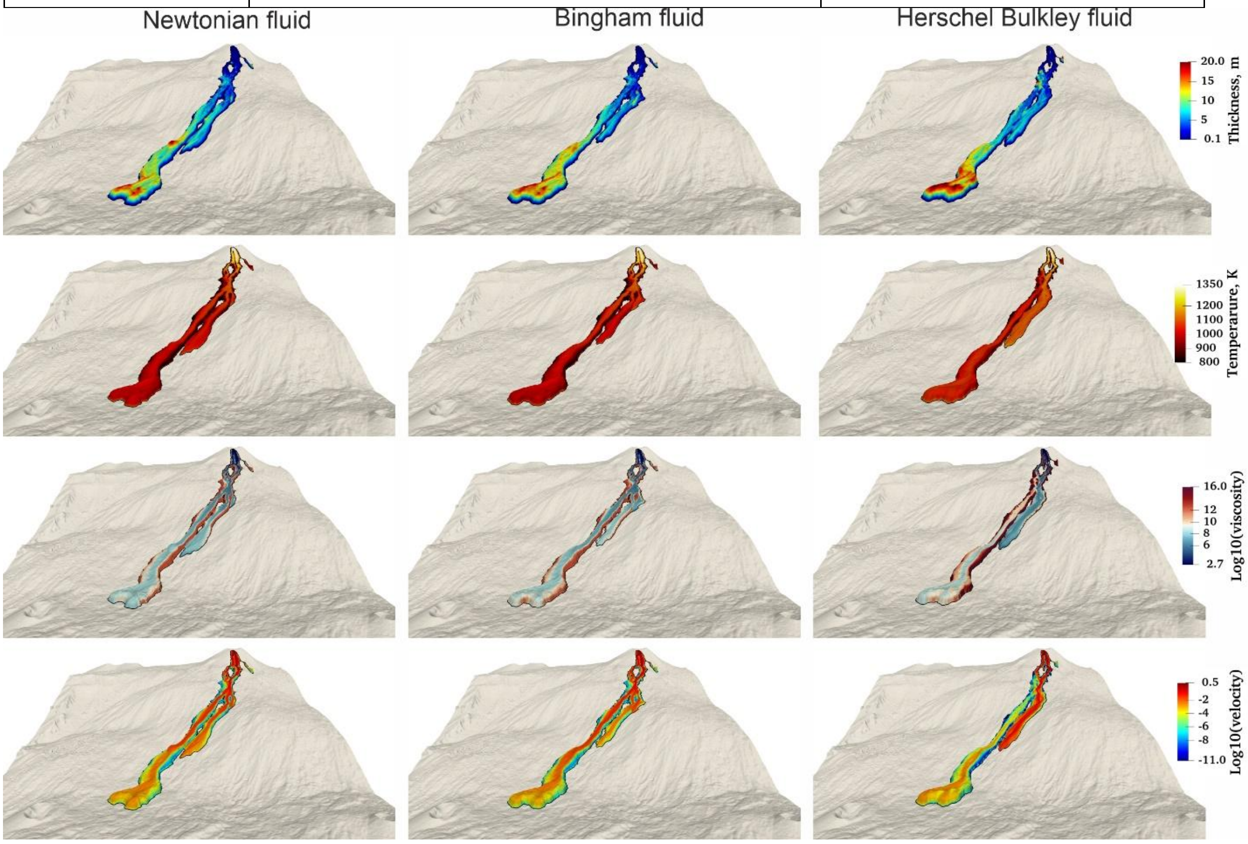

Figure 7.7: The modelled lava flow viscosity, thickness, temperature, and velocity magnitude in 48 hours after the lava eruption in the cases of Newtonian (the first column), Bingham (the second column), and Herschel-Bulkley (the third column) rheologies.

Figure 7.7 illustrates the distribution of the modelled viscosity, lava flow thickness, temperature, and velocity magnitudes after 48 hours of lava eruption. The lava flow in all three cases develop three branches: the long one (which advances farther than the other two), the middle one (the second longest) and the shortest one (it advances to the right-hand side and is the shortest among the three lava flow branches). For simplicity, we will refer to the long lava flow branch as the main one, the second longest as the middle lava flow branch, and the shortest one as the shortest lava flow branch. Comparing the main lava flow branches, Newtonian and Bingham models display similar viscosity patterns. Both models show low viscosity values, varying from about $10^{2.7}$ Pa s to about 10^{6} Pa s across the central part of the flow, and high viscosity value around 10^{12} Pa s near the flow margins. The Herschel-Bulkley model exhibits viscosity values of 10^9 Pa s within the flow and reaches the highest viscosity values, up to 10^{16} Pa s, along the periphery of the flow.

In the middle lava flow branch, the lava in the Newtonian model advances further due to a lower viscosity value of about 10^7 Pa s compared to the lava in the Bingham case, where the viscosity reaches 10^8 Pa s. The lava in the Herschel-Bulkley model has the lowest viscosity around 10^6 Pa s in this region and develops a wider branch flow than the ones in the Newtonian and Bingham cases.

In the shortest branch, Newtonian and Bingham models again show similar viscosity and flow characteristics, with moderate advancement of the lava. However, the lava flow branch in the Herschel-Bulkley model is notably shorter, indicating that the high peripheral viscosity significantly restricts flow in this area compared to the other models.

The thickness distribution of the lava in Newtonian and Bingham cases is similar, as in both cases the lava thickness reaches approximately 20 m, whereas in the Herschel-Bulkley case it rises up to 23 m. The lava flow remains relatively hot (1150 K) in all three rheological models, cooling to 1000 K as it advances downstream. We see from Figure 7.7(the third raw) that the lowest temperature (800 K) occurs at the periphery of the flow.

Figure 7.8 illustrates that at 16 hours after the lava eruption and its advancement, the Newtonian and Bingham cases show the thickness distribution varying from 4 to 8 m. Meantime, in the Herschel-Bulkley case, the lava flow thickness reaches up to around 12 m at the flow front. At 32 hours of lava flow advancement, the lava reaches a maximum thickness of 18 m in the main flow branch in the Newtonian case. This main flow branch is narrower, while the flow length of the middle branch in the Newtonian case is longer than in the Bingham case. The Herschel-Bulkley case presents a similar flow thickness and width to the Newtonian case but lacks the development of the shortest branch. After 48 hours of modelling time, the Bingham case exhibits a significant increase in thickness at the flow front, reaching up to 20 m, with a broader spread in the main branch compared to the Newtonian case. By this stage the Herschel-Bulkley case demonstrates the lava advancement similar to the Bingham case, although with slightly greater thickness.

To better evaluate the impact of temperature on the lava flow advancement, we conducted an additional set of experiments using purely isothermal Newtonian, Bingham, and Herschel-

Bulkley rheological models and compared them with the temperature-dependent model results. The model domain, simulation duration, and constant discharge rate were kept consistent across both isothermal and non-isothermal models.

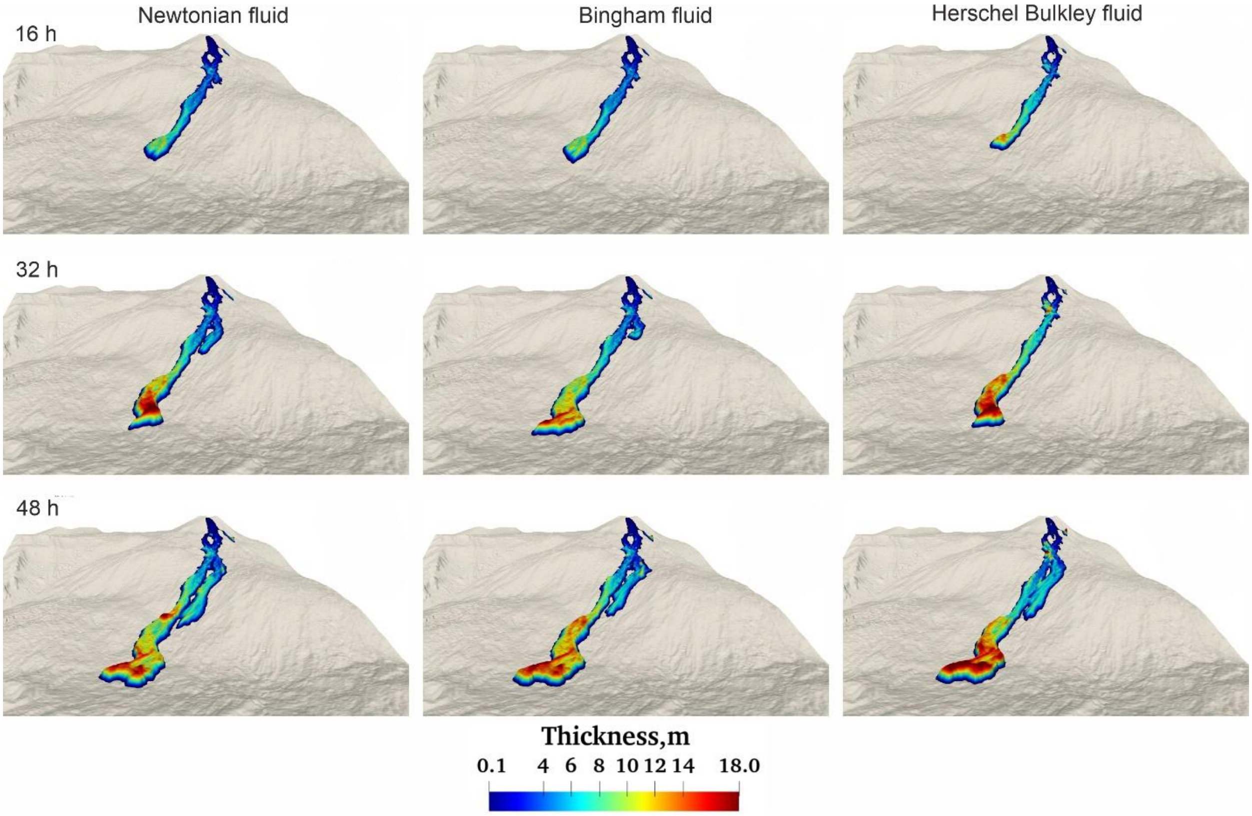

Figure 7.8: Lava flow advancement at 16, 32, and 48 hours showing the flow thickness in the case of three rheological models.

Figure 7.9 demonstrates the comparison between the results of isothermal and temperature-dependent (thermal) Newtonian rheological model. In these results, the isothermal lava flow spreads more widely and advances much faster than the thermal lava flow, eventually moving beyond the model boundaries within the same timeframe (Figure 7.9). The results from the thermal Newtonian case demonstrate that as temperature decreases, the viscosity of the lava increases, causing lava to thicken and thereby restricting its further advancement.

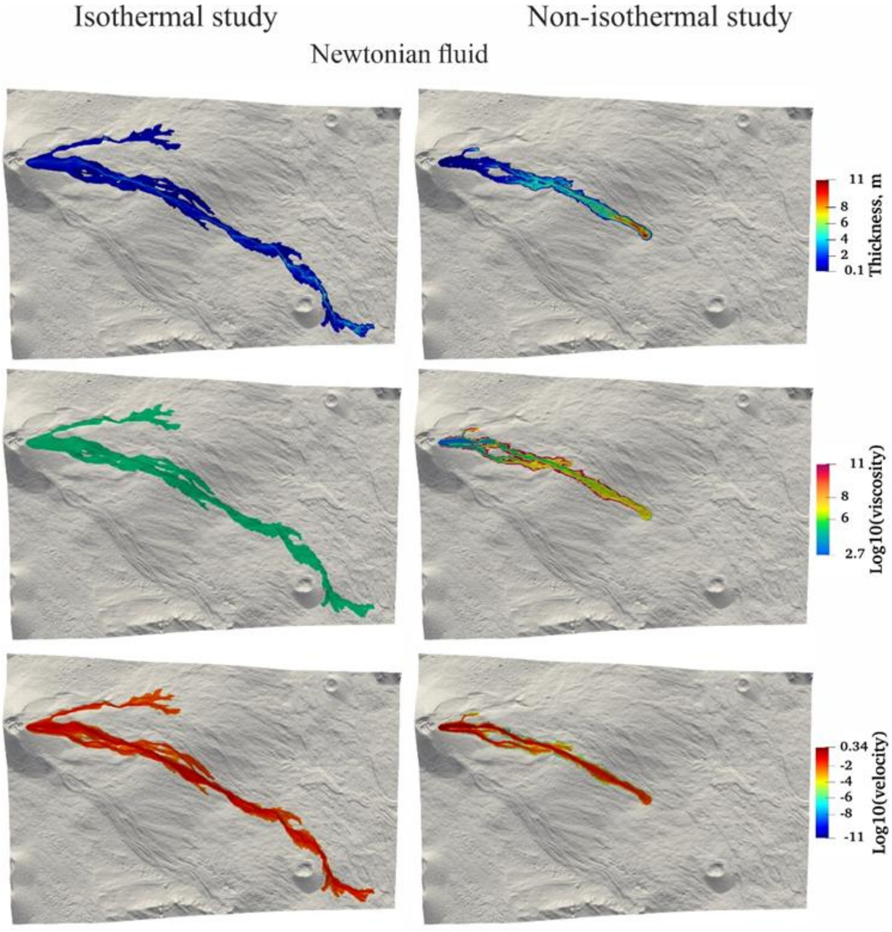

Figure 7.9: Comparison between isothermal (left hand side) and non-isothermal (right hand side) cases of the Newtonian rheology after 12 hours of the lava eruption.

In the isothermal Bingham case, the yield strength threshold is set to $\tau_0 = 10^4$ Pa. In the non-isothermal Bingham case, the yield strength varies with temperature. Figure 7.10 shows that the lava in the thermal case advances less than in the isothermal case due to increased thickness and high viscosity along the flow margins (Figure 7.10). The flow in the thermal case is narrower than in the isothermal case, indicating that the high viscosity along the flow margins prevents the fluid from spreading as easily as in the isothermal case.

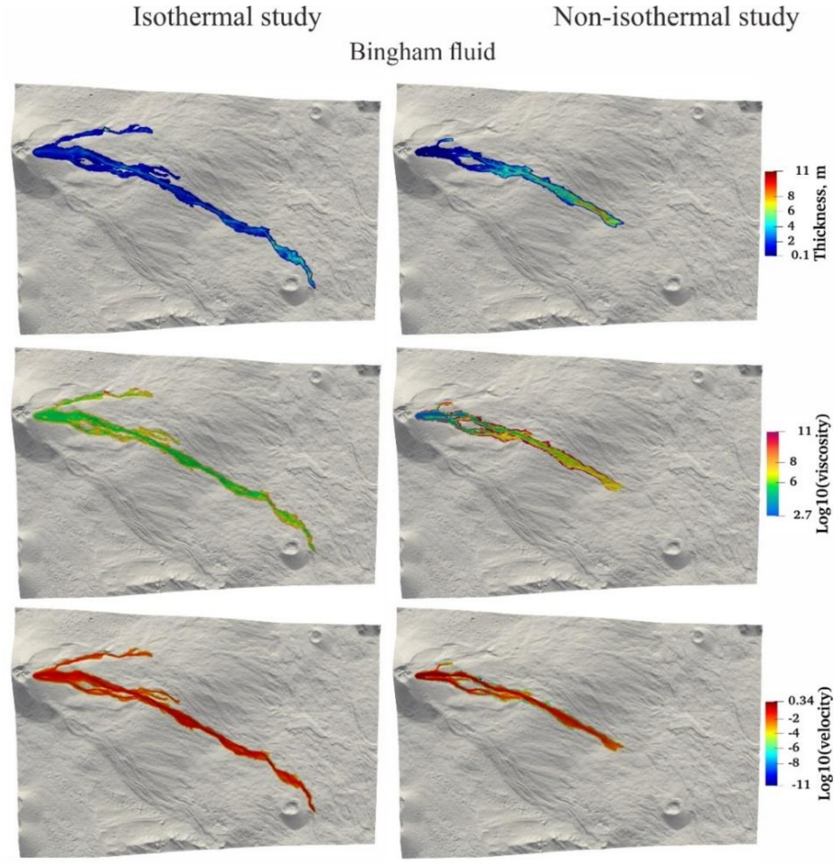

Figure 7.10: Lava flow advancement and its thickness in the isothermal case (the left panel for τ_0 =10^4 Pa) and non-isothermal case (the right panel) for the Bingham rheology at 12 hours after the lava eruption.

In the isothermal Herschel-Bulkley (HB) case, we set the yield strength value to τ_0 = 10^4 Pa. In the non-isothermal HB case, the yield strength varies with temperature. The lava in the isothermal HB case does not advance as far as in the previously discussed cases (Figure 7.9-Figure 7.10) suggesting that the nonlinear effects influence the lava flow morphology and restrict its rapid advancement. Comparing the isothermal and thermal HB cases we see that the flow width in the isothermal one is greater, the length of the flow is longer. The lava flow in the thermal case is much more compact and narrower and does not advance as far as in the isothermal case (Figure 7.11). This could be due to increased viscosity at the flow margins and the thickness accumulation at the front of the flow.

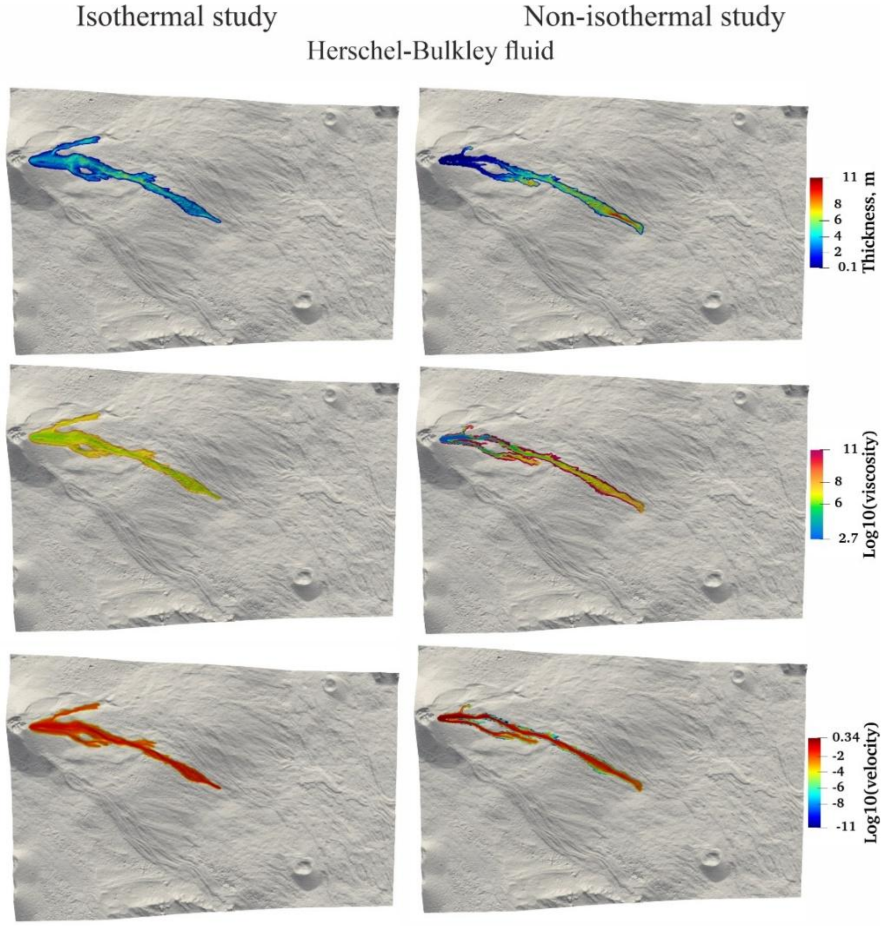

Figure 7.11: Lava flow advancement and its thickness in the isothermal case (the left panel for τ_0 = 10^4 Pa) and non-isothermal case (the right panel) for the Herschel-Bulkley rheology at 12 hours after the lava eruption.

7.7 Numerical modelling of lava flows at Mt. Etna during the 2015 eruption

In this section we apply a depth averaged model to simulate a lava flow that occurred in December 2015 at Mount Etna. During the modelling to accurately reproduce the lava deposits observed in the field, we adjust the effusion rate according to the data provided by Ganci et al. (2019). The main objective of this study is to evaluate the influence of the temperature dependent rheological models including Newtonian, Bingham and Herschel Bulkley fluids on the lava flow morphology.

7.7.1 Types of volcanic activities at Mount Etna and the December 2015 Etna Eruption

Mount Etna, Sicily is the most active volcano in Europe with a current height of 3400 m. Global Volcanism Program, 2013 considered Mt. Etna as one of the most persistently active volcanoes in the world. The eruptive activity usually originates from one or more of its four summit crates Voragine (VOR), Northeast Crater (NEC), Bocca Nuova (BN), and Southeast Crater (SEC). The volcanic activity on Mt. Etna in the summit and on its flanks is generally characterised by both effusive and explosive eruptions. Such eruptions can vary significantly in terms of eruptive style, magnitude and intensity (Rittmann A, 1973; Guest, 1982), continuously altering the morphology and topography of a summit area due to the accumulation of tephra and lava deposits. Although explosive eruptions have periodically occurred at Mt. Etna (Coltelli et al., 2000; Guidoboni et al., 2014) resulting in the ejection of tephra into the atmosphere, posing severe risks to aviation (e.g., Poret, Corradini, et al., 2018; Poret, Costa, et al., 2018), the major volcanic hazard is still related to the lava flow.

One of the indications of the effusive style dominance for the past 2000 years is that the flanks of Mount Etna are mainly covered by lava flow fields (Branca et al., 2011). The frequency of the effusive eruptions and the dense urbanization at the base of the volcano pose significant risks to the surrounding population. Many cities, villages and critical infrastructure have been repeatedly destroyed or damaged by lava flows (Barberi & Carapezza, 2004). Numerous studies have documented the consequences of such eruptions, noting their impacts on human settlements and infrastructure (Andronico & Lodato, 2005; Behncke et al., 2005, 2016; Rocco Rongo et al., 2011; Cappello et al., 2012, 2013; Negro et al., 2013).

In the December 2015 eruption at Mount Etna all four summit craters of the volcano produced a remarkable series of eruptive events. Our primary interest lies in the Strombolian effusive activity that originated at the New Southeast Crater (now referred to as SEC) during the eruption from December 6 to 8, 2015. This phase of the eruption was characterized over the next two days by moderate variations in the discharge rate (Ganci et al., 2019). The lava initially flowed eastward, spreading across the flat terrain of the Valle del Bove (Corsaro et al., 2017). The main flow advanced along the western wall of the Valle del Bove ultimately reaching a maximum length of 3.8 km, and an altitude of 1680 m above sea level (a.s.l.), close to the eastern base of the Mt. Centenari scoria cone. Two shorter lava flows, respectively 0.7 and 1.5 km long, advanced toward the Valle del Leone descending to an altitude of 2560 m a.s.l. (Corsaro et al., 2017). The lava flows accounted for the most of the eruption's emplacement covering an area of 435 x 10^3 m^2 and representing 86% of the total deposit volume. The bulk volume of the total deposits was estimated at 2.35 ± 0.85 x 10^6 m^3 (Ganci et al., 2019).

7.7.2 Model description and solution method

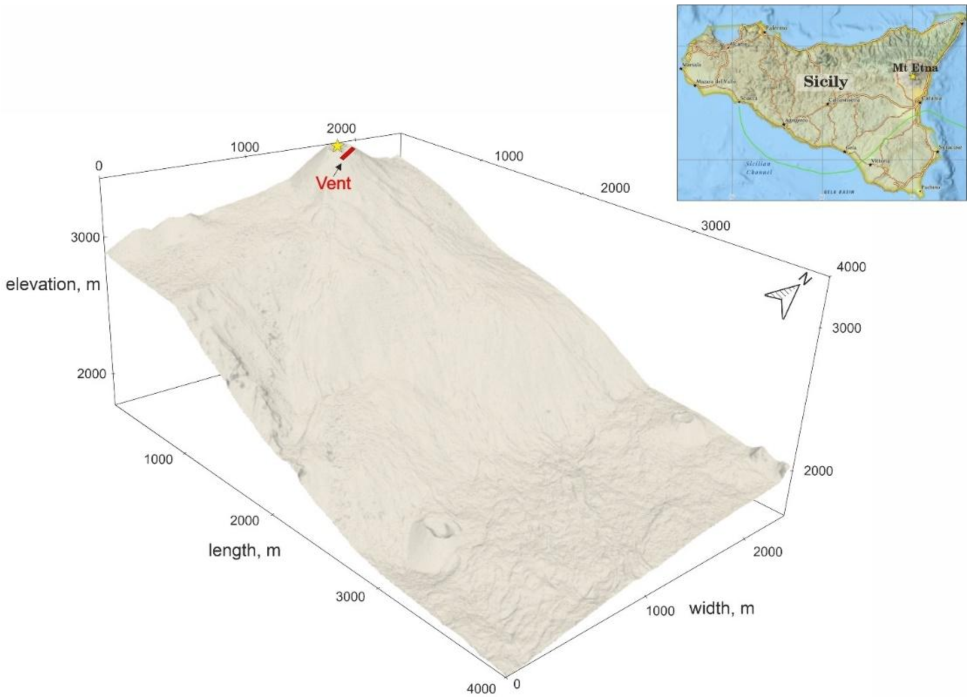

Figure 7.12: The terrain surface of the south-east flank of Mt. Etna (Ganci et al. 2019). The red rectangular marks the location of the model vent, the arrow indicates North, and the yellow star marks

the South-East Crater (SEC) of Mt. Etna. The insertion (top right corner) features a map of Sicily indicating Mt. Etna's SEC (maps source: NCEI.NOAA).

A depth-averaged flow model, based on the shallow water approximation (SWA) of the governing equations (Navier-Stokes, continuity and energy equations), is employed in this work. We use Eqs. (7.5)-(7.15) (see Section 7.2.3) to solve a problem of an incompressible laminar viscous fluid flow over a surface topography (Figure 7.12). The equations are obtained by averaging the governing equations over the flow thickness. This derivation assumes that the horizontal length scales are significantly larger than the vertical length scale, and that the vertical dynamics are negligible in comparison to the horizontal effects.

7.7.3 Numerical results

In this section, we present simulation results of the lava flow advancement during the effusive phase of Mount Etna's eruption from December 6 to 8, 2015. The simulation is based on the available topographic data and field observations of the eruption. As a topographic basis (Figure 7.12), we used the pre-eruptive Digital Surface Model (DSM) derived by Ganci et al. (2019) with a spatial resolution of 5 m which covers the summit craters area and a portion of the south-east flank of the volcano, including the Valle del Bove terrain. Since precise vent locations were unavailable, we empirically determined the vent area in the model to best approximate and align with observed eruptive features (Table 7.2). Below we develop the non-isothermal models using Newtonian, Bingham and Herschel-Bulkley fluids. The simulation results presented at time 48 hours.

Table 7.2 The model vent geometric description

Sub-area	X_c, m	Y_c, m	R, m
1 bottom	500316	4177709	16
2 upper	500268.47	4177803.41	23
3 middle	500283.47	4177746.41	30

To accurately reproduce the lava deposits observed in the field, we selected the average Total Area Discharge Rate (TADR) (Figure 7.13) observed during the eruption (Ganci et al., 2019). The modelled lava flow volume estimates 1.15 x 10^6 m ^{3} which matches the observed average lava flow deposition (Ganci et al., 2019). The model parameters value for typical Etna lava flows are listed in Table 7.1, with the exception that the fractional area of the exposed inner core (*f*) has been lowered to 0.14.

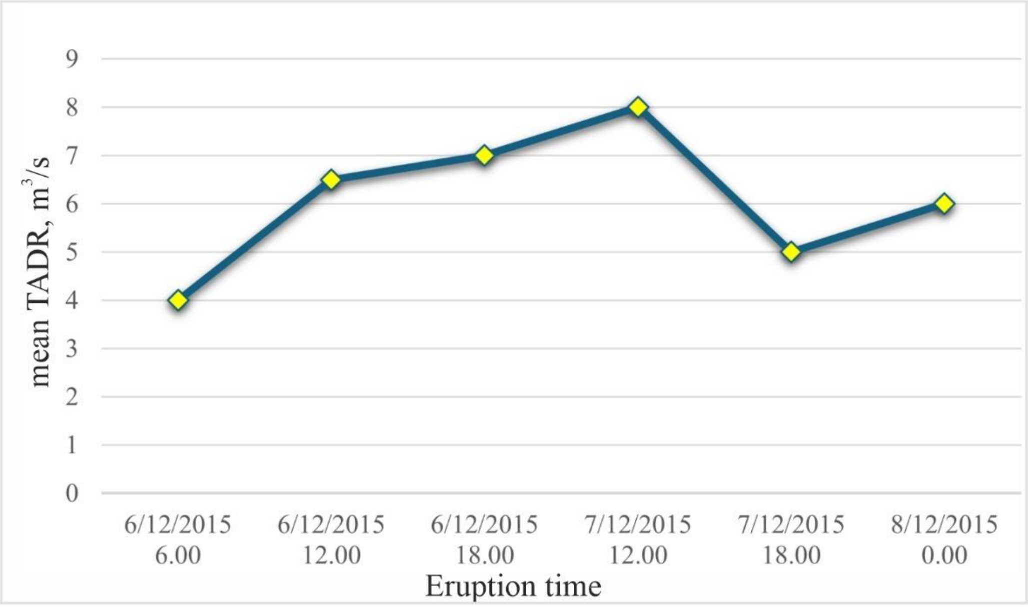

Figure 7.13: Mean values for TADR from 6 to 8 December 2015 Eruption at Mt Etna used in the model (data: Ganci et al. (2019)).

Figure 7.14 shows that the morphology of lava flows in Newtonian and Bingham cases are similar. The only difference between two cases is that the upper branch of lava flow advances further in the Newtonian case than in the Bingham case. The distribution of the temperature, viscosity and velocity in both cases are very close. The HB case shows a distinct difference from above mentioned cases. The viscosity in the HB case is higher than in the Newtonian and Bingham, which doesn’t allow the flow advance further.

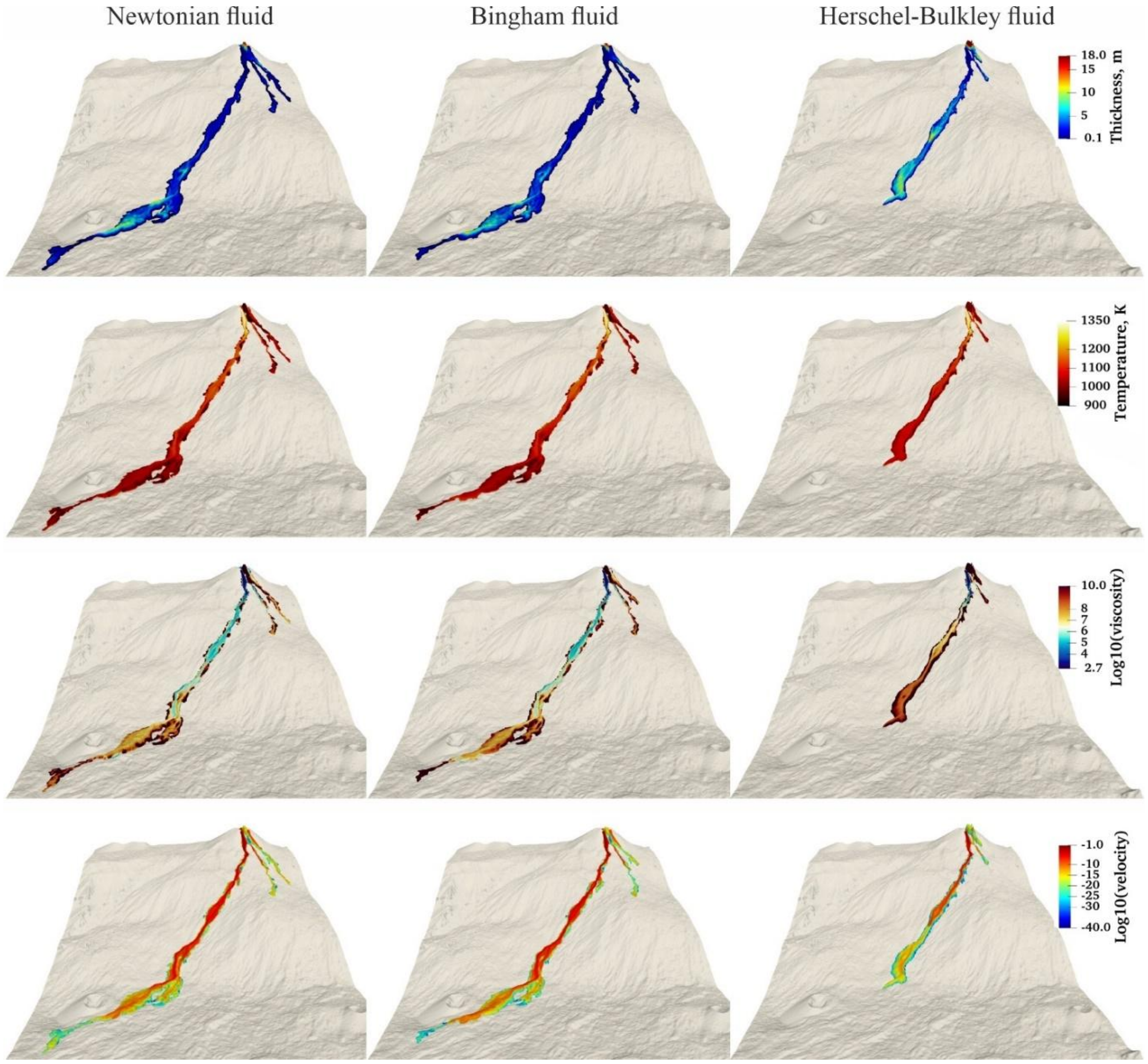

Figure 7.14: The modelled thickness, temperature, viscosity and velocity distributions in Newtonian, Bingham and Herschel-Bulkley (HB) cases presented at time 48 hours.

We want to note that the observed lava flow near the volcano crater developed a thickness of approximately 20 meters, and our modelling results closely replicate this pattern. Specifically, the thickness in both the Newtonian and Bingham modelled cases reaches 20 meters in this region, whereas the Herschel-Bulkley case results in a slightly greater thickness of around 25 meters. We suggest that the combination of the effusion rate and the presence of the irregularities in the topography (such as a pit located near the crater) likely caused lava to accumulate, resulting in the observed thickness.

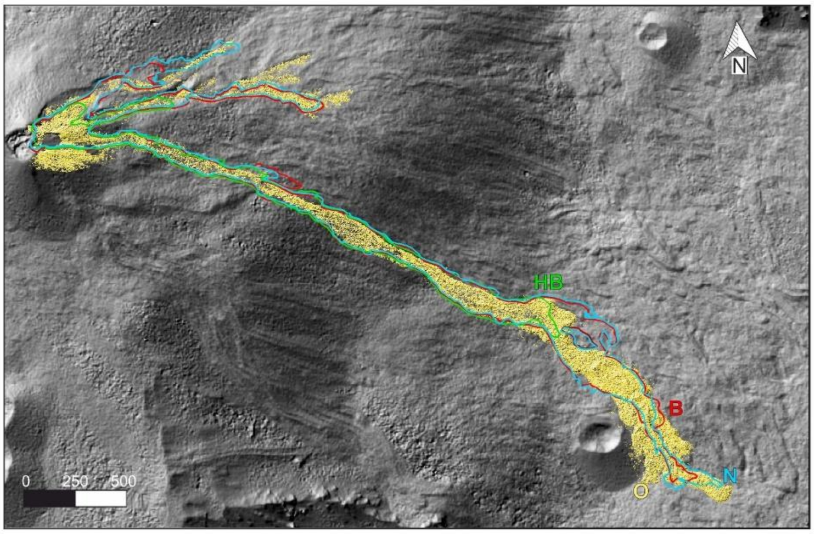

Figure 7.15: The comparison between modelled lava contours in the Newtonian (the blue contour with index N), Bingham (the red contour with index B) and Herschel-Bulkley rheological models (the green contour with index HB) with the real lava flow emplacement from the December 2015 eruption at Mt. Etna (the yellow surface).

Figure 7.15 shows the comparison between modelled lava flow contours and the real lava flow emplacement. All modelled contours capture perfectly the observed flow width and spread developing three branches as observed in the reality. The HB case represented by green contour doesn’t advance in the main branch as far as the real lava flow. The misfit could be explained by an elevated viscosity which leads to the rapid solidification. We can also see that the same situation is happening in the upper two branches, both modelled upper branches do not reach the observed distances. The Bingham case demonstrated by the red contour show better fit to the real lava emplacement in comparison to the HB case. The main lower modelled branch captures perfectly the real flow widths and almost reaches the flow distance. The upper modelled branch doesn’t advance as the real one, however the middle-modelled branch almost captures the observed flow length. The Newtonian case represented by the blue contour matches the best the observational contour. The lower modelled branch fits almost perfectly to the real flow branch showing a good agreement in both length and width of the flow. Only in the Newtonian case the length of the modelled and observed branches are very close. The only observed qualitative discrepancy is that the modelled middle branch is not divided into three little streams as we see in the observations.

Figure 7.16 presents the influence of the solidification parameter on lava flow advancement. Simulations were conducted using the Bingham model and the varied TADR, based on data in

Figure 7.12 (Ganci et al., 2019). As shown in Figure 7.16, reducing the crust parameter enables the lava to advance further.

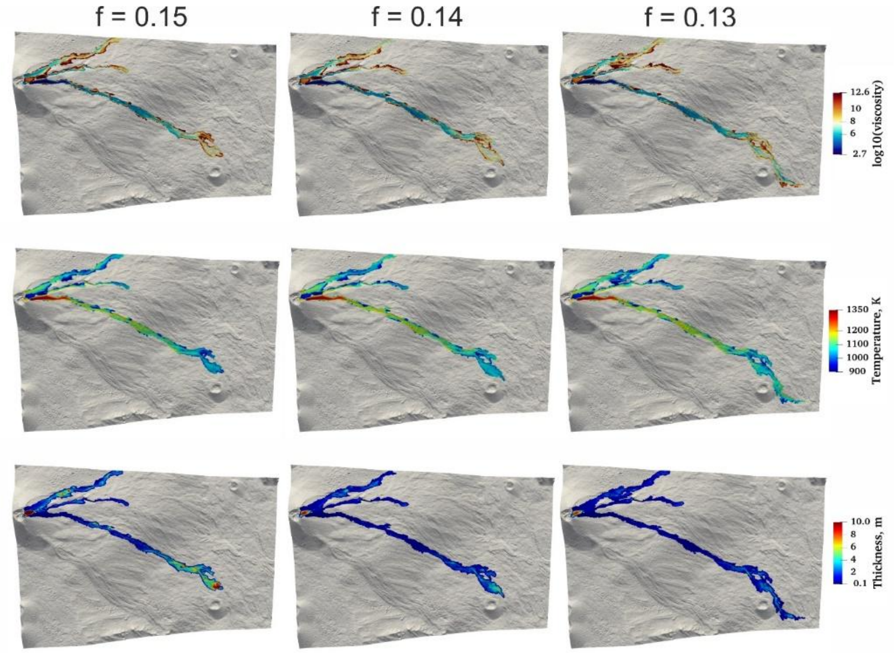

Figure 7.16: The modelled viscosity, temperature and thickness of lava flow for different crust existence parameters; left panels f = 0.15, middle panels f = 0.14, right panels f = 0.13 at time 48 hours.

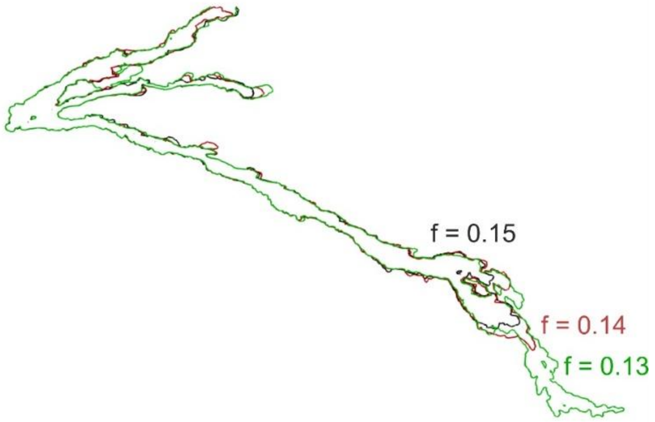

Figure 7.17: Comparison of the lava flow contours modelled using three different crust existence parameters at time 48 hours.

Figure 7.17 displays the comparison between the modelled contours with varying value for the solidification parameter. We clearly see that even slight decreasing of the parameter value significantly affects the lava morphology. The lava instead of advancing downstream accumulates thickness.

7.8 Discussion and conclusion

In this work we examined the influence of rheological models, including Newtonian, Bingham and Herschel-Bulkley fluids, under isothermal and non-isothermal conditions, on lava flow morphology. We verified the 3-D numerical codes and the 2-D depth averaged model against the analytical solution for the axisymmetric viscous gravity currents problem. To access the impact of temperature on lava flow morphology, we performed a set of simulations using temperature dependent Newtonian, Bingham and Herschel-Bulkley rheological models. Additionally, we conducted experiments modeling isothermal fluid flow for Newtonian, Bingham, and Herschel-Bulkley cases to better reveal the impact of temperature on the lava flow morphology. To compare the results with the observations, we applied Newtonian, Bingham and Heschel Bulkley rheological thermal models to simulate a natural lava flow emplacement, using observational data from the December 2015 eruption at Mt Etna.

To validate the numerical codes, we conducted a classical benchmark test against the analytical solution of fluid flow motion under gravity, originally performed by Huppert (1982). The results across all three numerical codes show good agreement with Huppert's solution. Given that both Huppert's solution and the depth averaged model share the shallow water approximation as a foundational principle, the SWE model exhibits the best agreement with the analytical solution. Numerical results from Fluent and OpenFOAM slightly deviate from the analytical solution, which can be either attributed to the complexity of the 3-D models and limitation in the vertical resolution defined by the mesh or the based-on assumptions and simplifications in the analytical solution. Comparing Fluent and OpenFOAM with the analytics, we see that the results from Fluent match better the analytical solution than those from OpenFOAM.

The importance of rheology in lava flow modelling cannot be underestimated. Rheology governs flow behaviour and influences the morphology of advancing lava. Newtonian fluids under the gravity force, characterized by constant viscosity under isothermal conditions, offer a simple representation, but most lava behaves as a non-Newtonian fluid with varying viscosity depending on the strain rate and shear stress. Isothermal modelling of lava flow using different rheological models confirmed the consistency of AFT and OFM model results, as both codes are based on the finite volume and volume of fluid methods. The thickness and velocity distributions in both 3-D models show close resemblance confirming the robustness of the models. The modelled results in the SWE model slightly differ from the 3-D modelled results. The modelled lava flow advances further in the isothermal case of the Newtonian fluid, while the modelled lava in the cases of Bingam and Herschel-Bulkley fluids seizes its advancement with the increase of the yield strength threshold. The deviation can be attributed to the fundamental assumption of the depth averaged model, being that SWE is valid only when the horizontal component is much larger than the vertical one. The results highlight the influence of non-linear rheology and the yield strength on lava flow morphology even under isothermal conditions. Lavas with higher yield strength in Bingham or Herschel-Bulkley models, tend to flow shorter distances compared to Newtonian model. For example, lava flows with higher yield strength tend to form more compact, dome-like structures rather than extensive flows (Cashman et al., 1999; Pinkerton & Stevenson, 1992). Thus, the nonlinearity not only affects flow distance but also modifies flow thickness, a feature critical in the understanding of lava emplacement dynamics and hazard assessments.

To access the effect of temperature variation on lava flow morphology we conducted numerical simulations using the SWE model. In these experiments we extended the modelling time and enlarged the modelled domain to show the influence of the thermal effects occurring due to the combined impact of radiation, convection, conduction and viscous heating. The results demonstrate similar viscosity distributions in Newtonian and Bingham thermal cases ranging from $10^{2.7\text{-}6}$ Pa s in the central parts of the flow branches to 10^{12} Pa s at the flow margins. The lava in the Herschel Bulkley thermal case exhibited higher viscosity values, reaching up to 10^{16} Pa s along the periphery of the flow. To better reveal the impact of temperature on lava flow morphology we performed additional experiments, simulating lava flow under the same conditions (same modelling time and same model domain) but now without accounting for temperature. Comparing the isothermal cases with the thermal ones, we observe that lava in the isothermal cases advances faster and more broadly, and within the same modelling time it spreads beyond the boundary of the model domain, whereas in the thermal cases lava ceases its rapid advancement due to increased thickness at the flow front and high viscosity. The lava flow in the thermal cases exhibits narrower flow width since the highest viscosity values are observed at the periphery of the flow.

Lastly, we applied Newtonian, Bingham and Heschel Bulkley rheological models to simulate a natural lava flow emplacement, using observational data from the December 2015 eruption at Mt Etna. The eruption from December 6 to 8, 2015 demonstrated the Strombolian effusive activity that originated at the New Southeast Crater (now referred to as SEC) and was characterized by moderate variations in the discharge rate over the next two days. To accurately simulate the observed lava deposits, we varied the average TADR based on the data recorded during the eruption. As a result, the modelled lava flow volume matches the observed average lava flow deposition (Ganci et al., 2019). Each rheological model accurately captures the observed flow width and the development of the three lava flow branches. The Heschel Bulkley case due to higher viscosity doesn’t match the observed lava flow extent. The Bingham model provides a closer match to the real emplacement, although the modelled upper branch does not extend as far as observed. The Newtonian model shows the closest resemblance to the actual flow, matching the observed width and extent across all three branches. Additionally, the modelled thickness distribution closely matches the observational data, demonstrating lava accumulation near the volcano crater and at the flow front, particularly in the cases of Newtonian and Bingham fluids.

Authors contribution

AIZ, IT, and NZ (a PhD student) contributed to the conceptualization of the paper. NZ and IT processed the data, developed a numerical model and performed numerical experiments. IT contributed to the development of numerical codes. AIZ, IT and NZ contributed to interpretation of the results and performed writing–original draft preparation and figures.

Chapter 8: Conclusion and future work

In this work we performed the numerical modelling of effusive type of volcanic activity. The first part of the thesis is related to the numerical modelling of lava domes. We explore the dynamics of the endogenous long forming lava dome building at Volcán de Colima from 2007 to 2009. This particular dome growth was characterised by low discharge rates and an uninterrupted magma extrusion.

The isothermal modelling of lava dome growth at Volcan de Colima showed that:

i. Crystal-free magma viscosity controls the height and extent of lava domes.
ii. The increasing of the relaxation time leads to the horizontal advancement of lava.
iii. The extrusion rate controls the overall volume of the extruded lava.
iv. The real crater base was most likely inclined westward on the left side of the vent and was flat on its right side.
v. The modelled viscosity distributions are consistent with the lava viscosities at Volcan de Colima ranging from 10^9 to 10^{12} Pa s.
vi. The carapace formation plays an important role in long dome forming eruptions. The modelled dome in this case developed a steep flank on its left side, which fits observations at Volcán de Colima rather well, the modelled dome heights at different growth stages are in a good agreement with the observations.

The thermo-mechanical modelling of lava dome growth at Volcan de Colima demonstrated that:

i. Convective heat loss at the lava air interface promotes the development of a high viscous carapace. The carapace restraints the horizontal advancement forcing the upward dome growth.
ii. Non-linear convective-radiative heat flux results in an even thicker carapace, leading to higher modelled lava dome height compared to the case with convective heat transfer.
iii. The release of the latent heat due to crystallization leads to the temperature elevation within the dome. The increased temperature within the dome interior promotes dome

flattening and its lateral advancement to the right. The lava is more fluid within the dome due to relatively low viscosity and high temperature and cooled and rigid (due to convective or convective-radiative heat loss) in the upper lava-air layer of the dome.

iv. The viscous heating is negligible in the models where the conduit doesn't represent a long narrow channel. The shear rates in our case are much smaller than those in narrow conduits, therefore the change in the lava viscosity due to the viscous dissipation is almost invisible.

v. The changes in the thermal boundary conditions do not significantly affect the morphological shape of the lava domes but influence the distribution of the crystal content and temperature within the modelled dome.

vi. While changes in the initial value of the volume fraction of crystals do not influence the dome dynamics and its morphology (since the crystals had already reached equilibrium in the conduit due to the prolonged dome growth), the temperature dependent volume fraction of crystals at the equilibrium state leads to a slight decrease in the lava viscosity. This decrease is caused by the delayed crystallization due to the latent heat release, which results in a flattening of the lava dome and its horizontal advancement.

Application of the thermo-mechanical model to simulate the long-term lava dome growth at Volcán de Colima from 2007 to 2009:

i. The modelled domes forms a carapace which restrains the lateral advancement of the lava and develops steep flanks.

ii. The modelled morphology closely matches the observed morphology at Volcan de Colima, with a few metres difference in the dome length.

iii. The modelled dome heights at different growth stages closely align with the observed lava dome heights at Volcán de Colima.

We want to note that the dynamics of dome growth can be more complicated than assumed in our studies due to various processes occurring during the dome formation (e.g., magma decompression, degassing, pore-fluid dynamics, the strain-rate dependent viscosity, crystal size and other rheological properties of the erupted lava). Therefore, it is important to acknowledge that no numerical model can fully represent the exact processes driving lava dome growth dynamics. The models presented in our studies account for the main dynamic processes and characteristics within the shallow conduit and the lava dome, such as the mass and heat transfer, the degassing-induced crystallization kinetics, latent heat of crystallization, convective and radiative heat flux at the lava interface with the air, conductive heat flux at the crater surface and the shallow conduit wall, and lava viscosity as a function of the volume fraction of crystals and temperature. Additionally, we have systematically demonstrated the effect of each parameter on the dome morphology, beginning with a simplified model and progressively developing it into a more comprehensive one that includes all the aforementioned processes.

The developed isothermal and thermomechanical models of the lava dome evolution can be used at other volcanoes during effusive eruptions, long episodes of lava dome building and the dome carapace formation. It is also possible to further incorporate the water content and strain-rate dependence into the lava viscosity model. We plan to perform a study of the dome growth that couples the processes appearing within both the conduit and the dome. Such a model could shed light on how the lava dynamics in the conduit influence the dynamics within the dome.

The second part of this thesis is related to the numerical modelling of lava flows. In this work we study the lava flow dynamics from the December 2015 eruption at Mount Etna. The eruption was characterised by the Strombolian effusive activity and moderate fluctuations in the observed discharge rates.

Using GPUFLOW model, we showed that:

i. Increasing of the volume fraction of crystal content value either at the lava eruption or at the equilibrium state) leads to a reduced advancement of the lava flow; favours vertical growth of the lava flow and results in slower lava flow advancement due to the higher viscosity caused by crystallization.

ii. When relaxation times are longer than the lava flow runout times, the crystal content grows slowly allowing the lava flow to advance farther at a viscosity close to the melt viscosity.

iii. Lowering the melt viscosity facilitates a lava to flow, elevating the melt viscosity encourages shorter and thicker lava flows.

iv. The slope angle of the volcano topography, yield strength, and melt viscosity influence the critical lava thickness and thus control lava advancements. The interplay between these parameters can alter the direction of flow, thickness and advancement pattern.

Using a three-dimensional fluid dynamics model and its simplified depth-averaged model we showed:

i. In the case of isothermal flow models, the increased yield strength significantly influences lava flow morphology by restricting flow advance and promoting upward growth of lava flows.
ii. In the case of thermal rheological models, the Newtonian and Bingham fluids demonstrate similar lava flow morphologies and thickness distributions.
iii. The Herschel-Bulkley model due to the highest viscosity values results in the shortest flow across all three thermal rheological models.
iv. Comparing the isothermal cases with the thermal cases: in the isothermal cases the lava advances faster and more broadly, whereas in the thermal cases the lava ceases its rapid advance due to the increased thickness at the flow front and the high viscosity.

Application of Newtonian, Bingham and Heschel Bulkley thermal rheological models to simulate the natural lava flow emplacement from the December 2015 eruption at Mt Etna:

i. Each thermal rheological model accurately captures the observed flow width and the development of the three lava flow branches.
ii. The Herschel-Bulkley case, due to its higher viscosity, do not match the observed lava flow extent.
iii. The Bingham model provides a closer match to the real emplacement, although the modelled upper branch does not extend as far as observed.
iv. The Newtonian model shows the closest resemblance to actual flow, matching the observed width and extent of all three branches.
v. The modelled thickness distribution in the cases of Newtonian and Bingham fluids closely matches the observational data, demonstrating lava accumulation near the volcano crater and at the flow front.

To validate the numerical codes used in the study, we performed benchmark tests against the analytical solution of the axisymmetric viscous gravity current problem. The results of the numerical models align closely with the analytical outcome.

Lava has a complex nature and consists of melt, crystals, volatiles and bubbles. The viscosity of lava can vary significantly, ranging from a low-viscosity regime that allows for long-distance flow to a high-viscosity regime that results in the formation of levees and domes. As a future direction for lava flow simulations, the lava viscosity model could be further developed to incorporate the effects of bubbles. While we have previously explored the impact of crystals and melt on lava flow advancement separately, it would be valuable to investigate the combined effects of both parameters on lava morphology.

Appendix

A1: Appendix Numerical Approach for simulating the development of a highly viscous dome carapace

The numerical solver uses an implicit scheme of integration for the governing equations (Eqs. 1-5) with the relevant boundary and initial conditions described in sec. 3.2. The model domain is discretized by about 54,000 hexahedral cells. The pressure is discretized by the second-order staggered scheme PRESTO! (e.g., Peyret (1996)). To approximate the Laplacian, we use the numerical scheme of the second-order accuracy, and the monotonic schemes are used to discretize convective terms in the equations (e.g., Ismail-Zadeh & Tackley (2010)). The pressure-velocity coupling is handled by the SIMPLE method (S. V. Patankar & Spalding, 1972), where the relaxation parameters are chosen to be 0.015 and 0.3 for the velocity and pressure, respectively. We assign 0.5 to the relaxation parameter for the function α , and the volume fraction of crystals. Considering a discontinuity between the lava and air viscosities, the choice of the relaxation parameters is critical and sometimes it was lowered to ensure the solution's stability. A time step is chosen in the range of 0.1 to 40 s depending on the stability and optimization of the velocity to assure a convergence of a set of linear algebraic equations (SLAE), which is obtained after the discretization of the Navier-Stokes equations. The implicit scheme results in stable computations with a relatively large timestep. We note that an employment of explicit schemes in the model led to unstable numerical results even for the small Courant number. In the modelling, we employ the conjugate-gradient method to solve SLAE. The numerical accuracy attains 10^{-3} for the velocity and pressure and 10^{-6} for the function α and the volume fraction of crystals. Numerical experiments were carried out on the multi-processor high-performance computer (bwHPC) of the Karlsruhe Institute of Technology. In the modelling, 1 day of the lava dome evolution takes about 4 min of the computational time depending on the time step size.

The problem of magma extrusion and lava dome growth involves the interface between the lava and the air. Numerical schemes usually produce errors, originating from discontinuities of physical parameters at the interface (e.g., the density and viscosity), and related smearing of the parameters along the interface. To minimize such errors and smearing, special numerical methods have been developed: the methods are rather simple for the case of discontinuous density (e.g., Christensen, 1992; Naimark & Ismail-Zadeh, 1995), but more difficult for the case of discontinuous viscosity (e.g., Naimark et al. (1998)). In this modeling the viscosity jump at the lava-air interface is significant (many orders of the magnitude), and this generates indeed smearing at the interface. To reduce the smearing, a finer mesh can be introduced around the interface.

At the initial time $t = 0$ the conduit (sub-domain Ω_1) is filled by the old magma. To determine the initial velocity in the entire model domain, we consider $\mathbf{u}(t = 0, \mathbf{x}) = 0$ and small time step (10^{-1} - 10^{-3} s), and perform a numerical experiment for 100 to 1000 time steps. The velocity obtained at the end of this experiment we take as the initial velocity $\mathbf{u}_0$ to run further computations with larger time steps. We note that the Reynolds number for the lava dome dynamics is small for the slow flow and the high lava viscosity, and hence, the influence of the inertial terms in the Navier-Stokes equations is insignificant. Therefore, the initial condition for velocity influence insignificantly the dynamics of lava flow and dome growth evolution. On the contrary, the Reynolds number is large for the air dynamics, and the inertial terms play a significant role. The described approach yields to a laminar flow in the air subdomain ensuring the stability of further calculations. The influence of the air phase on lava dome growth is negligible because of a large density and viscosity contrast between the magma and the air.

To simulate numerically the development of a highly viscous dome carapace due to cooling, a ‘thermal boundary layer’ is introduced at the interface between the lava dome and its surrounding. This allows to avoid introducing and solving the heat equation, and hence do not complicate the existing model. In experiment 10, the viscosity of the boundary layer is assumed to be by a factor of 200 higher than the viscosity of the dome core. The thickness of the layer is about 5-6 computational cells adjacent perpendicularly to the interface, and each cell is of about 1 m thick. Figure A1 presents the model carapace.

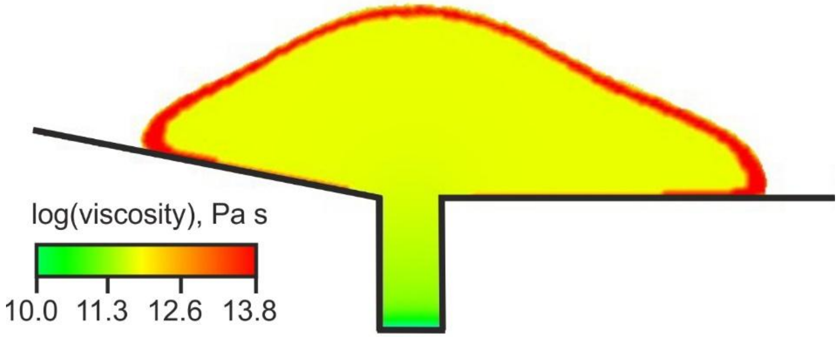

Figure A1: A layer (red) of the higher viscosity introduced in numerical experiment 10 to simulate a dome carapace.

A2: Appendix Determination of the model extrusion rates using the extruded lava volume data

Since January 2007 a slow endogenous growth of the lava dome continued until the end of 2009. Figure 3.2 presents the values of the lava dome volume and the discharge rates U_{dis} (m^3 s^{-1}) for the time intervals, where the data on the dome lava volumes have been available (Figure 3.2a). When solving numerically 2-D models of the lava extrusion, difficulties arise with the calculation of the model extrusion rate, which will correspond to the observed effusion rate. Below we derive the formulas for conversion of the observed discharge rate U_{dis} into the model extrusion rate u_{ext} (measured in m s^{-1}), which have been used in our 2-D model. This approach is applicable in the case of endogenous lava dome growth.

We approximate a lava dome shape by a half-spheroid with the equal *a*- and *b*-semi-axis ($a = b$) and height *c* (Fig. A2). In Fig. A2, *r* is the radius of the conduit, z^* is the height of the lava dome, $r + x^*$ is the radius of the lava dome, d_x and d_z are the increments of the radius and height of the lava dome for the time t_2 - t_1, respectively. We calculate the difference between the volume V_2 of the outer half spheroid (the volume of lava at time t_2) and the volume V_1 of the inner half-spheroid (the volume of lava at time t_1). This difference will characterize the volume of the lava extruded for time interval t_2 - t_1.

$$\frac{1}{2}\left[V_2 - V_1\right] = \frac{2\pi}{3}\left[(r+x^*+d_x)^2(z^*+d_z)-(r+x^*)^2 z^*)\right] =$$
$$\frac{2\pi}{3}\left[(r+x^*)^2 d_z + (2(r+x^*)+d_x)(z^*+d_z)d_x\right] \tag{A2.1}$$

The volume of the extruded lava for time interval t_2-t_1 can be found using the discharge rate as $U_{dis}(t_2 - t_1)$. Hence Eq. (A1) can be re-written as:

$$U_{dis}(t_2 - t_1) = \frac{2\pi}{3}\left[(r+x^*)^2 d_z + (2(r+x^*)+d_x)(z^*+d_z)d_x\right] \tag{A2.2}$$

Considering the 2-D case study, we calculate the difference between the area of the cross-section through the center of the outer half spheroid S_2 at time t_2 and the area of the cross-section through the center of the inner half-spheroid S_1 at time t_1. This difference will characterize the area of the lava, which was extruded during time interval t_2 - t_1:

$$\frac{1}{2}\left[S_2 - S_1\right] = \frac{\pi}{2}\left[(r+x^*+d_x)(z^*+d_z)-(r+x^*)z^*\right] = \frac{\pi}{2}\left[d_x z^* + (r+x^*)d_z + d_x d_z\right] \tag{A2.3}$$

The lava area extruded for time interval t_2-t_1 equals to $2u_{ext} r(t_2 - t_1)$, and Eq. (A3) can be re-written as:

$$2u_{ext} r(t_2 - t_1) = \frac{\pi}{2}\left[d_x z^* + (r+x^*)d_z + d_x d_z\right] \tag{A2.4}$$

Inserting (t_2 - t_1) from Eq. (A2) into Eq. (A4) we can get the conversion formula from the observed discharge rate to the model extrusion rate:

$$u_{ext} = \frac{3\left[d_x z^* + (r+x^*)d_z + d_x d_z\right]}{8r\left[(r+x^*)^2 d_z + (2(r+x^*)+d_x)(z^*+d_z)d_x\right]} U_{dis} \tag{A2.5}$$

The parameters x^*, z^*, d_x, and d_z are accessed from the images of the 2-D morphological shapes of the growing lava dome (see Figure 3.1e; Bretón-González et al., 2013). The extrusion rate u_{ext} is then calculated using Eq. (A5), where the discharge rate U_{dis} is presented in Figure 3.2b. This extrusion rate is used in numerical experiments 7-9.

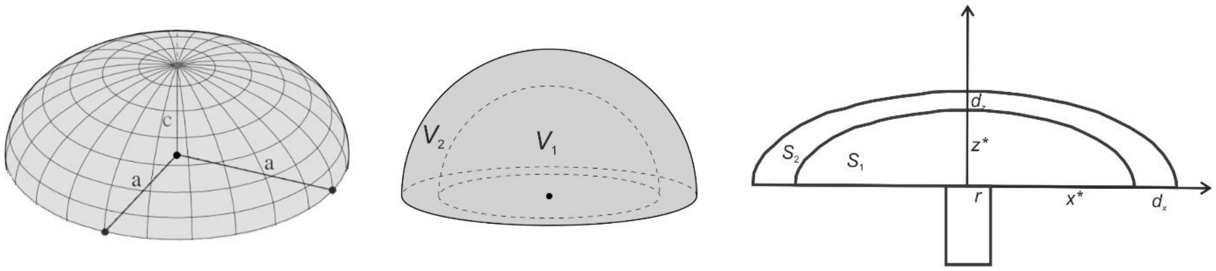

Figure A2: Geometry of the half-spheroid (left and central panels) and the 2-D cross-section of the half-spheroid (right panel).

B: Appendix Heat source due to the viscous dissipation

We have shown that the effect of the viscous dissipation on the thermal state and dynamics of lava dome is negligible. Here we provide a justification for that. In the case of exp. 1.1, the heat equation Eq. (4.3) takes the form:

$$\frac{\partial(c\rho T)}{\partial t}+\nabla\cdot\left(\mathbf{u}(c\rho T)\right)=\nabla\cdot\left(k\nabla T\right),$$

and in the case of exp. 1.2, the heat equation is presented as

$$\frac{\partial(c\rho T)}{\partial t}+\nabla\cdot\left(\mathbf{u}(c\rho T)\right)=\nabla\cdot\left(k\nabla T\right)+VD,$$

where $VD=\eta\left(\nabla\mathbf{u}+\nabla\mathbf{u}^T\right):\nabla\mathbf{u}$ is the viscous dissipation. See the main for the heat equation and exps 1.1 and 1.2.

Figure B1 presents the temperatures in exp. 1.1 (left column) and exp. 1.2 (right column). We see that the temperature difference is negligible (within 1K). To understand the contribution of the viscous dissipation to this small temperature change, we have calculated the heat conduction term $\nabla\cdot\left(k\nabla T\right)$ (Figure B2a) and the viscous dissipation term *VD* (Figure B2b). The contribution of the heat conduction term to the right-hand side of the heat equation is about 4-5 orders of magnitude larger than the contribution of the viscous dissipation. This explains the insignificant change in the model results in exp. 1.2 compared to exp. 1.1.

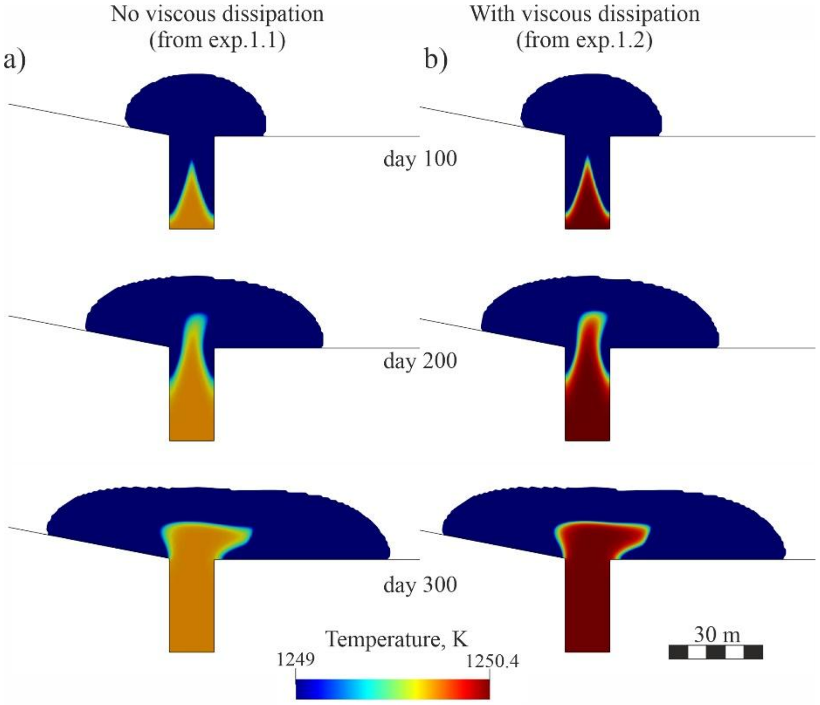

Figure B1: Temperature distribution in the models of lava dome growth in exps. 1.1 (a) and 1.2 (b).

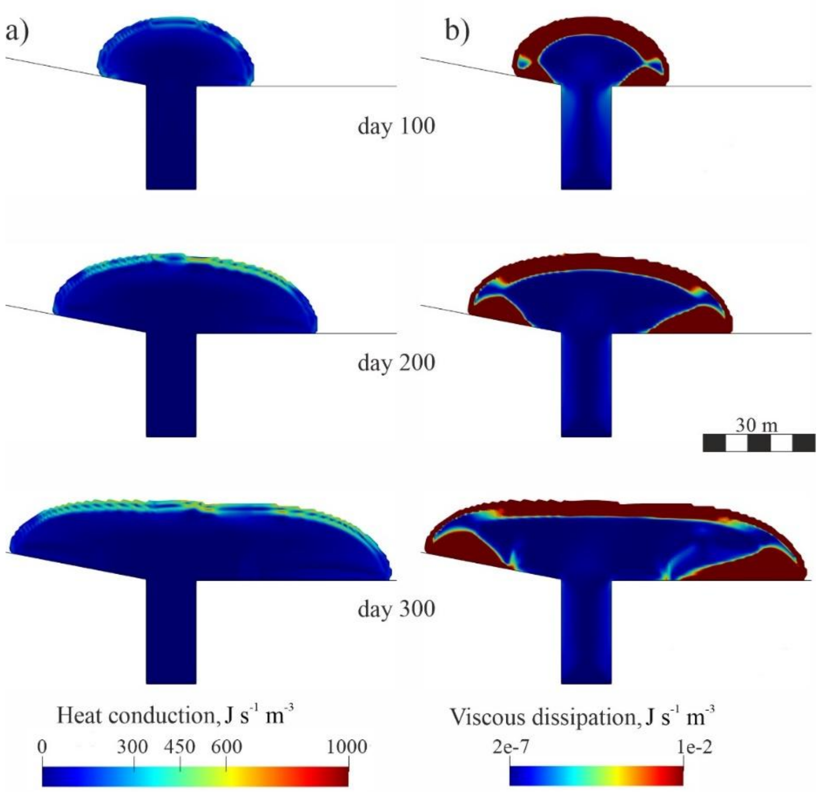

Figure B2: The heat conduction term (a) and the viscous dissipation term (b) in exp. 1.2.

Bibliography

Acocella, V. (2021). *Volcanoes and Volcanic Activity* (pp. 1–39). https://doi.org/10.1007/978-3-030-65968-4_1

Adam, G., & Gibbs, J. H. (1965). On the Temperature Dependence of Cooperative Relaxation Properties in Glass-Forming Liquids. *The Journal of Chemical Physics*, *43*(1), 139–146. https://doi.org/10.1063/1.1696442

Allard, P., Carbonnelle, J., Dajlevic, D., Bronec, J. Le, Morel, P., Robe, M. C., Maurenas, J. M., Faivre-Pierret, R., Martin, D., Sabroux, J. C., & Zettwoog, P. (1991). Eruptive and diffuse emissions of CO2 from Mount Etna. *Nature*, *351*(6325), 387–391. https://doi.org/10.1038/351387a0

Anderson, S. W., & Fink, J. H. (1990). *The Development and Distribution of Surface Textures at the Mount St. Helens Dome* (pp. 25–46). https://doi.org/10.1007/978-3-642-74379-5_2

Andronico, D., & Lodato, L. (2005). Effusive activity at Mount Etna volcano (Italy) during the 20th century: A contribution to volcanic hazard assessment. *Natural Hazards*, *36*(3), 407–443. https://doi.org/10.1007/s11069-005-1938-2

Angell, C. A. (1991). Relaxation in liquids, polymers and plastic crystals — strong/fragile patterns and problems. *Journal of Non-Crystalline Solids*, *131–133*, 13–31. https://doi.org/10.1016/0022-3093(91)90266-9

Avolio, M. V., Crisci, G. M., Di Gregorio, S., Rongo, R., Spataro, W., & Trunfio, G. A. (2006). SCIARA $\gamma 2$: An improved cellular automata model for lava flows and applications to the 2002 Etnean crisis. *Computers & Geosciences*, *32*(7), 876–889. https://doi.org/10.1016/j.cageo.2005.10.026

Avramov, I., & Milchev, A. (1988). Effect of disorder on diffusion and viscosity in condensed systems. *Journal of Non-Crystalline Solids*, *104*(2–3), 253–260. https://doi.org/10.1016/0022-3093(88)90396-1

Avramov, I. (2013). The role of entropy on viscosity of silicates. *Journal of Non-Crystalline Solids*, *362*(1), 120–123. https://doi.org/10.1016/j.jnoncrysol.2012.11.008

Balmforth, N. J., Craster, R. V., & Sassi, R. (2002). Shallow viscoplastic flow on an inclined plane. *Journal of Fluid Mechanics*, *470*, 1–29. https://doi.org/10.1017/S0022112002001660

Balmforth, N. J., Craster, R. V., Rust, A. C., & Sassi, R. (2006). Viscoplastic flow over an inclined surface. *Journal of Non-Newtonian Fluid Mechanics*, *139*(1–2), 103–127. https://doi.org/10.1016/j.jnnfm.2006.07.010

Balmforth, N. J., Craster, R. V., Perona, P., Rust, A. C., & Sassi, R. (2007). Viscoplastic dam breaks and the Bostwick consistometer. *Journal of Non-Newtonian Fluid Mechanics*, *142*(1–3), 63–78. https://doi.org/10.1016/j.jnnfm.2006.06.005

Barberi, F., & Carapezza, M. L. (2004). *The control of lava flows at Mt. Etna* (pp. 357–369). https://doi.org/10.1029/143GM22

Barca, D., Crisci, G. M., Gregorio, S. Di, & Nicoletta, F. (1994). Cellular automata for simulating lava flows: A method and examples of the Etnean eruptions. *Transport Theory and Statistical Physics*, *23*(1–3), 195–232. https://doi.org/10.1080/00411459408203862

Barca, D., Crisci, G. M., Rongo, R., Di Gregorio, S., & Spataro, W. (2004). *Application of the cellular automata model SCIARA to the 2001 Mount Etna crisis* (pp. 343–356). https://doi.org/10.1029/143GM21

Barmin, A., Melnik, O., & Sparks, R. S. J. (2002). Periodic behavior in lava dome eruptions. *Earth and Planetary Science Letters*, *199*(1–2), 173–184. https://doi.org/10.1016/S0012-821X(02)00557-5

Behncke, B., & Neri, M. (2003). The July-August 2001 eruption of Mt. Etna (Sicily). *Bulletin of Volcanology*, *65*(7), 461–476. https://doi.org/10.1007/s00445-003-0274-1

Behncke, B., Neri, M., & Nagay, A. (2005). Lava flow hazard at Mount Etna (Italy): New data from a GIS-based study. In *Kinematics and dynamics of lava flows*. Geological Society of America. https://doi.org/10.1130/0-8137-2396-5.189

Behncke, B., Fornaciai, A., Neri, M., Favalli, M., Ganci, G., & Mazzarini, F. (2016). Lidar surveys reveal eruptive volumes and rates at Etna, 2007–2010. *Geophysical Research Letters*, *43*(9), 4270–4278. https://doi.org/10.1002/2016GL068495

Biagioli, E. (2021). *Depth–averaged and 3D Finite Volume numerical models for viscous fluids, with application to the simulation of lava flows. PhD thesis.* University of Genova.

Biagioli, E., de' Michieli Vitturi, M., & Di Benedetto, F. (2021). Modified shallow water model for viscous fluids and positivity preserving numerical approximation. *Applied Mathematical Modelling*, *94*, 482–505. https://doi.org/10.1016/j.apm.2020.12.036

Biagioli, E., de' Michieli Vitturi, M., Di Benedetto, F., & Polacci, M. (2023). Benchmarking a new 2.5D shallow water model for lava flows. *Journal of Volcanology and Geothermal Research*, *444*. https://doi.org/10.1016/j.jvolgeores.2023.107935

Bilotta, G., Russo, G., Hérault, A., & del Negro, C. (2011). Moving least-squares corrections for smoothed particle hydrodynamics. *Annals of Geophysics*, *54*(5), 622–633. https://doi.org/10.4401/ag-5344

Bilotta, G., Cappello, A., Hérault, A., Vicari, A., Russo, G., & Del Negro, C. (2012). Sensitivity analysis of the MAGFLOW Cellular Automaton model for lava flow simulation. *Environmental Modelling & Software*, *35*, 122–131. https://doi.org/10.1016/j.envsoft.2012.02.015

Bilotta, G., Hérault, A., Cappello, A., Ganci, G., & Del Negro, C. (2016). GPUSPH: a Smoothed Particle Hydrodynamics model for the thermal and rheological evolution of lava flows. *Geological Society, London, Special Publications*, *426*(1), 387–408. https://doi.org/10.1144/SP426.24

Blong, R. J. (1984). Volcanic Hazards and Buildings. In *Volcanic Hazards* (pp. 187–240). Elsevier. https://doi.org/10.1016/B978-0-12-107180-6.50010-X

Bonne, K., Kervyn, M., Cascone, L., Njome, S., Van Ranst, E., Suh, E., Ayonghe, S., Jacobs, P., & Ernst, G. (2008). A new approach to assess long-term lava flow hazard and risk using GIS and low-cost remote sensing: the case of Mount Cameroon, West Africa. *International Journal of Remote Sensing*, *29*(22), 6539–6564. https://doi.org/10.1080/01431160802167873

Bottinga, Y., & Weill, D. F. (1972). The viscosity of magmatic silicate liquids; a model calculation. *American Journal of Science*, *272*(5), 438–475. https://doi.org/10.2475/ajs.272.5.438

Bourgouin, L., Mühlhaus, H. B., Jane Hale, A., & Arsac, A. (2007). Studying the influence of a solid shell on lava dome growth and evolution using the level set method. *Geophysical Journal International*, *170*(3), 1431–1438. https://doi.org/10.1111/j.1365-246X.2007.03471.x

Branca, S., Coltelli, M., Groppelli, G., & Lentini, F. (2011). Geological map of Etna volcano, 1:50,000 scale. *Italian Journal of Geosciences*, *Vol. 130, n. 3*, 265–291. https://doi.org/10.3301/IJG.2011.15

Branca, S., De Beni, E., & Proietti, C. (2013). The large and destructive 1669 AD eruption at Etna volcano: reconstruction of the lava flow field evolution and effusion rate trend. *Bulletin of Volcanology*, *75*(2), 694. https://doi.org/10.1007/s00445-013-0694-5

Bretón-González, M. , Campos, A. , & Leon, Z. (2013). The 2007-2012 lava dome growth in the crater of Volcán de Colima, México, derived from video monitoring system. *Complex Monitoring of Volcanic Activity: Methods and Results*, 153–169.

Burguete, J., García-Navarro, P., & Aliod, R. (2002). Numerical simulation of runoff from extreme rainfall events in a mountain water catchment. *Natural Hazards and Earth System Sciences*, *2*(1/2), 109–117. https://doi.org/10.5194/nhess-2-109-2002

Calder, E. S., Luckett, R., Sparks, R. S. J., & Voight, B. (2002). Mechanisms of lava dome instability and generation of rockfalls and pyroclastic flows at Soufrière Hills Volcano, Montserrat. *Geological Society, London, Memoirs*, *21*(1), 173–190. https://doi.org/10.1144/GSL.MEM.2002.021.01.08

Calder, E. S., Lavallée, Y., Kendrick, J. E., & Bernstein, M. (2015). Lava Dome Eruptions. In *The Encyclopedia of Volcanoes* (pp. 343–362). Elsevier. https://doi.org/10.1016/B978-0-12-385938-9.00018-3

Caltabiano, T., Burton, M., Giammanco, S., Allard, P., Bruno, N., Murè, F., & Romano, R. (2004). *Volcanic gas emissions from the summit craters and flanks of Mt. Etna, 1987–2000* (pp. 111–128). https://doi.org/10.1029/143GM08

Campagnola, S., Romano, C., Mastin, L. G., & Vona, A. (2016). Confort 15 model of conduit dynamics: applications to Pantelleria Green Tuff and Etna 122 BC eruptions. *Contributions to Mineralogy and Petrology*, *171*(6), 60. https://doi.org/10.1007/s00410-016-1265-5

Cappello, A., Vicari, A., & Del Negro, C. (2011). Assessment and modeling of lava flow hazard on Mt. Etna volcano. *Bollettino Di Geofisica Teorica Ed Applicata*, *52*(2), 1–10. https://doi.org/10.4430/bgta0003

Cappello, A., Neri, M., Acocella, V., Gallo, G., Vicari, A., & Del Negro, C. (2012). Spatial vent opening probability map of Etna volcano (Sicily, Italy). *Bulletin of Volcanology*, *74*(9), 2083–2094. https://doi.org/10.1007/s00445-012-0647-4

Cappello, A., Bilotta, G., Neri, M., & Negro, C. Del. (2013). Probabilistic modeling of future volcanic eruptions at Mount Etna. *Journal of Geophysical Research: Solid Earth*, *118*(5), 1925–1935. https://doi.org/10.1002/jgrb.50190

Cappello, A., Ganci, G., Calvari, S., Pérez, N. M., Hernández, P. A., Silva, S. V., Cabral, J., & Del Negro, C. (2016). Lava flow hazard modeling during the 2014-2015 Fogo eruption, Cape Verde. *Journal of Geophysical Research: Solid Earth*, *121*(4), 2290–2303. https://doi.org/10.1002/2015JB012666

Cappello, A., Hérault, A., Bilotta, G., Ganci, G., & Negro, C. Del. (2016). MAGFLOW: A physics-based model for the dynamics of lava-flow emplacement. *Geological Society Special Publication*, *426*(1), 357–373. https://doi.org/10.1144/SP426.16

Cappello, A., Bilotta, G., & Ganci, G. (2022). Modeling of Geophysical Flows through GPUFLOW. *Applied Sciences (Switzerland)*, *12*(9). https://doi.org/10.3390/app12094395

Caricchi, L., Burlini, L., Ulmer, P., Gerya, T., Vassalli, M., & Papale, P. (2007). Non-Newtonian rheology of crystal-bearing magmas and implications for magma ascent dynamics. *Earth and Planetary Science Letters*, *264*(3–4), 402–419. https://doi.org/10.1016/j.epsl.2007.09.032

Cashman, K. V., Thornber, C., & Kauahikaua, J. P. (1999). Cooling and crystallization of lava in open channels, and the transition of Pāhoehoe Lava to ’A’ā. *Bulletin of Volcanology*, *61*(5), 306–323. https://doi.org/10.1007/s004450050299

Cashman, K., & Blundy, J. (2000). Degassing and crystallization of ascending andesite and dacite. *Philosophical Transactions of the Royal Society of London. Series A:*

Mathematical, Physical and Engineering Sciences, *358*(1770), 1487–1513. https://doi.org/10.1098/rsta.2000.0600

Cashman, K. V., & Scheu, B. (2015). Magmatic Fragmentation. In *The Encyclopedia of Volcanoes* (pp. 459–471). Elsevier. https://doi.org/10.1016/B978-0-12-385938-9.00025-0

Cashman, K. V. (2020). Crystal Size Distribution (CSD) Analysis of Volcanic Samples: Advances and Challenges. *Frontiers in Earth Science*, *8*. https://doi.org/10.3389/feart.2020.00291

Castruccio, A., & Contreras, M. A. (2016). The influence of effusion rate and rheology on lava flow dynamics and morphology: A case study from the 1971 and 1988–1990 eruptions at Villarrica and Lonquimay volcanoes, Southern Andes of Chile. *Journal of Volcanology and Geothermal Research*, *327*, 469–483. https://doi.org/10.1016/j.jvolgeores.2016.09.015

Centorrino, V., Bilotta, G., Cappello, A., Ganci, G., Corradino, C., & Del Negro, C. (2021). A particle swarm optimization–based heuristic to optimize the configuration of artificial barriers for the mitigation of lava flow risk. *Environmental Modelling & Software*, *139*, 105023. https://doi.org/10.1016/j.envsoft.2021.105023

Chester, D. K., Duncan, A. M., Guest, J. E., & Kilburn, C. R. J. (1985). *Mount Etna*. Springer Netherlands. https://doi.org/10.1007/978-94-009-4079-6

Chevrel, M. O., Platz, T., Hauber, E., Baratoux, D., Lavallée, Y., & Dingwell, D. B. (2013). Lava flow rheology: A comparison of morphological and petrological methods. *Earth and Planetary Science Letters*, *384*, 109–120. https://doi.org/10.1016/j.epsl.2013.09.022

Chevrel, M. O., Pinkerton, H., & Harris, A. J. L. (2019). Measuring the viscosity of lava in the field: A review. *Earth-Science Reviews*, *196*, 102852. https://doi.org/10.1016/j.earscirev.2019.04.024

Christensen, U. R. (1992). An Eulerian technique for thermomechanical modeling of lithospheric extension. *Journal of Geophysical Research: Solid Earth*, *97*(B2), 2015–2036. https://doi.org/10.1029/91JB02642

Cimarelli, C., Costa, A., Mueller, S., & Mader, H. M. (2011). Rheology of magmas with bimodal crystal size and shape distributions: Insights from analog experiments. *Geochemistry, Geophysics, Geosystems*, *12*(7). https://doi.org/10.1029/2011GC003606

Coltelli, M., Del Carlo, P., & Vezzoli, L. (2000). Stratigraphic constraints for explosive activity in the past 100 ka at Etna Volcano, Italy. *International Journal of Earth Sciences*, *89*(3), 665–677. https://doi.org/10.1007/s005310000117

Cordonnier, B., Lev, E., & Garel, F. (2016). Benchmarking lava-flow models. *Geological Society Special Publication*, *426*(1), 425–445. https://doi.org/10.1144/SP426.7

Corsaro, R. A., Andronico, D., Behncke, B., Branca, S., Caltabiano, T., Ciancitto, F., Cristaldi, A., De Beni, E., La Spina, A., Lodato, L., Miraglia, L., Neri, M., Salerno, G., Scollo, S., & Spata, G. (2017). Monitoring the December 2015 summit eruptions of Mt. Etna (Italy): Implications on eruptive dynamics. *Journal of Volcanology and Geothermal Research*, *341*, 53–69. https://doi.org/10.1016/j.jvolgeores.2017.04.018

Costa, A. (2005). Viscosity of high crystal content melts: Dependence on solid fraction. *Geophysical Research Letters*, *32*(22), 1–5. https://doi.org/10.1029/2005GL024303

Costa, A., & Macedonio, G. (2005a). Computational modeling of lava flows: A review. In *Kinematics and dynamics of lava flows*. Geological Society of America. https://doi.org/10.1130/0-8137-2396-5.209

Costa, A., & Macedonio, G. (2005b). Numerical simulation of lava flows based on depth-averaged equations. *Geophysical Research Letters*, *32*(5), 1–5. https://doi.org/10.1029/2004GL021817

Costa, A., Melnik, O., & Sparks, R. S. J. (2007). Controls of conduit geometry and wallrock elasticity on lava dome eruptions. *Earth and Planetary Science Letters*, *260*(1–2), 137–151. https://doi.org/10.1016/j.epsl.2007.05.024

Costa, A., Melnik, O., & Vedeneeva, E. (2007). Thermal effects during magma ascent in conduits. *Journal of Geophysical Research: Solid Earth*, *112*(12). https://doi.org/10.1029/2007JB004985

Costa, A., Caricchi, L., & Bagdassarov, N. (2009). A model for the rheology of particle-bearing suspensions and partially molten rocks. *Geochemistry, Geophysics, Geosystems*, *10*(3). https://doi.org/10.1029/2008GC002138

Costa, A., Wadge, G., & Melnik, O. (2012). Cyclic extrusion of a lava dome based on a stick-slip mechanism. *Earth and Planetary Science Letters*, *337–338*, 39–46. https://doi.org/10.1016/j.epsl.2012.05.011

Courant, R., Friedrichs, K., & Lewy, H. (1928). Über die partiellen Differenzengleichungen der mathematischen Physik. *Mathematische Annalen*, *100*(1), 32–74. https://doi.org/10.1007/BF01448839

Crisci, G. M., Gregorio, Di., Pindaro, O., & Ranieri, G. A. (1986). Lava Flow Simulation Bv A Discrete Cellular Model: First Implementation. *International Journal of Modelling and Simulation*, *6*(4), 137–140. https://doi.org/10.1080/02286203.1986.11759975

Crisci, G. M., Iovine, G., Di Gregorio, S., & Lupiano, V. (2008). Lava-flow hazard on the SE flank of Mt. Etna (Southern Italy). *Journal of Volcanology and Geothermal Research*, *177*(4), 778–796. https://doi.org/10.1016/j.jvolgeores.2008.01.041

Crisp, J., & Baloga, S. (1990). A model for lava flows with two thermal components. *Journal of Geophysical Research: Solid Earth*, *95*(B2), 1255–1270. https://doi.org/10.1029/JB095iB02p01255

Crisp, J., Cashman, K. V., Bonini, J. A., Hougen, S. B., & Pieri, D. C. (1994). Crystallization history of the 1984 Mauna Loa lava flow. *Journal of Geophysical Research: Solid Earth*, *99*(B4), 7177–7198. https://doi.org/10.1029/93JB02973

Cutter, S. L., Ismail-Zadeh, A., Alcántara-Ayala, I., Altan, O., Baker, D. N., Briceño, S., Gupta, H., Holloway, A., Johnston, D., McBean, G. A., Ogawa, Y., Paton, D., Porio, E., Silbereisen, R. K., Takeuchi, K., Valsecchi, G. B., Vogel, C., & Wu, G. (2015). Global risks: Pool knowledge to stem losses from disasters. *Nature*, *522*(7556), 277–279. https://doi.org/10.1038/522277a

Damiani, M. L., Groppelli, G., Norini, G., Bertino, E., Gigliuto, A., & Nucita, A. (2006). A lava flow simulation model for the development of volcanic hazard maps for Mount Etna (Italy). *Computers & Geosciences*, *32*(4), 512–526. https://doi.org/10.1016/j.cageo.2005.08.011

Del Negro, C., Cappello, A., Neri, M., Bilotta, G., Hérault, A., & Ganci, G. (2013). Lava flow hazards at Mount Etna: Constraints imposed by eruptive history and numerical simulations. *Scientific Reports*, *3*. https://doi.org/10.1038/srep03493

Dingwell, D. B. (1986). Viscosity-temperature relationships in the system Na2Si2O5-Na4Al2O5. *Geochimica et Cosmochimica Acta*, *50*(6), 1261–1265. https://doi.org/10.1016/0016-7037(86)90409-6

Dragoni, M., Bonafede, M., & Boschi, E. (1986). Downslope flow models of a Bingham liquid: Implications for lava flows. *Journal of Volcanology and Geothermal Research*, *30*(3–4), 305–325. https://doi.org/10.1016/0377-0273(86)90059-4

Dragoni, M. (1989). A dynamical model of lava flows cooling by radiation. *Bulletin of Volcanology*, *51*(2), 88–95. https://doi.org/10.1007/BF01081978

Einstein, A. (1906). Eine neue Bestimmung der Moleküldimensionen. *Annalen Der Physik*, *324*(2), 289–306. https://doi.org/10.1002/andp.19063240204

Fagents, S. A., Gregg, T. K. P., & Lopes, R. M. C. (2013). Introduction. In *Modeling Volcanic Processes: The Physics and Mathematics of Volcanism* (Vol. 9780521895439, pp. 1–4). Cambridge University Press. https://doi.org/10.1017/CBO9781139021562.001

Favalli, M., Pareschi, M. T., Neri, A., & Isola, I. (2005). Forecasting lava flow paths by a stochastic approach. Geophysical Research Letters, 32(3). https://doi.org/10.1029/2004GL021718

Ferrari, S., & Saleri, F. (2004). A new two-dimensional Shallow Water model including pressure effects and slow varying bottom topography. *ESAIM: Mathematical Modelling and Numerical Analysis*, *38*(2), 211–234. https://doi.org/10.1051/m2an:2004010

Filippucci, M., Tallarico, A., & Dragoni, M. (2010). A three-dimensional dynamical model for channeled lava flow with nonlinear rheology. *Journal of Geophysical Research: Solid Earth*, *115*(B5). https://doi.org/10.1029/2009JB006335

Filippucci, M., Tallarico, A., & Dragoni, M. (2017). Viscous dissipation in a flow with power law, temperature-dependent rheology: Application to channeled lava flows. *Journal of Geophysical Research: Solid Earth*, *122*(5), 3364–3378. https://doi.org/10.1002/2016JB013720

Fink, J. H., Malin, M. C., & Anderson, S. W. (1990). Intrusive and extrusive growth of the Mount St Helens lava dome. *Nature*, *348*(6300), 435–437. https://doi.org/10.1038/348435a0

Fink, J. H., & Griffiths, R. W. (1998). Morphology, eruption rates, and rheology of lava domes: Insights from laboratory models. *Journal of Geophysical Research: Solid Earth*, *103*(1), 527–545. https://doi.org/10.1029/97jb02838

Frontoni, A., Costa, A., Vona, A., & Romano, C. (2022). A comprehensive database of crystal-bearing magmas for the calibration of a rheological model. *Scientific Data*, *9*(1). https://doi.org/10.1038/s41597-022-01363-w

Ganci, G., Cappello, A., Bilotta, G., Corradino, C., & Del Negro, C. (2019). Satellite-Based Reconstruction of the Volcanic Deposits during the December 2015 Etna Eruption. *Data*, *4*(3), 120. https://doi.org/10.3390/data4030120

Gent, A. N. (1960). Theory of the parallel plate viscometer. *British Journal of Applied Physics*, *11*(2), 85–87. https://doi.org/10.1088/0508-3443/11/2/310

Gerbeau, J.-F., & Perthame, B. (2001). *Derivation of Viscous Saint-Venant System for Laminar Shallow Water; Numerical Validation*. https://inria.hal.science/inria-00072549v1

Giordano, D., & Dingwell, D. B. (2003). Viscosity of hydrous Etna basalt: Implications for Plinian-style basaltic eruptions. *Bulletin of Volcanology*, *65*(1), 8–14. https://doi.org/10.1007/s00445-002-0233-2

Giordano, D., Russell, J. K., & Dingwell, D. B. (2008). Viscosity of magmatic liquids: A model. *Earth and Planetary Science Letters*, *271*(1–4), 123–134. https://doi.org/10.1016/j.epsl.2008.03.038

Gonnermann, H. M., & Manga, M. (2013). Dynamics of magma ascent in the volcanic conduit. In *Modeling Volcanic Processes: The Physics and Mathematics of Volcanism* (Vol. 9780521895439, pp. 55–84). Cambridge University Press. https://doi.org/10.1017/CBO9781139021562.004

Griffiths, R. W. (2000). The Dynamics of Lava Flows. *Annual Review of Fluid Mechanics*, *32*(1), 477–518. https://doi.org/10.1146/annurev.fluid.32.1.477

Guest, J. E., & Murray, J. B. (1979). An analysis of hazard from Mount Etna volcano. *Journal of the Geological Society*, *136*(3), 347–354. https://doi.org/10.1144/gsjgs.136.3.0347

Guest, J. E. (1982). Styles of eruption and flow morphology on Mt Etna. *Memorie Della Societa Geologica Italiana*, *23*, 49–73.

Guidoboni, E., Ciuccarelli, C., Mariotti, D., Comastri, A., & Bianchi, M. G. (2014). *L'Etna nella Storia. Catalogo delle eruzioni dall'antichità alla fine del XVII secolo*. Bononia University Press.

Hale, A. J., & Wadge, G. (2003). Numerical modelling of the growth dynamics of a simple silicic lava dome. *Geophysical Research Letters*, *30*(19). https://doi.org/10.1029/2003GL018182

Hale, A. J., Bourgouin, L., & Mühlhaus, H. B. (2007). Using the level set method to model endogenous lava dome growth. *Journal of Geophysical Research: Solid Earth*, *112*(3). https://doi.org/10.1029/2006JB004445

Hale, A. J., Wadge, G., & Mühlhaus, H. B. (2007). The influence of viscous and latent heating on crystal-rich magma flow in a conduit. *Geophysical Journal International*, *171*(3), 1406–1429. https://doi.org/10.1111/j.1365-246X.2007.03593.x

Hale, A. J. (2008). Lava dome growth and evolution with an independently deformable talus. *Geophysical Journal International*, *174*(1), 391–417. https://doi.org/10.1111/j.1365-246X.2008.03806.x

Hale, A. J., & Wadge, G. (2008). The transition from endogenous to exogenous growth of lava domes with the development of shear bands. *Journal of Volcanology and Geothermal Research*, *171*(3–4), 237–257. https://doi.org/10.1016/j.jvolgeores.2007.12.016

Harnett, C. E., Thomas, M. E., Purvance, M. D., & Neuberg, J. (2018). Using a discrete element approach to model lava dome emplacement and collapse. *Journal of Volcanology and Geothermal Research*, *359*, 68–77. https://doi.org/10.1016/j.jvolgeores.2018.06.017

Harnett, C. E., Thomas, M. E., Calder, E. S., Ebmeier, S. K., Telford, A., Murphy, W., & Neuberg, J. (2019). Presentation and analysis of a worldwide database for lava dome collapse events: the Global Archive of Dome Instabilities (GLADIS). *Bulletin of Volcanology*, *81*(3). https://doi.org/10.1007/s00445-019-1276-y

Harris, A., & Rowland, S. (2001). FLOWGO: a kinematic thermo-rheological model for lava flowing in a channel. *Bulletin of Volcanology*, *63*(1), 20–44. https://doi.org/10.1007/s004450000120

Harris, A. J., Rose, W. I., & Flynn, L. P. (2003). Temporal trends in lava dome extrusion at Santiaguito 1922–2000. *Bulletin of Volcanology*, *65*(2–3), 77–89. https://doi.org/10.1007/s00445-002-0243-0

Harris, A. J. L., Favalli, M., Mazzarini, F., & Hamilton, C. W. (2009). Construction dynamics of a lava channel. *Bulletin of Volcanology*, *71*(4), 459–474. https://doi.org/10.1007/s00445-008-0238-6

Harris, A., Favalli, M., Wright, R., & Garbeil, H. (2011). Hazard assessment at Mount Etna using a hybrid lava flow inundation model and satellite-based land classification. *Natural Hazards*, *58*(3), 1001–1027. https://doi.org/10.1007/s11069-010-9709-0

Harris, A. J. L. (2013). Lava flows. In *Modeling Volcanic Processes: The Physics and Mathematics of Volcanism* (Vol. 9780521895439, pp. 85–106). Cambridge University Press. https://doi.org/10.1017/CBO9781139021562.005

Harris, A. J. L., & Rowland, S. K. (2015). Lava Flows and Rheology. In *The Encyclopedia of Volcanoes* (pp. 321–342). Elsevier. https://doi.org/10.1016/B978-0-12-385938-9.00017-1

Harris AJL. (2015). Basaltic lava flow hazard. *In: Volcanic Hazards, Risks and Disasters (Ed. Papale P), Elsevier, Amsterdam*, 17–47.

Harris, A., De Groeve, T., Carn, S., & Garel, F. (2016). Risk evaluation, detection and simulation during effusive eruption disasters. *Geological Society Special Publication*, *426*(1), 1–22. https://doi.org/10.1144/SP426.29

Heap, M. J., Troll, V. R., Kushnir, A. R. L., Gilg, H. A., Collinson, A. S. D., Deegan, F. M., Darmawan, H., Seraphine, N., Neuberg, J., & Walter, T. R. (2019). Hydrothermal alteration of andesitic lava domes can lead to explosive volcanic behaviour. *Nature Communications*, *10*(1), 5063. https://doi.org/10.1038/s41467-019-13102-8

Heinrich, PH., Piatanesi, A., & Hébert, H. (2001). Numerical modelling of tsunami generation and propagation from submarine slumps: the 1998 Papua New Guinea event. *Geophysical Journal International*, *145*(1), 97–111. https://doi.org/10.1111/j.1365-246X.2001.00336.x

Hérault, A., Bilotta, G., Vicari, A., Rustico, E., & del Negro, C. (2011). Numerical simulation of lava flow using a GPU SPH model. *Annals of Geophysics*, *54*(5), 600–620. https://doi.org/10.4401/ag-5343

Hess, K.-U., & Dingwell, D. D. (1996). Viscosities of hydrous leucogranitic melts: A non-Arrhenian model. In *American Mineralogist* (Vol. 81).

Hidaka, M., Goto, A., Umino, S., & Fujita, E. (2005). VTFS project: Development of the lava flow simulation code Lava SIM with a model for three-dimensional convection, spreading, and solidification. *Geochemistry, Geophysics, Geosystems*, *6*(7). https://doi.org/10.1029/2004GC000869

Hirt, C. W., & Nichols, B. D. (1981). Volume of fluid (VOF) method for the dynamics of free boundaries. *Journal of Computational Physics*, *39*(1), 201–225. https://doi.org/10.1016/0021-9991(81)90145-5

Hogg, A. J., & Pritchard, D. (2004). The effects of hydraulic resistance on dam-break and other shallow inertial flows. *Journal of Fluid Mechanics*, *501*, 179–212. https://doi.org/10.1017/S0022112003007468

Hulme, G. (1974). The Interpretation of Lava Flow Morphology. *Geophysical Journal International*, *39*(2), 361–383. https://doi.org/10.1111/j.1365-246X.1974.tb05460.x

Huppert, H. E. (1982). The propagation of two-dimensional and axisymmetric viscous gravity currents over a rigid horizontal surface. In *J. Fluid Mech* (Vol. 121).

Husain, T., Elsworth, D., Voight, B., Mattioli, G., & Jansma, P. (2014). Influence of extrusion rate and magma rheology on the growth of lava domes: Insights from particle-dynamics modeling. *Journal of Volcanology and Geothermal Research*, *285*, 100–117. https://doi.org/10.1016/j.jvolgeores.2014.08.013

Husain, T., Elsworth, D., Voight, B., Mattioli, G., & Jansma, P. (2018). Influence of conduit flow mechanics on magma rheology and the growth style of lava domes. *Geophysical Journal International*, *213*(3), 1768–1784. https://doi.org/10.1093/GJI/GGY073

Husain, T., Elsworth, D., Voight, B., Mattioli, G., & Jansma, P. (2019). Morphologic variation of an evolving dome controlled by the extrusion of finite yield strength magma. *Journal of Volcanology and Geothermal Research*, *370*, 51–64. https://doi.org/10.1016/j.jvolgeores.2019.01.010

Hutchison, W., Varley, N., Pyle, D. M., Mather, T. A., & Stevenson, J. A. (2013). Airborne thermal remote sensing of the volcán de colima (mexico) lava dome from 2007 to 2010. *Geological Society Special Publication*, *380*(1), 203–228. https://doi.org/10.1144/SP380.8

Ishihara, K., Iguchi, M., & Kamo, K. (1990). *Numerical Simulation of Lava Flows on Some Volcanoes in Japan* (pp. 174–207). https://doi.org/10.1007/978-3-642-74379-5_8

Ismail-Zadeh, A., & Tackley, P. (2010). *Computational Methods for Geodynamics*. Cambridge University Press. https://doi.org/10.1017/CBO9780511780820

Ismail-Zadeh, A., Korotkii, A., & Tsepelev, I. (2016). *Data-Driven Numerical Modelling in Geodynamics: Methods and Applications*. Springer International Publishing. https://doi.org/10.1007/978-3-319-27801-8

Ismail-Zadeh, A., Korotkii, A., Melnik, O., Starodubtsev, I., Starodubtseva, Y., Tsepelev, I., & Zeinalova, N. (2023). Inverse Problems in Lava Dynamics. In *Applications of Data Assimilation and Inverse Problems in the Earth Sciences* (pp. 196–208). Cambridge University Press. https://doi.org/10.1017/9781009180412.013

Iverson, R. M. (1990). *Lava Domes Modeled as Brittle Shells that Enclose Pressurized Magma, with Application to Mount St. Helens* (pp. 47–69). https://doi.org/10.1007/978-3-642-74379-5_3

James, M. R., & Varley, N. (2012). Identification of structural controls in an active lava dome with high resolution DEMs: Volcán de Colima, Mexico. *Geophysical Research Letters*, *39*(22). https://doi.org/10.1029/2012GL054245

Jasak, H., Jemcov, A., & Tuković, Ž. (2007). *OpenFOAM: A C++ Library for Complex Physics Simulations*. https://api.semanticscholar.org/CorpusID:35226827

Jasak, H. (2009). OpenFOAM: Open source CFD in research and industry. *International Journal of Naval Architecture and Ocean Engineering*, *1*(2), 89–94. https://doi.org/10.2478/IJNAOE-2013-0011

Jeffrey, D. J., & Acrivos, A. (1976). The rheological properties of suspensions of rigid particles. *AIChE Journal*, *22*(3), 417–432. https://doi.org/10.1002/aic.690220303

Kauahikaua, J. (2007). *Hawaiian Volcano Observatory Lava Flow Hazard Assessment, as of August 2007, for Kīlauea East Rift Zone Eruptions, Hawai'i Island*. http://www.usgs.gov/pubprod

Kelfoun, K., & Druitt, T. H. (2005). Numerical modeling of the emplacement of Socompa rock avalanche, Chile. *Journal of Geophysical Research: Solid Earth*, *110*(B12). https://doi.org/10.1029/2005JB003758

Kelfoun, K., & Vargas, S. V. (2016). VolcFlow capabilities and potential development for the simulation of lava flows. *Geological Society, London, Special Publications*, *426*(1), 337–343. https://doi.org/10.1144/SP426.8

Kilburn, C. R. J. (2000). *Lava flows and flow fields*. Academic Press.

Kilburn, C. R. J. (2015). Lava Flow Hazards and Modeling. In *The Encyclopedia of Volcanoes* (pp. 957–969). Elsevier. https://doi.org/10.1016/B978-0-12-385938-9.00055-9

Kirkpatrick, R. J. (1976). Towards a kinetic model for the crystallization of magma bodies. *Journal of Geophysical Research*, *81*(14), 2565–2571. https://doi.org/10.1029/JB081i014p02565

Komorowski, J. , T. D. et al. (2002). The January 2002 flank eruption of Nyiragongo volcano (Democratic Republic of Congo): chronology, evidence for a tectonic trigger, and impact of lava flows on the city of Goma. *Acta Vulcanologica*, *114*(15), 27–61.

Korotkii, A., Kovtunov, D., Ismail-Zadeh, A., Tsepelev, I., & Melnik, O. (2016). Quantitative reconstruction of thermal and dynamic characteristics of lava flow from surface thermal measurements. *Geophysical Journal International*, *205*(3), 1767–1779. https://doi.org/10.1093/gji/ggw117

La Spina, G., Burton, M., de' Michieli Vitturi, M., & Arzilli, F. (2016). Role of syn-eruptive plagioclase disequilibrium crystallization in basaltic magma ascent dynamics. *Nature Communications*, *7*(1), 13402. https://doi.org/10.1038/ncomms13402

Lavallée, Y., Hess, K. U., Cordonnier, B., & Dingwell, D. B. (2007). Non-Newtonian rheological law for highly crystalline dome lavas. *Geology*, *35*(9), 843–846. https://doi.org/10.1130/G23594A.1

Lavallée, Y., Meredith, P. G., Dingwell, D. B., Hess, K. U., Wassermann, J., Cordonnier, B., Gerik, A., & Kruhl, J. H. (2008). Seismogenic lavas and explosive eruption forecasting. *Nature*, *453*(7194), 507–510. https://doi.org/10.1038/nature06980

Lavallée, Y., Varley, N. R., Alatorre-Ibargüengoitia, M. A., Hess, K. U., Kueppers, U., Mueller, S., Richard, D., Scheu, B., Spieler, O., & Dingwell, D. B. (2012). Magmatic architecture of dome-building eruptions at Volcán de Colima, Mexico. *Bulletin of Volcanology*, *74*(1), 249–260. https://doi.org/10.1007/s00445-011-0518-4

Lejeune, A. M., & Richet, P. (1995). Rheology of crystal-bearing silicate melts: an experimental study at high viscosities. *Journal of Geophysical Research*, *100*(B3), 4215–4229. https://doi.org/10.1029/94JB02985

Lev, E., & James, M. R. (2014). The influence of cross-sectional channel geometry on rheology and flux estimates for active lava flows. *Bulletin of Volcanology*, *76*(7), 1–15. https://doi.org/10.1007/s00445-014-0829-3

LeVeque, R. (2002). *Finite Volume Methods for Hyperbolic Problems*. Cambridge University Press.

Lipman, P. W., Banks, N. G., & Rhodes, J. M. (1985). Degassing-induced crystallization of basaltic magma and effects on lava rheology. *Nature*, *317*(6038), 604–607. https://doi.org/10.1038/317604a0

Lister, J. R. (1992). Viscous flows down an inclined plane from point and line sources. In *J. Fluid Mech* (Vol. 242).

Liu, K. F., & Mei, C. C. (1990). Approximate equations for the slow spreading of a thin sheet of Bingham plastic fluid. *Physics of Fluids A: Fluid Dynamics*, *2*(1), 30–36. https://doi.org/10.1063/1.857821

Llewellin, E. W., & Manga, M. (2005). Bubble suspension rheology and implications for conduit flow. *Journal of Volcanology and Geothermal Research*, *143*(1–3), 205–217. https://doi.org/10.1016/j.jvolgeores.2004.09.018

Luhr, J. F., & Carmichael, I. S. E. (1980). The Colima Volcanic Complex, Mexico I. Post-Caldera Andesites From Volcfin Colima. In *Contrib. Mineral. Petrol* (Vol. 71).

Macedonio, G., & Longo, A. (1999). Lava flow in a channel with a bifurcation. *Physics and Chemistry of the Earth, Part A: Solid Earth and Geodesy*, *24*(11–12), 953–956. https://doi.org/10.1016/S1464-1895(99)00141-6

Manga, M., Castro, J., Cashman, K. V, & Loewenberg, M. (1998). Rheology of bubble-bearing magmas. In *Journal of Volcanology and Geothermal Research* (Vol. 87).

Mardles, E. W. J. (1940). The viscosity of suspensions in non-aqueous liquids. *Transactions of the Faraday Society*, *36*, 1007. https://doi.org/10.1039/tf9403601007

Marsh, B. D. (1981). On the crystallinity, probability of occurrence, and rheology of lava and magma. *Contributions to Mineralogy and Petrology*, *78*(1), 85–98. https://doi.org/10.1007/BF00371146

Matsson, J. E. (2024). *An Introduction to Ansys Fluent 2024*. SDC Publications.

Mauro, J. C., Yue, Y., Ellison, A. J., Gupta, P. K., & Allan, D. C. (2009). Viscosity of glass-forming liquids. *Proceedings of the National Academy of Sciences*, *106*(47), 19780–19784. https://doi.org/10.1073/pnas.0911705106

Melnik, O., & Sparks, R. S. J. (1999). Nonlinear dynamics of lava dome extrusion. *Nature*, *402*(6757), 37–41. https://doi.org/10.1038/46950

Melnik, O., & Sparks, R. S. J. (2005). Controls on conduit magma flow dynamics during lava dome building eruptions. *Journal of Geophysical Research: Solid Earth*, *110*(B2). https://doi.org/10.1029/2004JB003183

Mériaux, C. A., May, D. A., & Jaupart, C. (2022). The impact of vent geometry on the growth of lava domes. *Geophysical Journal International*, *229*(3), 1680–1694. https://doi.org/10.1093/gji/ggac005

Miyamoto, H., & Sasaki, S. (1998). Numerical simulations of flood basalt lava flows: Roles of parameters on lava flow morphologies. *Journal of Geophysical Research: Solid Earth*, *103*(B11), 27489–27502. https://doi.org/10.1029/98JB00438

Moore, G., & Carmichael, I. S. E. (1998). The hydrous phase equilibria (to 3 kbar) of an andesite and basaltic andesite from western Mexico: constraints on water content and conditions of phenocryst growth. *Contributions to Mineralogy and Petrology*, *130*(3–4), 304–319. https://doi.org/10.1007/s004100050367

Morse, S. A. (2011). The fractional latent heat of crystallizing magmas. *American Mineralogist*, *96*(4), 682–689. https://doi.org/10.2138/am.2011.3613

Naimark, B. M., & Ismail-Zadeh, A. T. (1995). Numerical models of a subsidence mechanism in intracratonic basins: application to North American basins. *Geophysical Journal International*, *123*(1), 149–160. https://doi.org/10.1111/j.1365-246X.1995.tb06667.x

Naimark, B. M., Ismail-Zadeh, A. T., & Jacoby, W. R. (1998). Numerical approach to problems of gravitational instability of geostructures with advected material boundaries. *Geophysical Journal International*, *134*(2), 473–483. https://doi.org/10.1111/j.1365-246X.1998.tb07140.x

Nakada, S. (1999). at Unzen: effusion pulsation and groundmass crystallization. In *Motomurar Journal of Volcanology and Geothermal Research* (Vol. 89).

Nakada, S., Zaennudin, A., Yoshimoto, M., Maeno, F., Suzuki, Y., Hokanishi, N., Sasaki, H., Iguchi, M., Ohkura, T., Gunawan, H., & Triastuty, H. (2019). Growth process of the lava dome/flow complex at Sinabung Volcano during 2013–2016. *Journal of Volcanology and Geothermal Research*, *382*, 120–136. https://doi.org/10.1016/j.jvolgeores.2017.06.012

Nakamura, Y., & Aoki, K. (1980). The 1977 eruption of Nyiragongo volcano, eastern Africa, and chemical composition of the ejecta. *Bull. Volc. Soc. Jpn*, *25*(1), 17–32.

Neri, A. (1998). A local heat transfer analysis of lava cooling in the atmosphere: application to thermal diffusion-dominated lava flows. In *Neri r Journal of Volcanology and Geothermal Research* (Vol. 81).

Nichols, R. L. (1939). Viscosity of Lava. *The Journal of Geology*, *47*(3), 290–302. https://doi.org/10.1086/624778

Parfitt, E. A., & Wilson, L. (2008). *Fundamentals of physical volcanology*.

Parmigiani, A., Latt, J., Begacem, M. B., & Chopard, B. (2013). A lattice Boltzmann simulation of the Rhone river. *International Journal of Modern Physics*, *24*.

Patankar, S. V., & Spalding, D. B. (1972). A calculation procedure for heat, mass and momentum transfer in three-dimensional parabolic flows. *International Journal of Heat and Mass Transfer*, *15*(10), 1787–1806. https://doi.org/10.1016/0017-9310(72)90054-3

Patankar, S. V. (1980). *Numerical Heat Transfer and Fluid Flow* . Taylor & Francis.

Persikov, E. S. (1991). *The Viscosity of Magmatic Liquids: Experiment, Generalized Patterns. A Model for Calculation and Prediction. Applications* (pp. 1–40). https://doi.org/10.1007/978-1-4612-3128-8_1

Peyret, R. (1996). *Handbook of Computational Fluid Mechanics*. Academic Press Limited, USA.

Philpotts, A., & Ague, J. (2009). *Principles of Igneous and Metamorphic Petrology*. Cambridge University Press. https://doi.org/10.1017/CBO9780511813429

Pinel, V., Hooper, A., De la Cruz-Reyna, S., Reyes-Davila, G., Doin, M. P., & Bascou, P. (2011). The challenging retrieval of the displacement field from InSAR data for andesitic stratovolcanoes: Case study of Popocatepetl and Colima Volcano, Mexico. *Journal of Volcanology and Geothermal Research*, *200*(1–2), 49–61. https://doi.org/10.1016/j.jvolgeores.2010.12.002

Pinkerton, H., & Sparks, R. S. J. (1978). Field measurements of the rheology of lava. *Nature*, *276*(5686), 383–385. https://doi.org/10.1038/276383a0

Pinkerton, H., & Stevenson, R. J. (1992). Methods of determining the rheological properties of magmas at sub-liquidus temperatures. In *Journal of Volcanology and Geothermal Research* (Vol. 53).

Poret, M., Corradini, S., Merucci, L., Costa, A., Andronico, D., Montopoli, M., Vulpiani, G., & Freret-Lorgeril, V. (2018). Reconstructing volcanic plume evolution integrating satellite and ground-based data: application to the 23 November 2013 Etna eruption. *Atmospheric Chemistry and Physics*, *18*(7), 4695–4714. https://doi.org/10.5194/acp-18-4695-2018

Poret, M., Costa, A., Andronico, D., Scollo, S., Gouhier, M., & Cristaldi, A. (2018). Modeling Eruption Source Parameters by Integrating Field, Ground-Based, and Satellite-Based Measurements: The Case of the 23 February 2013 Etna Paroxysm. *Journal of Geophysical Research: Solid Earth*, *123*(7), 5427–5450. https://doi.org/10.1029/2017JB015163

Procter, J. N., Cronin, S. J., Fuller, I. C., Sheridan, M., Neall, V. E., & Keys, H. (2010). Lahar hazard assessment using Titan2D for an alluvial fan with rapidly changing geomorphology: Whangaehu River, Mt. Ruapehu. *Geomorphology*, *116*(1–2), 162–174. https://doi.org/10.1016/j.geomorph.2009.10.016

Ramsey, M., Chevrel, M., Coppola, D., & Harris, A. (2019). The influence of emissivity on the thermo-rheological modeling of the channelized lava flows at Tolbachik volcano. *Annals of Geophysics*, *61*(Vol 61 (2018)). https://doi.org/10.4401/ag-8077

Reubi, O., & Blundy, J. (2008). Assimilation of Plutonic Roots, Formation of High-K ‘Exotic’ Melt Inclusions and Genesis of Andesitic Magmas at Volcán De Colima, Mexico. *Journal of Petrology*, *49*(12), 2221–2243. https://doi.org/10.1093/petrology/egn066

Rhodes, E., Kennedy, B. M., Lavallée, Y., Hornby, A., Edwards, M., & Chigna, G. (2018). Textural insights into the evolving lava dome cycles at Santiaguito Lava Dome, Guatemala. *Frontiers in Earth Science*, *6*. https://doi.org/10.3389/feart.2018.00030

Richet, P., & Bottinga, Y. (1995). Rheology and configurational entropy of silicate melts. In *Structure, Dynamics, and Properties of Silicate Melts* (pp. 67–94). De Gruyter. https://doi.org/10.1515/9781501509384-005

Riker, J. M., Blundy, J. D., Rust, A. C., Botcharnikov, R. E., & Humphreys, M. C. S. (2015). Experimental phase equilibria of a Mount St. Helens rhyodacite: a framework for interpreting crystallization paths in degassing silicic magmas. *Contributions to Mineralogy and Petrology*, *170*(1), 6. https://doi.org/10.1007/s00410-015-1160-5

Rittmann A. (1973). Mount Etna and the 1971 eruption - Structure and evolution of Mount Etna. *Philosophical Transactions of the Royal Society of London. Series A, Mathematical and Physical Sciences*, *274*(1238), 5–16. https://doi.org/10.1098/rsta.1973.0021

Robson, G. R. (1967). Thickness of Etnean Lavas. *Nature*, *216*(5112), 251–252. https://doi.org/10.1038/216251a0

Rocco Rongo, Maria Vittoria, Boris Behncke, Donato D'Ambrosio, Salvatore Di Gregorio, Valeria Lupiano, Marco Neri, William Spataro, & Gino M. (2011). Defining high-detail hazard maps by a cellular automata approach: application to Mount Etna (Italy). *Annals of Geophysics*, *54*(5). https://doi.org/10.4401/ag-5340

Rogers, N. (2015). The Composition and Origin of Magmas. In *The Encyclopedia of Volcanoes* (pp. 93–112). Elsevier. https://doi.org/10.1016/B978-0-12-385938-9.00004-3

Roscoe, R. (1952). The viscosity of suspensions of rigid spheres. *British Journal of Applied Physics*, *3*(8), 267–269. https://doi.org/10.1088/0508-3443/3/8/306

Rossler, E., Hess, K.-U., & Novikov, V. N. (1998). Universal representation of viscosity in glass forming liquids. In *Journal of Non-Crystalline Solids* (Vol. 223).

Rowland, S. K., & Walker, G. P. (1990). Pahoehoe and aa in Hawaii: volumetric flow rate controls the lava structure. *Bulletin of Volcanology*, *52*(8), 615–628. https://doi.org/10.1007/BF00301212

Russell, J. K., Giordano, D., & Dingwell, D. B. (2003). High-temperature limits on viscosity of non-Arrhenian silicate melts. *American Mineralogist*, *88*(8–9), 1390–1394. https://doi.org/10.2138/am-2003-8-924

Russell, J. K., & Giordano, D. (2017). Modelling configurational entropy of silicate melts. *Chemical Geology*, *461*, 140–151. https://doi.org/10.1016/j.chemgeo.2016.07.019

Russell, J. K., Hess, K. U., & Dingwell, D. B. (2022). Models for Viscosity of Geological Melts. In *Reviews in Mineralogy and Geochemistry* (Vol. 87, pp. 841–885). Mineralogical Society of America. https://doi.org/10.2138/rmg.2022.87.18

Rustico, E., Bilotta, G., Hérault, A., del Negro, C., & Gallo, G. (2011). Scalable multi-gpu implementation of the magflow simulator. *Annals of Geophysics*, *54*(5), 592–599. https://doi.org/10.4401/ag-5342

Salzer, J. T., Nikkhoo, M., Walter, T. R., Sudhaus, H., Reyes-Dávila, G., Bretón, M., & Arámbula, R. (2014). Satellite radar data reveal short-term pre-explosive displacements and a complex conduit system at Volcán de Colima, Mexico. *Frontiers in Earth Science*, *2*. https://doi.org/10.3389/feart.2014.00012

Schmincke, H.-U. (2004). Rheology, Magmatic Gases, Bubbles and Triggering of Eruptions. In *Volcanism* (pp. 35–58). Springer Berlin Heidelberg. https://doi.org/10.1007/978-3-642-18952-4_4

Sheldrake, T. E., Sparks, R. S. J., Cashman, K. V., Wadge, G., & Aspinall, W. P. (2016). Similarities and differences in the historical records of lava dome-building volcanoes: Implications for understanding magmatic processes and eruption forecasting. *Earth-Science Reviews*, *160*, 240–263. https://doi.org/10.1016/j.earscirev.2016.07.013

Sheridan, M. F., Stinton, A. J., Patra, A., Pitman, E. B., Bauer, A., & Nichita, C. C. (2005). Evaluating Titan2D mass-flow model using the 1963 Little Tahoma Peak avalanches, Mount Rainier, Washington. *Journal of Volcanology and Geothermal Research*, *139*(1–2), 89–102. https://doi.org/10.1016/j.jvolgeores.2004.06.011

Simmons, J., Elsworth, D., & Voight, B. (2005). Classification and idealized limit-equilibrium analyses of dome collapses at Soufrière Hills volcano, Montserrat, during growth of the first lava dome: November 1995–March 1998. *Journal of Volcanology and Geothermal Research*, *139*(3–4), 241–258. https://doi.org/10.1016/j.jvolgeores.2004.08.009

Snir, M., Otto, S. W., Huss-Lederman, S., Walker, D. W., & Dongarra, J. (1995). *MPI - The Complete Reference*. The MIT Press.

Sparks, R. S. J., Pinkerton, H., & Hulme, G. (1976). Classification and formation of lava levees on Mount Etna, Sicily. *Geology*, *4*(5), 269. https://doi.org/10.1130/0091-7613(1976)4<269:CAFOLL>2.0.CO;2

Starodubtseva, Yu. V., Starodubtsev, I. S., Ismail-Zadeh, A. T., Tsepelev, I. A., Melnik, O. E., & Korotkii, A. I. (2021). A Method for Magma Viscosity Assessment by Lava Dome Morphology. *Journal of Volcanology and Seismology*, *15*(3), 159–168. https://doi.org/10.1134/S0742046321030064

Starodubtsev, I. S., Starodubtseva, Y. V., Tsepelev, I. A., & Ismail-Zadeh, A. T. (2023). Three-Dimensional Numerical Modeling of Lava Dynamics Using the Smoothed Particle Hydrodynamics Method. *Journal of Volcanology and Seismology*, *17*(3), 175–186. https://doi.org/10.1134/S0742046323700185

Stevenson, J. A., & Varley, N. (2008). Fumarole monitoring with a handheld infrared camera: Volcán de Colima, Mexico, 2006–2007. *Journal of Volcanology and Geothermal Research*, *177*(4), 911–924. https://doi.org/10.1016/j.jvolgeores.2008.07.003

Tallarico, A., & Dragoni, M. (2000). A three-dimensional Bingham model for channeled lava flows. *Journal of Geophysical Research: Solid Earth*, *105*(B11), 25969–25980. https://doi.org/10.1029/2000JB900201

Tampubolon, J., Nainggolan, H., Ginting, A., & Aritonang, J. (2018). Mount Sinabung Eruption: Impact on Local Economy and Smallholder Farming in KaroRegency, North Sumatra. *IOP Conference Series: Earth and Environmental Science*, *178*, 012039. https://doi.org/10.1088/1755-1315/178/1/012039

Tarquini, S., & Favalli, M. (2016). Simulating the area covered by lava flows using the DOWNFLOW code. *Geological Society, London, Special Publications*, *426*(1), 293–312. https://doi.org/10.1144/SP426.15

Tsepelev, I., Ismail-Zadeh, A., Melnik, O., & Korotkii, A. (2016). Numerical modeling of fluid flow with rafts: An application to lava flows. *Journal of Geodynamics*, *97*, 31–41. https://doi.org/10.1016/j.jog.2016.02.010

Tsepelev, I., Ismail-Zadeh, A., Starodubtseva, Y., Korotkii, A., & Melnik, O. (2019). Crust development inferred from numerical models of lava flow and its surface thermal measurements. *Annals of Geophysics*, *61*(Vol 61 (2018)). https://doi.org/10.4401/ag-7745

Tsepelev, I., Ismail-Zadeh, A., & Melnik, O. (2020). Lava dome morphology inferred from numerical modelling. *Geophysical Journal International*, *223*(3), 1597–1609. https://doi.org/10.1093/gji/ggaa395

Tsepelev, I., Ismail-Zadeh, A., & Melnik, O. (2021a). 3D Numerical Modeling of the Summit Lake Lava Flow, Yellowstone, USA. *Izvestiya, Physics of the Solid Earth*, *57*(2), 257–265. https://doi.org/10.1134/S1069351321020129

Tsepelev, I., Ismail-Zadeh, A., & Melnik, O. (2021b). Lava Dome Evolution at Volcán de Colima, México During 2013: Insights from Numerical Modeling. *Journal of Volcanology and Seismology*, *15*(6), 491–501. https://doi.org/10.1134/S0742046321060117

Vicari, A., Alexis, H., Del Negro, C., Coltelli, M., Marsella, M., & Proietti, C. (2007). Modeling of the 2001 lava flow at Etna volcano by a Cellular Automata approach. *Environmental Modelling and Software*, *22*(10), 1465–1471. https://doi.org/10.1016/j.envsoft.2006.10.005

Voight, B., Sparks, R. S. J., Miller, A. D., Stewart, R. C., Hoblitt, R. P., Clarke, A., Ewart, J., Aspinall, W. P., Baptie, B., Calder, E. S., Cole, P., Druitt, T. H., Hartford, C., Herd, R. A., Jackson, P., Lejeune, A. M., Lockhart, A. B., Loughlin, S. C., Luckett, R., … Young, S. R. (1999). Magma Flow Instability and Cyclic Activity at Soufriere Hills Volcano, Montserrat, British West Indies. *Science*, *283*(5405), 1138–1142. https://doi.org/10.1126/science.283.5405.1138

Voight, B., & Elsworth, D. (2000). Instability and collapse of hazardous gas-pressurized lava domes. *Geophysical Research Letters*, *27*(1), 1–4. https://doi.org/10.1029/1999GL008389

Wadge, G. (1978). Effusion rate and the shape of aa lava flow-fields on Mount Etna. *Geology*, *6*(8), 503. https://doi.org/10.1130/0091-7613(1978)6<503:ERATSO>2.0.CO;2

Wadge, G., Young, P. A. V., & McKendrick, I. J. (1994). Mapping lava flow hazards using computer simulation. *Journal of Geophysical Research*, *99*(B1), 489–504. https://doi.org/10.1029/93JB01561

Wadge, G., Robertson, R. E. A., & Voight, B. (2014). *The Eruption of Soufrière Hills Volcano, Montserrat, from 2000 to 2010* (Vol. 39). Geol. Soc. London Mem. .

Walker. (1967). Thickness and viscosity of Etnean lavas. *Nature*, *213*, 484–485.

Walter, T. R., Harnett, C. E., Varley, N., Bracamontes, D. V., Salzer, J., Zorn, E. U., Bretón, M., Arámbula, R., & Thomas, M. E. (2019). Imaging the 2013 explosive crater excavation and new dome formation at Volcán de Colima with TerraSAR-X, time-lapse cameras and modelling. *Journal of Volcanology and Geothermal Research*, *369*, 224–237. https://doi.org/10.1016/j.jvolgeores.2018.11.016

Wang, Y., & Hutter, K. (2001). Comparisons of numerical methods with respect to convectively dominated problems. *International Journal for Numerical Methods in Fluids*, *37*(6), 721–745. https://doi.org/10.1002/fld.197

Wantim, M. N., Kervyn, M., Ernst, G. G. J., del Marmol, M. A., Suh, C. E., & Jacobs, P. (2013). Numerical experiments on the dynamics of channelised lava flows at Mount Cameroon volcano with the FLOWGO thermo-rheological model. *Journal of Volcanology and Geothermal Research*, *253*, 35–53. https://doi.org/10.1016/j.jvolgeores.2012.12.003

Watts, R. B., Herd, R. A., Sparks, R. S. J., & Young, S. R. (2002). Growth patterns and emplacement of the andesitic lava dome at Soufrière Hills Volcano, Montserrat. *Geological Society Memoir*, *21*(1), 115–152. https://doi.org/10.1144/GSL.MEM.2002.021.01.06

Webb, SharonL., & Dingwell, DonaldB. (1990). The onset of non-Newtonian rheology of silicate melts. *Physics and Chemistry of Minerals*, *17*(2). https://doi.org/10.1007/BF00199663

Xia, X., & Liang, Q. (2018). A new depth-averaged model for flow-like landslides over complex terrains with curvatures and steep slopes. *Engineering Geology*, *234*, 174–191. https://doi.org/10.1016/j.enggeo.2018.01.011

Yokoyama, I. (2009). Growth rates of lava domes with respect to viscosity of magmas. *Annals of Geophysics*, *48*(6). https://doi.org/10.4401/ag-3246

Young, P., & Wadge, G. (1990). FLOWFRONT: Simulation of a lava flow. *Computers & Geosciences*, *16*(8), 1171–1191. https://doi.org/10.1016/0098-3004(90)90055-X

Zago, V., Bilotta, G., Cappello, A., Dalrymple, R. A., Fortuna, L., Ganci, G., Hérault, A., & Del Negro, C. (2017). Simulating complex fluids with smoothed particle hydrodynamics. *Annals of Geophysics*, *60*(6). https://doi.org/10.4401/ag-7362

Zago, V., Bilotta, G., Hérault, A., Dalrymple, R. A., Fortuna, L., Cappello, A., Ganci, G., & Del Negro, C. (2018). Semi-implicit 3D SPH on GPU for lava flows. *Journal of Computational Physics*, *375*, 854–870. https://doi.org/10.1016/j.jcp.2018.07.060

Zeinalova, N., Ismail-Zadeh, A., Melnik, O., Tsepelev, I., & Zobin, V. (2021). Lava Dome Morphology and Viscosity Inferred From Data-Driven Numerical Modeling of Dome Growth at Volcán de Colima, Mexico During 2007-2009. *Frontiers in Earth Science*, *9*. https://doi.org/10.3389/feart.2021.735914

Zeinalova, N., Ismail-Zadeh, A., Tsepelev, I., Melnik, O., & Schilling, F. (2024). Numerical thermomechanical modelling of lava dome growth during the 2007-2009 dome-building eruption at Volcán de Colima. *Geophysical Journal International*, *236*(1), 290–304. https://doi.org/10.1093/gji/ggad415

Zobin, V. M., Luhr, J. F., Taran, Y. A., Bretón, M., Cortés, A., De La Cruz-Reyna, S., Domínguez, T., Galindo, I., Gavilanes, J. C., Muñíz, J. J., Navarro, C., Ramírez, J. J., Reyes, G. A., Ursúa, M., Velasco, J., Alatorre, E., & Santiago, H. (2002). Overview of the 1997–2000 activity of Volcán de Colima, México. *Journal of Volcanology and Geothermal Research*, *117*(1–2), 1–19. https://doi.org/10.1016/S0377-0273(02)00232-9

Zobin, V. M., Arámbula, R., Bretón, M., Reyes, G., Plascencia, I., Navarro, C., Téllez, A., Campos, A., González, M., León, Z., Martínez, A., & Ramírez, C. (2015). Dynamics of the January 2013–June 2014 explosive-effusive episode in the eruption of Volcán de Colima, México: insights from seismic and video monitoring. *Bulletin of Volcanology*, *77*(4), 31. https://doi.org/10.1007/s00445-015-0917-z

Zobin, V. M., Tellez, A., Aguilar, J. E., & Cruz, K. G. (2017). Seismic signals of rockfalls as indicators of the origin of lava fragments emplaced during the 2010 endogenous and exogenous growth in the crater of Volcán de Colima, México. *Bulletin of Volcanology*, *79*(6), 47. https://doi.org/10.1007/s00445-017-1130-z

Zobin, V. M., & Tellez, A. (2019). Precursors to intra-eruptive reposes during the 1998–2019 lava dome-building eruption at Volcán de Colima, México. *Bulletin of Volcanology*, *81*(8), 45. https://doi.org/10.1007/s00445-019-1307-8